Nanoparticules fluorescentes cœur-coquille organique@silicates pour l'imagerie vasculaire in vivo

Shridevi Shenoi Perdoor

Communauté
UNIVERSITÉ Grenoble Alpes

THÈSE

Pour obtenir le grade de

DOCTEUR DE LA COMMUNAUTÉ UNIVERSITÉ GRENOBLE ALPES

Spécialité : Chimie Biologie

Arrêté ministériel : 25 mai 2016

Présentée par

Shridevi SHENOI PERDOOR

Thèse dirigée par **Xavier CATTOËN, Chargé de recherche, Institut Néel, CNRS** et
codirigée par **Fabien DUBOIS, Maitre de conférence, Université Grenoble Alpes**

préparée au sein du **CNRS, à l'Institut Néel**
dans **l'École Doctorale Chimie et Sciences du Vivant**

Nanoparticules fluorescentes cœur-coquille organique@silicates pour l'imagerie vasculaire in vivo

Fluorescent organic@silicate core-shell nanoparticles for in vivo vascular imaging

Thèse soutenue publiquement le **27 Septembre 2018**,
devant le jury composé de :

Madame Veronica de Zea Bermudez
Professeur, Universidade de Trás-os-Montes e Alto Douro, Rapporteur
Madame Magali Gary-Bobo
Chargé de Recherche, Université de Montpellier, CNRS, Rapporteur
Monsieur Cyrille Train
Professeur, Université Grenoble Alpes, Président
Monsieur Yann Bretonnière
Chargé de Recherche, CNRS, ENS Lyon, Examinateur

Acknowledgements

I am extremely grateful for having been given the opportunity to work on this exciting, challenging, and innovative project, that not only helped build the foundation for my future professional career but also helped me grow personally. This thesis work could not have been possible without the help of so many colleagues and friends!

First and foremost, I would like to express my profound gratitude and deep regards to my supervisors, Xavier Cattoën and Fabien Dubois. They have not only guided me in my everyday work but have also been very patient, extremely encouraging, and enthusiastic throughout the course of this project.

I would like to thank Xavier for being a wonderful thesis director, for constantly supporting and motivating me, proposing interesting ideas and solutions, and for his availability at all times during the course of this thesis. I truly appreciate all the scientific discussions we had throughout the course of this PhD, which helped solve several problems that were encountered along the way, thanks to his immense knowledge in the field of sol-gel chemistry. I am especially grateful to him for helping me with all the organic synthesis experiments, which he always made seem so simple, reflecting his remarkable expertise in this field. I also thank him for his detailed and accurate feedback on my scientific writing, meaningful suggestions, and insightful discussions, which helped me enhance my technical writing skills. Furthermore, I would also like to thank him for facilitating administrative procedures in his best capacity, for helping me get settled in Grenoble, and for going out of his way to help me with non-work related tasks ranging from filling out official forms in French, to translation of documents from French to English, which simplified life in so many different ways.

I would like to thank Fabien for being extremely patient, understanding, and supportive throughout this PhD, which made working with him easy and delightful. I am also greatly indebted to him for helping me find solutions to many difficult problems that we faced during this project, thanks to his profound knowledge in the field of fluorescence spectroscopy and nanoparticle concentration strategies. I highly esteem his immense scientific expertise, incredible optimism, and constant encouragement throughout my PhD. I could not have imagined having better directors for my PhD thesis, who made working with them wonderful and enriched this project with their varied expertise.

This project would have been incomplete without Alain Ibanez, who first welcomed me into the laboratory when he was serving as the director of PLUM department (MCMF then). He has been a pillar of support and guiding beacon throughout this PhD, always sharing his wisdom and profound knowledge in the field of crystallization, spray-drying, and sol - gel chemistry. Despite his busy schedule and involvement in several different scientific projects, he always found the time to propose consistently excellent improvements and stimulating

scientific ideas. He has not only guided me in my research but also shared anecdotes, jokes, and life lessons that I will cherish forever. His genuine interest in different aspects of science and technology, experimental intuition, and sincere dedication to constantly learn and master new concepts and techniques, are truly inspiring to me. His accurate feedback of my technical writing has been invaluable, and he also managed the difficult task of keeping in touch with all our current and potential future collaborators, giving a new shape and direction to this project. Furthermore, I am truly thankful for his selfless dedication to both my academic and personal development, and for being a great mentor.

I would like to acknowledge and thank Chantal Andraud and Yann Bretonnière, for collaborating with us on this project. I thank Chantal for facilitating interactions with the different collaborators of this project, despite her incredibly busy schedule and providing access to the different research facilities at ENS Lyon. I am extremely grateful to Yann for not only synthesizing and providing the red dyes that I worked on during this project, but also for all the stimulating scientific exchanges we had, which helped us answer several questions during this project. I am also thankful to him for carrying out the optical measurements on my samples and sharing his exceptionally deep knowledge on fluorescence spectroscopy and design of organic dyes. Finally, I would also like to thank him for agreeing to be a part of the jury and PhD examination process, and providing insightful remarks and suggestions during the wonderful scientific discussion we had.

I am extremely grateful to Patrice Baldeck for the two-photon experiments that helped complete a big part of my thesis objectives and explore a rather challenging facet of this work. I appreciate his interest in my work and taking it further, his insightful remarks and interesting discussions on difficult questions we were faced with during this project. I also acknowledge Noëlle Lascoux for performing the two-photon experiments and helping me analyze the data.

I am highly indebted to Olivier Pascual at Claude Bernard University, Lyon for performing the *in vivo* tests in mice, which added a new dimension to my project and helped me realize a major objective of my thesis. I am extremely grateful to him for performing these tests at a very short notice, literally weeks before the submission of my thesis, his valuable feedback, and sincere efforts to help me complete my PhD project successfully. I also acknowledge Ines Hristovska for preparing the experimental setup and analyzing the data from these experiments.

I take this opportunity to express a deep sense of gratitude to the reviewers of my thesis, Veronica de Zea Bermudez and Magali Gary-Bobo for accepting to be a part of my thesis committee and for their insightful remarks and comments on my work, their words of encouragement and appreciation. I am lucky to have had such wonderful reviewers, with whom I was able to have an insightful and mature scientific discussion. I am also grateful to

Cyrille Train, the President of my thesis jury, for accepting to be a part of my thesis committee and for his wonderful comments and suggestions.

I would like to acknowledge Olivier Stephan, for giving me access to the Dynamic Light Scattering setup at Liphy, which helped me complete a significant part of my work. I thank Béatrice Gennaro at DCM for performing the ^{29}Si NMR experiments on my sols and for her genuine interest in resolving the challenges we encountered and proposal of different ideas to delve deeper into the subject.

I would also like to extend my gratitude to Mickaël Sanchez for his cordial support and guidance, which helped me through various stages of this project, when I first started working at Institute Neel as a master thesis intern. At this time, I also met Marine Liotaud who helped me generously, not only with my project but also helping me find a house in Grenoble and even helping me furnish it. I truly appreciate her optimism, kindness and genuine support and encouragement.

I am thankful to all the researchers, technicians, and engineers in the laboratory, who have helped me with different aspects of my project. A special thanks to Christophe Bouchard and Alain Prat for maintaining the spray-drying reactor that I used extensively during my time in the lab and for always promptly fixing parts that I broke (accidentally, of course) on multiple occasions. I also appreciate their efforts in improving the design of the reactor, which made it more convenient for me to work efficiently.

I thank Sébastien Pairis for teaching me how to operate the Scanning Electron Microscope, a tool that I used extensively during my thesis. I am grateful to Stéphanie Kodjikian for performing the Transmission Electron Microscopy experiments and her constant efforts to tailor the experiments to resolve the challenges associated with my incredibly sensitive and delicate samples. I also appreciate her valuable scientific feedback, discussions, and kind words of encouragement throughout my PhD. I am indebted to Olivier Leynaud for helping me with the X-ray Diffraction measurements, that were not easy to perform and analyze. I truly appreciate his sincere efforts and patience in trying different setups to investigate the crystallinity of my samples and his readiness to resolve issues and find solutions promptly. I thank Mathieu Salaün for performing the Thermogravimetric analysis measurements, which were also scheduled at very short notice and for his valuable scientific feedback. A special thanks to Philippe Plaindoux for not only helping me with Differential Scanning Calorimetry measurements but for also helping me get settled in Grenoble.

I also take this opportunity to thank Aude Barbara for the Dynamic Light Scattering measurements at Institute Néel and helping me understand the underlying physics of the measurement technique. This not only added depth to my work but also helped clarify several questions that arose during this work. I am grateful to her for always finding the time to

perform measurements on the home-built setup at Neel, the valuable scientific feedback on my thesis manuscript and her genuine efforts to always help me with a smile, which made working with her a truly wonderful experience.

I am grateful to Geraldine Dantelle for helping me with the photostability measurements I performed on my samples and I also appreciate her warmth and kind words of support. I thank Isabelle Gautier-Luneau for her kindness, words of encouragement and warmth during my time here in the lab. A big thank you to Benoit Boulanger and the entire team of Optima, who welcomed me and gave me numerous opportunities to present and discuss my work in a stress-free setting. I also acknowledge Etienne Bustarret, director of Institute Néel and Serge Huant, director of PLUM department for giving me access to all the research facilities at Institute Néel. I am grateful to Muriel Boyer for helping me with the administrative procedures, when I first started working here as a Master Thesis intern. I appreciate her readiness and willingness to help, kind words and warmth. I am also very thankful to Florence Pois and Elodie Bernard, for always helping me with administrative difficulties, helping me understand the French taxes and health insurance system and clarifying all my questions related to non-work issues as well. A special thanks to Yohan Milin for his kind words of encouragement and prompt processing of travel requests and returns.

This incredibly adventurous journey was made even more special, thanks to all my friends, fellow doctorate students, post-docs, and interns, who provided immense moral support, encouragement and hope at the most difficult times. I not only had the chance to grow professionally, but also personally as it was truly enriching to meet people from around the world and experience new cultures. A special thanks to Cyril, who embarked on this journey with me and grew to become one of my closest friends in the lab (or as he says, 'Labstie'), sharing my joys and sorrows, ups and downs, entertaining all of us in the lab with his unique sense of humor and motivating me to go to the gym every week. I would also like to thank Elodie, Sydney, Marlon, Christophe, Swati, Nitika, Goutham, Ana, Michelle, Hugo, Smail, Alexandra, Sylvain, Augustin, Ashutosh and Vartika for creating such a pleasant atmosphere at Néel, which made working here a lot of fun. I would like to thank Mario for being a great friend and my savior during the course of the two-year long REI label training, which helped me obtain credits. I am forever indebted to him for patiently translating all the classes and meetings (in French) and helping me finish the training successfully. I will cherish our (million) coffee-breaks, pizza dinners and deep discussions on life and science. I also thank Alvaro, for not only being a friend but for also being the co-organizer of the Non-Permanent Seminars, and helping me with all the different tasks we had to undertake.

A special thanks to Jorge, one of my closest friends (or should I say, friends-like family) in Grenoble, who also shared this journey with me. I can't thank him enough for being such an amazing friend, for always being there for me, cheering me up on bad days and helping me with countless things ranging from helping me move, to helping organize my defense

reception, to all the wonderful dinners and trips we went on. I also thank Tomas, another one of my close friends, who I have known for almost five years now, for always being there for me, constantly making me laugh, providing endless entertainment with his interesting stories and adventures, making the most amazing pizzas and desserts and for also being my contact at Liphy. A big thank you to Lilou, Marila, Vanni and Raquel for all the dinners, lunches, Uno sessions, parties, and fun times, that made my stay here in Grenoble incredibly fun and memorable. I am surely going to miss them all.

A heartfelt thank you to my best friends, Amaris and Ricardo, for not only being my support system here in Grenoble, but also my family and home away from home. I am convinced that Amaris is truly an angel disguised in human form and can't thank her enough for being such an amazing person, my confidante, for constantly supporting and encouraging me, cooking incredibly delicious Mexican food, and taking care of me like her little sister. I am also extremely grateful to her for proof-reading my thesis and giving me her valuable feedback. I am grateful to Ricardo for constantly being there for me, for helping me with innumerable things, particularly various tech issues, and for bringing my laptop back to life when it gave up on me while writing my thesis. A big thank you to both for making my stay in Grenoble extremely memorable and for creating such wonderful memories that I will cherish forever.

I also take this opportunity to thank my friends outside Grenoble, Vamsi, Finub, Divya, Manoj, Sriram, Dhanya, Yash and Harita, my Indian family in Europe. A special thank you to Vamsi, for not only proof-reading my thesis but for also being an amazing human being, always supporting and motivating me with his words of wisdom and being an incredible pillar of support, especially during difficult times.

None of the words I could possibly find are enough to describe how much I owe my success to my family. I am extremely lucky to have been blessed with such loving parents and wonderful sister. I deeply and sincerely thank my family for always believing in me, encouraging me, standing by me, and supporting all my decisions. They have always been there for me, uplifted my spirits in difficult times, constantly looked out for me, and have been my support system, despite being 4400 miles away from me. I am extremely thankful to my parents for flying all the way here to attend my defense and preparing the most amazing and perfect reception. I owe everything to them and words cannot describe the unconditional love and support they have always given me. A big thank you and massive hug to my sister for her unconditional love, support, and encouragement, which played a big role in helping me complete my thesis.

I am lucky to have embarked on this journey with the support of so many wonderful people and I will cherish these three years of my life forever. A big thank you to everyone, from the bottom of my heart.

Table of Contents

List of abbreviations

AzPTES	(3-Azidopropyl) triethoxysilane
BSA	Bovine Serum Albumin
CMONS	α(4'-Methoxyphenyl) methylene]-4-nitro-benzeneacetonitrile
CuAAC	Cu(I)-catalyzed 1,3- cycloaddition of organic azides to alkynes
DCM	Dichloromethane
DLS	Dynamic Light Scattering
DTA	Differential Thermal Analysis
Dye I	(E)-2-(benzo[d]thiazol-2-yl)-3-(4-diphenylamino)phenyl)acrylonitrile
Dye II	(Z)-2-(4-nitrophenyl)-3-(3,4,5-trimethoxyphenyl)acrylonitrile
Dye III	(Z)-3-(9-ethyl-9H-carbazol-3-yl)-2-(4-nitrophenyl)acrylonitrile
Dye IV	(E)-4-(2-(9-ethyl-9H-carbazol-3-yl)vinyl)-5-5'-dimethyl-3-(phenylsulfonyl)furan-2(5H)-one
FESEM	Field Emission Scanning Electron Microscopy
FNP	Functionalized Nanoparticle
FTIR	Fourier Transform InfraRed
GM	Goeppert Mayer
M_n	Number-averaged Molecular weight
MRI	Magnetic Resonance Imaging
MSN	Mesoporous Silica Nanoparticle
MWCO	Molecular Weight Cut-Off
NC	Nanocrystal
NLO	Non Linear Optics
NMR	Nuclear Magnetic Resonance
NP	Nanoparticle

List of abbreviations

OPE	One-Photon excitation
PB	Phosphate Buffer
PBS	Phosphate Buffer Saline
PEG	Polyethylene glycol
PES	Polyethersulfone
PET	Positron Emission Tomography
PZC	Point of Zero Charge
QD	Quantum Dot
RES	Reticulo-Endothelial System
SBF	Simulated Body Fluid
SPECT	Single Photon Emission Computed Tomography
TEM	Transmission Electron Microscopy
TGA	Thermogravimetric Analysis
THF	Tetrahydrofuran
THPTA	Tris(3-hydroxypropyltriazolylmethyl)amine
TMOS	Tetramethoxysilane
TMSE	1,2-bis (trimethoxysilyl)ethane
TPA	Two-Photon Absorption
TPE	Two-Photon Excitation
TPF	Two-Photon Fluorescence
UCNP	Up-Converting Nanoparticles
XRD	X-Ray Diffraction

General Introduction

Developments in the field of non-linear optical probes have led to several advances in bioimaging. These have not enabled early diagnosis of diseases, but have also helped determine efficient treatment strategies. Optical probes need to fulfill several criteria such as biocompatibility, sensitivity, specificity and advanced photophysical properties to be employed as tracers for bioimaging. The primary objective of this work is the development and optimization of a family of fluorescent organic@silicate core-shell nanoparticles (NPs) containing an organic core surrounded by a silicate shell, with a high loading of crystal-state emitting dyes (30-40 %wt) for two-photon imaging of tumor vasculature.

Chapter I deals with general advances in the field of bioimaging, with a focus on optical imaging techniques and the different nanoparticulate tracers that have been developed over the years for use in such applications. Factors influencing the colloidal stability of NPs in different biological media have also been highlighted to study their effect on the *in vitro* behavior and their role in determining the *in vivo* fate. Furthermore, the concepts of nanocrystallization and sol-gel chemistry for the synthesis of composite organic@inorganic core-shell nanoparticles have been described. Lastly, click functionalization strategies have been described as a possible route to functionalize the synthesized NPs to improve their biocompatibility.

Chapter II deals with the encapsulation of crystal-state emitters in sol-gel matrices. This chapter focusses on the development and optimization of a family of red-emitting fluorescent organic@silicate core-shell nanoparticles (NPs). These core-shell NPs, which comprise an organic dye nanocrystal core (ca 40-50 nm) surrounded by a silicate crust, are prepared by an original spray-drying technique combining sol-gel chemistry and nanocrystallization, developed in our group. The synthesis of these core-shell NPs requires precise control over both the nanocrystallization process and the sol-gel chemistry to optimize the self-assembling one-step process for the preparation of core-shell NPs. This chapter also presents a comprehensive physico-chemical characterization of the morphology of the synthesized NPs and their crystallinity using X-Ray diffraction and electron microscopy techniques. Finally, the optical properties of these core-shell NPs using fluorescence spectroscopy are also presented.

Chapter III deals with the preparation of stable colloidal NP suspensions for biological applications. This in turn requires optimization of post-synthesis treatment strategies to obtain colloidally stable suspensions in physiologically relevant conditions. Furthermore, the study of the colloidal stability of the core-shell NPs suspensions in different biological media using Dynamic Light Scattering is presented. The use of click functionalization strategies to render the NPs furtive and increase their blood circulation time, and its effects on the colloidal stability of the NPs is also described. Finally, the conditions necessary for *in vivo* vascular imaging in mice

are presented. Evaluation of the NPs *in vivo* highlights the need for a more thorough size selection of NPs (< 100 nm) to enable longer circulation time in blood. Although it was difficult to achieve high furtivity, the NPs so obtained display good colloidal stability in physiological conditions and show high brightness under two-photon excitation, a feature that makes these novel nanotracers highly promising for future work.

Chapter I- Introduction

1.1. Bioimaging

Bioimaging, lies at the interface between biology and imaging, and refers to the visualization, characterization, and measurement of biological processes in humans and other living systems such as animal models (mouse, rat, rabbit, monkey, etc) as shown in Figure 1.1.[1–3] The development of bioimaging has not only enabled the study of fundamental biological processes, which in turn helps in understanding disease pathways better, but has also led to more accurate diagnosis of diseases. In addition to early screening of diseases, bioimaging can also determine the extent of disease, identify and evaluate the treatment strategy required for a more personalized treatment that is not only targeted to the disease but is also patient-specific, leading to more effective treatment.[2]

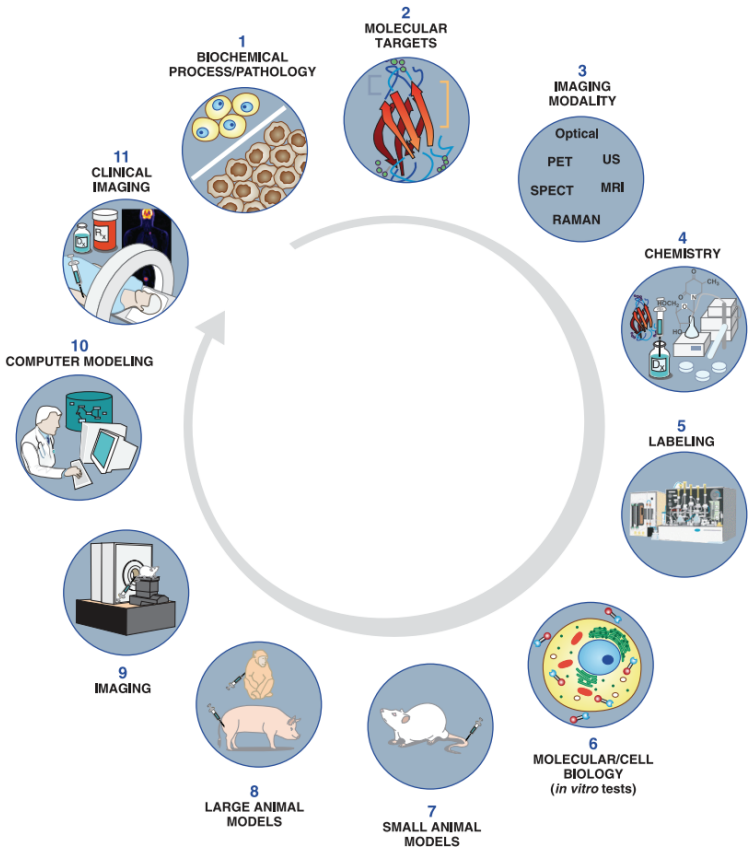

Figure 1. 1. Steps involved in bioimaging [4]

In addition to personalized medicine, bioimaging is also widely being employed in the field of drug development. Typically, drug development is a time intensive and expensive process with

several steps starting from target identification and compound optimization to preclinical and clinical trials.[5] Bioimaging has significantly contributed to the field of drug discovery and development thanks to its ability to non-invasively evaluate the pharmacokinetic and pharmacodynamic properties of the candidate drug, at different stages of development thereby significantly reducing attrition rates and saving time and money. [5]

Bioimaging utilizes different imaging modalities and their corresponding contrast agents to provide a wide range of information about a biological target at different levels of resolution. The most widely used modalities are Magnetic Resonance Imaging (MRI), Positron Emission Tomography (PET), Single Photon Emission Computed Tomography (SPECT), ultrasound imaging and optical imaging (Figure 1.2).

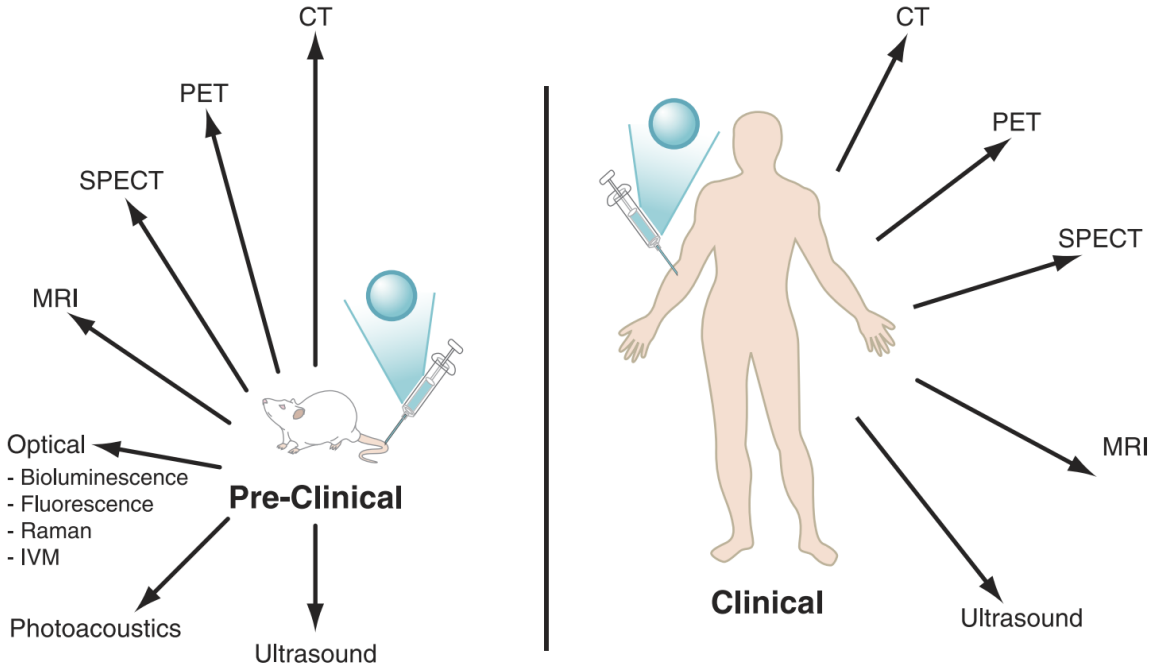

Figure 1. 2. Key bioimaging modalities used for preclinical and/or clinical applications [4]

These imaging modalities use different types of contrast agents and span the electromagnetic spectrum ranging from the use of radio frequency waves for MRI to ultrasonic waves for ultrasound imaging to visible-infrared light for optical imaging and gamma rays for PET and SPECT (Figure 1.3). They also have different spatial resolutions, advantages, and limitations, which are summarized in Table 1.1.

Table 1. 1. Different bioimaging modalities

Type	Energy form used	Imaging time	Advantages	Limitations	References
Magnetic resonance imaging (MRI)	Radio frequency waves	Minutes to hours	• Moderate spatial resolution (< 1–3 mm^3) • Unlimited depth penetration • Whole body imaging possible	• Low sensitivity • Expensive • Long acquisition time	[3,6,7]
Positron Emission Tomography (PET)	Gamma rays	Minutes	• High sensitivity • Unlimited depth penetration • Quantitative • Whole body imaging possible	• Low spatial resolution (~3-5 mm^3) • Radiation hazard • Long acquisition time	[3,7–9]
Single Photon Emission Computed Tomography (SPECT)	Gamma rays	Minutes	• High sensitivity • Unlimited depth penetration • Quantitative • Whole body imaging possible	• Low spatial resolution (~5 mm^3) • Radiation hazard • Long acquisition time	[3,7,10,11]
Optical Imaging	Visible-Infrared Light	Seconds to minutes	• High sensitivity • High spatial resolution (~1-2 µm) • No ionizing radiation • Inexpensive • Short acquisition time/ Real-time imaging • Multiplexing	• Limited depth penetration • Reduced imaging area	[3,7,12–18]
Ultrasound Imaging	High-frequency sound waves	Seconds to minutes	• High sensitivity • No ionizing radiation • Inexpensive • Short acquisition time/ Real-time imaging • Moderate spatial resolution (1 mm)	• Whole body imaging not possible • Limited contrast agents	[3,7,19–22]

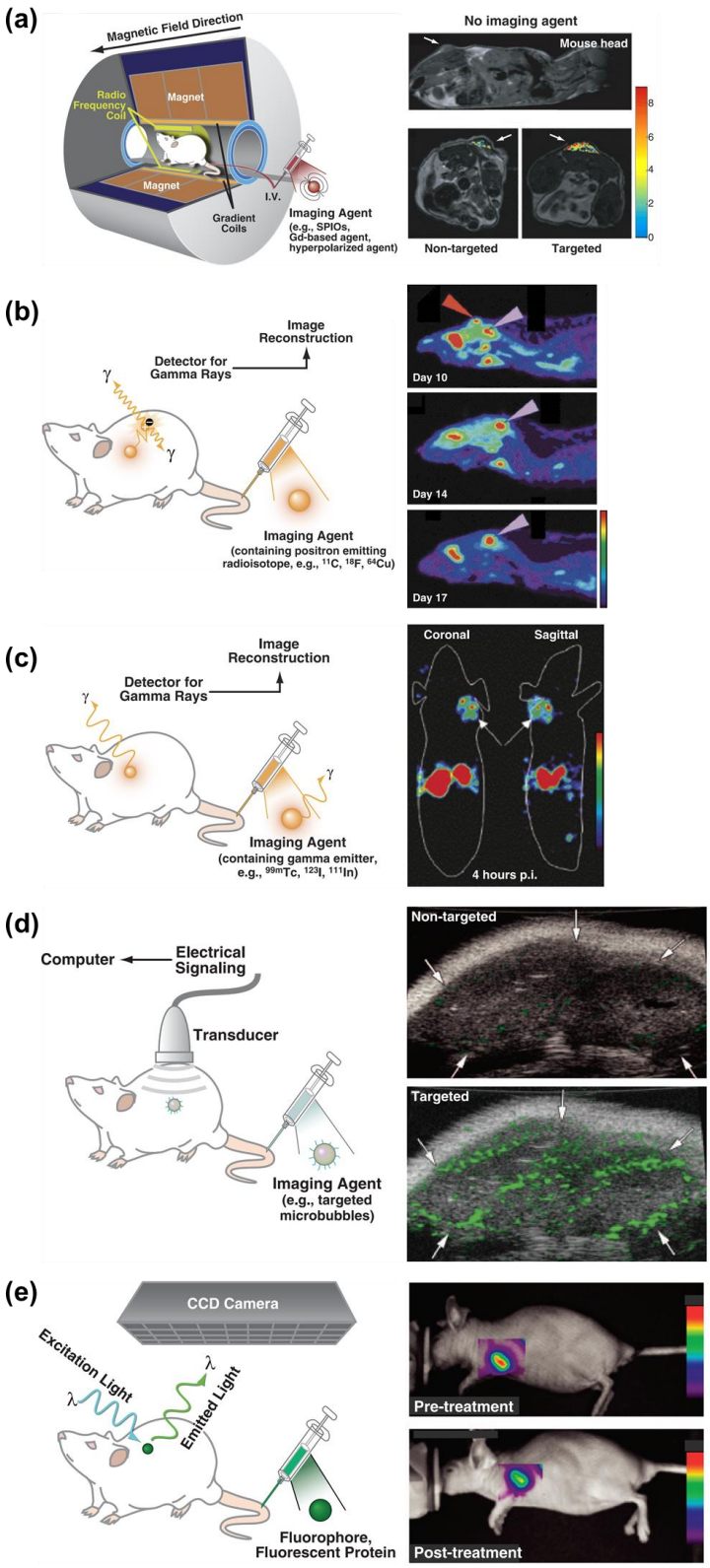

Figure 1. 3. (a) Small animal magnetic resonance imaging (MRI), (b) Small animal positron emission tomography (PET), (c) Small animal single photon emission computed tomography (SPECT), (d) Small animal ultrasound (US), and (e) Optical fluorescence imaging.[4]

Optical Imaging

While PET, SPECT and MRI have already established a firm foothold in clinical tests, optical imaging is mainly used for small animal testing, due to limited depth penetration. However, there have been several advances in the field of optical imaging, which could aid in its clinical transition. Optical imaging techniques, such as bioluminescence and fluorescence imaging, offer several advantages over currently used clinical imaging modalities such as MRI, SPECT and PET in that they are safe (depending on the type of contrast agent), inexpensive and offer high sensitivity, high spatial resolution, high signal to noise ratio in the near infrared spectral region and the use of low concentrations of contrast agent. [14–16,23]

Optical Imaging Techniques

While bioluminescence imaging is very commonly used for bioimaging in small-animal models and typically uses luciferase enzymes for the production of light, *in vivo* fluorescence imaging offers different levels of resolution and imaging depths depending on the technique used. Intravital microscopy techniques enable cellular and sub-cellular analysis, while fluorescence molecular tomography (FMT) can image bigger volumes spanning a few cubic centimeters, allowing whole-animal imaging in small animal models and imaging of entire human organs, albeit at a low resolution.[14,23] The problem of limited depth penetration, which has mainly restricted the use of optical imaging to dermal and ocular applications, can now be overcome with non-linear optics and the development of multiphoton microscopy techniques. For deep tissue imaging (depth greater than a few millimeters), near infrared fluorophore probes and dyes are required to overcome the problem of autofluorescence, light scattering and attenuation by tissues and the absorption of light by hemoglobin, lipids and water (Figure 1.4).

There are several high-resolution *in vivo* optical imaging techniques that can provide information ranging from the quantification of cancer biomarkers to the imaging of signaling pathways. Confocal microscopy is a real-time imaging tool that makes use of a pinhole to reject out of focus light from the specimen to generate high contrast images of thin optical sections of the specimen within intact cell cultures or thick tissues by raster scanning the sample. This ability to isolate thin layers of the specimen enables real-time imaging of morphological indicators of cancer progression such as nuclear size and nuclear-to-cytoplasmic ratio [24] using non-specific exogenous contrast agents such as Acriflavine. When used with molecular-specific exogenous contrast agents, confocal microscopy can be used to target overexpressed receptors in cancer cells. Examples include the use of a monoclonal antibody conjugated to an organic dye (Alexa Fluor 660) for the detection of vascular endothelial growth factor [25], fluorescent dye Cy5.5-labeled anti-EGFR monoclonal antibody Erbitux to detect EGFR expression level in MDA-MB-231 and MCF-7

breast cancer xenografts [26], and cathepsin-inducible near infra-red fluorescent probes to visualize intestinal polyps of mice hemizygous. [27]

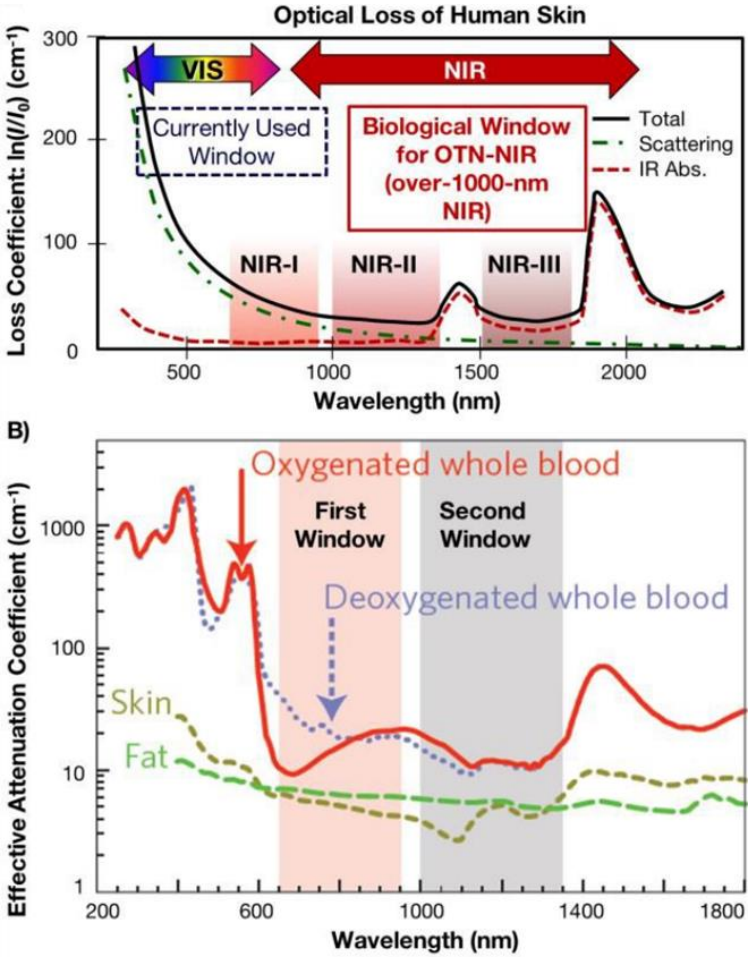

Figure 1. 4. (a) Absorption spectrum of human skin showing the first (NIR-I), second (NIR-II) and third (NIR-III) biological windows and (b) plot of effective attenuation coefficient versus wavelength for oxygenated and deoxygenated blood, skin and fatty tissue[28]

Confocal microscopy can be performed either in reflectance or fluorescence mode. Although it can be used to produce high-contrast images enabling the extraction of significant information at the cellular level, for deep-tissue imaging at high resolution, several novel non-linear optical microscopy techniques such as multiphoton fluorescence and harmonic generation, (Figure 1.5) have been developed.

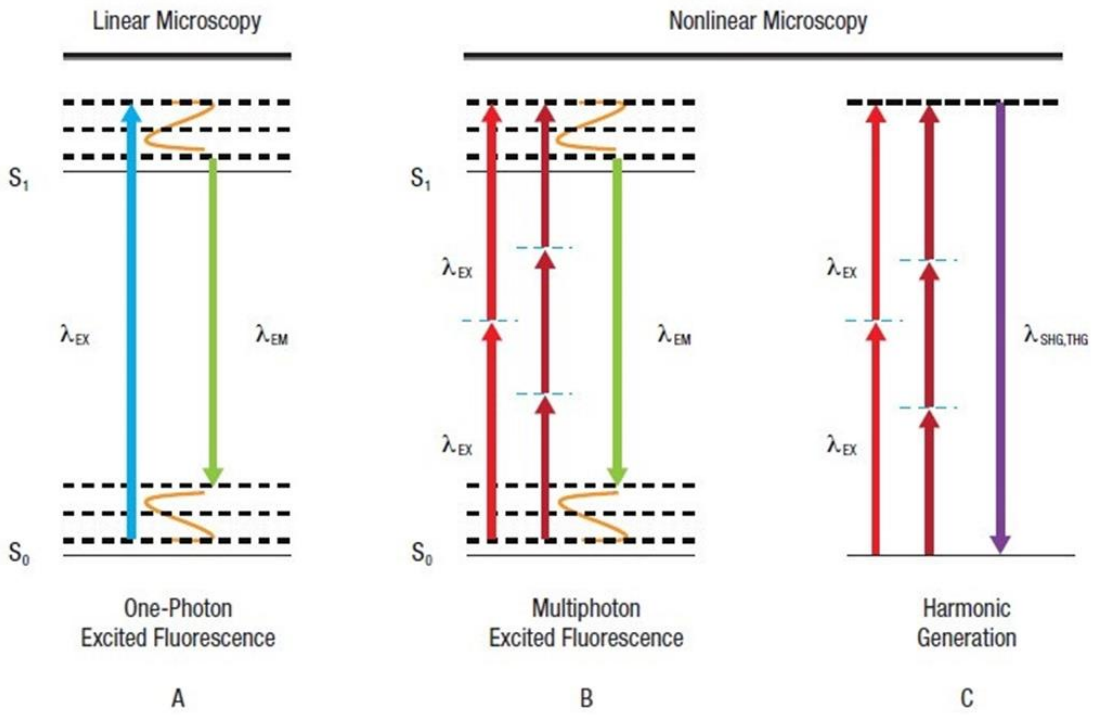

Figure 1. 5. Signal Generation in Laser Scanning Microscopy. In processes A and B, absorption of one (or more) excitation photons (λ_{EX}) promotes the molecule from the ground state (S_0) to the excited state (S_1) and fluorescence (λ_{EM}) is emitted when the molecule returns to the ground state. In process C, the excitation photons (λ_{EX}) simultaneously convert into a single photon ($\lambda_{SHG, THG}$) of the sum energy and half (for SHG) or one-third (for THG) the wavelength without being absorbed. [29]

Multiphoton microscopy, which makes use of the simultaneous absorption of two (or more) photons, each with half the energy (and twice the wavelength) of the corresponding single photon transition, to excite the fluorophore enables deeper tissue penetration as it typically shifts the excitation wavelength from the blue to the biological transparency window in the NIR range. There are significant differences between the optical configurations of confocal and multiphoton (*for example,* two-photon) microscopes as shown in Figure 1.6. In a confocal microscope, the excitation light (UV or visible) is reflected by a dichroic mirror to the microscope objective and focused into the specimen. The one-photon fluorescence signal generated from the focal spot is captured by the same objective, and passed through a pinhole to reject out of focus light, before reaching the detector. In a two-photon microscope, the excitation light (pulsed NIR laser) is reflected by a dichroic mirror to the microscope objective into the specimen and the two-photon induced fluorescence generated at the diffraction-limited volume[30] is collected by the same objective and sent to the detector, without the need for a pinhole. This results from the ability of multiphoton microscopy to collect scattered emission photons as a useful signal as the probability of photon absorption is a non-linear function of excitation radiance, thereby avoiding out of focus light, without pinhole.

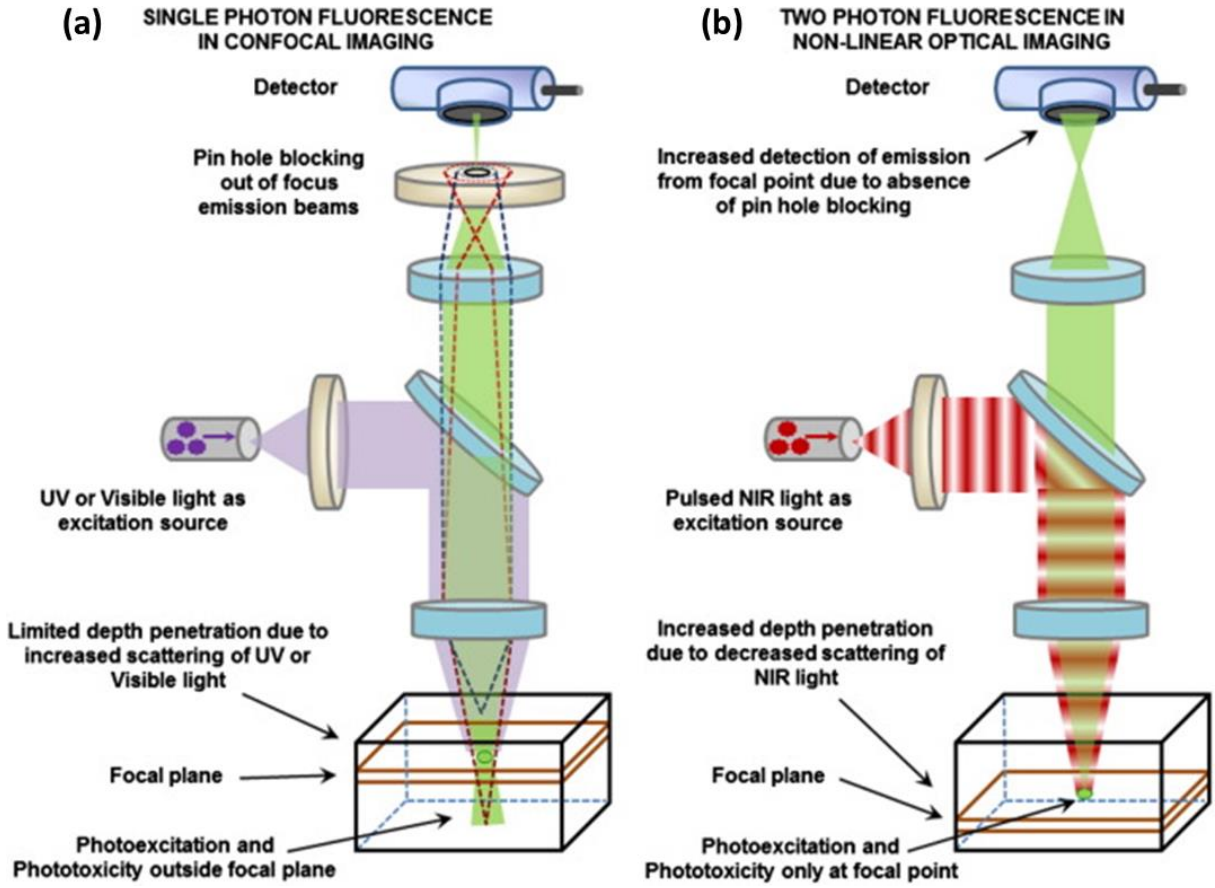

Figure 1. 6. Difference between single photon fluorescence confocal imaging and two photon fluorescence imaging[31]

Deeper tissue penetration is a direct result of reduced scattering, owing to the use of longer wavelengths in the infrared range for excitation. Additionally, photodamage is greatly minimized due to the use of lower energy photons and confinement of fluorescence emission to a diffraction limited spot.[30] This makes two-photon microscopy ideal for high-resolution (down to the µm), deep-tissue, real-time imaging and tracking of dynamic processes in cell biology.[31] This, in turn, has enabled the visualization of a multitude of processes at depths beyond several hundred microns allowing the quantification of receptors over-expressed in cancer cells and the imaging of tumor vasculature formed by angiogenesis. Two-photon microscopy has been used for both *in vivo* and *ex vivo* studies. *Ex vivo* applications typically involve the observation of microstructures of animal or human tissue to compare morphological changes in normal and cancerous samples and image overexpressed receptors in cancer cells. This has been used to study human esophageal tumor progression,[32] differentiation between normal and cancerous gall bladder tissues[33], identification of prostatic and periprostatic structures in freshly excised tissue from human radical prostatectomy specimens[34] and imaging of HER2-overexpressing SK-BR-3 breast cancer cells.[35] *In vivo* studies have mainly been carried out in small animal models. Some examples include monitoring of endocytosis in submandibular salivary glands in live rats,[36]

intravital imaging of colorectal liver metastasis development in live mice to observe metastatic nodules containing viable cancer cells and surrounding stroma with tumor vessels,[37] and sub-cellular imaging of cancer cells expressing GFP using an Alexa Fluor 594-conjugated anti-carcinoembryonic antigen (CEA) antibody in mouse models.[38]

In addition to imaging with fluorescent probes, other non-linear optical techniques have been developed such as second harmonic generation (SHG) and Coherent anti-Stokes Raman Scattering (CARS). Second harmonic microscopy is based on the generation of an optical field of twice the frequency (*i.e.* half the wavelength) of the incident light upon interaction with non-linear materials lacking inversion symmetry. The biggest advantage of second harmonic microscopy is that photobleaching and phototoxicity of dye molecules can be completely avoided as this process relies on endogenous molecular properties. A typical example of a material that can be examined using second harmonic microscopy is collagen, which is known to be a key component in tumor microenvironments. SHG has been used to visualize and study collagen-fibril structures and bundle orientation in normal and cancerous tissues for ovarian cancer,[39] breast cancer,[40–42] stage 1 colorectal adenocarcinoma,[41] brain tumors[43] and for noninvasive estimation of drug accessibility in tumors and measurement of enzymatic modification of tumor collagen, by dynamic imaging of collagen fibers *in vivo*.[44] Two-photon microscopy combined with second harmonic microscopy has been used to examine the characteristics of carcinoma invasion in human colorectum tissue,[45] early changes of colonic submucosa in a mouse model of colorectal cancer[46] and to monitor pathological progression in oesophageal diseases at the molecular level, especially for early oesophageal cancer.[32]

CARS microscopy is a third-order non-linear optical method that allows the imaging of specific molecular species in a complex microenvironment by tuning two collinear laser beams such that their frequency difference matches the frequency of the molecular vibration of interest in order to generate a strong signal at the anti-Stokes frequency. CARS has been used to investigate morphological differences between normal and cancerous kidney tissues,[47] for differential diagnosis of lung carcinomas,[48] imaging of lipids in cancer metastasis[49] and lipid-rich circulating tumor cells in human prostate cancer cell lines,[50] and to delineate brain tumors in orthotopic mouse models and human glioblastoma.[51]

These advances in non-linear optical imaging techniques are often complemented with the development of efficient non-linear optical probes. It is indeed crucial to develop fluorescent probes, with suitable properties for their use as tracers in optical bioimaging. These tracers should not only exhibit advanced photophysical properties and non-linear optical phenomena such as two-photon absorption, but also be fluorescent in the near infrared to enable deep tissue penetration and minimize the effects of tissue autofluorescence. Additionally, they should be biocompatible, highly sensitive and specific. Nanoparticles (NPs) fulfill these criteria, offer several advantages and are hence, increasingly being explored for use as tracers.

1.2. Nanoparticulate tracers

In addition to new technologies and sophisticated instrumentations, multifunctional nanoparticulate tracers play a huge role in the advancement of bioimaging. In the case of optical imaging, fluorescent NPs are excellent candidates because they offer several advantages over molecular dyes such as advanced photophysical and chemical properties, leading to higher brightness and multifunctionality, which results from the possibility to decorate the surface of NPs with different functional groups and the ability to activate or deactivate the NPs in response to external chemical or physical stimuli.[52] Several different types of fluorescent NPs have been developed over the years such as quantum dots, metallic NPs, upconverting NPs and dye-doped silicate/polymeric NPs.[53] The main requisites for these nanoparticulate tracers comprise biocompatibility, colloidal stability in body fluids, easy clearance from the body, high brightness, photostability and emission in the biological transparency window, typically 650-1050 nm.[23,54,55] The following section covers the most widely used nanoparticulate tracers used in optical imaging.

1.2.1. Quantum dots

Quantum dots are semiconductor nanocrystals comprising elements from the II-VI, III-V, IV-VI groups of the periodic table (Figure 1.7a). They have a large absorption cross-section, a narrow emission spectrum, which can be extended to the near infrared region, and excellent photostability, making them ideal candidates for bioimaging.[56] Their emission wavelength can be further tuned based on their size (Figure 1.7b), which in turn can be well controlled by varying the precursor concentration and growth conditions during their synthesis. They are insoluble in water with a hydrophobic outer shell, hence to work in biological media their surface needs to be modified to impart biocompatibility. Though they require surface modification for use in bioimaging, they are still widely used for imaging at the R&D level and are commercially available.

Several water-soluble quantum dots such as CdSe@ZnS nanocrystals, have been developed for multicolor imaging of biological samples.[57] These QDs have been used as fluorescent angiography probes in live mice to image vasculature in a 250-μm thick region within the animal tissue, and also detect blood-flow velocity and heart rate, all of which is possible due to the high two photon absorption cross section of these quantum dots. [58] Several bio-conjugated Cd-based QDs have been developed for both non-specific and targeted imaging of cancer cells, tumor vasculature and lymph node mapping,[59–64] (which can help predict the spread of certain kinds of cancers) and deep tissue visualization.[65–67]

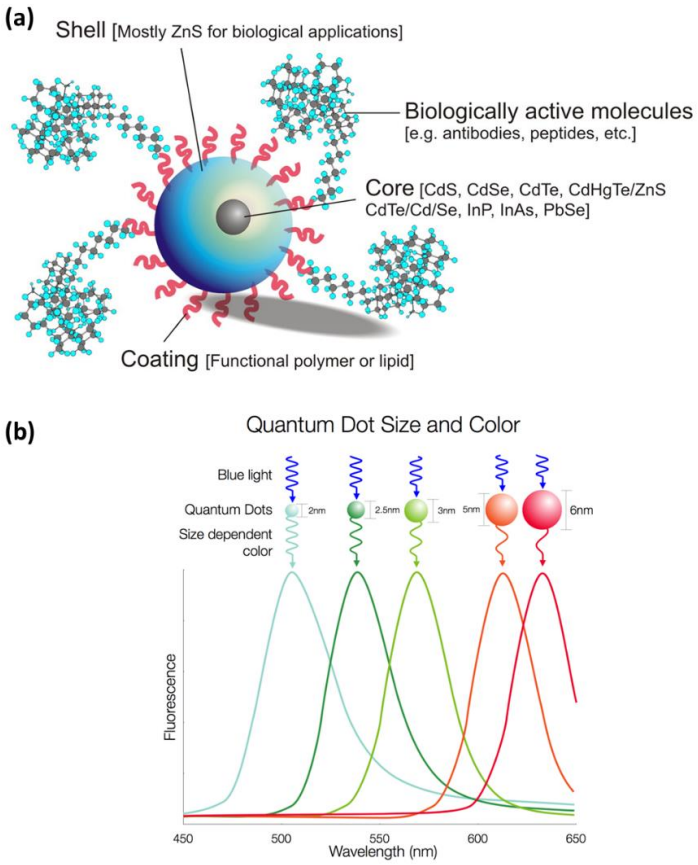

Figure 1. 7. (a) Structure of a quantum dot[68] and (b) Emission wavelength as a function of size for CdTe QDs[69]

However, due to the use of toxic elements such as Cd and Te, CdTe@ZnS nanocrystals show the potential risk of non-specific accumulation of metal ions in the biological environment.[55] To overcome these toxicity effects, Cd and Te-free QDs have been developed such as ZnS nanocrystals doped with Mn(II) ions for targeted cellular imaging using high resolution three-photon imaging.[70] Another class of Cd-free QDs is the NIR-II emitting Ag_2S QDs, whose emission wavelength can be tuned from 500 to 1200 nm by adjusting their size from 2 to 6 nm,[56] which have been used for deep tissue visualization and improved spatial resolution ~10 μm,[71,72] due to reduced light scattering in the NIR-II region ($1000 \leq \lambda \leq 1400$ nm).[73]

Although QDs present several advantages, it is important to note that fluorescence of QDs is also dependent on temperature[54] and therefore it is important to control the physicochemical properties of QDs. This is achieved by tuning their surface chemistry, which often requires several long, sophisticated and expensive steps. It is also important to understand the factors that affect the biodistribution of QDs in organisms, owing to the toxicity effects of QDs upon agglomeration *in vivo* due to their small size.[56]

1.2.2. Upconverting nanoparticles (UCNPs)

Upconverting NPs are rare-earth doped NPs, which exhibit fluorescence emission upon NIR light excitation. This upconversion luminescence results from sequential absorption of multiple photons or energy transfers leading to the conversion of low-energy NIR light into high-energy visible light.[74,75] UCNPs consist of an inorganic host doped with a sensitizer and an activator, typically hexagonal $NaYF_4$ nanocrystals doped with trivalent lanthanide ions such as Er^{3+}, Yb^{3+} or Tm^{3+} (Figure 1.8a-b).

In comparison with conventional contrast agents, UCNPs offer several advantages such as minimal autofluorescence, deeper penetration depth as a result of NIR excitation, large anti-Stokes shift tunable emission, narrow emission, resistance to photobleaching, no blinking under continuous irradiation, rather low toxicity and excellent stability.[53,74,75] The concentration of dopants is typically low, in order to avoid quenching caused by undesired cross relaxations.[76] Monodisperse UCNPs have been synthesized by thermal decomposition and hydro(solvo)thermal synthesis techniques. However, these UCNPs, like QDs, require surface modification as they are hydrophobic in nature and need further surface functionalization. Several one-step strategies have also been developed to simplify synthesis and post-treatment,[77] albeit with little control over uniformity and size.[53]

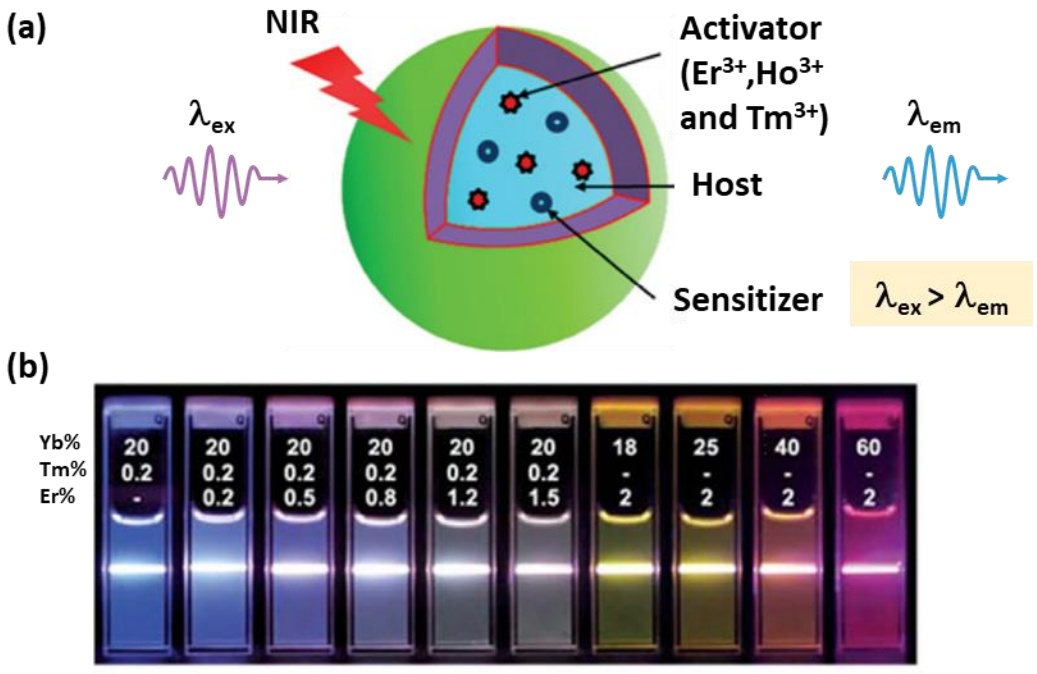

Figure 1. 8. Schematic illustration of upconverting NPs and (b) Multicolor fine-tuning of lanthanide-doped $NaYF_4$ NPs with different ratios of dopants.[78]

UCNPs have been utilized in several high-resolution and high-contrast bioimaging applications for *in vivo* imaging of blood vessels[79], transillumination imaging[80], immunolabelling and zero-background imaging of cancer cells[81,82], quantitative analysis of overexpressed receptors in cancer cells[83–85],mapping of lymphatic systems[77,86] and dynamic real-time tracking of cell migration *in vivo*,[87] due to their minimal autofluorescence.

The long term stability of UCNPs has also enabled dynamic real-time tracking of cell migration *in vitro* and *in vivo* in living mice, using confocal microscopy.[86,87] A number of polymer-coated (PEG, PVP, PEI, PAA) UCNPs have also been developed to perform *in vivo* biodistribution imaging[88] and charge dependent cellular imaging.[89] Silica coated UCNPs offer improved *in vitro* and *in vivo* biocompatibility[90] with clearance within a week of injection and have been used for multicolor luminescence imaging,[91] targeted imaging of tumor cells[92] and photodynamic therapy.[93]

Despite these advantages, the use of UCNPs is limited by the lack of generalized protocols for reproducible and scalable production, complicated surface modification strategies, low quantum yield, the use of sensitizer ions which have an absorption band coinciding with that of water resulting in light attenuation and heating and the lack of sufficient information concerning the long term toxicity of these UCNPs.[53,74,75]

1.2.3. Dye-doped silicate nanoparticles

Among all fluorescent nanotracers, silica-based NPs have attracted great attention owing to the existence of a myriad of well-established synthesis protocols with controlled size, their low intrinsic toxicity and the ease of surface modification which enables increasing their colloidal stability.[52,94] The fluorophore is usually covalently linked to the inorganic scaffold, or physically entrapped within the silicate particle, but with a risk of leaching of the dye in solution. This matrix shields the dye molecules from the external environment thereby imparting stability, is optically transparent, inert and biocompatible.[52,95] The silicate matrix also allows NP functionalization through silica surface chemistry. The synthesis of such NPs, which can be done either via Stöber synthesis, reverse microemulsion method or direct micelle assisted method, is straightforward (Figure 1.9). Depending on the synthesis route, different types of silica NPs can be obtained with different size distributions and dye-doping/grafting strategies.

PluS NPs which are silica NPs based on aggregates of Pluronic F127 surfactant or co-aggregates of F127 and derivatized F127 as templates (to yield NPs between 5-90 nm), have been studied for several *in vitro* and *in vivo* applications.[52,94] This synthesis strategy often results in well-defined NPs, with excellent colloidal stability, that makes them ideal candidates for use in biological applications. Furthermore, these NPs are coated with PEG to form a core-shell structure to increase their blood circulation time. Several PluS NPs doped with different NIR

emitting dyes such as Cy7 and IR780 have been investigated for sentinel lymph node mapping and *in vivo* imaging of tumors.[96,97]

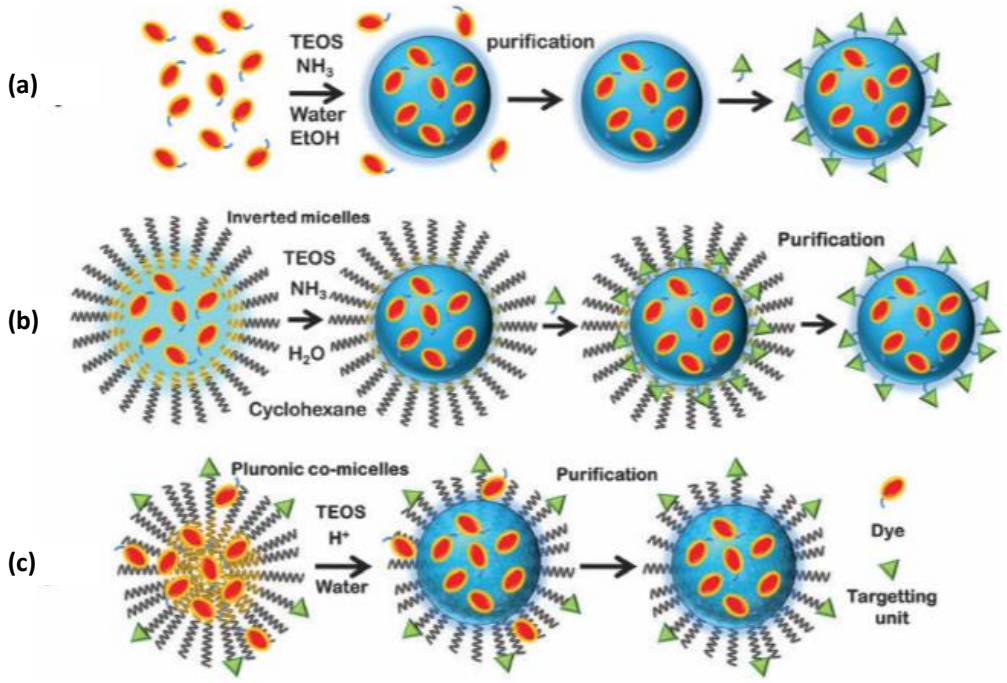

Figure 1. 9. Synthesis of dye-doped silicate NPs using (a) Stober method, (d) reverse microemulsion method and (c) direct micelle assisted method [94]

Prasad and co-workers have developed several dye doped silica NPs containing two-photon active dyes.[98,99] They also developed organically modified silica (Ormosil) NPs with a size range of 20–30 nm, doped with different two-photon active dyes for two-photon imaging.[100–102] It has also been reported that these organosilica NPs largely avoid leaching of the dye from the particle due to lower condensation of organosilica as compared to silica.[100] Several groups have incorporated two-photon active dyes based on aggregation induced emission[101,103–109], zwitterionic hemicyanine dyes,[110] silole derivatives, oxazine dyes,[111] distyrylbenzene based dyes[112] into silica NPs for bioimaging (Table 1.2).

Ultrasmall silica NPs (< 10 nm) called Cornell dots (C-dots) have even been approved by the Food and Drug Administration as an Investigational New Drug (IND).[113,114] These C-dots were designed to have high fluorescence by covalent incorporation of the organic dye (Cy5.5 dye) into the silica matrix, resulting in high brightness (200-300%) and photostability (2-3 fold) in comparison with the free dye in solution.[114] These were further coated with polyethylene glycol (PEG) to prevent opsonization and uptake by the reticuloendothelial system. These NPs have entered clinical trials in melanoma patients for sentinel lymph node mapping and other image-guided applications using either optical or dual optical-PET imaging platforms.[113–115]

Table 1. 2. Different types of dye-doped silicate NPs and their applications

Dye	Application	References
Cyanine	- Sentinel Lymph Node mapping and *in vivo* imaging of tumors	96
	- Optical-PET imaging probe	113
	- NIR imaging of porcine muscle	116
	- Labelling of human Mesenchymal stem cells	117
	- Immunospecific labels	118
IR 780	- Sentinel Lymph Node mapping and *in vivo* imaging of tumors	97
RubPY	- Bioimaging	119,120
	- MCF-7 cancer cell detection	121
FITC	- Labelling Cells	122
	- BioImaging	123
Perylenediimide	- Bioimaging	124
Pincer-type Pt(II) complexes	- Two-photon cellular imaging	125

However, a point to consider in the case of dye-doped silicate NPs, where the dye molecules are dispersed inside the silicate matrix, is that the fluorescence of the dyes can be partially quenched by molecule aggregation in the particle, which typically limits the loading to less than 1%wt.[52,126,127] This may be a point of concern for deep tissue imaging where a low concentration of dye may result in loss of signal as penetration depth increases. To address this problem of low concentration of dye due to low loadings, new classes of nanoparticulate tracers are being developed and investigated. One such example is the organic@inorganic core-shell NPs discussed in the following section.

1.2.4. Organic@inorganic core-shell nanoparticles

Core-shell NPs are comprised of an inner core surrounded by an outer shell, as suggested by the name. There are several different types of core/shell NPs (inorganic/inorganic, inorganic/organic, organic/inorganic and organic/organic core-shell NPs) including quantum dots and upconverting NPs as discussed in the previous sections. The goal of this work is to develop organic@inorganic core-shell NPs, as an alternative to existing nanoparticulate tracers.

These organic@silicate NPs, developed at Institut Néel since 2010, consist of an organic core surrounded by an inorganic silicate shell. The organic core is usually a nanocrystalline dye that can be employed for bioimaging, surrounded by an organosilicate crust that imparts stability. There exists a wide variety of solid-state dyes which have been designed to exhibit high

fluorescence emissions in the red to near IR biological transparency window to enable deep-tissue imaging.[128–131] The nanocrystals are a few tens of nanometers in size but consist of 10^5 to 10^7 molecules, thereby showing high fluorescence intensity in the solid state, due to the enhancement of their absorption and emission cross sections, making them ideal for *in vivo* vascular imaging. The silicate crust not only protects the organic nanocrystal from the external environment and impart high photostability, but can also be easily functionalized by silica chemistry to make these NPs biocompatible and impart further stability. Bioconjugation can also enable the use of these NPs for targeted drug delivery to cancer cells by targeting receptors over-expressed by cancer cells.

These core-shell NPs have only been synthesized by the 'spray-drying' method developed by A. Ibanez et al.[132], and can be made in an inexpensive, controllable and single step process. This one-step synthesis is made possible thanks to the control of both the sol-gel chemistry (polycondensation) and the nanocrystallization process, which occur simultaneously. Therefore, it is important to understand the fundamental aspects of these processes in order to optimize the self-assembling one-step approach for the preparation of these hybrid nanocomposite particles.

1.2.4.1. Sol-gel chemistry

All processes related to the formation of the silicate matrix involve sol-gel chemistry. The sol-gel method is a wet-chemical technique used for the synthesis of metal oxide materials, typically those of silicon and titanium.[133] The process involves the evolution of a solution of molecular precursors into a colloidal sol then into a gel consisting of a bi-continuous liquid/solid phase.

Silicate-based sol-gel materials are often synthesized from monomeric tetrafunctional silicon alkoxide precursors and water, using either an acid (HCl), a base (NH_3) or eventually a nucleophile (F^-) as catalyst. The most common tetraalkoxysilanes are tetramethoxysilane (TMOS) and tetraethoxysilane (TEOS). However, it is also possible to use organotrialkoxysilanes ($R'Si(OR)_3$) or diorganodialkoxysilanes ($R'_2Si(OR)_2$), where R' is a non-hydrolyzable substituent, to either derivatize or impart organic character to the siloxane network. [133]

Silicon alkoxides are popular precursors because they mildly react with water. This reaction is called hydrolysis because a hydroxyl ion gets attached to the metal atom, due to the nucleophilic attack of the oxygen atom in water.

$$\mathbf{Si(OR)_4 + H_2O \underset{\text{Esterification}}{\overset{\text{Hydrolysis}}{\rightleftharpoons}} (RO)_3Si\text{-}OH + R\text{-}OH} \qquad \textit{(Eq. 1.2.4.1.1)}$$

Here, R may either be a proton or a ligand. Depending on the amount of water and catalyst present, the complete hydrolysis could result in the replacement of all the OR groups by OH.

$$Si(OR)_4 + 4H_2O \longrightarrow Si(OH)_4 + 4R\text{-}OH \qquad (Eq.\ 1.2.4.1.2)$$

Hydrolysis could also stop when the metal is partially hydrolyzed $Si(OR)_{4-n}(OH)_n$. Two partially hydrolyzed molecules could link together in a condensation reaction by the elimination of a water or alcohol molecule, resulting in the formation of siloxane bridges.

$$(RO)_3Si\text{-}OH + (RO)_3Si\text{-}OH \underset{\text{Hydrolysis}}{\overset{\text{Water condensation}}{\rightleftharpoons}} (RO)_3Si\text{-}O\text{-}Si(OR)_3 + H_2O \qquad (Eq.\ 1.2.4.1.3)$$

$$(RO)_3Si\text{-}OH + Si(OR)_4 \underset{\text{Alcoholysis}}{\overset{\text{Alcohol condensation}}{\rightleftharpoons}} (RO)_3Si\text{-}O\text{-}Si(OR)_3 + R\text{-}OH \qquad (Eq.\ 1.2.4.1.4)$$

Under most conditions, condensation begins before complete hydrolysis. Repeated hydrolysis and condensation reactions result in the formation of polymeric siloxane networks. It is important to note that alcohol is not simply a solvent. It could participate in esterification and alcoholysis reactions as shown in Eq (1.2.4.1.1) and Eq (1.2.4.1.4).

Reaction rates for hydrolysis and condensation have an important pH dependence.[134] At pH < 5, hydrolysis is favored and condensation is the rate limiting step while the contrary is true at pH > 5 (Figure 1.10b). This is because the minimal reaction rate for hydrolysis is at around pH 7 and at around pH 4.5 for condensation, which also corresponds to the point of zero charge of silica. At pH < 2, silicic species get positively charged, condensation rate is proportional to the H^+ concentration. The nature of the alkoxide also plays an important role, with the bulkiest alkoxides leading to slower hydrolysis and condensation than the less bulky ones, which makes methoxysilanes the most reactive species. Furthermore, organically substituted alkoxysilanes $R´Si(OR)_3$ react faster than the corresponding tetraalkoxysilanes $Si(OR)_4$ under acidic conditions and slower under basic conditions.[133,134]

Under acid-catalyzed conditions, these discrete oligomeric networks start assembling into small, weakly interconnected linear polymeric chains. Indeed, as hydrolysis and condensation proceed, the silicon atom becomes more electrophilic as -OSi substituents are less electron-donating than OR or OH.[134] Therefore, reactions at the central Si atoms (atoms with 2 to 3 Si-O-Si bonds) get slower than the reactions at the terminal Si atoms, which results in chain-like networks (Figure 1.10a). By contrast, under basic conditions, reactions at central Si atoms are accelerated, resulting in the formation of highly branched and condensed networks.

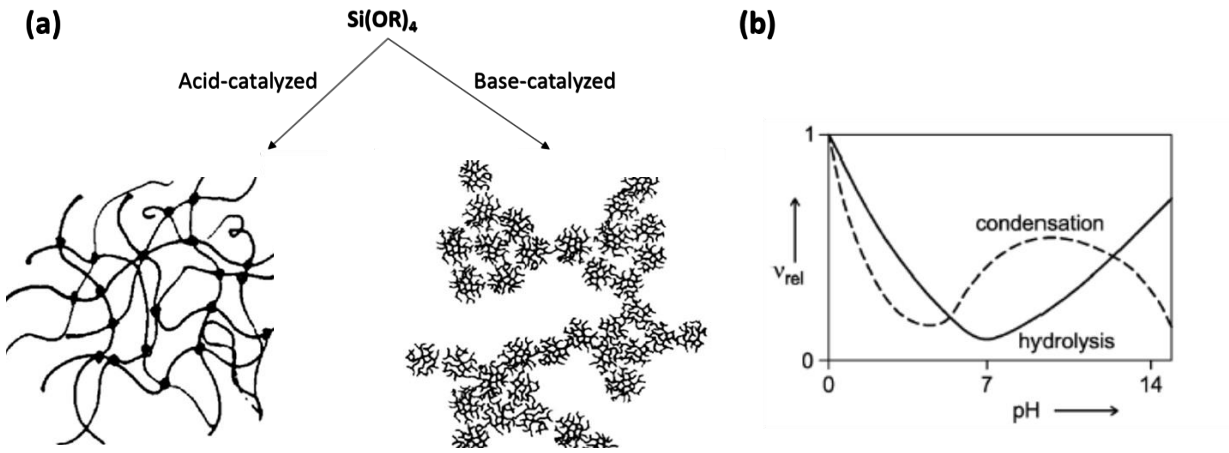

Figure 1. 10. (a) Typical structures from acid and base catalyzed sols[135] and (b) Dependence of relative rates of hydrolysis and condensation on pH [134]

1.2.4.2. Crystallization

At equilibrium, molecules can be dissolved in a solvent up to a concentration called solubility (C_0). This solubility value can be overcome, but leads to a metastable state, that will ultimately result in the formation of crystals in the presence of the saturated solution at C_0 to reach equilibrium. The formation of a new crystal from a supersaturated solution starts with the nucleation step, which refers to the process in solution by which atoms or molecules (solute) rearrange through a dynamic and stochastic process into a cluster called nucleus.[136] If this nucleus is larger than a critical radius, it has the ability to grow irreversibly to a macroscopically bigger size, in a second step known as crystal growth.[137] The rates of nucleation and crystal growth depend on the supersaturation, expressed as the ratio between the concentration in solution (C) and the solubility (C_0).

$$S = \frac{C}{C_0} \qquad \textit{(Eq. 1.2.4.2.1.)}$$

The nucleation theory states that the work necessary to form a cluster of *n* molecules is the difference between the free energy of the system in its final and initial states and an additional term accounting for the formation of an interface between the nucleus and solution. Assuming that the nucleus is spherical, the Gibbs free energy variation associated with the formation of a spherical nucleus can be expressed in the following form:

$$\Delta G_T = -\Delta G_v + \Delta G_S = -\frac{4}{3}\pi.\frac{r^3}{V}\,kT\,\ln S + 4\pi\,r^2\gamma \qquad \textit{(Eq. 1.2.4.2.2)}$$

where ΔG_v is the gain of free energy of growth units (molecule of solute) from solution to crystal state, ΔG_s is the cost of free energy due to formation solid-liquid interface, ν is the volume of dissolved molecules, r is the radius of the nucleus and γ is the interfacial energy solid/solution. In the plot of ΔG_T as a function of r (Figure 1.11), the point where the function reaches a maximum is the energy barrier that must be overcome to achieve nucleation (ΔG^*). The value of 'r' at this maximum (r^*) defined as the critical radius or nucleus size is:

$$r^* = \frac{2\gamma \cdot V}{kT \ln S} \qquad \textit{(Eq. 1.2.4.2.3)}$$

and the free energy barrier that must be overcome to achieve nucleation (ΔG^*) and form stable nuclei is then represented by:

$$\Delta G^* = \frac{16\pi V^2 \gamma^3}{3[kT ln S]^2} \qquad \textit{(Eq. 1.2.4.2.4)}$$

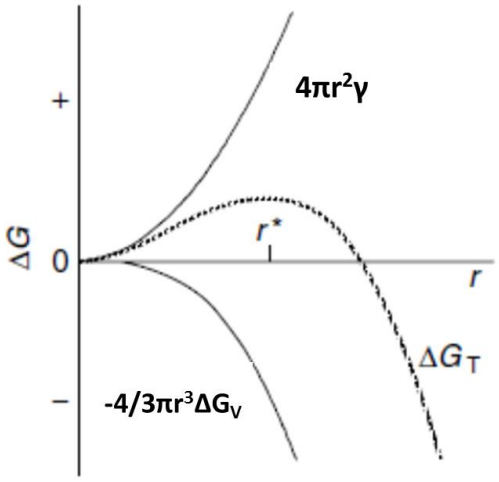

Figure 1. 11. Total free energy versus nucleus size [138]

If r<r*, the nuclei will redissolve. In turn, if r>r*, the nuclei will start growing.

The higher the supersaturation, the higher the probability of nucleation (which is a stochastic process) as the energy barrier ΔG^* decreases when 'S' increases. This also leads to a decrease of the value of $r*$ as the supersaturation increases.

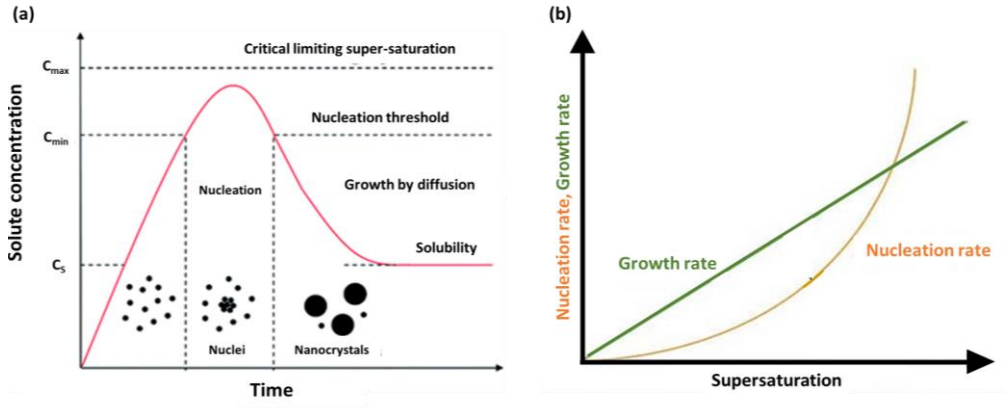

Figure 1. 12. (a) LaMer diagram for the nucleation and growth of nanocrystals.[139] (b) Dependence of nucleation and growth rate of crystallization on supersaturation[140]

The number of nuclei formed per unit time per unit volume is expressed as J, the stationary nucleation rate which is the Nucleation frequency / Rate of nucleation and is represented as:

$$J = k_0 exp\left(-\frac{16\pi V^2\gamma^3}{3(kT)^3[lnS]^2}\right) \qquad \textit{(Eq. 1.2.4.2.5)}$$

From, the LaMer diagram in Figure 1.12a, it can be seen that at high supersaturation, the solute concentration, C_S, significantly exceeds the nucleation threshold, C_{min} and the nucleation rate tends to infinity, resulting in the precipitation of the solute and the formation of a high number of nuclei. This in turn rapidly reduces the amount of solute dissolved in the solution in the metastable zone, which in turn decreases the supersaturation and ultimately stops the nucleation step. The nuclei so formed in the nucleation step then grow into nanocrystals. This time confinement of nucleation allows to efficiently reduce the size distribution of the nanocrystals. It is important to note that the nuclei growth rate should be negligible during the nucleation step in order to obtain monodisperse nanocrystals.

In the plot of J as a function of supersaturation (S) (Figure 1.12b) the nucleation rate is very small until a critical value of supersaturation (above the nucleation threshold) is reached, after which an exponential increase in growth is seen. This critical supersaturation defines the so-called metastable zone where crystal growth can proceed without concomitant nucleation taking place.

The probability, P, of forming a stable nucleus in a volume of solution, 'V' during a period of time, dt is

$$P = JVdt \qquad \textit{(Eq. 1.2.4.2.6)}$$

where J is the stationary nucleation rate. The nucleation probability is proportional to the volume of free solution.

Nanocrystallization should strongly be confined in time (as shown in Figure 1.12a) and/or space. While a confinement in time can be achieved by applying a supersaturation as high as possible, as introduced above, confinement in space can typically be achieved by forcing the crystallization to occur in small volumes, such as emulsions, micelles, or in this work, sol droplets.[136] In the synthesis of organic nanocrystal@silicate NPs, the nucleation of the organic dye is induced in the drying droplets, which act as nanometer scale reactors for the nanocrystal growth.[136] Such a space confinement of nucleation, as in the case of this study (microdroplets coupled with the formation of a sol-gel matrix), can only occur at high very supersaturations since mass transport only occurs by diffusion.

It is also noteworthy that under these space confined conditions, the probability of nucleation decreases and even tends to zero as the volume of the growth solution decreases.[136] As the droplets formed during the spray-drying synthesis are quite small, with evaporation induced supersaturation, there is a very low probability of multiple nucleations, thereby resulting in the formation of a single nucleus with the highest probability and hence the growth of a single crystal in the core of the droplet at the final stage of drying. Consequently, very high supersaturations and in turn very high nucleation rates, J, are required to initiate the nucleation process in the droplets formed during the nebulization. This space confinement is beneficial in controlling the nanocrystallization, in that a single nanocrystal is formed as a result of a single burst of nuclei in the droplets, at high supersaturation.

1.2.4.3. Spray Drying

Solid-state fluorophores have been encapsulated as nanocrystals in sol-gel matrices.[132,136,141,142] This was first investigated when stable organic nanocrystals were grown in the pores of monolithic gel-glass matrices to obtain composite organic-inorganic materials.[136,141] The nanocrystals so obtained exhibited enhanced stabilities compared to their corresponding molecular organic crystals and high non-linear optical (NLO) properties, while the amorphous gel glass led to advantages such as high stability, convenient processing, and shaping. A narrow size distribution between 10 and 20 nm was observed for the bulk samples. This was further extended to sol-gel thin films, prepared by spin coating on various substrates such as microscope glass slides, silicon wafers and polymers. It was also observed here that, nanocrystallization in sol-gel thin films was a one-step process, due to the coating process time of few seconds as opposed to the preparation of organic nanocrystals in bulk gel-glasses, where the matrix polymerization, nucleation and growth of the nanocrystal were well-separated steps in time. Furthermore, a DNA

sensor based on such fluorescent molecular nanocrystals anchored in sol-gel thin films was also investigated. Here, the NCs were confined in a sol-gel thin film using spin coating, after which layer by layer dissolution of the thin film yielded bare nanocrystals that could be grafted with hairpin-shaped DNA fragments functionalized with a probe molecule, resulting in quenching of NC fluorescence due to Forster Resonance Energy Transfer (FRET).[142] Hybridization of the hairpin with its complementary DNA resulted in turning on the fluorescence again, thereby opening up the possibility to create label-free generic sensors.

In-depth investigation of the formation of NCs in thin films prepared by spin coating revealed that spatial confinement was responsible for the NCs being buried in the films as shown in Figure 1.13a. In figure 1.13a, A_1 shows the dye molecules and silicate oligomers in solution, which is followed by the formation of a skin (or crust) at the surface as a result of fast solvent evaporation, as in A_2. This skin is much more interconnected when compared to the regions below the crust, due to more drying. As the solution is more confined in space, the volume of the solution is smaller in the skin, which in turn implies that the probability of nucleation at the skin is much lower (from Eq 1.2.4.6) as compared to below the surface (in the depth). This in turn results in the formation of nanocrystals buried in the film (Figure 1.13a, A_3) due to spatial confinement.

This concept was further extended to investigate the formation of core-shell nanostructures to form organic nanocrystals within silicate NPs using spray-drying.[132] This preparation method is an efficient way to produce uniformly spherical solid particles by atomizing sol suspensions, though with a significant size dispersion.[143,144] It is a simple, controllable and productive method to not only produce silica micro- and nano- particles[145,146] but also mesostructured silica.[147–150] It is based on the production of micron-sized droplets, through the nebulization of silica-based sols by an atomizer. The resulting sprays are then dried by circulating in an oven. The concentrations of catalyst and silicate oligomers strongly increase upon evaporation of the solvent, which accelerates the hydrolysis-condensation reactions and finally leads to well-condensed silica-based NPs. When an organic compound such as a fluorophore is incorporated within the starting sol, the sol-gel reactions and the crystallization of the organic compound are coupled in the oven as shown in Figure 1.13b.

The droplets produced by the atomizer of the spray-drying reactor initially contain a random dispersion of silicate oligomers, dye molecules and solvent as shown in B_1. Evaporation of the solvent first results in the formation of a crust as seen in B_2. This is then followed by confined nucleation of the dye in the center of the droplet (B_3) by the same mechanism of spatial confinement observed for the thin film, described above. The formation of the crust results in a much lower probability of nucleation at the crust due to reduced volume of solution here and a much higher probability of nucleation in the core of the droplet, as a result of spatial confinement. This is then followed by NC growth and complete drying and condensation of the

silicate crust (B_4). The interplay between the polycondensation and nanocrystallization processes may lead to unusual core-shell organic nanocrystal@silicate NPs.

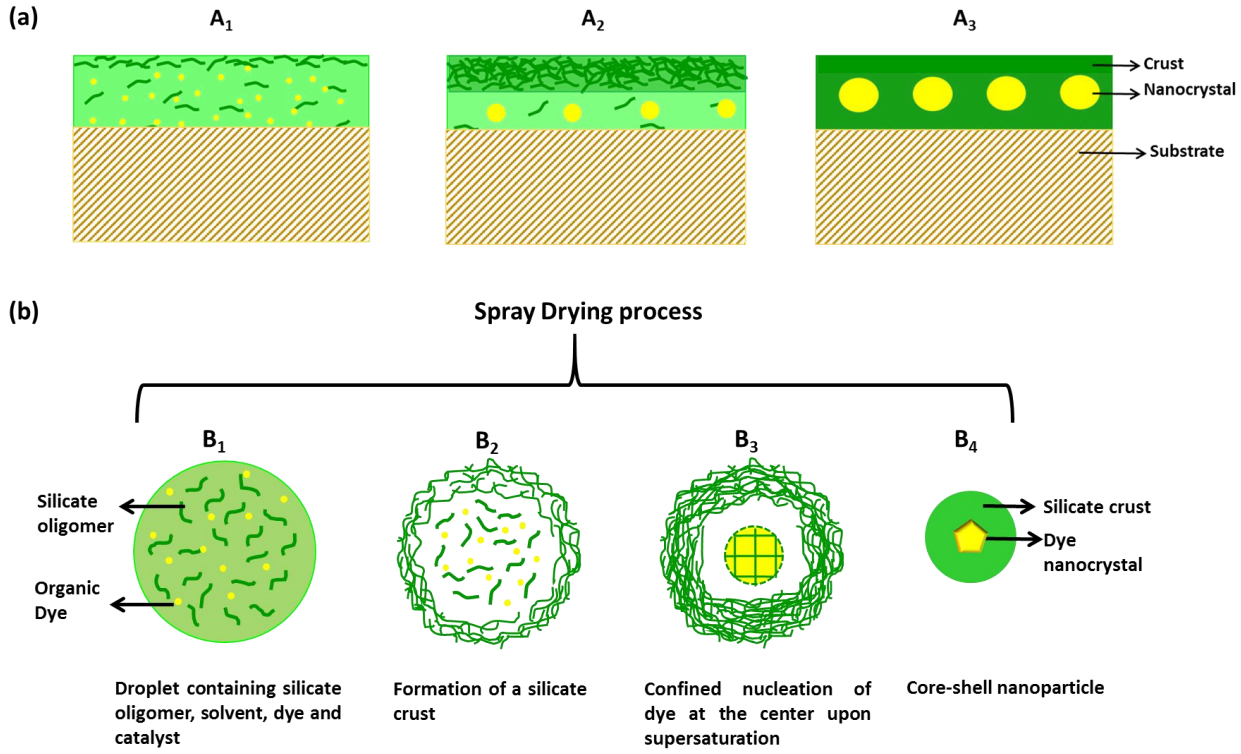

Figure 1. 13. Scheme illustrating the principle behind the formation of (a) buried nanocrystals in thin films by spin coating and (b) core-shell NPs by spray-drying

The spray-drying process needs simultaneous control over sol-gel chemistry and nanocrystallization, to allow the scalable synthesis of different types of core-shell NPs, with ease and reproducibility. An inherent drawback is, however, the NP polydispersity so produced, which is due to the different sized droplets formed during the synthesis process and particularly their coalescence, which has a random outcome, thereby resulting in broad size distributions. Despite this drawback, spray-drying is a viable technique to produce dry NP with high brightness and good yields for further treatment and processing. Indeed, the average size of NPs can be reduced by increasing the amount of solvent in the initial sols, while the targeted diameter can be selected after preparation (ultrafiltration, dialysis, ultracentrifugation).

The design of the spray-drying reactor for the synthesis of such core-shell NPs was first optimized by C.Philippot[151] while the optimization of the spray-drying process to produce CMONS NPs was realized by J. Zimmerman.[152] Preliminary experiments to investigate the colloidal stability of these NPs for potential use as tracers were also carried out. Moreover, a family of red-emitting dyes for possible encapsulation in such core-shell NPs was designed and evaluated for their

optical properties, by G. Eucat[153]. To date, such NPs have been reported only for CMONS and rubrene[132,154], while related lanthanide complexes@silicate doped NPs were also produced.[155,156] Notably, in the case of CMONS, different polymorphs were obtained depending on the composition of the organosilica shell,[157] which highlights the challenges in controlling the fluorescence properties.

This work predominantly focuses on the development of a family of red-emitting fluorescent nanocrystal@silicate composite NPs, by tuning the sol-gel chemistry and spray-drying process, to develop tracers for bioimaging. The challenge then is to disperse the NPs to form colloidal suspensions, and to control their surface properties to get a proper colloidal stability in biological media for 3D tissue imaging which requires a long circulation time in the blood (several hours) as will be discussed in the next section.

1.3. Colloidal stability of NPs in biological media

A comprehensive understanding of the factors influencing the colloidal stability of NPs in different biological media is of paramount importance primarily because the colloidal stability of NPs is greatly affected when introduced into complex media. This is due to the wide range of forces that the NPs experience in such environments leading to loss of colloidal stability and hence their aggregation. This aspect is often understated but is of utmost importance especially when using these NPs in biological applications as it significantly alters their *in vitro* behavior and also directly determines their *in vivo* fate.

1.3.1. Nano-Bio Interface

Blood is a very complex medium comprising numerous components of various types. It consists of two main components, (i) Plasma, which is a clear extracellular fluid and (ii) Formed elements, which are made up of the blood cells and platelets, as shown in Figure 1.14. It is therefore important to test the colloidal NP stability in media that mimic this environment to be in physiologically relevant conditions.

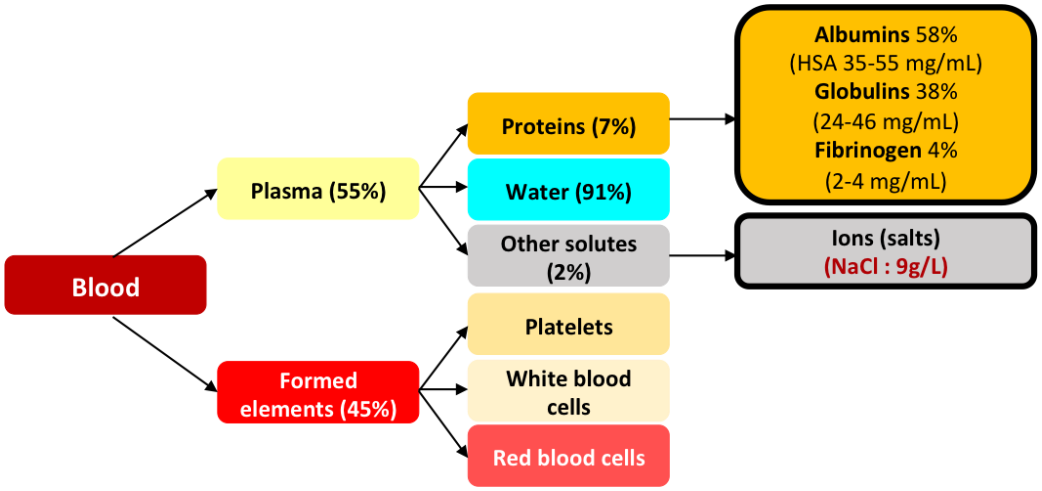

Figure 1. 14. Composition of blood

The first hurdle to colloidal stability is the high ionic strength of the medium (0.15 mol/L), mainly arising from the high concentration of sodium chloride. Typical interactions between SiO_2 NPs in water include attractive Van der Waals (VdW) forces and repulsive forces based on electrostatic double layer (EDL), resulting from surface charges from the dissociation of silanol groups (Si-OH) and solvation forces, illustrated in Figure 1.15. Colloidal stability is determined by these intermolecular and surface forces. The sum of the attractive VdW and repulsive electrostatic forces results in the net charge of the system being balanced by the formation of a cloud of the Stern layer composed of counter-ions adsorbed to the particle and a diffuse layer, which is an atmosphere of ions of opposite net charge surrounding the NP. This yields the well-established Derjaguin–Landau–Verwey–Overbeek (DLVO) theory. According to this theory, colloidal stability increases with increasing net surface charge, which also depends on pH. At a pH close to the isoelectric point of the NPs, aggregation is promoted due to the overall neutral surface charge of the NPs, which favors attractive VdW forces over the repulsive EDL. The EDL also depends on the ionic strength of the NP suspension. The ionic strength of biological media is very high (150 mM) resulting in the compression of the EDL, which again promotes aggregation due to screening of electrostatic charges within a few nanometers of the surface. Solvation forces are significant for inorganic and hydrophilic NPs. These solvation forces result from water molecules adhering to the particle surface and forming steric layers, resulting in hydrophilic repulsion and imparting stability.

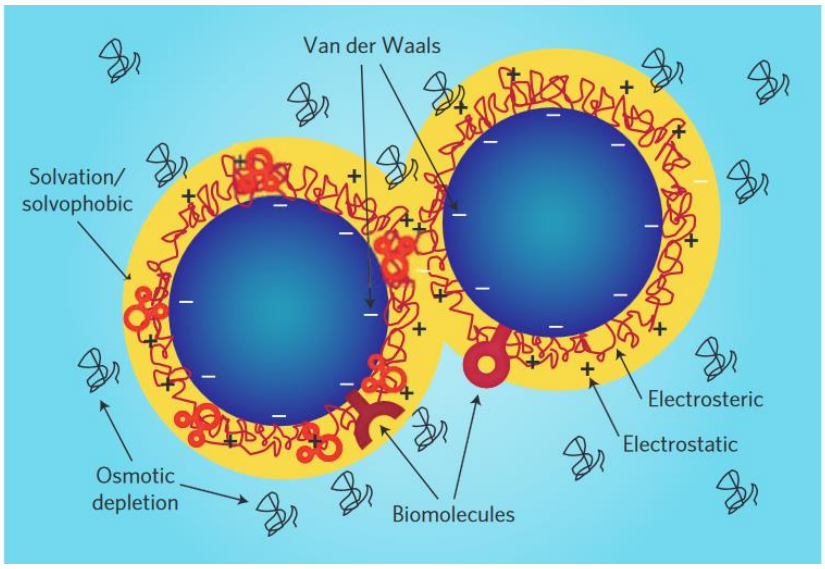

Figure 1. 15. Typical interactions and forces between particles in a biological medium[158]

Furthermore, when NPs are introduced into biological media, a number of nano-bio interfaces form that not only depend on colloidal forces but also depend on bio-physicochemical interactions that are exceptionally dynamic in nature. The main forces governing the interfacial interactions between the NPs and biological media are hydrodynamic interactions, electrodynamic forces, electrostatic forces, solvent interactions, steric and polymer bridging interactions.[158,159] These interactions result in the formation of protein coronas, particle wrapping, intracellular uptake and biocatalytic processes.[158] These can either result in biocompatibility or a bioadverse outcome resulting in the NP clearance by the reticuloendothelial system (RES) in a process known as opsonization. Therefore, the protein corona strongly determines the fate of the nanoparticle.

1.3.2. Formation of Protein corona

As soon as NPs are introduced into biological media, a protein corona is formed. This essentially refers to the coating of NP surface with proteins by adsorption. The nature/properties of the NPs, determine the formation of the protein corona when introduced into a biological medium, as illustrated in Figure 1.16a. This includes size (radius of curvature), hydrophobicity, surface charge, and coatings/functional groups.[158–161] As soon as NPs are introduced into a biological medium, such as cell culture medium, several proteins form transient complexes with the NPs.[158,162] The most abundant proteins such as human serum albumin and fibrinogen, may first bind and dominate the NP surface for short periods of time in the 'soft' corona and eventually get displaced by lower abundance proteins with higher affinities and slower kinetics to form a 'hard' corona, in a phenomenon known as Vroman effect.[163] It is noteworthy that it is the protein

corona and not the NP properties itself,[158,159,170,160,161,164–169] that determines the fate of the nanoparticle, *in vivo* organ distribution and the clearance of the NPs from the body, due to the impact on the protein structure and function (Figure 1.16b). This makes it extremely important to comprehensively characterize the protein corona. Majority of the studies on protein corona formation have been done either by the incubation of NPs in plasma/serum or by the incubation of NPs with individual proteins or attachment of individual proteins to the surface of the NPs.[167]

The formation of protein coronas is extremely rapid and it is crucial to evaluate this dynamic process comprehensively. Label-free snapshot proteomics has been used to obtain quantitative time-resolved profiles of human plasma coronas formed on silica and polystyrene NPs of different sizes (Ø ≈ 35 nm, 120 nm, 140 nm) and surface functionalization (amine, carboxylate, unmodified).[169] Complex time- and nanoparticle-specific coronas were found to form in less than 30 seconds, consisting of almost 300 different proteins. Additionally, these protein coronas were found to evolve with time in terms of amount of bound protein but not in composition. The rapid formation of coronas could have an imperative effect on different biological aspects including NP toxicity, immunological recognition, targeting capability, biodistribution and NP uptake. As the formation of protein coronas is a highly dynamic process, exposure of the NPs to a dynamic environment could present physiologically relevant *in vitro* data that could be extrapolated to predict the *in vivo* behavior of the NPs.[171] In a study involving Au NPs, ranging from 4 nm to 40 nm, the time evolution of protein coronas was followed and found to enhance the biocompatibility of these NPs upon adsorption of albumin.[170] In a study involving lipid and silica NPs (NPs) incubated with human plasma, the protein coronas so formed were found to be enriched with immunoglobulins, complement factors, and coagulation proteins that elicit phagocytosis. However, it was also found that the protein-coated NPs were protected from uptake by macrophage cells, showing a stealth effect.[172]

The time evolution and final composition of the corona can also be predicted using models which take into account the affinities, stoichiometry and rate constants. This has been tested for polymeric NPs. [173]

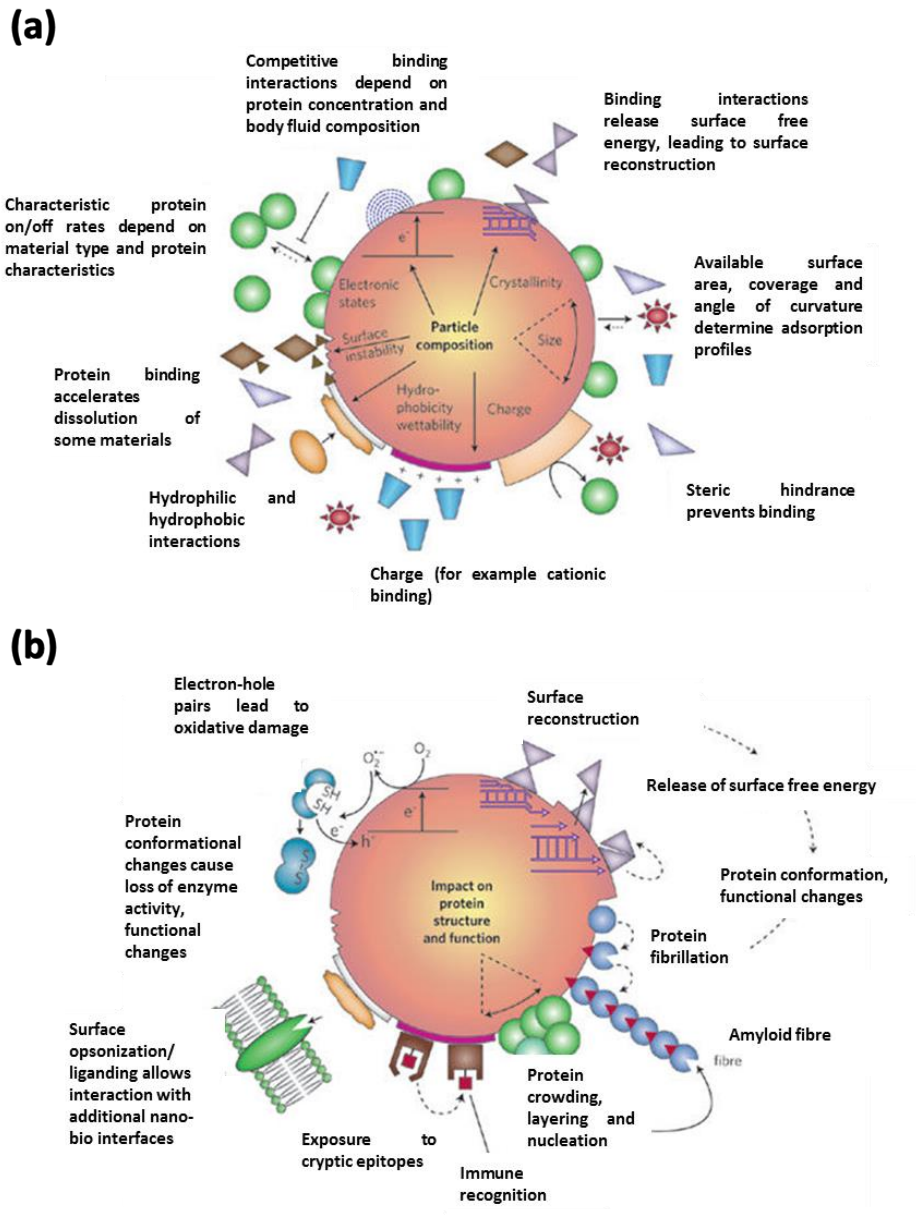

Figure 1. 16. (a) Influence of nature/properties of the NPs on the formation of protein corona and (b) Potential changes in protein structure and function as a result of interacting with the nanoparticle surface [158]

1.3.3. Factors influencing protein corona

Size of NPs plays an important role in their uptake, circulation half-lives and clearance.[158,163,174–176] Typically, extremely small NPs (< 8 nm) are excreted by the kidney, while bigger NPs (> 200 nm) are easily detected by the RES and eliminated by the liver and spleen. In a study involving amorphous silica NPs, dose- and time-dependent toxicity was observed for 30 nm NPs while smaller (Ø = 20 nm) and larger particles (Ø = 100 nm) displayed only low toxicity, at the same

zeta potential. Interestingly, the bio-adverse effects triggered by the 30 nm NPs were significantly ameliorated upon formation of the protein corona.[177]

Surface charge also has a direct impact on protein binding. Neutrally charged particles have been shown to have slower opsonization rate as compared to charged particles.[178,179] In a study involving polystyrene NPs, it was shown that positively charged NPs adsorbed proteins with isoelectric points less than 5.5 (such as albumin), while negatively charged NPs predominantly bound proteins with isoelectric points greater than 5.5 (such as IgG).[180] Cationic NPs are also more cytotoxic and hemolytic as compared to neutral or anionic NPs. Native, amine-modified and carboxylic acid-modified SiO_2 NPs were tested in mammalian growth media containing fetal bovine serum for different time periods. It was shown that SiO_2-COO^- showed slower agglomeration rates, formed smaller aggregates and exhibited lower cytotoxicity in comparison with native and SiO_2-NH_2 NPs. The protein corona that was formed in each case was also unique showing the influence of the surface charge on the corona formation.[181]

In another study highlighting the importance of electrostatic interactions in the adsorption of proteins, the binding of two globular proteins Lyzosymes and ß-Lactoglobulin onto negatively charged silica NPs was investigated at different ionic strengths and pH ranges. Two adsorption regimes were observed for both proteins when pH < pI. At low pH, a single monolayer of protein molecules was observed due to the competing attractive protein-protein and repulsive protein-protein forces. At pH values closer to pI, repulsive interactions between protein molecules were less important resulting in the adsorption of more than one monolayer of protein at low ionic strength.[182]

The hydrophobicity of NP surfaces not only influences the amounts of protein bound to the NP, but also determines their identities.[183] Hydrophobic NPs have shorter circulation half-lives (seconds to minutes) compared to hydrophilic NPs as hydrophobic particles are opsonized more quickly than hydrophilic particles, due to the enhanced adsorption of plasma proteins onto their surfaces.[178,184–186]

Therefore, for most biological applications, neutral/anionic hydrophilic NPs with sizes between 40-200 nm are utilized as illustrated in Figure 1.17.

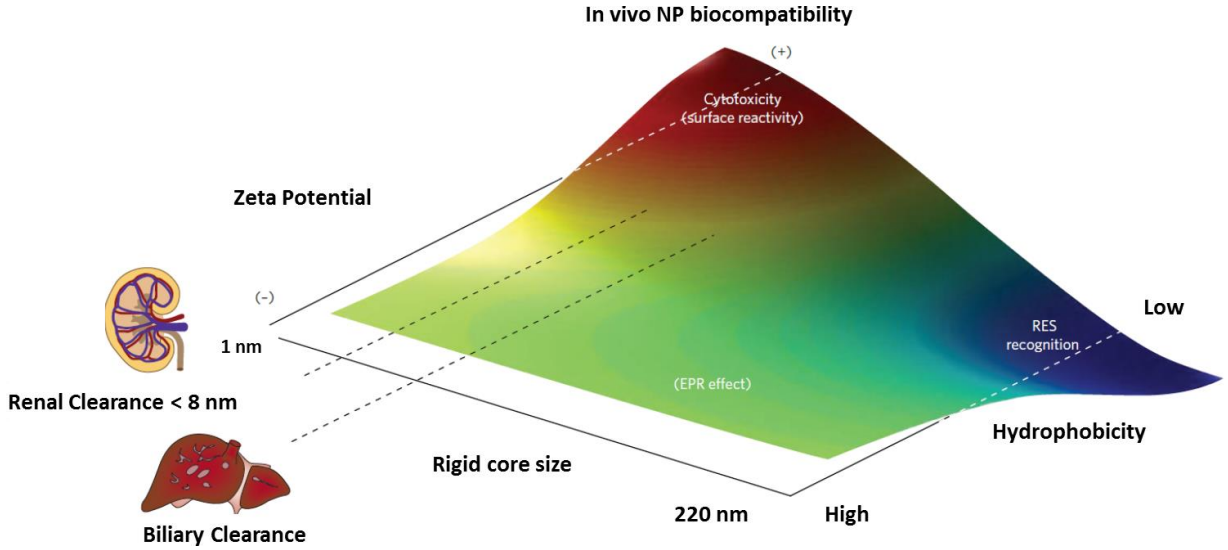

Figure 1. 17. Three-dimensional phase diagram displaying the qualitative biocompatibility trends revealed after in vivo screening of around 130 NPs of various chemical nature, including fullerenes, metal oxides, polymers, liposomes, dendrimers, quantum dots and gold colloids, intended for therapeutic use. Biocompatibility is reflected in the color spectrum, with red representing likely toxicity, blue likely safety and blue-green–yellow intermediate levels of safety (in the same order).[158, 187]

Characterization of the protein corona

There are several techniques available for the characterization of the protein corona, including direct and indirect methods. Direct methods analyze the proteins that are adsorbed on the NP surface, while indirect methods measure changes in the properties of the NPs, such as changes in their size, charge, density, mass, absorbance, and fluorescence, which can then be correlated with the amount of adsorbed protein.[188]

Direct methods include gel electrophoresis (GE) like Sodium Dodecyl Sulphate-Polyacrylamide Gel electrophoresis (SDS-PAGE) for qualitative analysis of the corona composition and are often complemented with mass-spectrometry (MS) techniques (Inductively coupled plasma (ICP-MS), Liquid chromatography (LC-MS) and Matrix-assisted laser desorption/ionization-time of flight (MALDI-ToF)) to obtain quantitative information and identification about the adsorbed proteins. Structural changes in the proteins can be studied using Circular dichroism (CD) and Fourier-Transform-Infrared spectroscopy (FT-IR).

Indirect methods, summarized in Figure 1.18 include techniques like Transmission electron microscopy (TEM), scanning electron microscopy (SEM), AFM, nanoparticle tracking analysis (NTA), dynamic light scattering (DLS), fluorescence correlation spectroscopy (FCS), NMR, differential centrifugal sedimentation (DCS), and GE, which can help measure the thickness of the adsorbed protein layer using the hydrodynamic diameter of the NPs before and after the formation of the protein corona.[188] Of these, DLS, which measures the fluctuations caused by the

diffusion of NPs in a given focal volume, that can be converted into a hydrodynamic diameter by fitting the autocorrelation function, is very widely used due to the ease of performing experiments and its wide availability. FCS, is a related technique which measures the fluctuation of the fluorescence intensity of fluorescently labelled NPs that is particularly advantageous because it allows *in situ* measurements which circumvents the need for washing steps and allows kinetics studies as well.[188,189]

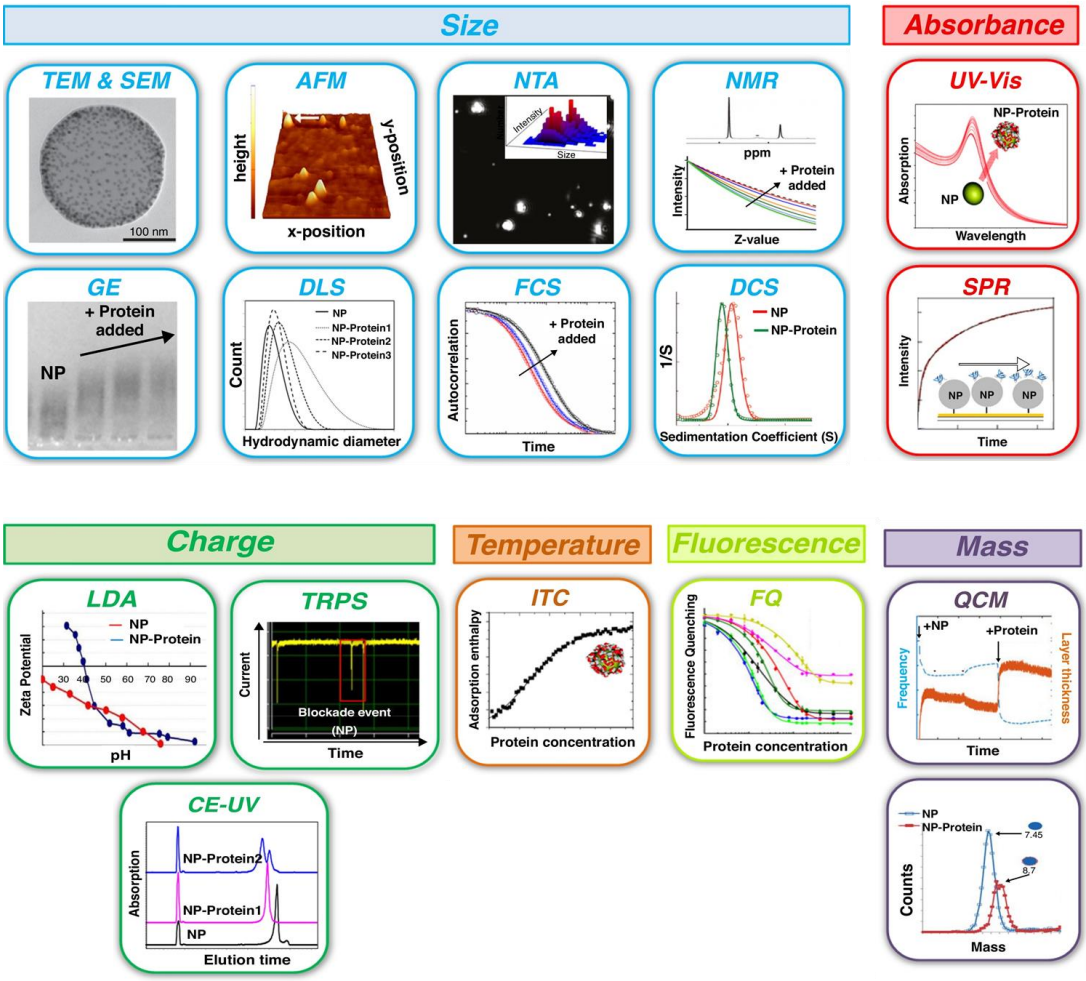

Figure 1. 18. Indirect methods to analyze adsorbed proteins on NP surface[188]

There are several other methods, which measure different parameters such as surface charge (Zeta potential, Laser Doppler Anemometry (LDA), Tunable Resistive Pulse Sensing (TRPS), and Capillary Electrophoresis (CE)), mass (Quartz Crystal Microbalance (QCM), and Suspended Microchannel Resonator (SMR)), absorbance (used with plasmonic NPs because incubation of NPs with proteins usually leads to a red-shift and widening of the plasmon peak) as well as thermodynamic parameters of the protein corona formation using Isothermal Titration Calorimetry (ITC).[188]

Indirect methods such as DLS and Zeta potential measurements will be particularly adapted in this study in order to observe the changes in the NPs surface potential and their aggregation as a function of the components added to the suspensions.

1.3.4. PEGylation

There are various ways to stabilize NPs in biological media. This includes electrostatic stabilization, which makes use of surface charge to keep the NPs away from each other. However, this strategy works poorly in cell culture medium which contains polyvalent electrolytes that can easily screen these charges.[159] Another strategy is steric stabilization, which is achieved by the conjugation or adsorption of macromolecules such as natural polymers (dextran, chitosan, alginate) or synthetic biopolymers such as polyethylene glycol (PEG) on to the NP surface. Steric stabilization often helps improve the colloidal stability of NPs in biological media as has been demonstrated in several examples. A third strategy involves the combination of electrostatic and steric stabilizations called electrosteric stabilization, which makes use of charged polymer adsorption on the NP surface to impart colloidal stability in cell culture media.

PEGylation refers to coating the NPs surface with PEG and is the most commonly employed steric-stabilization strategy. PEG is a family of FDA-approved 'stealth' polymers, which are nontoxic, non-immunogenic, non-antigenic and hydrophilic and have been widely used to shield the NP surface from aggregation, opsonization and phagocytosis, thereby increasing furtivity and prolonging NPs circulation time.[190,191] There are several studies corroborating the efficacy of PEGylating silica NPs for improved colloidal stability and minimized protein adsorption and opsonization.[192–198]

The mechanistic details of NP PEGylation processes have been elucidated using FCS by Weisner *et al* who showed that PEGylation on ultrasmall silica NPs (< 10 nm) is a two-step process starting with adsorption of the PEG molecules followed by covalent attachment.[192]

There are several parameters like the molecular weight, grafting density and structure that influence the efficiency of steric stabilization using PEG. Increasing PEG MW has been shown to result in effective shielding. Adsorption of plasma proteins onto surfaces of PEGylated PLA (poly (lactic acid)) NPs was shown to decrease ~ 75% when PEG MW was increased to 5 kDa but no further decrease was observed with higher MW, 10, 15 and 20 kDa.[199] In another study involving mesoporous silica NPs, increasing PEG MW from 10 to 40 kDa, while maintaining constant NP size, resulted in reduced phagocytic blood cell association.[200] In a similar study, PEGylating MSNs (150 ± 20 nm) with different PEGxk-silanes (with x= 4, 6, 10, 20) and chain densities (0.05 wt%–3.75 wt%) yielded optimal MW as 10k with 0.75 wt% optimal chain density for minimal

adsorbance of HSA.[198] PEGylation also helps in increasing circulation half-life as shown in systemically administered PEGylated Au NPs (10-100 nm) by increasing PEG MW fom 2-10 kDa.[201]

The structural conformation of PEG molecules on the NP surface is an important factor that influences the shielding efficacy of the NP surface and is determined by the average distance between neighboring PEG chains on a NP surface (*D*).[190] If *D* is greater than the Flory radius of the PEG chain, $R_F/D \leq 1$, ($R_F \sim aN^{3/5}$, where *N* is the degree of polymerization, and thus is proportional to PEG MW, and *a* is the effective monomer length = 0.35 nm), neighboring PEG chains will not overlap and be in a "mushroom" conformational regime.[190] As the surface PEG density increases adjacent PEG chains start to overlap ($R_F/D > 1$) and the PEG must stretch away from the NP surface and forms a "brush" layer. Surface PEG densities in the mushroom-to-brush transition are required to resist adsorption of serum proteins and avoid uptake of NPs. Further, for longer PEG chains (≥10 kDa), higher R_F/D values may be required as they have a stronger tendency to entangle with neighboring chains.[202]

The effect of PEG surface density on NP stability in serum and/or circulation time in the blood has been investigated using PLA-PEG NPs. PLA-PEG NPs with higher content of 2 kDa PEG ($R_F/D >$ 1.73) efficiently resisted adsorption of complement proteins in comparison with similar NPs with slightly lower PEG content ($R_F/D \sim 1.5$).[203] Likewise, PLA-PEG NPs formulated with 30% w/w 20 kDa PEG content exhibited increased circulation times compared to NPs with 10% w/w PEG. [204]

The colloidal stability of silica NPs was studied in a protein-rich model system by incubation of the NPs in BSA/PBS solution. While pristine silica NPs formed small NPs–BSA clusters, which evolved into bigger aggregates within a few hours owing to protein bridging interactions, decreasing the NPs surface charge, Sil–PEG (mPEG-5000) hybrid NPs resisted BSA adsorption and persisted as single NPs even after 48 h. [205]

In another interesting study, dual PEGylation (DPEG) was employed to increase the blood circulation time of mesoporous silicon from 1 to 241 minutes.[197] Furthermore, this dual PEGylation changed the biodistribution of the NPs with coated particles mainly getting deposited in the spleen as compared to uncoated NPs which were rapidly deposited in the liver. The protein coronas of the particles were also different, with uncoated particles adsorbing more proteins as opposed to the coated particles which adsorbed proteins capable of suppressing cellular uptake.[197]

PEGylation has also shown to increase the stability of NPs, as was demonstrated using colloidal MSNs (~ 47 nm). These MSNs had a tunable PEG chain length (short M_w 550, long M_w 5000 or a mixture of two: 75% of 550 Da, 25% of 5000 Da), with stability in SBF at 37 °C for up to one month. It was shown that longer and denser polymer shells were most efficient in slowing down the biodegradation kinetics as compared to pristine MSNs. [194]

There are different strategies to PEGylate NPs for biological applications ranging from *in situ* grafting of PEG molecules during the synthesis of NPs or post-synthetic covalent grafting strategies. The next section focuses on click chemistry as a modular NP functionalization strategy.

1.4. Click Chemistry

The design of complex, multifunctional and versatile materials for biological applications ranging from cancer therapy to sensing requires simple and reliable functionalization methodologies. Click chemistry, a term first coined by Sharpless in 2001,[206] encompasses all reactions that enable easy linking of two reactive organic entities provided they are of wide scope, modular, selective, occur with high yields and under mild and green conditions using harmless reactants and benign solvents. This is similar to Lego chemistry, where a simple reaction enables easy covalent linking of any kind of organic moiety. Originally established in the context of synthetic organic chemistry for drug discovery, click chemistry quickly extended to polymer science and became a reliable functionalization method in materials chemistry, particularly for sol-gel materials.[207] The covalent immobilization of organic moieties in sol-gel materials was limited to: i) the grafting of organo(alkoxy)silanes or organo(chloro)silanes on preformed materials; ii) the sol-gel co-condensation of a silica precursor with an organo(alkoxy)silane; and iii) the formation of pure organo(silsesquioxanes) and in particular bridged silsesquioxanes,[208,209] illustrated in Figure 1.19 for silica-based materials. Furthermore, some studies relied on the use of chemical reactions on reactive functionalities previously incorporated within the material through one of the previous methods, but most often under rather harsh conditions, or lacking a good control on the conversion or on the selectivity.[210] These limitations can be overcome by click reactions.

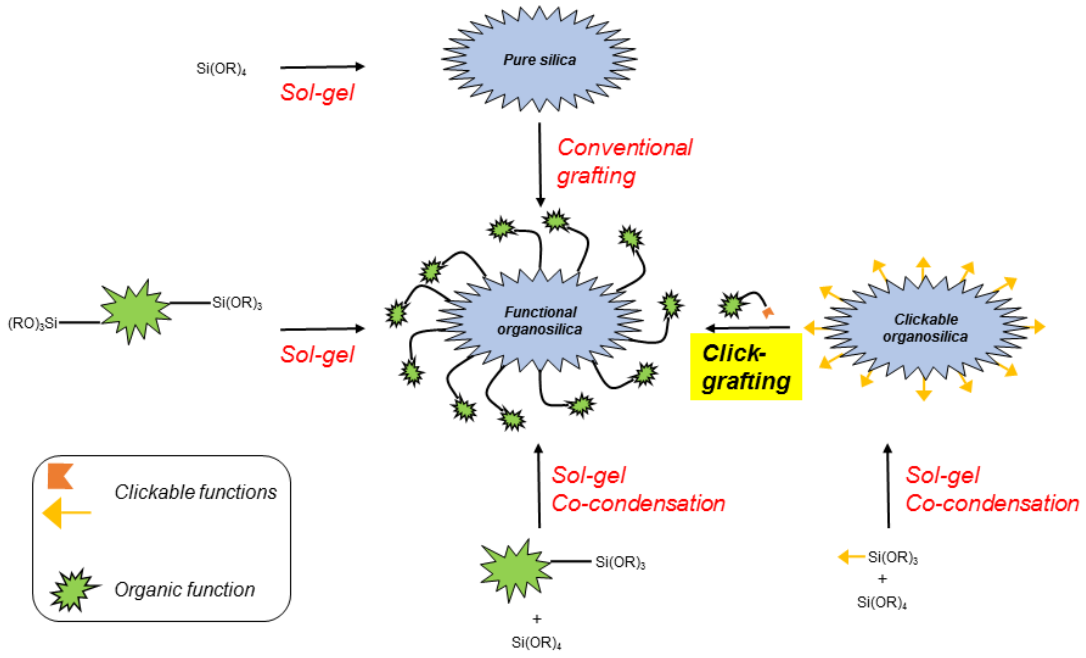

Figure 1. 19. Common routes and click-grafting to functional organosilicas.[210]

As a post-functionalization method, click chemistry is widely employed for the preparation of functional materials to be used in diverse applications as it offers several advantages[210] such as:

1) Incorporation of functional moieties while preserving the inorganic skeleton of the sol-gel material, and therefore the textural and morphological properties.
2) Possible covalent linkage of biomolecules such as enzymes or DNA fragments hardly grafted by previous methods, thanks to the versatility, wide scope and mild conditions associated with click reactions.
3) The precise design of materials using co-condensation strategies which enable random positioning of the functions throughout the material[211] as illustrated in Figure 1.20

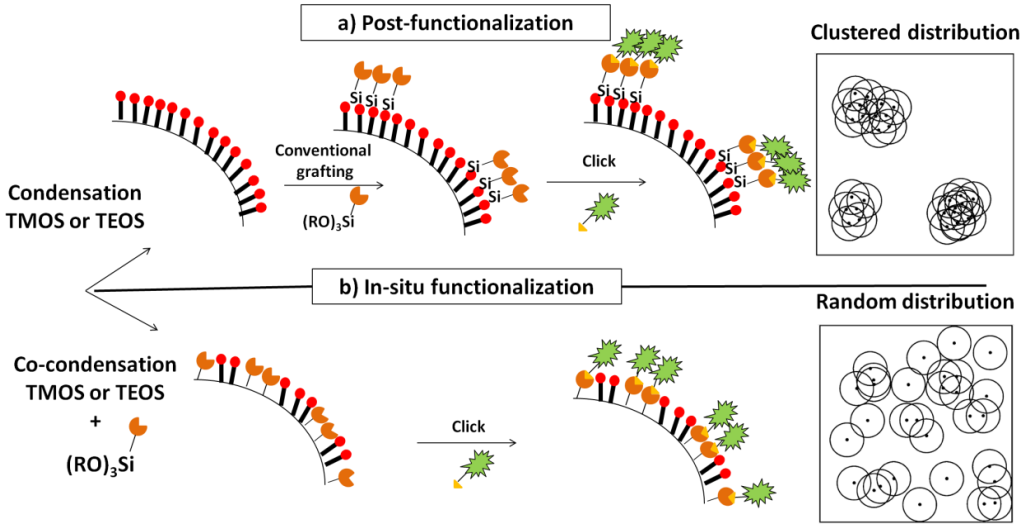

Figure 1. 20. Difference between(a) conventional grafting and (b) co-condensation methods with their corresponding graphical theoretical distribution (insets).[211]

The most common examples of click chemistry are the Cu(I)-catalyzed alkyne-azide cycloaddition to form a 1,2,3 triazole linkage, the thiol-ene reaction between a thiol and an alkene and to a lesser extent, reactions such as epoxide ring-opening or oxime ligation.

1.4.1. Copper(I) catalyzed Alkyne to azide cycloaddition (CuAAC)

The cycloaddition family of click reactions, particularly the Huisgen cycloaddition of azides and alkynes is very promising as it allows the simultaneous formation of two bonds with a cyclic structure. However, the biggest drawback of this reaction is that it requires elevated temperatures and typically yields a mixture of regioisomers.

In 2002, Meldal and Sharpless independently reported that copper (I) can efficiently catalyze the Huisgen cycloaddition,[206,212,213] yielding a single regioisomer under very mild conditions. This so-called CuAAC reaction underwent intensive research and became extremely popular in various areas of chemistry, thanks to the mild and tunable reaction conditions, and the almost infinite substrate scope of this reaction.

One of the biggest advantages of CuAAC is that it can be carried out under ambient atmospheric conditions, using both protic and aprotic solvents, including water. Additionally, it is extremely wide in scope as it is tolerant to a large number of functional groups and results in high conversions. When azide-silicas are used as substrates, FTIR analysis enables easy monitoring of the reaction, which results in the simple quantification of the conversion.[65,214] The use of Cu(I), to catalyze this cycloaddition eliminates the need to perform such reactions at elevated temperatures (reducing the risk of working with azides). Cu(I) can either be added to the reaction mixture directly or generated *in situ*.

While the combination of copper sulphate ($CuSO_4.5H_2O$) as the copper source and a reducing agent such as sodium ascorbate, (which not only reduces Cu(II) to Cu(I) but also reduces any oxygen species thus decreasing the formation of oxidative byproducts) is most preferred, other options include the use of Cu(I) salts directly (CuI, $CuOTf.C_6H_6$, $[Cu(NCCH_3)_4][PF_6]$). However, when working with such salts, it becomes necessary to perform the reaction under oxygen-free conditions to keep the Cu(I) active as Cu(I) tends to get oxidized to Cu(II) under ambient conditions. A number of ligands such as phosphine and/or amine-based systems have also been explored to complement the CuAAC reaction by stabilizing the active Cu(I) species by forming a ligand–Cu(I) complex thereby enhancing the rate of the click reaction.

Though a plausible mechanism featuring the formation of a simple copper acetylide and its reaction with organic azides was quickly widely accepted, the mechanism of the CuAAC was only quite recently clarified by V. Fokin and G. Bertrand.[215,216] Indeed, these studies evidenced the simultaneous participation of two copper centers during the catalytic cycle, as depicted in Figure 1.21.

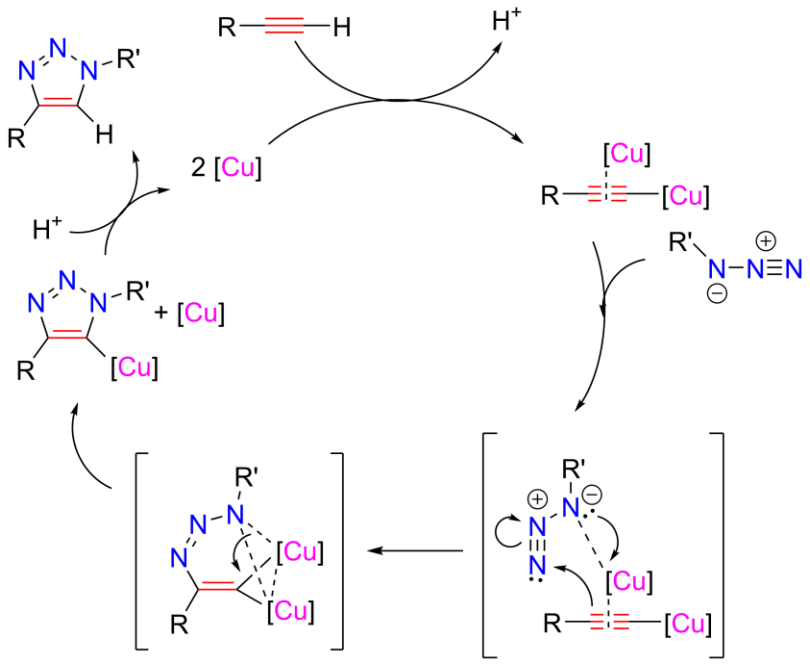

Figure 1. 21. Proposed mechanism of the CuAAC reaction using two active Copper centers[210]

1.4.2. Applications of CuAAC

The CuAAC reaction has been used on dense silica nanospheres to prepare several inorganic@polymer core-shell nanostructures such as SiO_2@PS and SiO_2@PNIPAM nanocomposites.[217,218] Azide groups could be directly grafted onto Ludox silica (20 nm) by

reaction with AzPTES in water/ethanol. This was used to graft previously prepared alkyne-modified poly-(L)-lysine polymers in tris buffer.[219]In another approach, the direct preparation of alkynyl-containing silica NPs was successfully achieved and used to prepare core-shell fluorescent NPs with PEG moieties.[66,220] Silica NPs containing azide groups have been functionalized in a competitive fashion by two different alkyne-derivatized functional groups, bearing either a fluorophore or a biotin moiety, enabling avidin recognition.[221] Though the relative loadings of functional groups were not quantified, this competitive approach appears very promising for the multiple functionalizations of silica materials. CuAAC has also been used to develop and anchor pore-gating mechanisms such as nanovalves at the external surface of MSNs carrying cargo inside the pores. The construction of such gatekeepers requires performing reactions under mild conditions (low temperature, in water) and was first demonstrated using CuAAC, by the groups of Zink and Stoddart.[222] Snap-Tops featuring bulky adamantyl groups and linked through ester or amide functions were built on MSNs by the CuAAC reaction in the presence of rhodamine B in the pores and adamantyl groups around triethylene glycol stalks at low temperature and in water. The nanocontainers featuring the ester function could be opened in the presence of porcine liver esterase to release their cargo, while those containing the amide groups did not exhibit cargo release. The same strategy was later employed on linkers built on disulfide groups upon activation with thiols.[223]

Other types of gate-keeping mechanisms that can be anchored by the CuAAC reaction systems include peptide-based enzyme-responsive nanosystems cleavable in the presence of proteases[224] and self-complementary DNA duplexes designed to release anti-cancer drugs in vitro, at human liver cancer cells. [225]

More sophisticated nanomachines make use of an antenna (donor) transferring energy, electrons or protons to an actuator (acceptor).[226–228] In this case, it may be important to control the precise relative position of the donor and the acceptor, in order to obtain optimized properties.

The only major limitation of CuAAC however, is the toxicity of copper residues on living species, limiting their use in biological applications.[229] Though it is possible to remove unwanted Cu from the final products by means of dialysis and copper complexing agents such as EDTA, even small traces of Cu(II) could be potentially detrimental for biological applications due to the production of reactive oxygen species from molecular oxygen. [230] A solution to this problem was proposed by Finn et al, who used a Cu-complexing ligand, tris-(3-hydroxypropyltriazolylmethyl)amine (THPTA) which not only accelerates the CuAAC, but also transforms the free copper species into a low-toxicity complex.[231] Another possible alternative is the use of strained alkynes, namely cyclooctynes to allow strain-promoted cycloaddition of alkynes and azides.[232] This copper-free Huisgen cycloaddition occurs at room temperature with comparable rates to the CuAAC, but has only been scarcely applied to sol-gel materials, due to the use of elaborated cyclooctyne substrates that involve complicated synthesis steps.[233] It is noteworthy that copper-free Huisgen

cycloadditions between simple alkynes and azides were recently reported under microwave irradiation at 100 °C for 30 min in the case of molecular compounds, thanks to the use of glycerol as a solvent.[234] This method will be very promising to exploit for materials functionalization.

The CuAAC reaction will be particularly adapted for our study as it can be performed in pure water without the need of additional organic solvent, which is absolutely necessary in order to avoid dissolving the crystalline organic core. In order to work in pure water, we will use the copper sulphate/sodium ascorbate catalytic system in the presence of THPTA to reduce the toxicity of Cu(I).

1.5. Objectives

The primary objective of this work is to develop red-emitting organic@silicate core-shell NPs using the spray-drying approach and a modified sol-gel synthesis protocol. The organic dyes used for the nanocrystalline core are non-commercial and specifically designed to be crystal-state emitters and have excellent properties for use in bioimaging applications. The synthesis of these core-shell NPs requires precise control over both the nanocrystallization process and the sol-gel chemistry to optimize the self-assembling one-step process for the preparation of core-shell NPs. These fluorescent organic@silicate core-shell NPs have potential applications in the *in vivo* vascular imaging of tumors using two-photon microscopy. This entails the following:

- Optimization of the synthesis protocol of the core-shell NPs using the spray-drying sol-gel process
- Comprehensive physico-chemical characterization of the core-shell NPs to study their morphology, crystallinity and optical properties
- Optimization of post-synthesis treatment strategies to obtain colloidally stable suspensions in physiologically relevant conditions
- Study of the colloidal stability of the core-shell NPs suspensions in different biological media using Dynamic Light Scattering
- Use of click functionalization strategies to not only render them furtive but to also increase their blood circulation time by making them more biocompatible
- *In vivo* two-photon imaging of the blood vessels in mice to determine the circulation time in blood.

1.6. Bibliography

(1) Mankoff, D. A. A Definition of Molecular Imaging. *J. Nucl. Med.* **2007**, *48* (6), 18N–21N.

(2) Jung, K.-H.; Lee, K.-H. Molecular Imaging in the Era of Personalized Medicine. *J. Pathol.*

Transl. Med. **2015**, *49* (1), 5–12.

(3) Pysz, M. A.; Gambhir, S. S.; Willmann, J. K. Molecular Imaging: Current Status and Emerging Strategies. *Clin Radiol* **2010**, *65* (7), 500–516.

(4) James, M. L.; Gambhir, S. S. A Molecular Imaging Primer: Modalities, Imaging Agents, and Applications. *Physiol. Rev.* **2012**, *92* (2), 897–965.

(5) Willmann, J. K.; van Bruggen, N.; Dinkelborg, L. M.; Gambhir, S. S. Molecular Imaging in Drug Development. *Nat. Rev. Drug Discov.* **2008**, *7* (7), 591–607.

(6) Cammoun, D.; Hendee, W. R.; Davis, K. A. Clinical Applications of Magnetic Resonance Imaging Current Status. *West. J. Med.* **1985**, *143* (6), 793–803.

(7) Naumova, A. V; Modo, M.; Moore, A.; Murry, C. E.; Frank, J. A. Clinical Imaging in Regenerative Medicine. *Nat. Biotechnol.* **2014**, *32* (8), 804–818.

(8) Dunphy, M. P.; Lewis, J. S. Radiopharmaceuticals in Preclinical and Clinical Development for Monitoring of Therapy with PET. *J. Nucl. Med.* **2009**, *50* (Suppl 1), 1–36.

(9) Anand, S. S.; Singh, H.; Dash, A. K. Clinical Applications of PET and PET-CT. *Med. J. Armed Forces India* **2009**, *65* (4), 353–358.

(10) Khalil, M. M.; Tremoleda, J. L.; Bayomy, T. B.; Gsell, W. Molecular SPECT Imaging: An Overview. *Int. J. Mol. Imaging* **2011**, *2011*, 1–15.

(11) Mariani, G.; Bruselli, L.; Kuwert, T.; Kim, E. E.; Flotats, A.; Israel, O.; Dondi, M.; Watanabe, N. A Review on the Clinical Uses of SPECT/CT. *Eur. J. Nucl. Med. Mol. Imaging* **2010**, *37* (10), 1959–1985.

(12) Phan, T. G.; Bullen, A. Practical Intravital Two-Photon Microscopy for Immunological Research: Faster, Brighter, Deeper. *Immunol. Cell Biol.* **2010**, *88* (4), 438–444.

(13) Wang, C.; Wang, Z.; Zhao, T.; Li, Y.; Huang, G.; Sumer, B. D.; Gao, J. Optical Molecular Imaging for Tumor Detection and Image-Guided Surgery. *Biomaterials* **2018**, *157*, 62–75.

(14) Luker, G. D.; Luker, K. E. Optical Imaging: Current Applications and Future Directions. *J. Nucl. Med.* **2007**, *49* (1), 1–4.

(15) Hadjipanayis, C.; Jiang, H.; Roberts, D.; Yang, L. Current and Future Clinical Applications for Optical Imaging of Cancer: From Intraoperative Surgical Guidance to Cancer Screening. *Semin. Oncol.* **2011**, *38* (1), 109–118.

(16) Choy, G.; Choyke, P.; Libutti, S. K. Current Advances in Molecular Imaging: Noninvasive in Vivo Bioluminescent and Fluorescent Optical Imaging in Cancer Research. *Mol Imaging* **2003**, *2* (4), 303–312.

(17) Arranz, A.; Ripoll, J. Advances in Optical Imaging for Pharmacological Studies. *Front. Pharmacol.* **2015**, *6*, doi: 10.3389/fphar.2015.00189.

(18) Wang, K.; Horton, N. G.; Charan, K.; Xu, C. Advanced Fiber Soliton Sources for Nonlinear

Deep Tissue Imaging in Biophotonics. *IEEE J. Sel. Top. Quantum Electron.* **2014**, *20* (2).

(19) Wilson, S. R.; Jang, H. J.; Tae, K. K.; Iijima, H.; Kamiyama, N.; Burns, P. N. Real-Time Temporal Maximum-Intensity-Projection Imaging of Hepatic Lesions with Contrast-Enhanced Sonography. *Am. J. Roentgenol.* **2008**, *190* (3), 691–695.

(20) Hsiao, Y.-H.; Kuo, S.-J.; Tsai, H.-D.; Chou, M.-C.; Yeh, G.-P. Clinical Application of High-Intensity Focused Ultrasound in Cancer Therapy. *J. Cancer* **2016**, *7* (3), 225–231.

(21) Carovac, A.; Smajlovic, F.; Junuzovic, D. Application of Ultrasound in Medicine. *Acta Inform. Medica* **2011**, *19* (3), 168.

(22) Hayashi, T. Application of Ultrasonography in Dentistry. *Jpn. Dent. Sci. Rev.* **2012**, *48* (1), 5–13.

(23) Pierce, M.; Javier, D.; Richards-Kortum, R. Optical Contrast Agents and Imaging Systems for Detection and Diagnosis of Cancer. *Int J Cancer* **2008**, *123* (9), 1979–1990.

(24) Tanaka, E.; Choi, H. S.; Fujii, H.; Bawendi, M. G.; Frangioni, J. V. Image-Guided Oncologic Surgery Using Invisible Light: Completed Pre-Clinical Development for Sentinel Lymph Node Mapping. *Ann. Surg. Oncol.* **2006**, *13* (12), 1671–1681.

(25) Hsu, E. R.; Gillenwater, A. M.; Hasan, M. Q.; Williams, M. D.; El-Naggar, A. K.; Richards-Kortum, R. R. Real-Time Detection of Epidermal Growth Factor Receptor Expression in Fresh Oral Cavity Biopsies Using a Molecular-Specific Contrast Agent. *Int. J. Cancer* **2006**, *118* (12), 3062–3071.

(26) Wang, K.; Wang, K.; Li, W.; Huang, T.; Li, R.; Wang, D.; Shen, B.; Chen, X. Characterizing Breast Cancer Xenograft Epidermal Growth Factor Receptor Expression by Using Near-Infrared Optical Imaging. *Acta radiol.* **2009**, *50* (10), 1095–1103.

(27) Gounaris, E.; Tung, C. H.; Restaino, C.; Maehr, R.; Kohler, R.; Joyce, J. A.; Plough, H. L.; Barrett, T. A.; Weissleder, R.; Khazaie, K. Live Imaging of Cysteine-Cathepsin Activity Reveals Dynamics of Focal Inflammation, Angiogenesis, and Polyp Growth. *PLoS One* **2008**, *3* (8).

(28) Hemmer, E.; Benayas, A.; Légaré, F.; Vetrone, F. Exploiting the Biological Windows: Current Perspectives on Fluorescent Bioprobes Emitting above 1000 Nm. *Nanoscale Horizons* **2016**, *1* (3), 168–184.

(29) https://www.thorlabs.com/newgrouppage9.cfm?objectgroup_id=10765.

(30) Svoboda, K.; Yasuda, R. Principles of Two-Photon Excitation Microscopy and Its Applications to Neuroscience. *Neuron* **2006**, *50* (6), 823–839.

(31) Thomas, G.; Van Voskuilen, J.; Gerritsen, H. C.; Sterenborg, H. J. C. M. Advances and Challenges in Label-Free Nonlinear Optical Imaging Using Two-Photon Excitation Fluorescence and Second Harmonic Generation for Cancer Research. *J. Photochem. Photobiol. B Biol.* **2014**, *141*, 128–138.

(32) Xu, J.; Kang, D.; Xu, M.; Zhuo, S.; Zhu, X.; Chen, J. Multiphoton Microscopic Imaging of Esophagus during the Early Phase of Tumor Progression. *Scanning* **2013**, *35* (6), 387–391.

(33) Hong, Z.; Chen, Y.; Chen, J.; Chen, H.; Xu, Y.; Zhu, X.; Zhuo, S.; Shi, Z.; Chen, J. Optical Diagnosis of Gallbladder Cancers via Two-Photon Excited Fluorescence Imaging of Unstained Histological Sections. *Lasers Med. Sci.* **2014**, *30* (1), 225–233.

(34) Tewari, A. K.; Shevchuk, M. M.; Sterling, J.; Grover, S.; Herman, M.; Yadav, R.; Mudalair, K.; Srivastava, A.; Rubin, M. A.; Zipfel, W. R.; et al. Multiphoton Microscopy for Structure Identification in Human Prostate and Periprostatic Tissue: Implications in Prostate Cancer Surgery. *BJU Int.* **2011**, *108* (9), 1421–1429.

(35) Bickford, L.; Sun, J.; Fu, K.; Lewinski, N.; Nammalvar, V.; Chang, J.; Drezek, R. Enhanced Multi-Spectral Imaging of Live Breast Cancer Cells Using Immunotargeted Gold Nanoshells and Two-Photon Excitation Microscopy. *Nanotechnology* **2008**, *19* (31), 315102.

(36) Masedunskas, A.; Weigert, R. Intravital Two-Photon Microscopy for Studying the Uptake and Trafficking of Fluorescently Conjugated Molecules in Live Rodents. *Traffic* **2008**, *9* (10), 1801–1810.

(37) Tanaka, K.; Morimoto, Y.; Toiyama, Y.; Matsushita, K.; Kawamura, M.; Koike, Y.; Okugawa, Y.; Inoue, Y.; Uchida, K.; Araki, T.; et al. In Vivo Time-Course Imaging of Tumor Angiogenesis in Colorectal Liver Metastases in the Same Living Mice Using Two-Photon Laser Scanning Microscopy. *J. Oncol.* **2012**, 265487.

(38) Koga, S.; Oshima, Y.; Honkura, N.; Iimura, T.; Kameda, K.; Sato, K.; Yoshida, M.; Yamamoto, Y.; Watanabe, Y.; Hikita, A.; et al. In Vivo Subcellular Imaging of Tumors in Mouse Models Using a Fluorophore-Conjugated Anti-Carcinoembryonic Antigen Antibody in Two-Photon Excitation Microscopy. *Cancer Sci.* **2014**, *105* (10), 1299–1306.

(39) Adur, J.; Pelegati, V. B.; de Thomaz, A. A.; Baratti, M. O.; Andrade, L. A. L. A.; Carvalho, H. F.; Bottcher-Luiz, F.; Cesar, C. L. Second Harmonic Generation Microscopy as a Powerful Diagnostic Imaging Modality for Human Ovarian Cancer. *J. Biophotonics* **2014**, *7* (1–2), 37–48.

(40) Falzon, G.; Pearson, S.; Murison, R. Analysis of Collagen Fibre Shape Changes in Breast Cancer. *Phys. Med. Biol.* **2008**, *53* (23), 6641–6652.

(41) Burke, K.; Smid, M.; Dawes, R. P.; Timmermans, M. A.; Salzman, P.; van Deurzen, C. H. M.; Beer, D. G.; Foekens, J. A.; Brown, E. Using Second Harmonic Generation to Predict Patient Outcome in Solid Tumors. *BMC Cancer* **2015**, *15:929* (1), DOI 10.1186/s12885-015-1911-8.

(42) Provenzano, P. P.; Eliceiri, K. W.; Campbell, J. M.; Inman, D. R.; White, J. G.; Keely, P. J. Collagen Reorganization at the Tumor-Stromal Interface Facilitates Local Invasion. *BMC Med.* **2006**, *4:38*, doi:10.1186/1741-7015-4-38.

(43) Jiang, L. W.; Wang, X. F.; Wu, Z. Y.; Lin, P. H.; Du, H. P.; Wang, S.; Li, L. H.; Fang, N.; Zhuo, S. M.; Kang, D. Z.; et al. Label-Free Detection of Fibrillar Collagen Deposition Associated with

Vascular Elements in Glioblastoma Multiforme by Using Multiphoton Microscopy. *J. Microsc.* **2017**, *265* (2), 207–213.

(44) Brown, E.; McKee, T.; diTomaso, E.; Pluen, A.; Seed, B.; Boucher, Y.; K.Jain, R. Dynamic Imaging of Collagen and Its Modulation in Tumors in Vivo Using Second Harmonic Generation. *Nat. Med.* **2003**, *9* (6), 796–800.

(45) Liu, N. R.; Chen, J. X.; Chen, G.; Yan, J.; Zhuo, S. M.; Jiang, X. S. Detecting the Imaging Characteristics of Colorectal Carcinoma Invading the Muscularis Propria with Multiphoton Microscopy. *Laser Phys. Lett.* **2012**, *9* (2), 155–159.

(46) Bianchi, M.; Adur, J.; Ruff, S. Y.; Izaguirre, M. F.; Carvalho, H. F.; Cesar, C. L.; Casco, V. H. Mouse Colorectal Cancer an Early Detection Approach Using Nonlinear Microscopy. *Biomed. Mater. Eng.* **2014**, *24* (6), 3419–3426.

(47) Galli, R.; Sablinskas, V.; Dasevicius, D.; Laurinavicius, A.; Jankevicius, F.; Koch, E.; Steiner, G. Non-Linear Optical Microscopy of Kidney Tumours. *J. Biophotonics* **2014**, *7* (1–2), 23–27.

(48) Gao, L.; Wang, Z.; Li, F.; Hammoudi, A. A.; Thrall, M. J.; Cagle, P. T.; Wong, S. T. C. Differential Diagnosis of Lung Carcinoma With Coherent Anti-Stokes Raman Scattering Imaging. *Arch. Pathol. Lab. Med.* **2012**, *136* (12), 1502–1510.

(49) Le, T. T.; Huff, T. B.; Cheng, J.-X. Coherent Anti-Stokes Raman Scattering Imaging of Lipids in Cancer Metastasis. *BMC Cancer* **2009**, *9* (1), 42.

(50) Mitra, R.; Chao, O.; Urasaki, Y.; Goodman, O.; Le, T. Detection of Lipid-Rich Prostate Circulating Tumour Cells with Coherent Anti-Stokes Raman Scattering Microscopy. *BMC Cancer* **2012**, *12* (1), 540.

(51) Uckermann, O.; Galli, R.; Tamosaityte, S.; Leipnitz, E.; Geiger, K. D.; Schackert, G.; Koch, E.; Steiner, G.; Kirsch, M. Label-Free Delineation of Brain Tumors by Coherent Anti-Stokes Raman Scattering Microscopy in an Orthotopic Mouse Model and Human Glioblastoma. *PLoS One* **2014**, *9* (9).

(52) Rampazzo, E.; Genovese, D.; Palomba, F.; Prodi, L.; Zaccheroni, N. NIR Fluorescent Dye Doped Silica Nanoparticles for in Vivo Imaging, Sensing and Theranostic. *Methods Appl. Fluoresc.* **2018**, *6*, 022002.

(53) Liu, G.; Sheng, J.; Zhao, Y. In Vivo Near-Infrared Fluorescence Imaging. In *Nanotechnology Characterization Tools for Biosensing and Medical Diagnosis. Springer, Berlin, Heidelberg*; 2018; pp 67–125.

(54) Wolfbeis, O. S. An Overview of Nanoparticles Commonly Used in Fluorescent Bioimaging. *Chem. Soc. Rev.* **2015**, *44* (14), 4743–4768.

(55) Liu, T. M.; Conde, J.; Lipiński, T.; Bednarkiewicz, A.; Huang, C. C. Revisiting the Classification of NIR-Absorbing/Emitting Nanomaterials for in Vivo Bioapplications. *NPG Asia Mater.* **2016**, *8* (8), 1–25.

(56) Park, Y.; Jeong, S.; Kim, S. Medically Translatable Quantum Dots for Biosensing and Imaging. *J. Photochem. Photobiol. C Photochem. Rev.* **2017**, *30*, 51–70.

(57) Chan, W. C. W.; Maxwell, D. J.; Gao, X.; Bailey, R. E.; Han, M.; Nie, S. Luminescent Quantum Dots for Multiplexed Biological Detection and Imaging. *Curr. Opin. Biotechnol.* **2002**, *13* (1), 40–46.

(58) Larson, D. R.; Larson. Water-Soluble Quantum Dots for Multiphoton Fluorescence Imaging in Vivo. *Science (80-.).* **2003**, *300* (5624), 1434–1436.

(59) Gao, X.; Cui, Y.; Levenson, R. M.; Chung, L. W. K.; Nie, S. In Vivo Cancer Targeting and Imaging with Semiconductor Quantum Dots. *Nat. Biotechnol.* **2004**, *22* (8), 969–976.

(60) Stroh, M.; Zimmer, J. P.; Duda, D. G.; Levchenko, T. S.; Cohen, K. S.; Brown, E. B.; Scadden, D. T.; Torchilin, V. P.; Bawendi, M. G.; Jain, R. K. NIH Public Access. **2009**, *11* (6), 678–682.

(61) Akerman, M. E.; Chan, W. C. W.; Laakkonen, P.; Bhatia, S. N.; Ruoslahti, E. Nanocrystal Targeting in Vivo. *Proc. Natl. Acad. Sci.* **2002**, *99* (20), 12617–12621.

(62) Cai, W.; Shin, D. W.; Chen, K.; Gheysens, O.; Cao, Q.; Wang, S. X.; Gambhir, S. S.; Chen, X. Peptide-Labeled near-Infrared Quantum Dots for Imaging Tumor Vasculature in Living Subjects. *Nano Lett.* **2006**, *6* (4), 669–676.

(63) Kim, S.; Lim, Y. T.; Soltesz, E. G.; De Grand, A. M.; Lee, J.; Nakayama, A.; Parker, J. A.; Mihaljevic, T.; Laurence, R. G.; Dor, D. M.; et al. Near-Infrared Fluorescent Type II Quantum Dots for Sentinel Lymph Node Mapping. *Nat. Biotechnol.* **2004**, *22* (1), 93–97.

(64) Kim, S.; Fisher, B.; Eisler, H. J.; Bawendi, M. Type-II Quantum Dots: CdTe/CdSe(Core/Shell) and CdSe/ZnTe(Core/Shell) Heterostructures. *J. Am. Chem. Soc.* **2003**, *125* (38), 11466–11467.

(65) Bürglová, K.; Noureddine, A.; Hodačová, J.; Toquer, G.; Cattoën, X.; Wong Chi Man, M. A General Method for Preparing Bridged Organosilanes with Pendant Functional Groups and Functional Mesoporous Organosilicas. *Chem. - A Eur. J.* **2014**, *20* (33), 10371–10382.

(66) Lu, X.; Sun, F.; Wang, J.; Zhong, J.; Dong, Q. A Facile Route to Prepare Organic/Inorganic Hybrid Nanomaterials by "Click Chemistry." *Macromol. Rapid Commun.* **2009**, *30* (24), 2116–2120.

(67) Ladomenou, K.; Nikolaou, V.; Charalambidis, G.; Coutsolelos, A. G. "Click"-Reaction: An Alternative Tool for New Architectures of Porphyrin Based Derivatives. *Coord. Chem. Rev.* **2016**, *306* (P1), 1–42.

(68) Pathak, S. Quantum Dot Applications to Neuroscience: New Tools for Probing Neurons and Glia. *J. Neurosci.* **2006**, *26* (7), 1893–1895.

(69) https://www.cd-bioparticles.com/t/Properties-and-Applications-of-Quantum-Dots_56.html.

(70) Yu, J. H.; Kwon, S.-H.; Petrášek, Z.; Park, O. K.; Jun, S. W.; Shin, K.; Choi, M.; Park, Y. Il; Park,

K.; Na, H. Bin; et al. High-Resolution Three-Photon Biomedical Imaging Using Doped ZnS Nanocrystals. *Nat. Mater.* **2013**, *12* (4), 359–366.

(71) Zhang, Y.; Hong, G.; Zhang, Y.; Chen, G.; Li, F.; Dai, H.; Wang, Q. Ag2S Quantum Dot: A Bright and Biocompatible Fluorescent Nanoprobe in the Second Near-Infrared Window. *ACS Nano* **2012**, *6* (5), 3695–3702.

(72) Hong, G.; Robinson, J. T.; Zhang, Y.; Diao, S.; Antaris, A. L.; Wang, Q.; Dai, H. In Vivo Fluorescence Imaging with Ag2S Quantum Dots in the Second Near-Infrared Region. *Angew. Chemie - Int. Ed.* **2012**, *51* (39), 9818–9821.

(73) Bashkatov, A. N.; Genina, E. A.; Kochubey, V. I.; Tuchin, V. V. Optical Properties of Human Skin, Subcutaneous and Mucous Tissues in the Wavelength Range from 400 to 2000 Nm. *J. Phys. D. Appl. Phys.* **2005**, *38* (15), 2543–2555.

(74) Mader, H. S.; Kele, P.; Saleh, S. M.; Wolfbeis, O. S. Upconverting Luminescent Nanoparticles for Use in Bioconjugation and Bioimaging. *Curr. Opin. Chem. Biol.* **2010**, *14* (5), 582–596.

(75) Xu, C. T.; Zhan, Q.; Liu, H.; Somesfalean, G.; Qian, J.; He, S.; Andersson-Engels, S. Upconverting Nanoparticles for Pre-Clinical Diffuse Optical Imaging, Microscopy and Sensing: Current Trends and Future Challenges. *Laser Photonics Rev.* **2013**, *7* (5), 663–697.

(76) Wang, F.; Banerjee, D.; Liu, Y.; Chen, X.; Liu, X. Upconversion Nanoparticles in Biological Labeling, Imaging, and Therapy. *Analyst* **2010**, *135* (8), 1839.

(77) Cao, T.; Yang, Y.; Gao, Y.; Zhou, J.; Li, Z.; Li, F. High-Quality Water-Soluble and Surface-Functionalized Upconversion Nanocrystals as Luminescent Probes for Bioimaging. *Biomaterials* **2011**, *32* (11), 2959–2968.

(78) Min, Y.; Li, J.; Liu, F.; Padmanabhan, P.; Yeow, E.; Xing, B. Recent Advance of Biological Molecular Imaging Based on Lanthanide-Doped Upconversion-Luminescent Nanomaterials. *Nanomaterials* **2014**, *4* (1), 129–154.

(79) Hilderbrand, S. A.; Shao, F.; Salthouse, C.; Mahmood, U.; Weissleder, R. Upconverting Luminescent Nanomaterials: Application to in Vivo Bioimaging. *Chem. Commun.* **2009**, 4188.

(80) Vinegoni, C.; Razansky, D.; Hilderbrand, S. A.; Shao, F.; Ntziachristos, V.; Weissleder, R. Transillumination Fluorescence Imaging in Mice Using Biocompatible Upconverting Nanoparticles. *Opt. Lett.* **2009**, *34* (17), 2566–2568.

(81) Wang, M.; Mi, C.; Zhang, Y.; Liu, J.; Li, F.; Mao, C.; Xu, S. NIR-Responsive Silica-Coated $NaYbF_4$:Er/Tm/Ho Upconversion Fluorescent Nanoparticles with Tunable Emission Colors and Their Applications in Immunolabeling and Fluorescent Imaging of Cancer Cells. *J. Phys. Chem. C* **2009**, *113* (44), 19021–19027.

(82) Wang, M.; Mi, C.; Wang, W.; Liu, C.; Wu, Y.; Xu, Z.; Mao, B.; Xu, S. Immunolabeling and NIR-Excited Fluorescent Imaging of HeLa Cells by Using NaYF4:Yb,Er Upconversion

Nanoparticles. *ACS Nano* **2009**, *3* (6), 1580–1586.

(83) Zako, T.; Nagata, H.; Terada, N.; Utsumi, A.; Sakono, M.; Yohda, M.; Ueda, H.; Soga, K.; Maeda, M. Cyclic RGD Peptide-Labeled Upconversion Nanophosphors for Tumor Cell-Targeted Imaging. *Biochem. Biophys. Res. Commun.* **2009**, *381* (1), 54–58.

(84) Nyk, M.; Kumar, R.; Ohulchanskyy, T. Y.; Bergey, E. J.; Prasad, P. N. High Contrast in Vitro and in Vivo Photoluminescence Bioimaging Using Near Infrared to Near Infrared Up-Conversion in Tm^{3+} and Yb^{3+} Doped Fluoride Nanophosphors. *Nano Lett.* **2008**, *8* (11), 3834–3838.

(85) Xiong, L.; Chen, Z.; Tian, Q.; Cao, T.; Xu, C.; Li, F. SI High Contrast Upconversion Luminescence Targeted Imaging in Vivo Using Peptide-Labeled Nanophosphors. *Anal. Chem.* **2009**, *81* (21), 8687–8694.

(86) Cheng, L.; Yang, K.; Zhang, S.; Shao, M.; Lee, S.; Liu, Z. Highly-Sensitive Multiplexed in Vivo Imaging Using Pegylated Upconversion Nanoparticles. *Nano Res.* **2010**, *3* (10), 722–732.

(87) Idris, N. M.; Li, Z.; Ye, L.; Wei Sim, E. K.; Mahendran, R.; Ho, P. C. L.; Zhang, Y. Tracking Transplanted Cells in Live Animal Using Upconversion Fluorescent Nanoparticles. *Biomaterials* **2009**, *30* (28), 5104–5113.

(88) Xiong, L.; Yang, T.; Yang, Y.; Xu, C.; Li, F. Long-Term in Vivo Biodistribution Imaging and Toxicity of Polyacrylic Acid-Coated Upconversion Nanophosphors. *Biomaterials* **2010**, *31* (27), 7078–7085.

(89) Jin, J.; Gu, Y. J.; Man, C. W. Y.; Cheng, J.; Xu, Z.; Zhang, Y.; Wang, H.; Lee, V. H. Y.; Cheng, S. H.; Wong, W. T. Polymer-Coated NaYF4:Yb3+, Er3+upconversion Nanoparticles for Charge-Dependent Cellular Imaging. *ACS Nano* **2011**, *5* (10), 7838–7847.

(90) Abdul Jalil, R.; Zhang, Y. Biocompatibility of Silica Coated NaYF4 Upconversion Fluorescent Nanocrystals. *Biomaterials* **2008**, *29* (30), 4122–4128.

(91) Li, Z.; Zhang, Y.; Jiang, S. Multicolor Core/Shell-Structured Upconversion Fluorescent Nanoparticles. *Adv. Mater.* **2008**, *20* (24), 4765–4769.

(92) Hu, H.; Xiong, L.; Zhou, J.; Li, F.; Cao, T.; Huang, C. Multimodal-Luminescence Core-Shell Nanocomposites for Targeted Imaging of Tumor Cells. *Chem. - A Eur. J.* **2009**, *15* (14), 3577–3584.

(93) Qian, H. S.; Guo, H. C.; Ho, P. C. L.; Mahendran, R.; Zhang, Y. Mesoporous-Silica-Coated up-Conversion Fluorescent Nanoparticles for Photodynamic Therapy. *Small* **2009**, *5* (20), 2285–2290.

(94) Montalti, M.; Prodi, L.; Rampazzo, E.; Zaccheroni, N. Dye-Doped Silica Nanoparticles as Luminescent Organized Systems for Nanomedicine. *Chem. Soc. Rev.* **2014**, *43* (12), 4243–4268.

(95) Bonacchi, S.; Genovese, D.; Juris, R.; Montalti, M.; Prodi, L.; Rampazzo, E.; Zaccheroni, N. Luminescent Silica Nanoparticles: Extending the Frontiers of Brightness. *Angew. Chemie* -

Int. Ed. **2011**, *50* (18), 4056–4066.

(96) Helle, M.; Rampazzo, E.; Monchanin, M.; Marchal, F.; Guillemin, F.; Bonacchi, S.; Salis, F.; Prodi, L.; Bezdetnaya, L. Surface Chemistry Architecture of Silica Nanoparticles Determine the Efficiency of in Vivo Fluorescence Lymph Node Mapping. *ACS Nano* **2013**, *7* (10), 8645–8657.

(97) Yan, L.; Wang, H.; Zhang, A.; Zhao, C.; Chen, Y.; Li, X. Bright and Stable Near-Infrared Pluronic–silica Nanoparticles as Contrast Agents for in Vivo Optical Imaging. *J. Mater. Chem. B* **2016**, *4* (33), 5560–5566.

(98) Lal, M.; Levy, L.; Kim, K. S.; He, G. S.; Wang, X.; Min, Y. H.; Pakatchi, S.; Prasad, P. N. Silica Nanobubbles Containing an Organic Dye in a Multilayered Organic/Inorganic Heterostructure with Enhanced Luminescence. *Chem. Mater.* **2000**, *12* (9), 2632–2639.

(99) Levy, L.; Sahoo, Y.; Kim, K. S.; Bergey, E. J.; Prasad, P. N. Nanochemistry: Synthesis and Characterization of Multifunctional Nanoclinics for Biological Applications. *Chem. Mater.* **2002**, *14* (9), 3715–3721.

(100) Ohulchanskyy, T. Y.; Roy, I.; Goswami, L. N.; Chen, Y.; Bergey, E. J.; Pandey, R. K.; Oseroff, A. R.; Prasad, P. N. Organically Modified Silica Nanoparticles with Covalently Incorporated Photosensitizer for Photodynamic Therapy of Cancer. *Nano Lett.* **2007**, *7* (9), 2835–2842.

(101) Kim, S.; Pudavar, H. E.; Bonoiu, A.; Prasad, P. N. Aggregation-Enhanced Fluorescence in Organically Modified Silica Nanoparticles: A Novel Approach toward High-Signal-Output Nanoprobes for Two-Photon Fluorescence Bioimaging. *Adv. Mater.* **2007**, *19* (22), 3791–3795.

(102) Kim, S.; Ohulchanskyy, T. Y.; Pudavar, H. E.; Pandey, R. K.; Prasad, P. N. Organically Modified Silica Nanoparticles Co-Encapsulating Photosensitizing Drug and Aggregation-Enhanced Two-Photon Absorbing Fluorescent Dye Aggregates for Two-Photon Photodynamic Therapy. *J. Am. Chem. Soc.* **2007**, *129* (9), 2669–2675.

(103) Wei, Y.; Liu, M.; Xu, D.; Wan, Q.; Huang, Q.; Jiang, R.; Shi, Y.; Deng, F.; Zhang, X. Synthesis, Surface Modification and Biological Imaging of Aggregation-Induced Emission (AIE) Dye Doped Silica Nanoparticles. *Appl. Surf. Sci.* **2017**, *403*, 396–402.

(104) Xia, Y.; Li, M.; Peng, T.; Zhang, W.; Xiong, J.; Hu, Q.; Song, Z.; Zheng, Q. In Vitro Cytotoxicity of Fluorescent Silica Nanoparticles Hybridized with Aggregation-Induced Emission Luminogens for Living Cell Imaging. *Int. J. Mol. Sci.* **2013**, *14* (1), 1080–1092.

(105) Zhu, Z.; Zhao, X.; Qin, W.; Chen, G.; Qian, J.; Xu, Z. Fluorescent AIE Dots Encapsulated Organically Modified Silica (ORMOSIL) Nanoparticles for Two-Photon Cellular Imaging. *Sci. China Chem.* **2013**, *56* (9), 1247–1252.

(106) Wang, Y.-F.; Che, J.; Zheng, Y.-C.; Zhao, Y.-Y.; Chen, F.; Jin, S.-B.; Gong, N.-Q.; Xu, J.; Hu, Z.-B.; Liang, X.-J. Multi-Stable Fluorescent Silica Nanoparticles Obtained from in Situ Doping with Aggregation-Induced Emission Molecules. *J. Mater. Chem. B* **2015**, *3* (45), 8775–8781.

(107) Miao, C.; Li, D.; Zhang, Y.; Yu, J.; Xu, R. Reprint of: "AIE Luminogen Functionalized Mesoporous Silica Nanoparticles as Efficient Fluorescent Sensor for Explosives Detection in Water." *Microporous Mesoporous Mater.* **2014**, *200*, 281–286.

(108) Li, Q.; Qian, Y. Aggregation-Induced Emission Enhancement and Cell Imaging of a Novel (Carbazol-N-Yl)Triphenylamine–BODIPY. *New J. Chem.* **2016**, *40* (8), 7095–7101.

(109) Mao, L.; Liu, X.; Liu, M.; Huang, L.; Xu, D.; Jiang, R.; Huang, Q.; Wen, Y.; Zhang, X.; Wei, Y. Surface Grafting of Zwitterionic Polymers onto Dye Doped AIE-Active Luminescent Silica Nanoparticles through Surface-Initiated ATRP for Biological Imaging Applications. *Appl. Surf. Sci.* **2017**, *419*, 188–196.

(110) Wu, W. B.; Liu, C.; Wang, M. L.; Huang, W.; Zhou, S. R.; Jiang, W.; Sun, Y. M.; Cui, Y. P.; Xu, C. X. Uniform Silica Nanoparticles Encapsulating Two-Photon Absorbing Fluorescent Dye. *J. Solid State Chem.* **2009**, *182* (4), 862–868.

(111) Godoy-Navajas, J.; Aguilar-Caballos, M.-P.; Gómez-Hens, A. Synthesis and Characterization of Oxazine-Doped Silica Nanoparticles for Their Potential Use as Stable Fluorescent Reagents. *J. Fluoresc.* **2010**, *20* (1), 171–180.

(112) Bertazza, L.; Celotti, L.; Fabbrini, G.; Loi, M. A.; Maggini, M.; Mancin, F.; Marcuz, S.; Menna, E.; Muccini, M.; Tonellato, U. Cell Penetrating Silica Nanoparticles Doped with Two-Photon Absorbing Fluorophores. *Tetrahedron* **2006**, *62* (44), 10434–10440.

(113) Phillips, E.; Penate-Medina, O.; Zanzonico, P. B.; Carvajal, R. D.; Mohan, P.; Ye, Y.; Humm, J.; Gönen, M.; Kalaigian, H.; Schöder, H.; et al. Clinical Translation of an Ultrasmall Inorganic Optical-PET Imaging Nanoparticle Probe. *Sci. Med.* **2015**, *6* (260), doi:10.1126/scitranslmed.3009524.

(114) Bradbury, M. S.; Phillips, E.; Montero, P. H.; Cheal, S. M.; Stambuk, H.; Durack, J. C.; Sofocleous, C. T.; Meesterc, R. J. C.; Wiesnerd, U.; Patel, S. Clinically-Translated Silica Nanoparticles as Dual-Modality Cancer-Targeted Probes for Image-Guided Surgery and Interventions. *Integr Biol* **2013**, *5* (1), 74–86.

(115) Bradbury, M. S.; Pauliah, M.; Zanzonico, P.; Weisner, U.; Patel, S. Intraoperative Mapping of SLN Metastases Using a Clinically- Translated Ultrasmall Silica Nanoparticle. *Wiley Interdiscip. Rev. Nanomedicine Nanobiotechnology* **2016**, *8* (4), 535–553.

(116) Quan, B.; Choi, K.; Kim, Y. H.; Kang, K. W.; Chung, D. S. Near Infrared Dye Indocyanine Green Doped Silica Nanoparticles for Biological Imaging. *Talanta* **2012**, *99*, 387–393.

(117) Accomasso, L.; Rocchietti, E. C.; Raimondo, S.; Catalano, F.; Alberto, G.; Giannitti, A.; Minieri, V.; Turinetto, V.; Orlando, L.; Saviozzi, S.; et al. Fluorescent Silica Nanoparticles Improve Optical Imaging of Stem Cells Allowing Direct Discrimination between Live and Early-Stage Apoptotic Cells. *Small* **2012**, *8* (20), 3192–3200.

(118) O'Connell, C. L.; Nooney, R.; McDonagh, C. Cyanine5-Doped Silica Nanoparticles as Ultra-Bright Immunospecific Labels for Model Circulating Tumour Cells in Flow Cytometry and Microscopy. *Biosens. Bioelectron.* **2017**, *91*, 190–198.

(119) Yao, G.; Wang, L.; Wu, Y.; Smith, J.; Xu, J.; Zhao, W.; Lee, E.; Tan, W. FloDots: Luminescent Nanoparticles. *Anal. Bioanal. Chem.* **2006**, *385* (3), 518–524.

(120) Chen, Z. Z.; Cai, L.; Dong, X. M.; Tang, H. W.; Pang, D. W. Covalent Conjugation of Avidin with Dye-Doped Silica Nanopaticles and Preparation of High Density Avidin Nanoparticles as Photostable Bioprobes. *Biosens. Bioelectron.* **2012**, *37* (1), 75–81.

(121) Cai, L.; Chen, Z. Z.; Chen, M. Y.; Tang, H. W.; Pang, D. W. MUC-1 Aptamer-Conjugated Dye-Doped Silica Nanoparticles for MCF-7 Cells Detection. *Biomaterials* **2013**, *34* (2), 371–381.

(122) Zhang, N.; Ding, E.; Feng, X.; Xu, Y.; Cai, H. Synthesis, Characterizations of Dye-Doped Silica Nanoparticles and Their Application in Labeling Cells. *Colloids Surfaces B Biointerfaces* **2012**, *89* (1), 133–138.

(123) Santra, S.; Dutta, D.; Moudgil, B. M. Functional Dye-Doped Silica Nanoparticles for Bioimaging, Diagnostics and Therapeutics. *Food Bioprod. Process.* **2005**, *83* (2 C), 136–140.

(124) Ribeiro, T.; Raja, S.; Rodrigues, A. S.; Fernandes, F.; Farinha, J. P. S.; Baleizão, C. High Performance NIR Fluorescent Silica Nanoparticles for Bioimaging. *RSC Adv.* **2013**, *3* (24), 9171.

(125) Chow, P. K.; Cheng, G.; Ong, G. S. M. T.; To, W. P.; Kwong, W. L.; Kowk, C. C.; Ma, C.; Che, C. M. Luminescent Pincer Platinum(II) Complexes with Emission Quantum Yields up to Almost Unity: Photophysics, Photoreductive c-c Bond Formation, and Materials Applications. *Angew. Chemie - Int. Ed.* **2015**, *54* (7), 2084–2089.

(126) Zhang, W.-H.; Hu, X.-X.; Zhang, X.-B. Dye-Doped Fluorescent Silica Nanoparticles for Live Cell and In Vivo Bioimaging. *Nanomaterials* **2016**, *6* (12), 81.

(127) Reisch, A.; Klymchenko, A. S. Fluorescent Polymer Nanoparticles Based on Dyes: Seeking Brighter Tools for Bioimaging. *Small* **2016**, *12* (15), 1968–1992.

(128) Redon, S.; Eucat, G.; Ipuy, M.; Jeanneau, E.; Gautier-Luneau, I.; Ibanez, A.; Andraud, C.; Bretonnière, Y. Tuning the Solid-State Emission of Small Push-Pull Dipolar Dyes to the Far-Red through Variation of the Electron-Acceptor Group. *Dye. Pigment.* **2018**, *156*, 116–132.

(129) Bouit, P. A.; Wetzel, G.; Berginc, G.; Loiseaux, B.; Toupet, L.; Feneyrou, P.; Bretonnière, Y.; Kamada, K.; Maury, O.; Andraud, C. Near IR Nonlinear Absorbing Chromophores with Optical Limiting Properties at Telecommunication Wavelengths. *Chem. Mater.* **2007**, *19* (22), 5325–5335.

(130) Ipuy, M.; Liao, Y.-Y.; Jeanneau, E.; Baldeck, P. L.; Bretonnière, Y.; Andraud, C. Solid State Red Biphotonic Excited Emission from Small Dipolar Fluorophores. *J. Mater. Chem. C* **2016**, *4* (4), 766–779.

(131) Pascal, S.; Getmanenko, Y. A.; Zhang, Y.; Davydenko, I.; Ngo, M. H.; Pilet, G.; Maury, O.; Ledoux-rak, I.; Barlow, S.; Marder, S. R.; et al. Design of Near-Infrared-Absorbing Unsymmetrical Polymethine Dyes with Large Quadratic Hyperpolarizabilities. *Chem. Mater.* **2018**, *30* (10), 3410–3418.

(132) Philippot, C.; Dubois, F.; Bacia, M.; Djurado, E.; Ibanez, A. Fluorescent Organic Nanocrystal Confined in Sol-Gel Matrix for Bio-Imaging. *J. Sol-Gel Sci. Technol.* **2011**, *57* (3), 253–257.

(133) Brinker, C.; Scherer, G. W. The Physics and Chemistry of Sol-Gel Processing. *Sol-Gel Sci. Phys. Chem. Sol-gel Process.* **1990**, *3*, 581–585.

(134) Schubert, U. Part One Sol – Gel Chemistry and Methods. *Sol-Gel Handb. Synth. Charact. Appl.* **2015**, 1–28.

(135) Sunarso, J.; Hashim, S. S.; Lin, Y. S.; Liu, S. M. Membranes for Helium Recovery: An Overview on the Context, Materials and Future Directions. *Sep. Purif. Technol.* **2017**, *176*, 335–383.

(136) Monnier, V.; Sanz, N.; Botzung-Appert, E.; Bacia, M.; Ibanez, A. Confined Nucleation and Growth of Organic Nanocrystals in Sol–gel Matrices. *J. Mater. Chem.* **2006**, *16* (15), 1401–1409.

(137) Cubillas, P.; Anderson, M. W. SynthesisMechanism: Crystal Growth and Nucleation. In *Zeolites and Catalysis, Synthesis, reactions and Applications*; 2010; pp 1–55.

(138) DeYoreo, J. J.; Vekilov, P. G. Principles of Crystal Nucleation and Growth. *Rev. Mineral. Geochemistry* **2003**, *54* (1), 57–93.

(139) Chang, J.; Waclawik, E. R. Colloidal Semiconductor Nanocrystals: Controlled Synthesis and Surface Chemistry in Organic Media. *RSC Adv.* **2014**, *4* (45), 23505–23527.

(140) Kadi, K. El; Janajreh, I. Desalination by Freeze Crystallization : An Overview. *Int . J . Therm. Environ. Eng.* **2017**, *15* (2), 103–110.

(141) Ibanez, A.; Maximov, S.; Guiu, A.; Chaillout, C.; Baldeck, P. L. Controlled Nanocrystallization of Organic Molecules in Sol-Gel Glasses. *Adv. Mater.* **1998**, *10* (18), 1540–1543.

(142) Dubuisson, E.; Szunerits, S.; Bacia, M.; Pansu, R.; Ibanez, A. Fluorescent Molecular Nanocrystals Anchored in Sol-Gel Thin Films: A Label-Free Signalization Function for Biosensing Applications. *New J. Chem.* **2011**, *35* (11), 2416–2421.

(143) Debecker, D. P.; Le Bras, S.; Boissiere, C.; Chaumonnot, A.; Sanchez, C. Aerosol Processing: A Wind of Innovation in the Field of Advanced Heterogeneous Catalysts. *Chem. Soc. Rev.* **2018**, *47*, 4112–4155.

(144) Iskandar, F.; Lenggoro, I. W.; Xia, B.; Okuyama, K. Functional Nanostructured Silica Powders Derived from Colloidal Suspensions by Sol Spraying. *J. Nanoparticle Res.* **2001**, *3* (4), 263–270.

(145) Ishimori, T.; Senna, M. Control of Microstructure and Disintegration Properties of Silica Granules from PVA Slurries by Spray Drying. *J. Mater. Sci.* **1995**, *30* (2), 488–495.

(146) Maskara, A.; Smith, D. Agglomeration during the Drying of Fine Silica Powders, Part II: The Role of Particle Solubility. *J. Am. Ceram. Soc.* **1997**, 1715–1722.

(147) Baccile, N.; Grosso, D.; Sanchez, C. Aerosol Generated Mesoporous Silica Particles. *J.*

Mater. Chem. **2003**, *13* (12), 3011.

(148) Julián-López, B.; Boissière, C.; Chanéac, C.; Grosso, D.; Vasseur, S.; Miraux, S.; Duguet, E.; Sanchez, C. Mesoporous Maghemite–organosilica Microspheres: A Promising Route towards Multifunctional Platforms for Smart Diagnosis and Therapy. *J. Mater. Chem.* **2007**, *17* (16), 1563–1569.

(149) Alonso, B.; Douy, a; Véron, E. Morphological and Textural Control of Spray-Dried Mesoporous Silica-Based Spheres. *J. Mater. Chem.* **2004**, No. 14, 2006–2016.

(150) Alonso, B.; Clinard, C.; Durand, D.; Véron, E.; Massiot, D. New Routes to Mesoporous Silica-Based Spheres with Functionalised Surfaces. *Chem. Commun.* **2005**, No. 13, 1746–1748.

(151) Philippot, C.; University of Grenoble; France. PhD Dissertation: Elaboration et Caractérisation de Nanocristaux Organiques Fluorescents Insérés En Coquille Sol-Gel : Vers Le Développement d'un Nouveau Type d'agent Imageant Biologique, 2010.

(152) Zimmerman, J.; University of Grenoble; France. PhD Dissertation: Fluorescent Organic Nanocrystals Embedded in Organosilicate Shells : Towards Very Bright Tracers for Medical Imaging, 2014.

(153) Eucat, G.; University of Grenoble; France. PhD Dissertation: Molecular Engineering of New Organic Fluorophores and Encapsulation in a Sol-Gel Shell for Medical Imaging, 2014.

(154) Philippot, C.; Dubois, F.; Maurin, M.; Boury, B.; Prat, A.; Ibanez, A. New Core–shell Hybrid Nanoparticles for Biophotonics: Fluorescent Organic Nanocrystals Confined in Organosilicate Spheres. *J. Mater. Chem.* **2012**, *22* (22), 11370.

(155) Philippot, C.; Bourdolle, A.; Maury, O.; Dubois, F.; Boury, B.; Brustlein, S.; Brasselet, S.; Andraud, C.; Ibanez, A. Doped Silica Nanoparticles Containing Two-Photon Luminescent Eu(Iii) Complexes for the Development of Water Stable Bio-Labels. *J. Mater. Chem.* **2011**, *21* (46), 18613.

(156) Bourdolle, A.; D'Aléo, A.; Philippot, C.; Baldeck, P. L.; Guyot, Y.; Dubois, F.; Ibanez, A.; Andraud, C.; Brasselet, S.; Maury, O. NIR-to-NIR Two-Photon Scanning Laser Microscopy Imaging of Single Nanoparticles Doped by Yb ^{III} Complexes. *ChemPhysChem* **2016**, *17* (1), 128–135.

(157) Philippot, C.; Zimmermann, J.; Dubois, F.; Bacia, M.; Boury, B.; Baldeck, P. L.; Brasselet, S.; Ibanez, A. Polymorphism of CMONS Nanocrystals Grown in Silicate Particles through a Spray-Drying Process. *Cryst. Growth Des.* **2013**, *13* (12), 5241–5248.

(158) Nel, A. E.; Mädler, L.; Velegol, D.; Xia, T.; Hoek, E. M. V.; Somasundaran, P.; Klaessig, F.; Castranova, V.; Thompson, M. Understanding Biophysicochemical Interactions at the Nano-Bio Interface. *Nat. Mater.* **2009**, *8* (7), 543–557.

(159) Moore, T. L.; Rodriguez-Lorenzo, L.; Hirsch, V.; Balog, S.; Urban, D.; Jud, C.; Rothen-Rutishauser, B.; Lattuada, M.; Petri-Fink, A. Nanoparticle Colloidal Stability in Cell Culture Media and Impact on Cellular Interactions. *Chem. Soc. Rev.* **2015**, *44* (17), 6287–6305.

(160) Wolfram, J.; Yang, Y.; Shen, J.; Moten, A.; Chen, C.; Shen, H.; Ferrari, M.; Zhao, Y. The Nano-Plasma Interface: Implications of the Protein Corona. *Colloids Surfaces B Biointerfaces* **2014**, *124* (11), 17–24.

(161) Mahmoudi, M.; Bertrand, N.; Zope, H.; Farokhzad, O. C. Emerging Understanding of the Protein Corona at the Nano-Bio Interfaces. *Nano Today* **2016**, *11* (6), 817–832.

(162) Lundqvist, M.; Stigler, J.; Cedervall, T.; Berggård, T.; Flanagan, M. B.; Lynch, I.; Elia, G.; Dawson, K. The Evolution of the Protein Corona around Nanoparticles: A Test Study. *ACS Nano* **2011**, *5* (9), 7503–7509.

(163) Bertrand, N.; Leroux, J. C. The Journey of a Drug-Carrier in the Body: An Anatomo-Physiological Perspective. *J. Control. Release* **2012**, *161* (2), 152–163.

(164) Caracciolo, G.; Farokhzad, O. C.; Mahmoudi, M. Biological Identity of Nanoparticles In Vivo: Clinical Implications of the Protein Corona. *Trends Biotechnol.* **2017**, *35* (3), 257–264.

(165) Monopoli, M. P.; Åberg, C.; Salvati, A.; Dawson, K. A. Biomolecular Coronas Provide the Biological Identity of Nanosized Materials. *Nat. Nanotechnol.* **2012**, *7* (12), 779–786.

(166) Brun, E.; Sicard – Roselli, C. Could Nanoparticle Corona Characterization Help for Biological Consequence Prediction? *Cancer Nanotechnol.* **2014**, *5* (1), 7.

(167) Aggarwal, P.; Hall, J. B.; McLeland, C. B.; Dobrovolskaia, M. A.; McNeil, S. E. Nanoparticle Interaction with Plasma Proteins as It Relates to Particle Biodistribution, Biocompatibility and Therapeutic Efficacy. *Adv. Drug Deliv. Rev.* **2009**, *61* (6), 428–437.

(168) Monopoli, M. P.; Walczyk, D.; Campbell, A.; Elia, G.; Lynch, I.; Baldelli Bombelli, F.; Dawson, K. A. Physical-Chemical Aspects of Protein Corona: Relevance to in Vitro and in Vivo Biological Impacts of Nanoparticles. *J. Am. Chem. Soc.* **2011**, *133* (8), 2525–2534.

(169) Tenzer, S.; Docter, D.; Kuharev, J.; Musyanovych, A.; Fetz, V.; Hecht, R.; Schlenk, F.; Fischer, D.; Kiouptsi, K.; Reinhardt, C.; et al. Rapid Formation of Plasma Protein Corona Critically Affects Nanoparticle Pathophysiology. *Nat. Nanotechnol.* **2013**, *8* (10), 772–781.

(170) Casals, E.; Pfaller, T.; Duschl, A.; Oostingh, G. J.; Puntes, V. SI - Time Evolution of Nanoparticle Protein Corona. **2010**, *4* (7), 3623–3632.

(171) Palchetti, S.; Pozzi, D.; Capriotti, A. L.; Barbera, G. La; Chiozzi, R. Z.; Digiacomo, L.; Peruzzi, G.; Caracciolo, G.; Laganà, A. Influence of Dynamic Flow Environment on Nanoparticle-Protein Corona: From Protein Patterns to Uptake in Cancer Cells. *Colloids Surfaces B Biointerfaces* **2017**, *153*, 263–271.

(172) Caracciolo, G.; Palchetti, S.; Colapicchioni, V.; Digiacomo, L.; Pozzi, D.; Capriotti, A. L.; La Barbera, G.; Laganà, A. Stealth Effect of Biomolecular Corona on Nanoparticle Uptake by Immune Cells. *Langmuir* **2015**, *31* (39), 10764–10773.

(173) Dell'Orco, D.; Lundqvist, M.; Oslakovic, C.; Cedervall, T.; Linse, S. Modeling the Time Evolution of the Nanoparticle-Protein Corona in a Body Fluid. *PLoS One* **2010**, *5* (6), 1–9.

(174) Hu, Z.; Zhang, H.; Zhang, Y.; Wu, R.; Zou, H. Nanoparticle Size Matters in the Formation of Plasma Protein Coronas on Fe3O4nanoparticles. *Colloids Surfaces B Biointerfaces* **2014**, *121*, 354–361.

(175) Lundqvist, M.; Stigler, J.; Elia, G.; Lynch, I.; Cedervall, T.; Dawson, K. A. Nanoparticle Size and Surface Properties Determine the Protein Corona with Possible Implications for Biological Impacts. *Proc. Natl. Acad. Sci. U. S. A.* **2008**, *105* (38), 14265–14270.

(176) Ernsting, M. J.; Murakami, M.; Roy, A.; Li, S. D. Factors Controlling the Pharmacokinetics, Biodistribution and Intratumoral Penetration of Nanoparticles. *J. Control. Release* **2013**, *172* (3), 782–794.

(177) Docter, D.; Bantz, C.; Westmeier, D.; Galla, H. J.; Wang, Q.; Kirkpatrick, J. C.; Nielsen, P.; Maskos, M.; Stauber, R. H. The Protein Corona Protects against Size- and Dose-Dependent Toxicity of Amorphous Silica Nanoparticles. *Beilstein J. Nanotechnol.* **2014**, *5* (1), 1380–1392.

(178) Owens, D. E.; Peppas, N. A. Opsonization, Biodistribution, and Pharmacokinetics of Polymeric Nanoparticles. *Int. J. Pharm.* **2006**, *307* (1), 93–102.

(179) Roser, M.; Fischer, D.; Kissel, T. Surface-Modified Biodegradable Albumin Nano- and Microspheres. II: Effect of Surface Charges on in Vitro Phagocytosis and Biodistribution in Rats. *Eur. J. Pharm. Biopharm.* **1998**, *46* (3), 255–263.

(180) Gessner, A.; Lieske, A.; Paulke, B.-R.; Müller, R. H. Functional Groups on Polystyrene Model Nanoparticles: Influence on Protein Adsorption. *J. Biomed. Mater. Res. Part A* **2003**, *65A* (3), 319–326.

(181) Mortensen, N. P.; Hurst, G. B.; Wang, W.; Foster, C. M.; Nallathamby, P. D.; Retterer, S. T. Dynamic Development of the Protein Corona on Silica Nanoparticles: Composition and Role in Toxicity. *Nanoscale* **2013**, *5* (14), 6372.

(182) Meissner, J.; Prause, A.; Bharti, B.; Findenegg, G. H. Characterization of Protein Adsorption onto Silica Nanoparticles: Influence of PH and Ionic Strength. *Colloid Polym. Sci.* **2015**, *293* (11), 3381–3391.

(183) Göppert, T. M.; Müller, R. H. Plasma Protein Adsorption of Tween 80- and Poloxamer 188-Stabilized Solid Lipid Nanoparticles. *J. Drug Target.* **2003**, *11* (4), 225—231.

(184) Carrstensen, H.; Müller, R. H.; Müller, B. W. Particle Size, Surface Hydrophobicity and Interaction with Serum of Parenteral Fat Emulsions and Model Drug Carriers as Parameters Related to RES Uptake. *Clin. Nutr.* **1992**, *11* (5), 289–297.

(185) Müller, R. H.; Wallis, K. H.; Tröster, S. D.; Kreuter, J. In Vitro Characterization of Poly(Methyl-Methaerylate) Nanoparticles and Correlation to Their in Vivo Fate. *J. Control. Release* **1992**, *20* (3), 237–246.

(186) Norman, M. E.; Williams, P.; Illum, L. Human Serum Albumin as a Probe for Surface Conditioning (Opsonization) of Block Copolymer-Coated Microspheres. *Biomaterials* **1992**,

13 (12), 841–849.

(187) McNeil, S. E. Nanoparticle Therapeutics: A Personal Perspective. *Wiley Interdiscip. Rev. Nanomedicine Nanobiotechnology* **2009**, *1* (3), 264–271.

(188) Carrillo-Carrion, C.; Carril, M.; Parak, W. J. Techniques for the Experimental Investigation of the Protein Corona. *Curr. Opin. Biotechnol.* **2017**, *46* (Figure 1), 106–113.

(189) Lynch, I.; Salvati, A.; Dawson, K. A. What Does the Cell See? *Nano Today* **2009**, *4*, 4–5.

(190) Suk, J. S.; Xu, Q.; Kim, N.; Hanes, J.; Ensign, L. M. PEGylation as a Strategy for Improving Nanoparticle-Based Drug and Gene Delivery. *Adv. Drug Deliv. Rev.* **2016**, *99*, 28–51.

(191) Veronese, F. M.; Pasut, G. PEGylation, Successful Approach to Drug Delivery. *Drug Discov. Today* **2005**, *10* (21), 1451–1458.

(192) Ma, K.; Zhang, D.; Cong, Y.; Wiesner, U. Elucidating the Mechanism of Silica Nanoparticle PEGylation Processes Using Fluorescence Correlation Spectroscopies. *Chem. Mater.* **2016**, *28* (5), 1537–1545.

(193) Rio-Echevarria, I. M.; Selvestrel, F.; Segat, D.; Guarino, G.; Tavano, R.; Causin, V.; Reddi, E.; Papini, E.; Mancin, F. Highly PEGylated Silica Nanoparticles: "Ready to Use" Stealth Functional Nanocarriers. *J. Mater. Chem.* **2010**, *20* (14), 2780.

(194) Cauda, V.; Argyo, C.; Bein, T. Impact of Different PEGylation Patterns on the Long-Term Bio-Stability of Colloidal Mesoporous Silica Nanoparticles. *J. Mater. Chem.* **2010**, *20* (39), 8693.

(195) Adumeau, L.; Genevois, C.; Roudier, L.; Schatz, C.; Couillaud, F.; Mornet, S. Impact of Surface Grafting Density of PEG Macromolecules on Dually Fluorescent Silica Nanoparticles Used for the in Vivo Imaging of Subcutaneous Tumors. *Biochim. Biophys. Acta - Gen. Subj.* **2017**, *1861* (6), 1587–1596.

(196) Şen Karaman, D.; Gulin-Sarfraz, T.; Hedström, G.; Duchanoy, A.; Eklund, P.; Rosenholm, J. M. Rational Evaluation of the Utilization of PEG-PEI Copolymers for the Facilitation of Silica Nanoparticulate Systems in Biomedical Applications. *J. Colloid Interface Sci.* **2014**, *418*, 300–310.

(197) Nissinen, T.; Näkki, S.; Laakso, H.; Kučiauskas, D.; Kaupinis, A.; Kettunen, M. I.; Liimatainen, T.; Hyvönen, M.; Valius, M.; Gröhn, O.; et al. Tailored Dual PEGylation of Inorganic Porous Nanocarriers for Extremely Long Blood Circulation in Vivo. *ACS Appl. Mater. Interfaces* **2016**, *8* (48), 32723–32731.

(198) He, Q.; Zhang, J.; Shi, J.; Zhu, Z.; Zhang, L.; Bu, W.; Guo, L.; Chen, Y. The Effect of PEGylation of Mesoporous Silica Nanoparticles on Nonspecific Binding of Serum Proteins and Cellular Responses. *Biomaterials* **2010**, *31* (6), 1085–1092.

(199) Gref, R.; Lück, M.; Quellec, P.; Marchand, M.; Dellacherie, E.; Harnisch, S.; Blunk, T.; Müller, R. H. "Stealth" Corona-Core Nanoparticles Surface Modified by Polyethylene Glycol (PEG): Influences of the Corona (PEG Chain Length and Surface Density) and of the Core

Composition on Phagocytic Uptake and Plasma Protein Adsorption. *Colloids Surfaces B Biointerfaces* **2000**, *18* (3–4), 301–313.

(200) Cui, J.; De Rose, R.; Alt, K.; Alcantara, S.; Paterson, B. M.; Liang, K.; Hu, M.; Richardson, J. J.; Yan, Y.; Jeffery, C. M.; et al. Engineering Poly(Ethylene Glycol) Particles for Improved Biodistribution. *ACS Nano* **2015**, *9* (2), 1571–1580.

(201) Perrault, S. D.; Walkey, C.; Jennings, T.; Fischer, H. C.; Chan, W. C. W. Mediating Tumor Targeting Efficiency of Nanoparticles Through Design. *Nano Lett.* **2009**, *9* (5), 1909–1915.

(202) Yang, Q.; Jones, S. W.; Parker, C. L.; Zamboni, W. C.; Bear, J. E.; Lai, S. K. Evading Immune Cell Uptake and Clearance Requires PEG Grafting at Densities Substantially Exceeding the Minimum for Brush Conformation. *Mol. Pharm.* **2014**, *11* (4), 1250–1258.

(203) Vittaz, M.; Bazile, D.; Spenlehauer, G.; Verrecchia, T.; Veillard, M.; Puisieux, F.; Labarre, D. Effect of PEO Surface Density on Long-Circulating PLA-PEO Nanoparticles Which Are Very Low Complement Activators. *Biomaterials* **1996**, *17* (16), 1575–1581.

(204) Mosqueira, V. C. F.; Legrand, P.; Morgat, J.-L.; Vert, M.; Mysiakine, E.; Gref, R.; Devissaguet, J.-P.; Barratt, G. Biodistribution of Long-Circulating PEG-Grafted Nanocapsules in Mice: Effects of PEG Chain Length and Density. *Pharm. Res.* **2001**, *18* (10), 1411–1419.

(205) Orts-Gil, G.; Natte, K.; Thiermann, R.; Girod, M.; Rades, S.; Kalbe, H.; Thünemann, A. F.; Maskos, M.; Österle, W. On the Role of Surface Composition and Curvature on Biointerface Formation and Colloidal Stability of Nanoparticles in a Protein-Rich Model System. *Colloids Surfaces B Biointerfaces* **2013**, *108*, 110–119.

(206) HC KOlb; Finn, M.; Sharpless, K. Click Chemistry: Diverse Chemical Function from a Few Good Reactions. *Angew. Chem. Int. Ed.* **2001**, *40* (11), 2004–2021.

(207) Moitra, N.; Moreau, J. J. E.; Cattoën, X.; Wong Chi Man, M. Convenient Route to Water-Sensitive Sol–gel Precursors Using Click Chemistry. *Chem. Commun.* **2010**, *46* (44), 8416.

(208) Hoffmann, F.; Cornelius, M.; Morell, J.; Fröba, M. Silica-Based Mesoporous Organic-Inorganic Hybrid Materials. *Angew. Chemie - Int. Ed.* **2006**, *45* (20), 3216–3251.

(209) Kickelbick, G. Hybrid Inorganic-Organic Mesoporous Materials. *Angew. Chemie - Int. Ed.* **2004**, *43* (24), 3102–3104.

(210) Shenoi-Perdoor, S.; Noureddine, A.; Dubois, F.; Wong Chi Man, M.; Cattoën, X. Click Functionalization of Sol--Gel Materials. In *Handbook of Sol-Gel Science and Technology*; 2018; pp 3001–3040.

(211) Nakazawa, J.; Smith, B. J.; Stack, T. D. P. Discrete Complexes Immobilized onto Click-SBA-15 Silica: Controllable Loadings and the Impact of Surface Coverage on Catalysis. *J. Am. Chem. Soc.* **2012**, *134* (5), 2750–2759.

(212) Tornøe, C. W.; Christensen, C.; Meldal, M. Peptidotriazoles on Solid Phase: [1,2,3]-Triazoles by Regiospecific Copper(I)-Catalyzed 1,3-Dipolar Cycloadditions of Terminal Alkynes to Azides. *J. Org. Chem.* **2002**, *67* (9), 3057–3064.

(213) Rostovtsev, V. V.; Green, L. G.; Fokin, V. V.; Sharpless, K. B. Supporting Information for " A Stepwise Huisgen Cycloaddition Process Catalyzed by Copper (I): Regioselective Ligation of Azides and Terminal Alkynes ." *Angew. Chem. Int. Ed.* **2002**, *41* (14), 2596–2599.

(214) Malvi, B.; Sarkar, B. R.; Pati, D.; Mathew, R.; Ajithkumar, T. G.; Sen Gupta, S. "Clickable" SBA-15 Mesoporous Materials: Synthesis, Characterization and Their Reaction with Alkynes. *J. Mater. Chem.* **2009**, *19* (10), 1409.

(215) Jin, L.; Tolentino, D. R.; Melaimi, M.; Bertrand, G. Isolation of Bis (Copper) Key Intermediates in Cu-Catalyzed Azide-Alkyne " Click Reaction ." *Sci. Adv.* **2015**, *1*, e1500304.

(216) Worrell, B. T.; Malik, J. A.; Fokin, V. V. Direct Evidence of a Dinuclear Copper Intermediate in Cu(I)- Catalyzed Azide–Alkyne Cycloadditions. *Science (80-.).* **2013**, *340* (6131), 457–460.

(217) Ranjan, R.; Brittain, W. J. Combination of Living Radical Polymerization and Click Chemistry for Surface Modification. *Macromolecules* **2007**, *40* (17), 6217–6223.

(218) Chen, J.; Liu, M.; Chen, C.; Gong, H.; Gao, C. Synthesis and Characterization of Silica Nanoparticles with Well-Defined Thermoresponsive PNIPAM via a Combination of RAFT and Click Chemistry. *ACS Appl. Mater. Interfaces* **2011**, *3* (8), 3215–3223.

(219) Kar, M.; Vijayakumar, P. S.; Prasad, B. L. V; Gupta, S. Sen. Synthesis and Characterization of Poly-l-Lysine-Grafted Silica Nanoparticles Synthesized via NCA Polymerization and Click Chemistry. *Langmuir* **2010**, *26* (8), 5772–5781.

(220) Tissandier, C.; Diop, N.; Martini, M.; Roux, S.; Tillement, O.; Hamaide, T. One-Pot Synthesis of Hybrid Multifunctional Silica Nanoparticles with Tunable Coating by Click Chemistry in Reverse W/O Microemulsion. *Langmuir* **2012**, *28* (1), 209–218.

(221) Achatz, D. E.; Heiligtag, F. J.; Li, X.; Link, M.; Wolfbeis, O. S. Colloidal Silica Nanoparticles for Use in Click Chemistry-Based Conjugations and Fluorescent Affinity Assays. *Sensors Actuators B Chem.* **2010**, *150* (1), 211–219.

(222) Patel, K.; Angelos, S.; Dichtel, W. R.; Coskun, A.; Yang, Y. W.; Zink, J. I.; Stoddart, J. F. Enzyme-Responsive Snap-Top Covered Silica Nanocontainers. *J. Am. Chem. Soc.* **2008**, *130* (8), 2382–2383.

(223) Ambrogio, M. W.; Pecorelli, T. A.; Patel, K.; Khashab, N. M.; Trabolsi, A.; Khatib, H. A.; Botros, Y. Y.; Zink, J. I.; Stoddart, J. F. Snap-Top Nanocarriers. *Org. Lett.* **2010**, *12* (15), 3304–3307.

(224) Coll, C.; Mondragón, L.; Martínez-Máñez, R.; Sancenón, F.; Marcos, M. D.; Soto, J.; Amorós, P.; Pérez-Payá, E. Enzyme-Mediated Controlled Release Systems by Anchoring Peptide Sequences on Mesoporous Silica Supports. *Angew. Chemie - Int. Ed.* **2011**, *50* (9), 2138–2140.

(225) Chen, C.; Geng, J.; Pu, F.; Yang, X.; Ren, J.; Qu, X. Polyvalent Nucleic Acid/Mesoporous Silica Nanoparticle Conjugates: Dual Stimuli-Responsive Vehicles for Intracellular Drug Delivery.

Angew. Chemie - Int. Ed. **2011**, *50* (4), 882–886.

(226) Croissant, J.; Chaix, A.; Mongin, O.; Wang, M.; Clément, S.; Raehm, L.; Durand, J. O.; Hugues, V.; Blanchard-Desce, M.; Maynadier, M.; et al. Two-Photon-Triggered Drug Delivery via Fluorescent Nanovalves. *Small* **2014**, *10* (9), 1752–1755.

(227) Croissant, J.; Maynadier, M.; Gallud, A.; Peindy N'Dongo, H.; Nyalosaso, J. L.; Derrien, G.; Charnay, C.; Durand, J. O.; Raehm, L.; Serein-Spirau, F.; et al. Two-Photon-Triggered Drug Delivery in Cancer Cells Using Nanoimpellers. *Angew. Chemie - Int. Ed.* **2013**, *52* (51), 13813–13817.

(228) Guardado-Alvarez, T. M.; Russell, M. M.; Zink, J. I. Nanovalve Activation by Surface-Attached Photoacids. *Chem. Commun.* **2014**, *50* (61), 8388–8390.

(229) Hong, V.; Presolski, S. I.; Ma, C.; Finn, M. â. G. Analysis and Optimization of Copper-Catalyzed Azide–Alkyne Cycloaddition for Bioconjugation. *Angew. Chem. Int. Ed.* **2009**, *48* (52), 9879–9883.

(230) Liu, P.-Y.; Jiang, N.; Zhang, J.; Wei, X.; Lin, H.-H.; Yu, X.-Q. The Oxidative Damage of Plasmid DNA by Ascorbic Acid Derivatives in Vitro: The First Research on the Relationship between the Structure of Ascorbic Acid and the Oxidative Damage of Plasmid DNA. *Chem. Biodivers.* **2006**, *3*, 958–966.

(231) Hong, V.; Steinmetz, N. F.; Manchester, M.; Finn, M. G. Labeling Live Cells by Copper-Catalyzed Alkyne−Azide Click Chemistry. *Bioconjug. Chem.* **2010**, *21* (10), 1912–1916.

(232) Baskin, J. M.; Prescher, J. A.; Laughlin, S. T.; Agard, N. J.; Chang, P. V.; Miller, I. A.; Lo, A.; Codelli, J. A.; Bertozzi, C. R. Copper-Free Click Chemistry for Dynamic in Vivo Imaging. *Proc. Natl. Acad. Sci.* **2007**, *104* (43), 16793–16797.

(233) Lee, S. B.; Kim, H. L.; Jeong, H. J.; Lim, S. T.; Sohn, M. H.; Kim, D. W. Mesoporous Silica Nanoparticle Pretargeting for PET Imaging Based on a Rapid Bioorthogonal Reaction in a Living Body. *Angew. Chemie - Int. Ed.* **2013**, *52* (40), 10549–10552.

(234) Rodríguez-Rodríguez, M.; Gras, E.; Pericàs, M. A.; Gõmez, M. Metal-Free Intermolecular Azide-Alkyne Cycloaddition Promoted by Glycerol. *Chem. - A Eur. J.* **2015**, *21* (51), 18706–18710.

Chapter II – Synthesis and characterization of core-shell NPs

Encapsulation of crystal-state emitters in sol-gel matrices is an efficient way to produce bright nanotracers for bio-imaging applications.[1–4] This chapter deals with the development and optimization of a family of fluorescent organic@silicate core-shell nanoparticles (NPs) containing an organic core surrounded by a silicate shell, with a high loading of dyes (30-40 %wt) for two-photon imaging of tumor vasculature. These core-shell NPs, which comprise an organic dye nanocrystal core (ca 40-50 nm) surrounded by a silicate crust (Figure 2.1a), are prepared by an original spray-drying technique combining sol-gel chemistry and nanocrystallization, developed in our group.[4,5] The spray-drying technique applied to sol-gel chemistry is an efficient way to produce uniformly spherical solid particles by atomizing sol suspensions, though with a significant size dispersion.[6,7] It is a simple, controllable and productive method to produce not only silica micro- and nano-particles[8,9] but also mesostructured silica.[10–13] It is based on the production of micron-size droplets through the nebulization of silica-based sols by an atomizer. The resulting sprays are then dried by circulating in the form of laminar flow in an oven. Upon evaporation of the solvent, the concentrations in catalyst and silicate oligomers strongly increase which accelerates the hydrolysis-condensation reactions and finally leads to well-condensed silica-based NPs. When an organic compound such as a fluorophore is incorporated within the starting sol, the sol-gel reactions and the crystallization of the organic compound are coupled in the oven. The interplay between these two processes may lead to the formation of unusual self-assembled core-shell organic nanocrystal@silicate NPs in a one-step process. To date, such NPs have been reported only for CMONS and rubrene, while related lanthanide complexes@silicate doped NPs were also produced.[5,14,15] Notably, in the case of CMONS, different polymorphs were obtained depending on the composition of the organosilica shell,[16] which highlights the challenges in controlling the fluorescence properties. Moreover, the fluorescence emission wavelength (540 nm) of the strongest emitting yellow form of CMONS is not satisfactory for a potential use in bio-imaging. The primary goal of this work is the development and characterization of a family of fluorescent organic@silicate core-shell nanoparticles (NPs) for use in bio-imaging.

The organic dyes used for the nanocrystalline core are non-commercial and specifically designed in collaboration with the Lab. de Chimie, ENS Lyon, to be crystal-state emitters with excellent properties for use in bio-imaging applications. Alkoxide precursors, TMOS (tetramethoxysilane) and TMSE (1.2-bis(trimethoxysilyl)ethane) are chosen to form the silicate shell. Additionally, an organosilane, (3-azidopropyl) triethoxysilane (AzPTES), is used to impart an azide functionality to the NPs for further functionalization with alkyne-modified moieties using the Cu(I)-catalysed 1,3-dipolar cycloaddition of organic azides to alkynes (CuAAC), as shown in Figure 2.1.

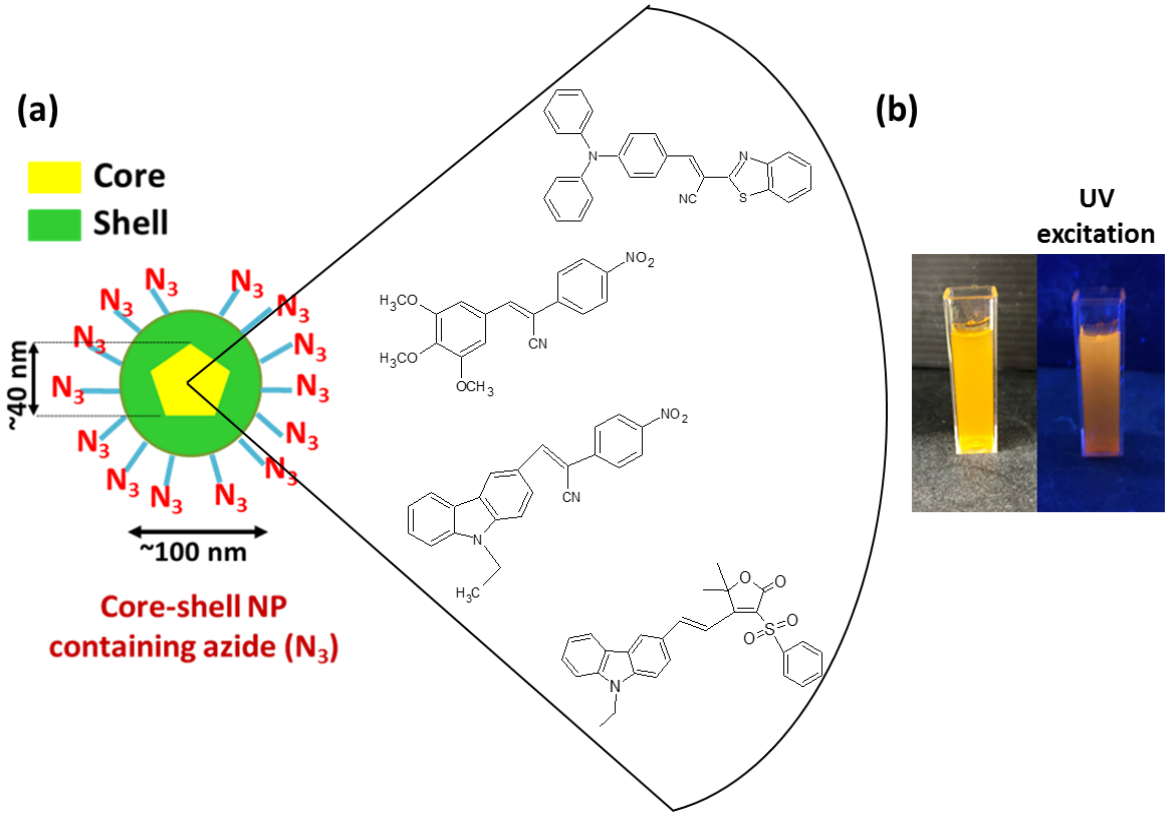

Figure 2. 1. (a) Schematic illustration of organic@silicate core-shell NPs and (b) core-shell NP suspension under UV excitation

The morphologies of the synthesized NPs were characterized, and their crystallinity was studied using X-Ray diffraction and electron microscopy techniques. Finally, the optical properties of these core-shell NPs have also been investigated using fluorescence spectroscopy for their potential use in imaging tumor vasculature. Bright, red-emitting core-shell NPs have been produced, which are promising for use in bio-imaging.

2.1. Synthesis of organic@silicate core-shell NPs

The spray-drying process for the synthesis of organic@silicate core-shell NPs has been described previously[4,5] and is based on the confined nucleation and growth of an organic nanocrystal, coupled with the formation of a silicate crust by fast drying of sprayed droplets containing silicate oligomers, fluorophores and solvent under an air flux at 140-200 °C. A good control of the preparation of sols and the spray-drying parameters is crucial in order to obtain defect-free core-shell NPs. There are three critical factors that play a crucial role in this self-assembling one-step process: (i) the choice of organic dye and its physical characteristics, (ii) the sol-gel chemistry and (iii) the spray-drying parameters. Different NP types can be synthesized by changing the organic dye forming the nanocrystalline core of the NPs and also by changing the composition of the

inorganic silicate crust. Depending on the nature of the dye and the chemical parameters of the sol, NPs with different morphologies are obtained.

The sols were prepared using a 2:1 ratio of TMOS and TMSE (Figure 2.2) and acidic water (1 M HCl) in THF according to parameters, s = [Solvent]/[Si] and h = [H_2O]/[-OR] (where [Si] is the molar concentration of silicon atoms and [-OR] is the molar concentration of alkoxide functions). To obtain clickable azide functions at the surface of the silica crust, varying amounts of an organosilane, AzPTES (Figure 2.2) was also added to the sols to yield 2TMOS + TMSE + AzPTES (1%/3%/5%).

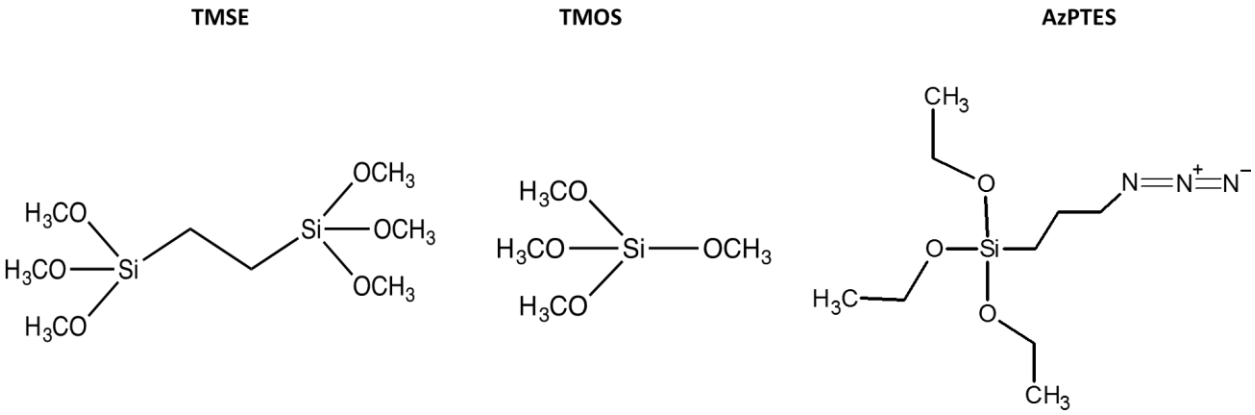

Figure 2. 2. Chemical structure of TMSE, TMOS and AzPTES.

2.1.1. Spray-drying

The organic@silicate core-shell NPs were synthesized in a home-built pneumatic spray-drying reactor (Figure 2.3). This process is based on confined nucleation and growth of the organic dye nanocrystal by fast drying of sprayed droplets containing silicate oligomers, organic dye and solvent under an air flux at 140-200 °C. Upon drying, the concentration of silicates and catalyst, and also the fluorophores undergo a fast increase. This leads to two independent processes: i) the formation of a silicate crust at the droplet surfaces as the sol-gel reactions strongly accelerate; ii) the nucleation and growth of a single nanocrystal in the core of the drying droplets as a high supersaturation is reached through fast solvent evaporation.

The mixture of sol and organic dye, which is first introduced into a 1 L flask, is sucked into a pneumatic atomizer (TSI model 3076- Constant Output Atomizer) by a nitrogen gas flow (56 L/h). This results in the formation of micrometer-sized droplets of the sol. These droplets, which contain a random dispersion of the silicate oligomers, organic dye and the solvent, are further diluted and driven into an oven by an air flow (8 L/h - 30 L/h). The oven is set to a particular temperature, depending on the melting point of the dye, and is a 1.4 m long stainless steel tube

of diameter 35 mm covered by a furnace. As the droplets start to move through the oven, a fast solvent evaporation take place inducing the formation of an inorganic silicate crust at the droplet surfaces, due to the increase in the concentration of the silicates and catalyst. Following solvent evaporation, confined nucleation and growth of the dye occurs under high dye supersaturation in the core of the droplet, where the remaining solution is less confined (higher volumes of free solution, see section 1.2.4.3 in Chapter I) At the end of the passage through the oven, there is complete evaporation of the solvent, resulting in the formation of organic nanocrystal @silicate core-shell nanoparticles. The oven is connected to an electrostatic filter charged at a potential of 10 kV, which charges and attracts NPs, thereby collecting them. The filter is also set to a temperature above 100 °C such that any traces of water or solvent, which when formed would be expelled through the exhaust and condense in the water trap. The NPs can either be collected directly from the filter, either in powder form or in water.

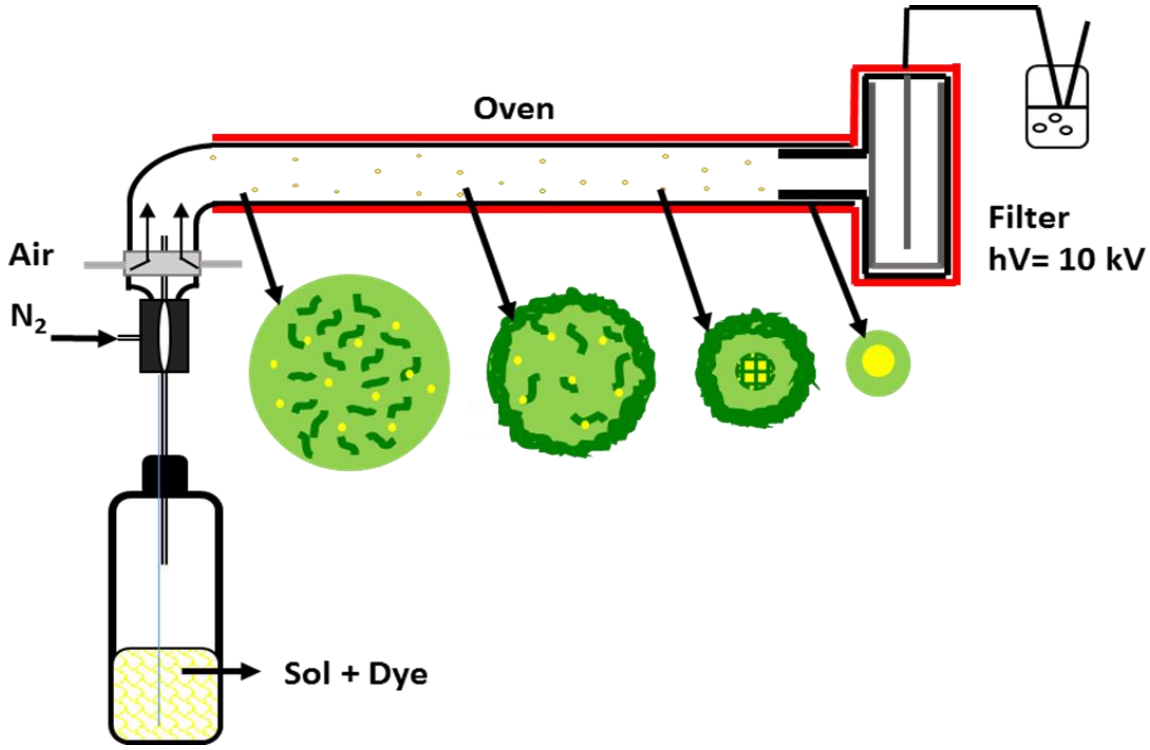

Figure 2. 3. Scheme of the home-built spray-drying reactor

This one-step synthesis is made possible thanks to the control of both the sol-gel chemistry (polycondensation) and the nanocrystallization process, which occur simultaneously. Other advantages include scalability and reproducibility, making it a reliable method of NP synthesis with a good yield. An inherent drawback, however, is that the NPs so produced are polydisperse in nature, due to the coalescence of sol droplets entering the oven during the drying process, resulting in a wide range of sizes.

2.1.2. Choice of organic dyes

The organic dyes for the nanocrystalline core, **I-IV** (Figure 2.4) are non-commercial and specifically designed at ENS-Lyon with a D-π-A dipolar structure to be crystal-state emitters. The presence of a permanent dipole moment that provokes strong dipole-dipole interactions, combined with the D-π-A structuration induced the formation of typical crystal organization that favors the presence of strong emissive solid phase. They also have the appropriate physico-chemical properties to enable their nanocrystallization using the spray-drying synthesis approach, such as excellent thermal, chemical and photo- stabilities, and a high solubility in THF solvent, except in the case of dye **III**, which exhibits a relatively low solubility in THF. They exhibit high fluorescence intensity in the crystal state (quantum yield between 8 % to 33 %) with an absorption maximum wavelength less than 550 nm to be excited by two-photon absorption process using typical lasers involved in fluorescence imaging (700-1000 nm). Moreover, these dyes exhibit fluorescence emission between 590 nm and 650 nm (red shifted in comparison to the CMONS reference), in the near infrared biological transparency window, especially in the case of the dye **I** (emission at 650 nm), making them excellent candidates for bio-imaging. The properties of the selected dyes are summarized in Table 2.1.

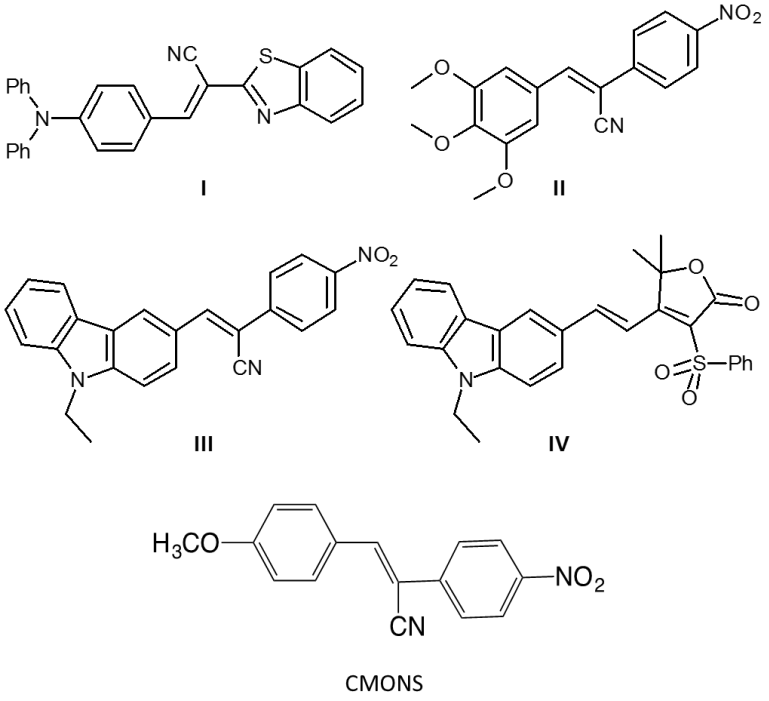

Figure 2. 4. Structure of the organic dyes

Table 2. 1. Properties of the dyes in solid state

Dye	Melting point (°C)	Molecular weight	Solubility in THF (M)	λ_{exc} (nm)	λ_{em} (nm)	ϕ_F (%)
I	173	429	$1.5 * 10^{-1}$	510	647	18
II	161	340	$1* 10^{-2}$	530	605	8
III	244	367	$6 * 10^{-3}$	530	603	28
IV	250	471	$3 * 10^{-2}$	540	598	33
CMONS	165	280	$1.5 * 10^{-1}$	400	540	40

The core-shell NPs containing the different dyes **I-IV** will henceforth be referred to as **NP-I**, **NP-II**, **NP-III** and **NP-IV**, respectively. In addition to the physico-chemical properties, another parameter that plays an important role is the concentration of the dye, d = [dye]/[Si]. The maximum amount of dye, d_{max}, that can be encapsulated in the NPs is determined by screening SEM images as a function of increasing values of d for each dye. When non-spherical objects start to be observed outside of the NPs, d_{max} is reached: limit of dye nanocrystal confinement by the silicate shell.

2.1.3. Sol-gel chemistry

TMOS and TMSE in a 2:1 ratio were chosen to form the silicate shell in accordance with previously reported results.[4,5] In addition, a small proportion of AzPTES (1-5 %) is added to obtain clickable azide groups for further functionalization of the NPs. This combination of silicate precursors enables a good encapsulation of the nanocrystalline core thanks to a proper hydrophilic/hydrophobic balance. It also ensures that there are no significant interactions between the dye and the silicate crust to enable the nucleation and growth of a monocrystal at the center of the NPs and consequently a good confinement of the dye in the core-shell NPs.

The sols were prepared according to parameters, s = [solvent]/[Si] and h = $[H_2O]$/[-OR] (where [Si] is the molar concentration in silicon atoms and [-OR] is the molar concentration of alkoxide functions). The solvent amount, s = [solvent]/[Si], plays a significant role in the NPs size. Higher 's' values imply decreased concentrations of silicate precursors and dye due to more dilute droplets during the atomization of the sol, thereby resulting in smaller NPs. Furthermore, the amount of dye to silicate precursors (TMOS, TMSE, AzPTES) d = [dye]/[Si] is limited to the d_{max} value, above which the confinement is no more possible and dye crystallization is observed outside the NP. (loss of dye confinement).

2.1.3.1. Influence of sol parameters and synthesis conditions

Different protocols of sol preparation yielded NPs with different morphologies. In the first method, protocol A, described in previous works,[5] the silicate precursors were weighed in a 100 mL bottle to which 60 mL of THF was added, followed by acidic water with s = 500 and h = 1 before ageing for two weeks at 60 °C. Unfortunately, this protocol yielded spherical, defect-free NPs only in the case of dye **IV** (Figure 2.5d). In all other cases, NPs with defects such as holes were observed (Figure 2.5a-c).

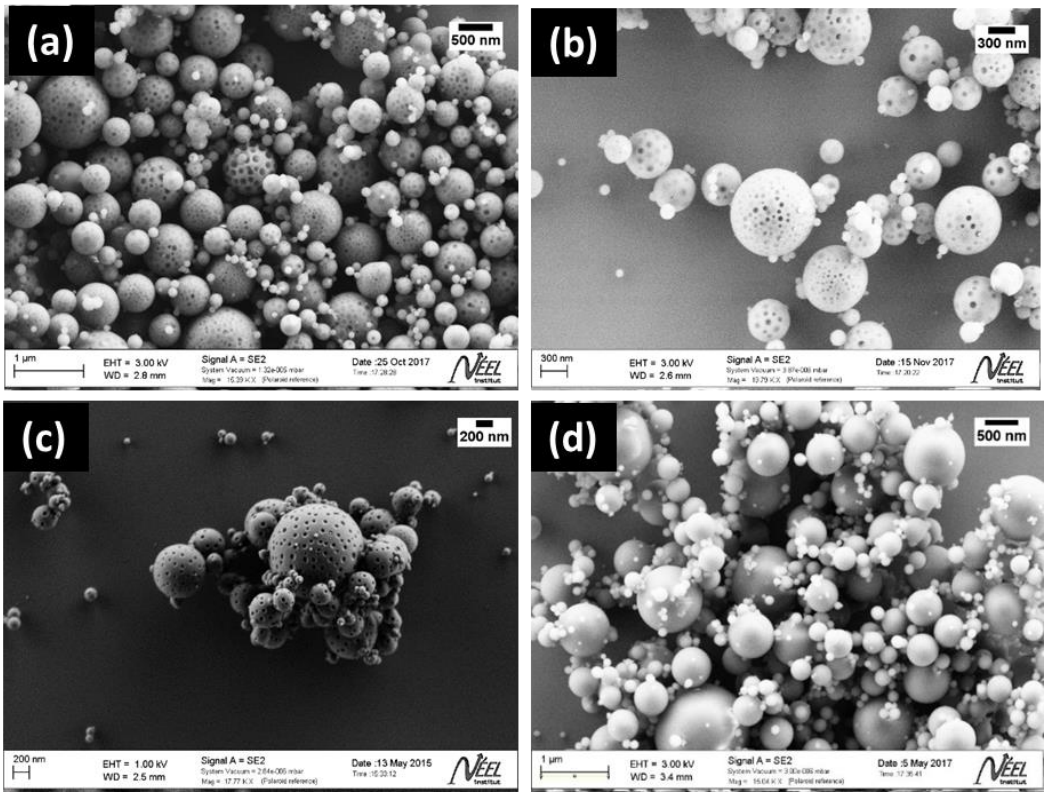

Figure 2. 5. FESEM images of core-shell (a) **NP-I**, (b) **NP-II**, (c) **NP-III** and (d) **NP-IV**, synthesized using protocol A

The varied results were hypothesized to be a result of two main factors: (i) drying temperature which is limited by the melting point of the dye and (ii) the degree of polycondensation of the silicate shell, which has an effect on the confinement of the dye in the NPs. It is noteworthy that the furnace temperature has to be set to a temperature significantly below the melting point of the dye as the nanocrystals may melt at lower temperature than the microcrystalline ones, resulting in their vaporization in the oven and condensation around the nanoparticles at the filter, leading to the formation of crystallites/needles. However, it is important to note that the drying temperature has to be between 140-200 °C for complete evaporation of the solvent to yield completely dried NPs. Insufficient drying could result in bombardment of the smaller dried NPs with bigger insufficiently dried NPs resulting in NPs with a 'golf-ball' like morphology. To

investigate this effect, dye-free NPs were synthesized at the lowest temperature used in former cases (154 °C) with protocol A. This yielded spherical defect-free NPs (Figure 2.6) implying that the synthesis temperature was sufficient for complete evaporation of the solvent.

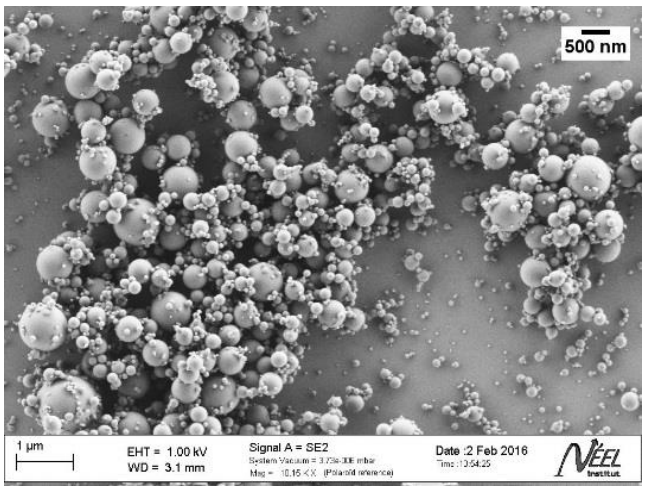

Figure 2. 6. FESEM image of dye-free NPs synthesized at 154 °C

When the dyes are introduced, the melting point of the dyes can play a significant role in determining the morphology of the NPs obtained. Defect-free NPs in the case of dye **IV** resulted possibly due to its high melting point of 250 °C, which allowed the spray-drying process to be performed at 185 °C (well below its melting point), with d_{max} being 0.08 beyond which, holes began to appear in the NPs. On the other hand, dyes **I** and **II**, have lower melting points of 171 °C and 161 °C respectively. Therefore, it was hypothesized that the defects in **NP-I** and **NP-II** originated from the drying temperature being too close to the melting point of the dye resulting in a partial sublimation (or evaporation) of the dye and leading to its crystallization outside the NPs. However, NPs with holes were obtained even when the synthesis was performed at a temperature well below the melting point of the dyes, 144 °C in the case of dye **I** and 150 °C in the case of dye **II**. Interestingly, no crystallite needles were observed, confirming the absence of dye sublimation. However, even dye **III**, which has a higher melting point of 244 °C, yielded NPs with holes (Figure 2.5c).

Other possible explanations for the formation of holes at the surface of the organosilicate shells, are the interactions between dye molecules and organosilicate chains in the sols which could disturb the polycondensation kinetics. Also, the growth of dye nanocrystals in the core of droplets can disturb the complete formation of the silicate crust. These varied results so obtained led to the new hypothesis that it was indeed the presence of the dye itself that induced these defects in the NPs, which in turn could be attributed to insufficient polycondensation of the silicate shell resulting in poor confinement of the dye.

This further demonstrated the need to increase the degree of polycondensation of the silicate species in the starting sols to force stronger reticulation of the organosilicate shell in the final NPs in order to enhance its dye confinement ability. To overcome the problem of insufficient polycondensation, new protocols were developed where the ageing of the sol was performed at much lower dilution, with an ageing time set at half the gelation time of the sol.

In this new method of sol preparation, protocol B, the acidic water was directly added to the silicate precursors in a small amount of THF (3 mL) under vigorous stirring, followed by ageing for two days at 60 °C with the addition of remaining amount of solvent (57 mL) after ageing. The condensation at the silicon atoms was then investigated by 500 MHz ^{29}Si-NMR in solution for this sol (Figure 2.7). The spectra (accumulation of 2048 scans) exhibits two main groups of signals, with signals at -52 and -58 ppm in the T region, which were assigned to T^1 and T^2 silicon environments (C-Si(OR)$_2$OSi and C-Si(OR)(OSi)$_2$, respectively with R = H, Me), and at -86, -96 and -104 ppm in the Q region, assignable to Q^1, Q^2 and Q^3 silicon environments (Si(OR)$_3$(OSi), Si(OR)$_2$(OSi)$_2$ and Si(OR)(OSi)$_3$, respectively). This suggests that siloxane chains with few ramifications are predominant, as it is usually the case for sols obtained under acidic catalysis. The cross-linkages between these chains are mainly due to the organic bridges, T^2 sites being predominant over the Q^3 environments. Unfortunately, the sols obtained from protocol A could not be analyzed similarly by ^{29}Si NMR, due to their low concentration.

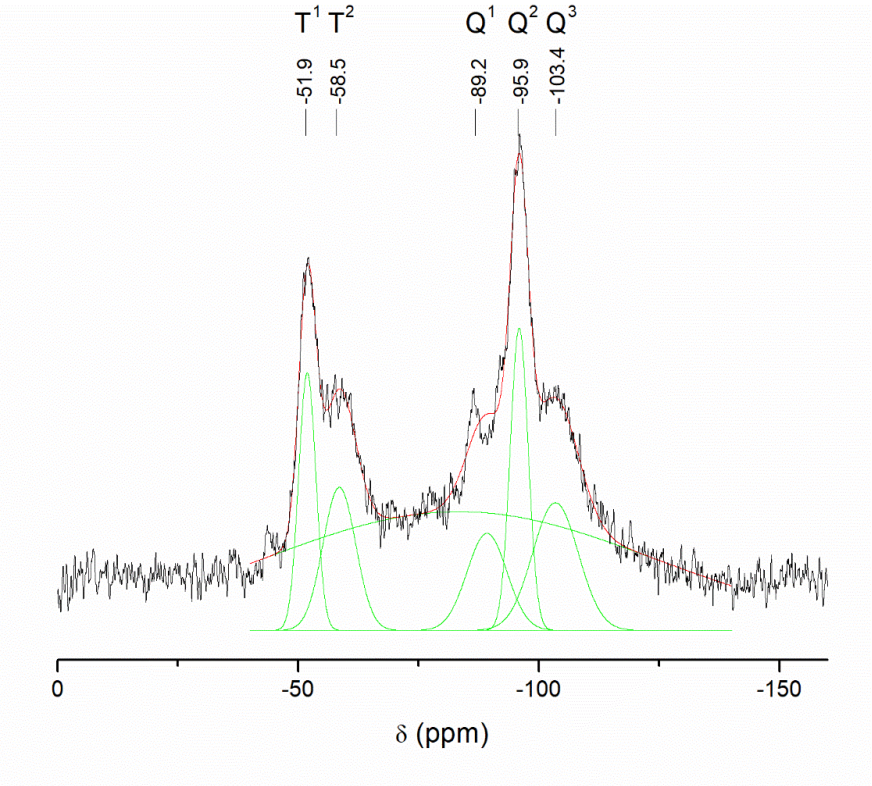

Figure 2. 7. ^{29}Si NMR-spectrum of sol made using protocol B

Analysis of this sol prepared using protocol B at different stages of ageing, using dynamic light scattering (DLS) yielded size distributions peaking at less than 40 nm (Figure 2.8), suggesting the presence of small silicate chains. It is important, however, to note that different methods of analysis (see Appendix II-DLS) yielded different size distributions, possibly due to the presence of varied species of different shapes and sizes in the sol, ranging from linear chains to folded chains, adding a factor of variability in the obtained results. Another point to note is that conversion of the autocorrelation curve into size distribution is typically performed by modelling the detected species as spherical entities. Overall, the sizes recorded were less than 50 nm in diameter, suggesting the presence of small chains, within 2 days of ageing, under such conditions.

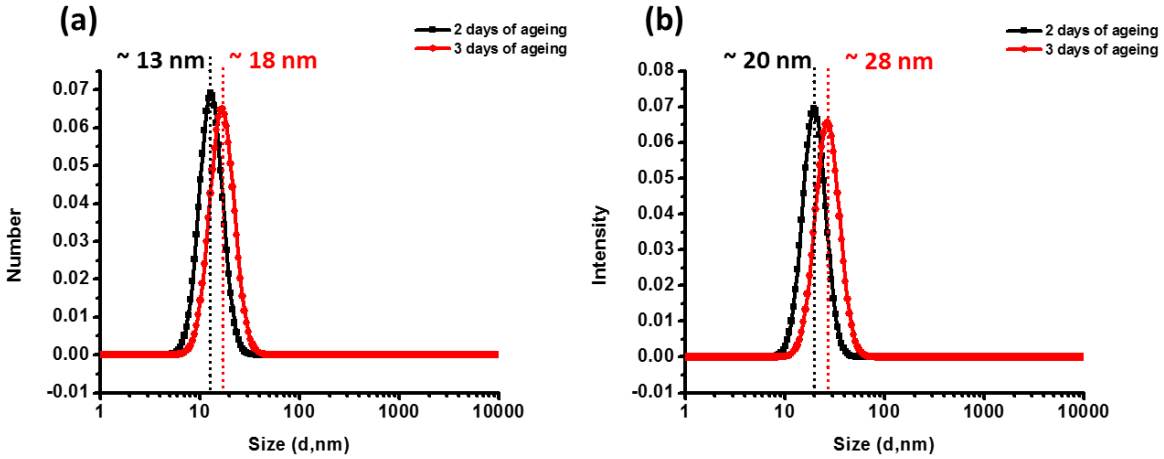

Figure 2. 8. DLS of sol prepared using protocol B (a) Number distribution and (b) Intensity distribution, at different stages of ageing, 2 days (black curve) and 3 days (red curve)

Protocol B yielded defect-free NPs for dyes **II** and **IV** (Figure 2.9b and 2.9d) with d_{max} in the range of 0.08-0.10. However, **NP-I** were observed to have a rough morphology when d exceeded 0.06 (Figure 2.9a), indicating insufficient silicate content to encapsulate high amounts of the dye. Dye **III** on the other hand, continued to yield NPs with defects (Figure 2.9c), indicating insufficient polycondensation, possibly due to the nature of the dye and its low solubility in the solvent.

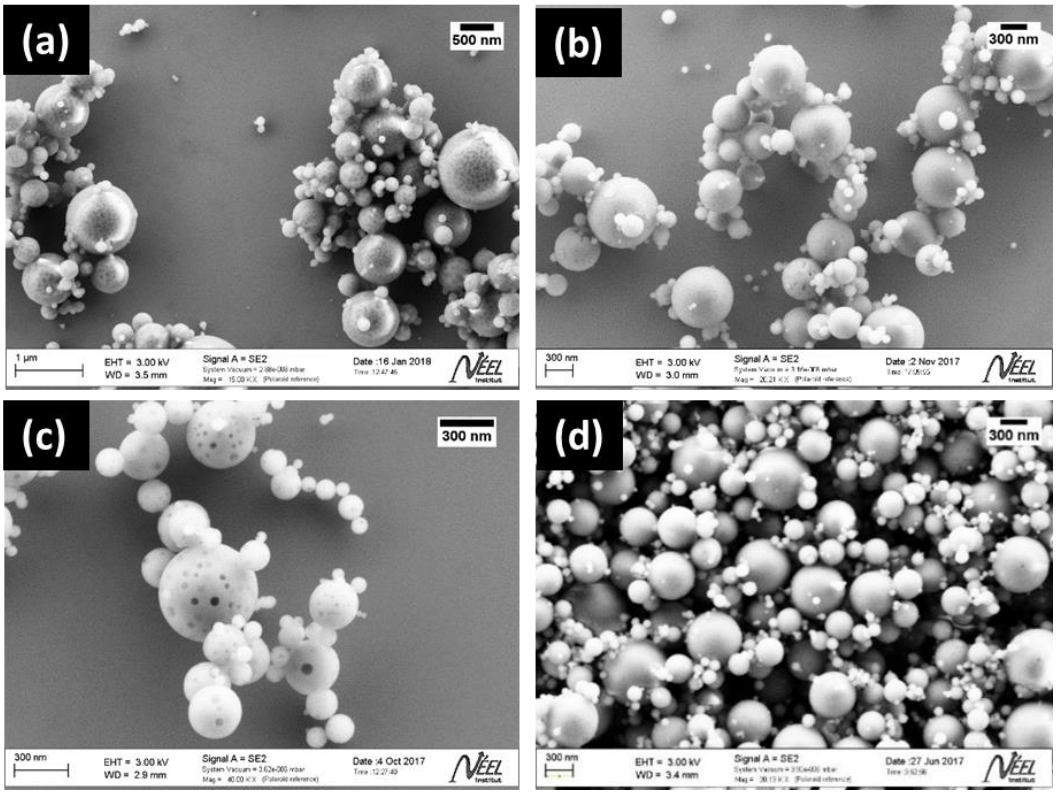

Figure 2. 9. FESEM images of core-shell (a) **NP-I**, (b) **NP-II**, (c) **NP-III** and (d) **NP-IV**, using protocol B.

Therefore, a modified protocol was developed, protocol C, where the concentration of silicate precursors was increased by decreasing the solvent amount from s = 500 to s = 380. Here, the acidic water was directly added to the silicate precursors in a small amount of THF (5 mL) under vigorous stirring, followed by ageing for either three or five days at 60 °C with the addition of remaining amount of solvent (55 mL) after ageing. This new protocol, yielded defect-free NPs in the case of dye **I** using a sol aged for 3 days, allowing to increase the d_{max} from 0.06 to 0.10 and resulting in defect-free NPs, with a smooth morphology (Figure 2.10a).

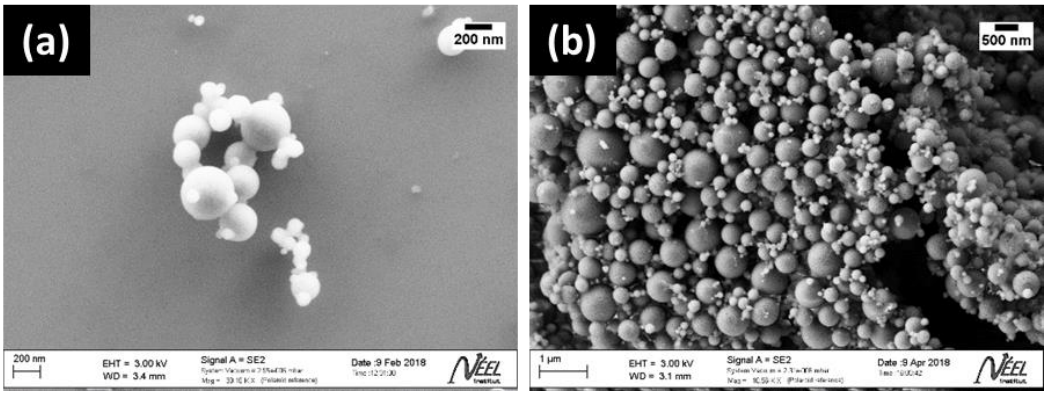

Figure 2. 10. FESEM images of core-shell (a) **NP-**I and (b) **NP-III** using protocol C.

On the other hand, dye **III** which presents a rather low solubility in THF, required a sol aged for 5 days, to further increase the degree of polycondensation. This ultimately resulted in defect-free NPs, and also allowed to significantly increase the d_{max} from 0.03 to 0.07 (Figure 2.10b). All three protocols are summarized in Table 2.2.

Table 2. 2. Different protocols for the preparation of sols

Protocol	s	h	Ageing	Preparation
A	500	1	14 days	- Silicate precursors + THF (60 mL) + HCl/H_2O
				- Ageing for two weeks at 60 °C
B	500	1	2 days	- Silicate precursors + THF (3 mL) + HCl/H_2O
				- Ageing for 2 days at 60 °C
				- Addition of 57 mL THF after ageing
C	380	1	3 days/5 days	- Silicate precursors + THF (5 mL) + HCl/H_2O
				- Ageing for 3/5 days at 60 °C
				- Addition of 55 mL THF after ageing

Although optimization of the sol-gel chemistry and spray-drying conditions resulted in spherical defect-free NPs for all the different dyes used, the NPs so-obtained were polydisperse in nature as can be seen from the FESEM images. This polydispersity is an inherent drawback of the spray-drying process, which occurs due to the coalescence of droplets during atomization of the sol. Figure 2.11 shows the size distribution of **NPs I-IV** just after synthesis and it can be seen that there is a wide distribution with NPs sizes ranging from less than 50 nm to more than 500 nm.

Although this distribution is wide, it can be seen that NPs bigger than 350 nm constitutes less than 10% of the total fraction. Interestingly, NPs < 200 nm constitute between 20-30% of the total fraction, with a similar trend for even smaller NPs (< 100 nm). This is highly promising as a size range below 200 nm is preferred for biological applications and it is possible to get rid of the larger NPs and aggregates by means of dissolution and filtration strategies discussed in Chapter III.

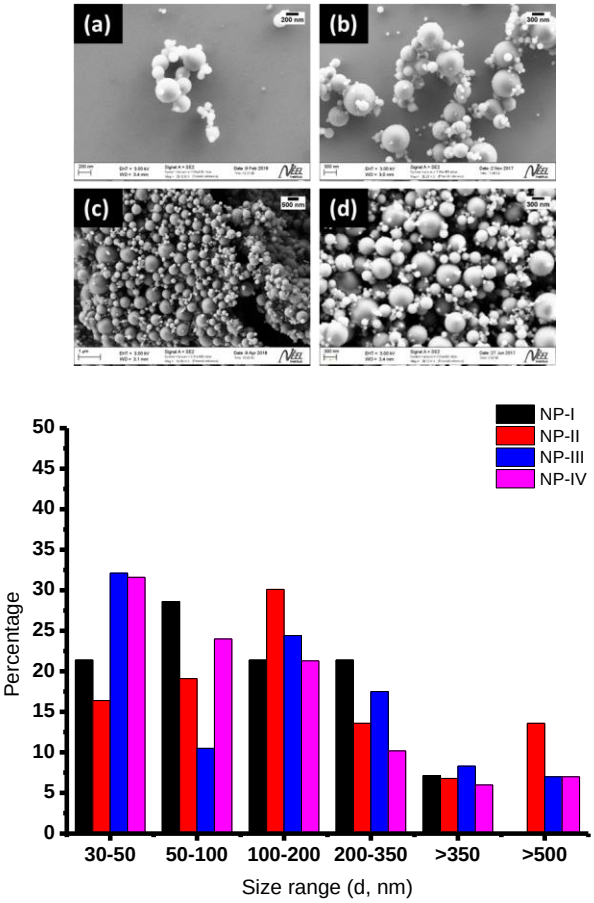

Figure 2. 11. Size distribution of core-shell NPs

2.1.3.2. Influence of spray-drying parameters

The physical parameters of the spray-drying reactor can also influence the morphology of the core-shell NPs. As explained in the section 2.1.3.1, the temperature of the oven must be set to a temperature significantly lower than the melting point of the dye, to avoid sublimation or evaporation of the dye, and its deposition outside the NPs in the form of crystallites/needles. On the other hand, the temperature of the electrostatic filter must also be set to a temperature above 100 °C to remove any traces of water or solvent that could result in insufficient drying of the NPs. In addition to temperature, the nitrogen flux and air flow rates also influence the morphologies of NPs.

2.1.3.2.1. Nitrogen flux

The pressure of nitrogen, P_{N_2} is an important parameter that influences the formation of the NPs. The atomizer can form droplets of the sol only if P_{N_2} is above a certain threshold value,

determined to be 0.6 bar.[5] Above 2.4 bar as determined by previous works,[5] the nozzle of the atomizer may get damaged. Hence, it is very important to work within this pressure range and optimize the pressure for the best results. The nitrogen pressure chosen for the synthesis of the core-shell NPs was 1 bar as optimized based on a previous work.[5] However, the flow rate of the nitrogen was adjusted and optimized to get the best results. A fast flow rate of more than 90 L/h of N_2 leads to NPs with defects (holes due to impact), as shown in Figure 2.12, which can be attributed to insufficient drying of the shell. This is due to the fact that higher flow rates of nitrogen lead to lower residence time (1.0 minutes calculated based on the geometry of the furnace) of the NPs in the oven. Lower flow rates (between 50 L/h and 60 L/h) led to better results due to longer residence time (1.6 and 1.3 minutes respectively) of the NPs in the oven, resulting in a more complete drying.

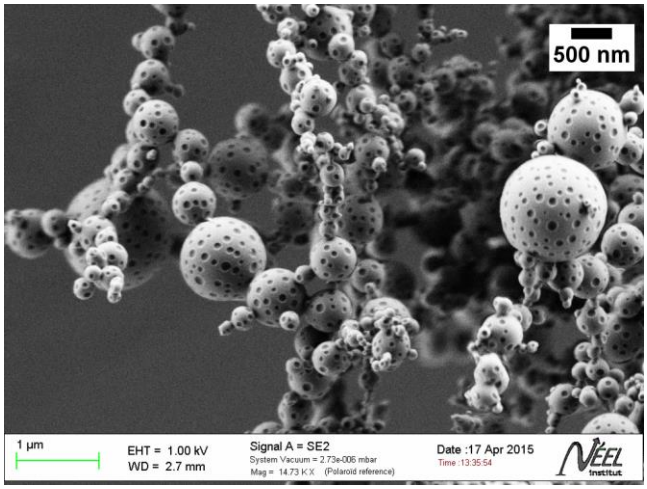

Figure 2. 12. FESEM image of **NP-IV** synthesized at a N_2 flow rate > 90 L/h

2.1.3.2.2. Air flow rate

Finally, the air flow rate (F_{air}) also influences the spray-drying process. An air flux is required to dilute the droplets produced by the atomizer and drive these droplets into the oven. The air flow rate also determines the residence time of the NPs in the oven and plays a role in the final yield of the nanoparticles as well. Different flow rates were chosen for different syntheses due to the varied properties of the dyes (melting point and solubility) and protocols used. A flow rate of 8 L/h was chosen for dyes **II** and **IV** while a higher flow rate of 16 L/h was chosen for dye **I**. In the case of dye **III**, a flow rate of 30 L/h was chosen after optimization to enable sufficient drying of the core-shell NPs. This resulted from the fact that, with lower air flow rates, big NPs (> 500 nm) showed small holes on the surface, indicating insufficient drying, while smaller NPs had a uniform morphology, with no holes on the surface. It is important to note that a high air flow rate has an antagonistic effect when combined with a reduced nitrogen flux, on the drying of the NPs. A very high flow rate could result in reduced residence time of the NPs in the oven resulting in

insufficiently dried NPs, but could compensate by helping in the fast evaporation of the solvent by diluting the spray in the gas flow, resulting in better drying. Finally, a flow rate higher than 30 L/h was avoided to minimize the coalescence of the droplets prior to controlled drying, in order to obtain NPs with smaller size distributions.

2.2. Investigation of the organic nanocrystalline core

The optical properties of the selected crystal-state fluorophores are very sensitive to their crystallinity and may strongly depend on their organization in the solid-state. Previous works indicated that the CMONS dye may be crystallized inside the NP as a nanocrystalline core, either in its yellow polymorphic form that is strongly fluorescent with an emission maximum at 539 nm, or in its orange form that exhibits a much lower fluorescence shifted at 596 nm, as a function of the composition of the organosilica shell.[16] The coupled effects of confined nucleation and growth and the nature of silicate matrix on crystallinity and polymorphism of the CMONS nanocrystals were characterized by electron microscopy techniques, absorption and fluorescence spectroscopy and second-harmonic generation (SHG) spectroscopies.[16] It is important to confirm the presence of the crystal core in the new NPs (**NP-I** to **NP-IV**), which can be characterized in a number of different ways including IR spectroscopy, thermogravimetric analysis and electron microscopy.

2.2.1. Infrared spectroscopy

A primary confirmation was first provided by Infrared spectroscopy, which enabled to identify bands corresponding to the pure dyes in the core-shell NPs. Figure 2.13 shows the IR spectra of **NP-I** compared to dye-free NPs and dye **I**. The IR bands corresponding to C≡N (2210 cm^{-1}) and C=C (1573 cm^{-1}) bonds in the pure dye **I** are present in **NP-I** and absent in dye-free NPs, thereby confirming the presence of the dye **I** in the **NP-I**.

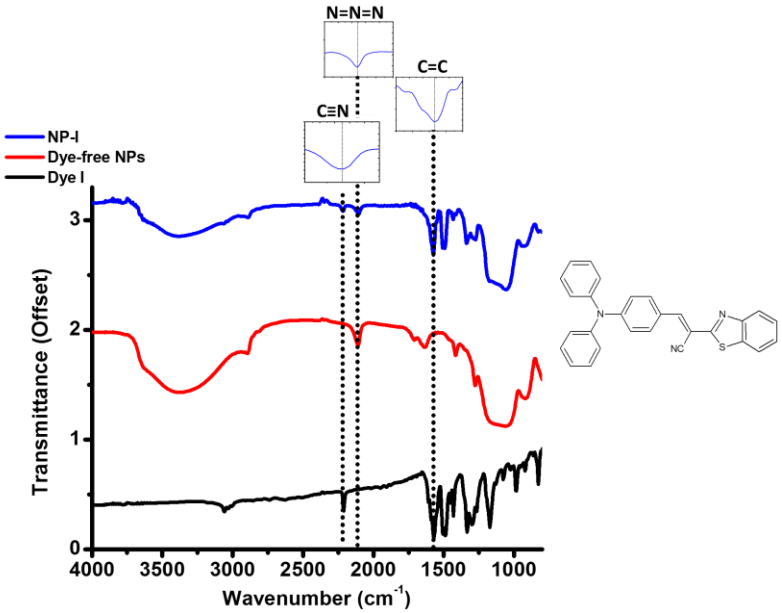

Figure 2. 13. IR spectra of **NP-I** (blue) compared to dye-free NPs (red) and **dye I** (black)

Similar results were obtained for **NP-II**, **NP-III** and **NP-IV**. Figure 2.14 shows the IR spectra of **NP-II** compared to dye-free NPs and dye **II**. The IR bands corresponding to C≡N (2213 cm^{-1}) and NO_2 (1511 cm^{-1}) bonds in the pure dye **II** are present in **NP-II** and absent in dye-free NPs, thereby confirming the presence of the dye **II** in the **NP-II**.

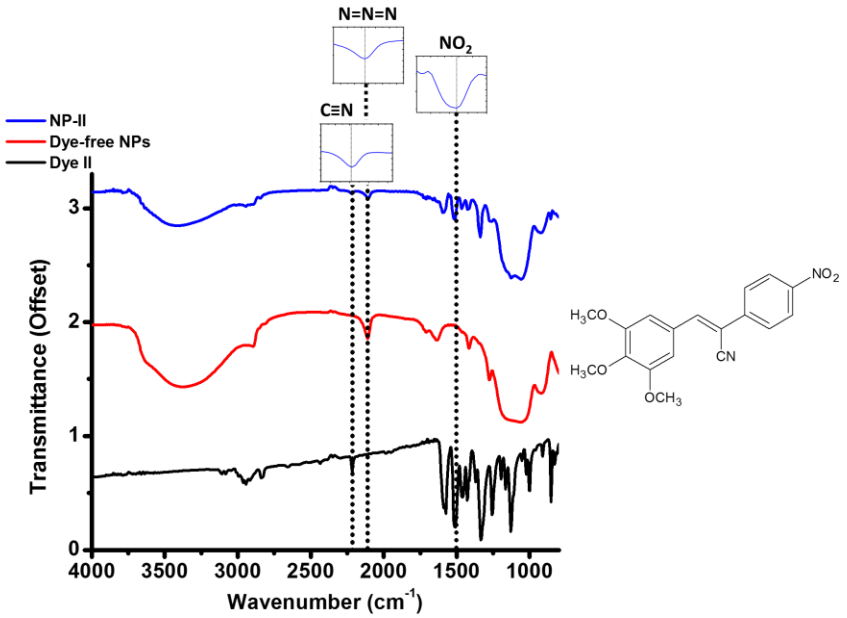

Figure 2. 14. IR spectra of **NP-II** (blue) compared to dye-free NPs (red) and dye **II** (black)

Figure 2.15 shows the IR spectra of **NP-III** compared to dye-free NPs and dye **III**. The IR bands corresponding to C≡N (2210 cm^{-1}) and NO_2 (1515 cm^{-1}) bonds in the pure dye **III** are present in **NP-III** and absent in dye-free NPs, thereby confirming the presence of the dye **III** in the **NP-III**.

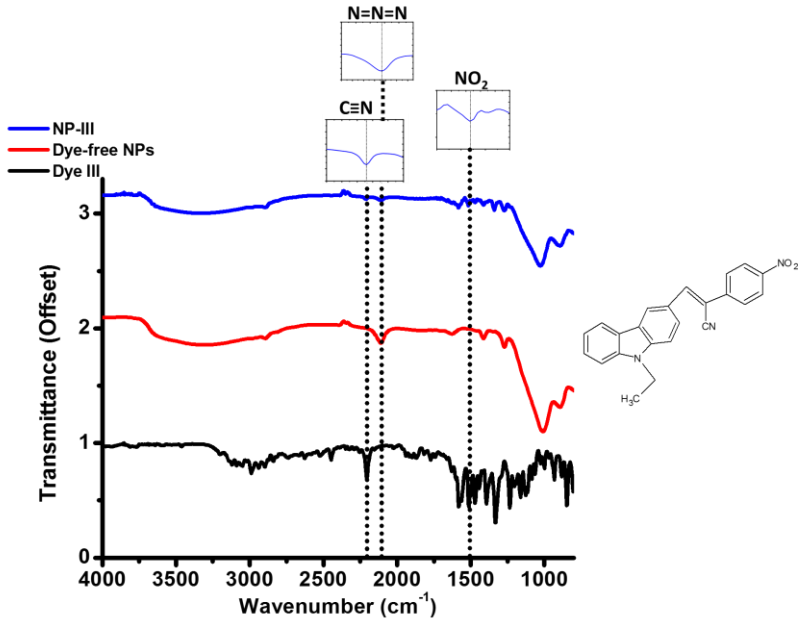

Figure 2. 15. IR spectra of **NP-III** (blue) compared to dye-free NPs (red) and **dye III** (black)

Figure 2.16 shows the IR spectra of **NP-IV** compared to dye-free NPs and dye **IV**. The IR band corresponding to C=O (1747 cm^{-1}) bond in the pure dye **IV** is present in **NP-IV** and absent in dye-free NPs, thereby confirming the presence of the dye **IV** in the **NP-IV**.

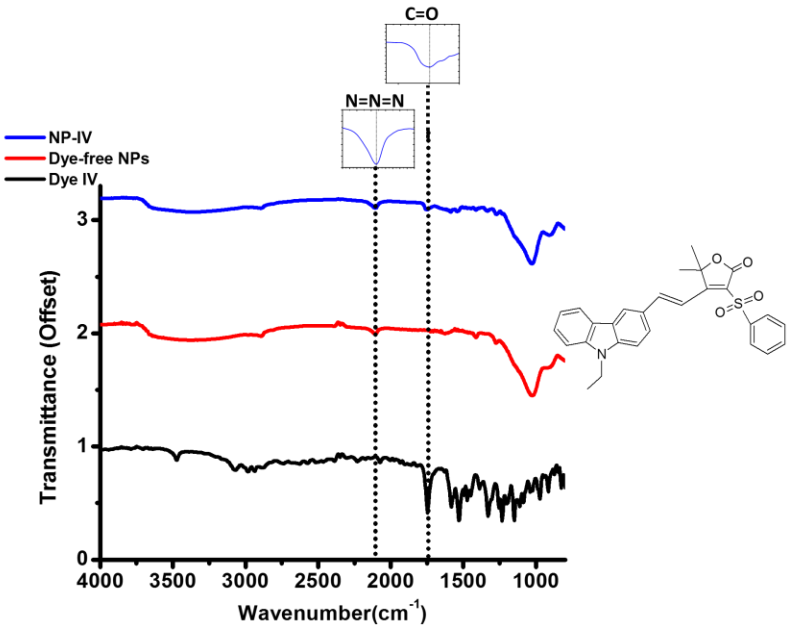

Figure 2. 16. IR spectra of **NP-IV** (blue) compared to dye-free NPs (red) and dye **IV** (black)

Finally, in all four cases, an important observation also is the presence the band at 2100 cm^{-1} which corresponds to the azide functionality (N=N=N) that is present in the dye-free NPs and the core-shell NPs but absent in the dye. This indicates the preservation of the clickable function during the spray-process, that unarguably demonstrates the possibility of functionalization of the NPs by click chemistry.

2.2.2. Electron microscopy

To characterize the crystallinity of the organic core, a basic etching of the silicate shell was performed. This consists of the basic treatment of the aqueous NP suspensions using sodium hydroxide at pH 12 for one week under stirring in order to completely dissolve the silicate shell. The suspension (5 mL) was then dialysed twice against pure water (2.5 L) before electron microscopy imaging (Figure 2.17).

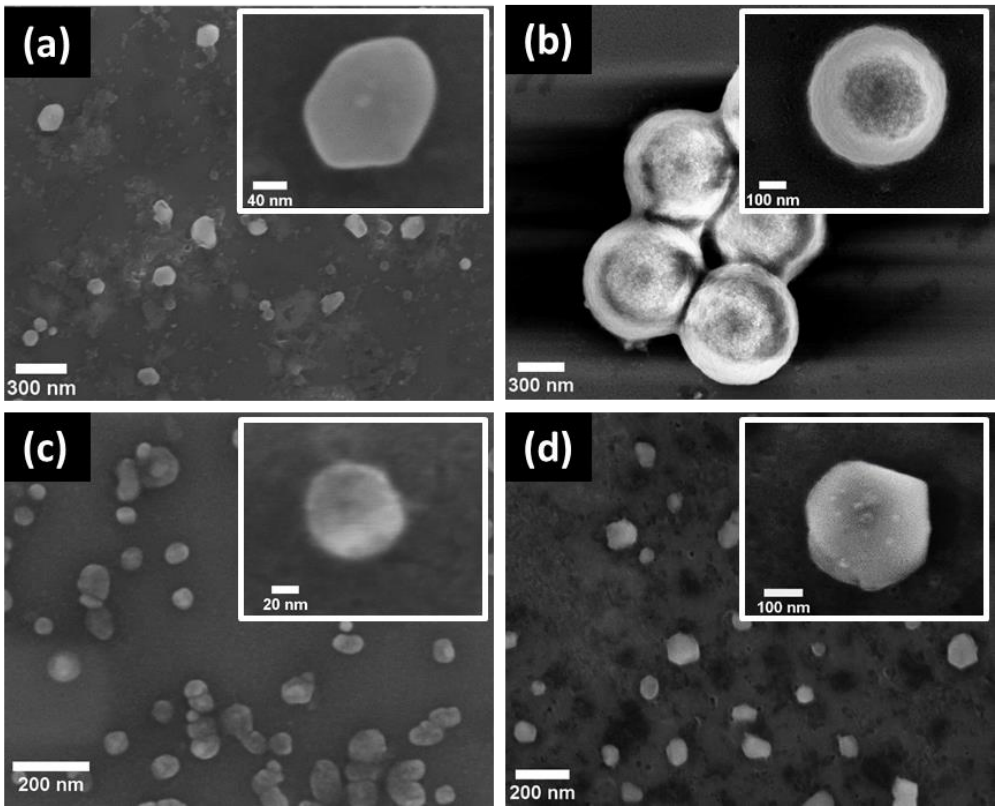

Figure 2. 17. FESEM images of nanocrystals from (a) **NP-I**, (b) **NP-II**, (c) **NP-III** and (d) **NP-IV**, after full dissolution of the silicate shell

The FESEM images in Figure 2.17a and 2.17d show rather facetted nano-objects suggesting the presence of well-defined crystal faces of the dye core, thus illustrating their good crystallinity, with varied sizes reflecting the polydispersity of the starting NPs. In the case of **NP-III**, size-disperse NPs were also obtained, though with a crystal morphology less defined (Figure 2.17c).

Finally, in **NP-II** (Figure 2.17b), all NPs featured the same size (ca 500 nm), though the starting NPs were polydisperse, which suggests that a parasitic phenomenon occurred during the basic treatment and that the imaged objects are not the cores initially present in the NPs.

TEM is a well-suited technique to get more information on the crystallinity and was also used for characterisation of the core. Indeed, by recording data in electron diffraction mode, it is possible to observe diffraction spots indicative of the crystallinity. However, the organic nanocrystals are extremely sensitive under the focussed electron beam and may be rapidly amorphized or degraded.[5,16] Therefore, the sample holder was cooled to 100 K while the intensity of the parallel beam was drastically reduced. In order to spare the particles any unnecessary electron irradiation, the TEM alignment was performed in a region of the grid that was not further exploited. Then the TEM grids were manually scanned in selected area diffraction mode, having the camera continuously recording in the rolling shutter mode with a short exposure time. The x,y scan was stopped as soon as a diffraction pattern was detected then saved, and only then the corresponding image was taken. It is noteworthy that even at 100 K, amorphization was observed within 30 s. This technique enabled us to get diffraction patterns in the case of **NP-IV**, evidencing the presence of well-crystallized cores (Figure 2.18g-h).

However, due to the sensitivity of the material, it was not possible to acquire many diffraction patterns on the same particle. So, we could not identify the crystal form of dye **IV**, as each electron diffraction pattern could not be indexed without ambiguity. **NP-I** (Figure 2.18a-b), **NP-II** (Figure 2.18c-d) and **NP-III** (Figure 2.18e-f) did not lead to distinguishable diffraction peaks under the same conditions. This could be the outcome of two factors, the first being that these dyes may form a core that is not crystalline enough; the second being that the nanocrystalline core is so sensitive to the electron beam that it amorphizes or transforms instantaneously into a weakly crystalline structure upon exposure to the beam. No diffraction contrast was visible inside the particles, which tends to confirm that the crystalline core is already amorphized after a few seconds of irradiation, even for **NP-IV**.

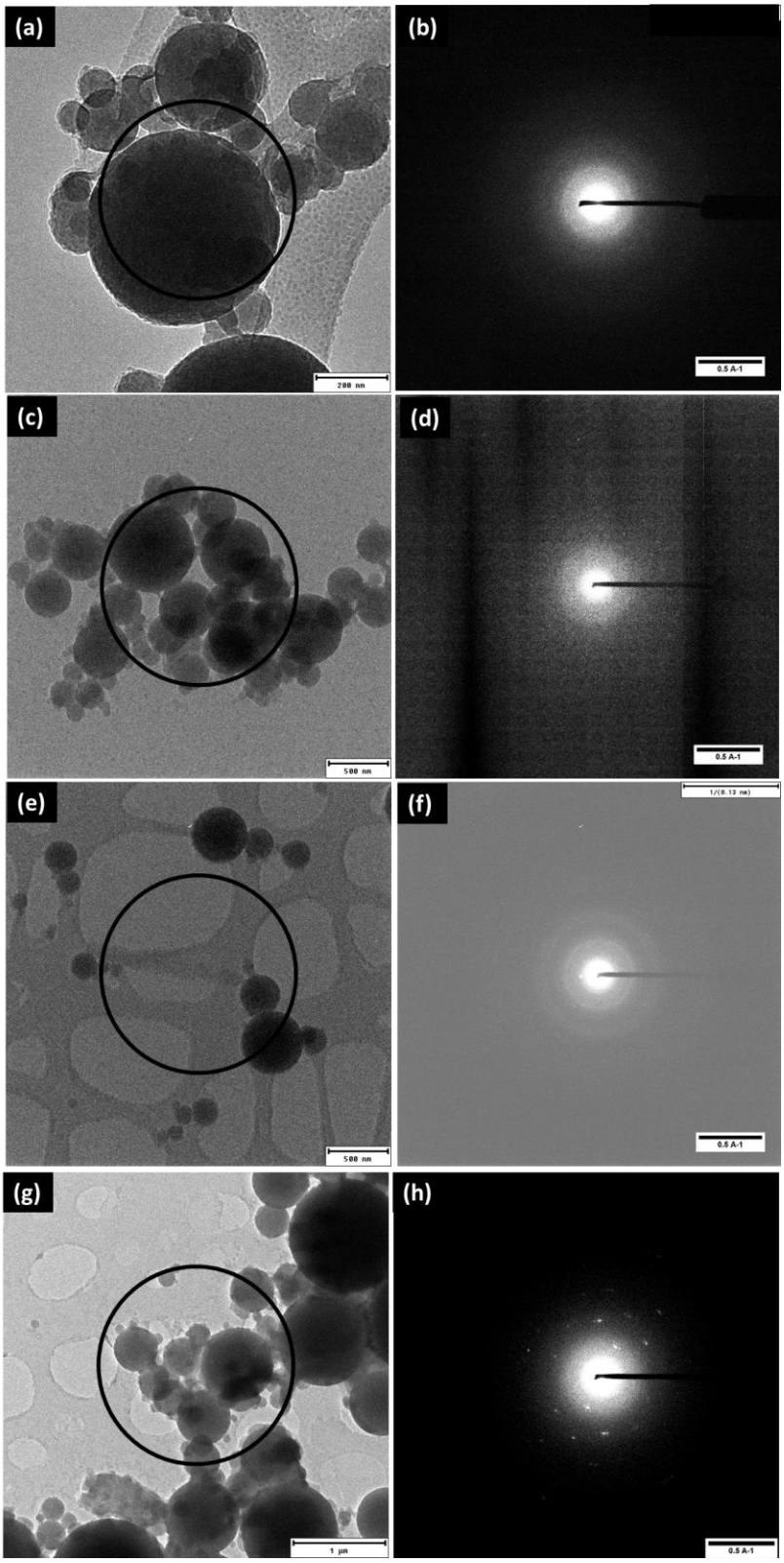

Figure 2. 18. TEM images of (a) **NP-I** and (b) corresponding diffraction pattern, (c) **NP-II** and (b) corresponding diffraction pattern, (e) **NP-III** and (b) corresponding diffraction pattern, (g) **NP-IV** and (h) corresponding diffraction pattern. The circle indicates the particles selected by the selected area aperture in the diffraction mode.

X-ray Diffraction was also employed to characterise the crystallinity of the NPs. However, the use of powder X-ray diffraction is complicated due to the reduced size of the NPs and the presence of the silica shell which features a broad and intense X-ray scattering peak as shown in Figure 2.19.

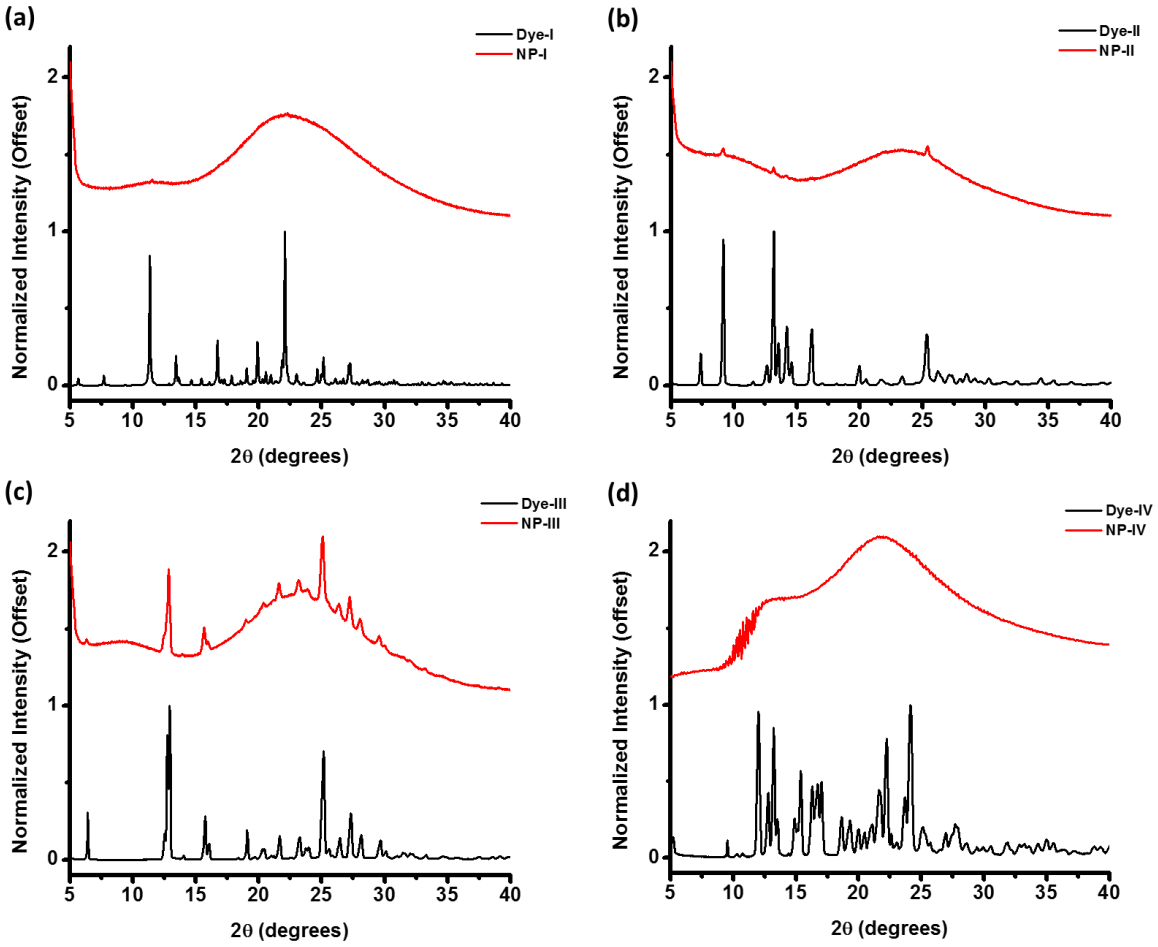

Figure 2. 19. XRD of (a) NP-I, (b) NP-II, (c) NP-III and (d) NP-IV (black line corresponds to pure dye and red line corresponds to core-shell NPs)

It can be seen from Figure 2.19a and 2.19d corresponding to **NP-I** and **NP-IV** respectively, that there are no peaks corresponding to the pure dye, present in the NPs. It is important to note that **NP-IV** was observed to be crystalline using electron diffraction as described earlier (Figure 2.18g-h). Therefore, the absence of any XRD peaks in **NP-I** and **NP-IV** could be a result of the small size of the nanocrystals and their sensitivity to the X-ray radiation and masking by the silicate shell. On the other hand, peaks corresponding to the pure dyes were present in **NP-II** (Figure 2.19b) and **NP-III** (Figure 2.19c), while the same samples yielded no electron diffraction patterns. It is possible that these strong peaks arise from the presence of bigger nanocrystals or microcrystals from bigger NPs. Although no needles or crystallites were observed for these samples using FESEM just after synthesis, it could also be the presence of a small fraction of dye platelets

formed as a result of dye sublimation during synthesis, that lead to these strong peaks, especially in the case of **NP-III**. Furthermore, the nanocrystals are also sensitive to the X-ray radiation and crystal quality may hence be significantly deteriorated.

2.2.3. Thermogravimetric analysis

It is noteworthy that the d_{max} values used in the synthesis of the core-shell NPs correspond to very high loadings of organic dye, reaching more than 40 %wt in the case of **NP-IV** and **NP-I**. The synthesis parameters have been summarized in Table 2.3 along with calculated weight percentage of dye in the NPs. These calculated amounts were further confirmed using thermogravimetric analysis of the NPs.

Table 2. 3. Synthesis parameters for the different organic dyes and amount of organic dyes in NPs

Dye	Protocol used	Ageing of sol (days)	d_{max}	T_{oven} (˚C)	Theoretical amount of organic dye in NPs (% wt)
I	C	3	0.10	141	40.5
II	B	2	0.10	150	35.1
III	C	5	0.07	160	29.0
IV	B	2	0.10	185	42.8

TGA of **NP-I** under an oxygen-argon atmosphere shows that the dye is stable within the NP until it degrades from 280 °C (Figure 2.20). The total weight loss (48%) is comparable to the calculated value (43.5%), with 40.5% arising from the loss of organic dye (Table 2.3) and 3% from the oxidation of the ethylene linker within the organosilicate shell. Additional weight losses at low and high temperatures are due to the loss of adsorbed water and enhanced condensation within the shell, respectively. The NPs are thermally stable up to 280 °C after which the organics start to decompose. An endothermic weight loss at 340 °C, assignable to a fragmentation reaction (breaking of molecular bonds), is followed soon after (355 °C) by the combustion of organic moieties leading to the production of water (m/z=18) and carbon dioxide (m/z=44). This highly exothermic combustion event then takes place typically from 450 to 600 °C. Similar results were obtained for **NP-II**, **NP-III** and **NP-IV**.

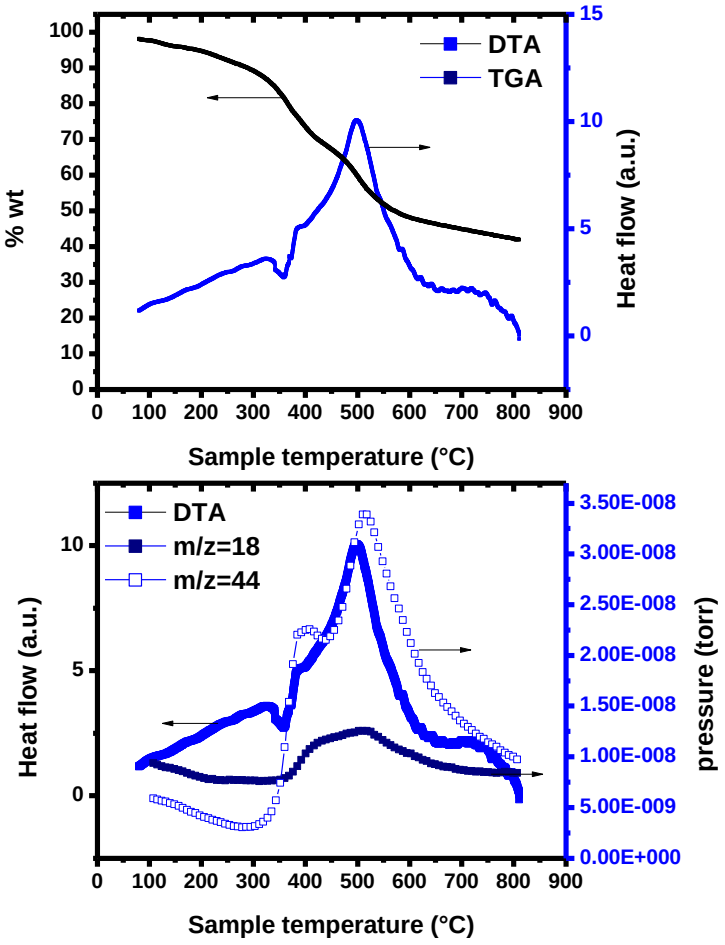

Figure 2. 20. TGA-DTA-MS analysis of **NP-I** at 8K/min under Ar/O_2

2.3. Optical properties

The organic dyes confined in the core-shell NPs are crystal-state emitters with optical properties highly suited for bioimaging with fluorescence emission in the red (Table 2.1). To study the fluorescence properties of the core-shell NPs, the chemically agglomerated NPs recovered from the electrostatic filter were subjected to a basic treatment, which involved controlled dissolution of the silicate shell of the NPs. This was achieved by sonicating the NP suspension (in water; 60 mL) for 20 minutes in an ultrasonic bath (150 W) before adding a 1 M NaOH solution until pH 12 and stirring the suspension for 24 h in a closed bottle. The NP suspension was then subjected to a centrifugation of 5 minutes at 5000 rpm and the supernatant was filtered using 5 µm, 1.2 µm and 0.8 µm filters, to ensure the removal of the biggest aggregates. This step was followed by neutralization of the NP suspension to pH 7.4 by the dropwise addition of 1 M HCl. The treated NP suspensions were then used for the fluorescence spectroscopy measurements.

The NP suspensions used for the measurement of the optical properties exhibited an optical density of around 0.2 as shown in the absorbance curves in Figure 2.21. The absorbance maxima were chosen from these spectra to record the one-photon fluorescence. These NP suspensions displayed a size distribution around 200 nm and were stable up to 10 days as determined by DLS (Figure 2.22).

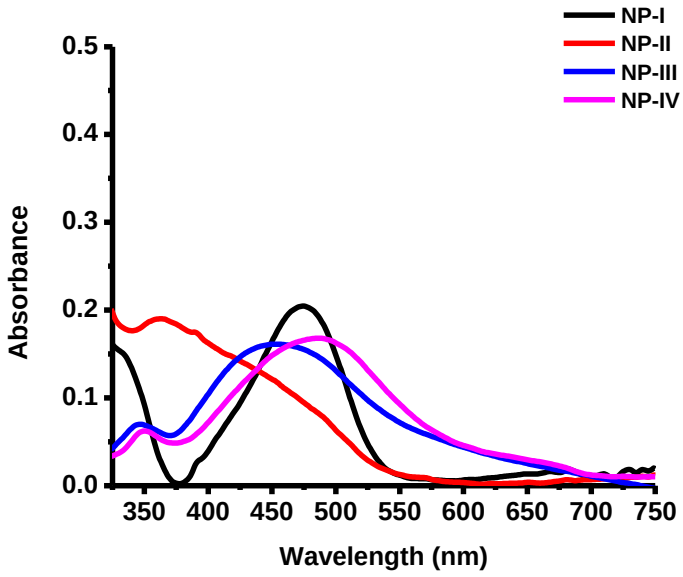

Figure 2. 21. Absorbance spectra of the core-shell NPs after basic treatment

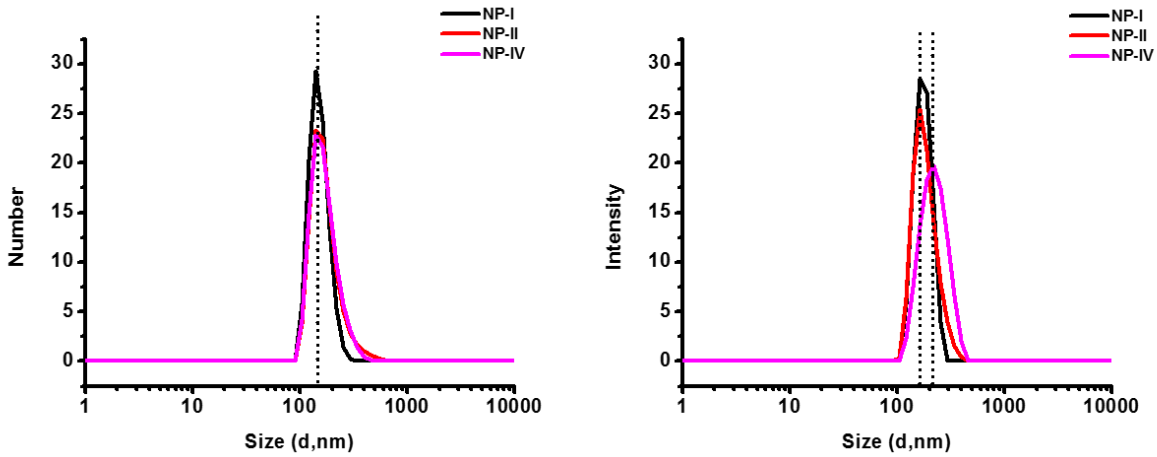

Figure 2. 22. DLS of core-shell NPs after the basic treatment. The distribution in diameter is centred at ca 200 nm.

2.3.1. One-photon fluorescence

The fluorescence spectra of the microcrystalline (bulk) dyes (Figure 2.23) were then compared with those of the treated NP suspensions (Figure 2.24).

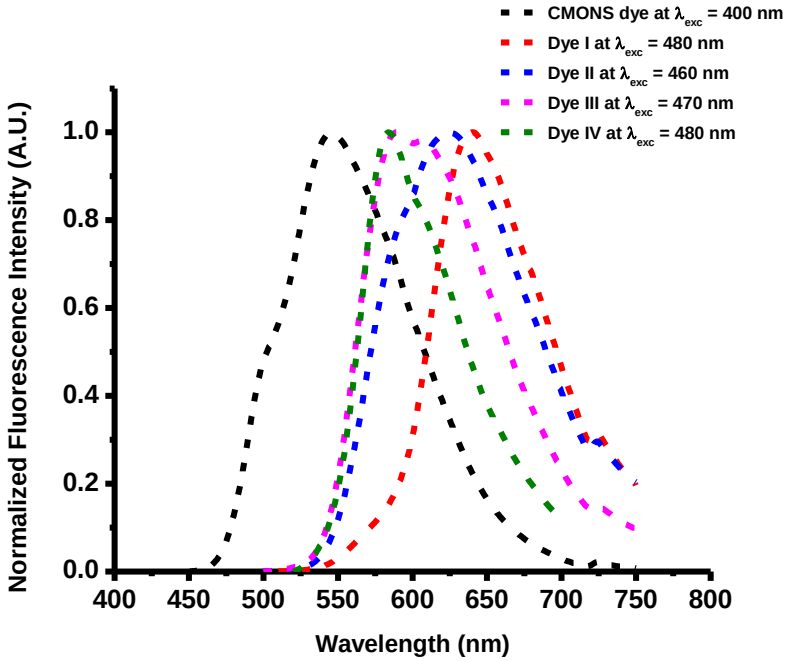

Figure 2. 23. Fluorescence spectra of organic dyes as microcrystals

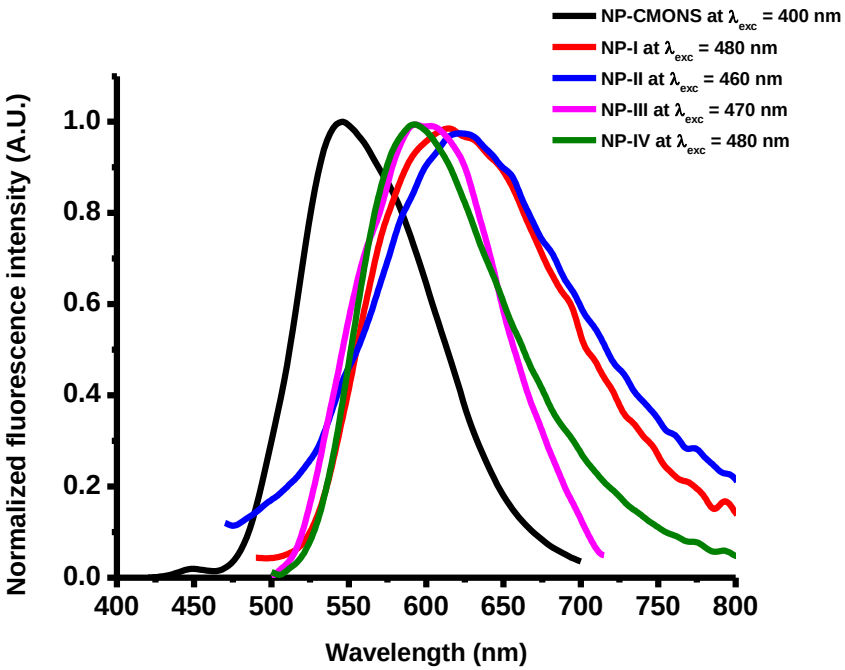

Figure 2. 24. Fluorescence spectra of organic dyes confined in NPs

While **NP-II**, **NP-III** and **NP-IV** did not exhibit any important modification after their confinement in the NPs, the fluorescence of **NP-I** was blue-shifted from 639 nm in the microcrystalline state to 614 nm in the core-shell NPs. Such a shift may be due to a different crystal-state structure between the microcrystalline powder or the NPs.[16] While dye **I** is microcrystalline and present as a single phase corresponding to the published structure,[17] no diffraction peak could be recorded in the corresponding NPs, the only indication of crystallinity being the well-facetted morphology of the core. Therefore, it is difficult to conclude if the observed fluorescence shift for **NP-I** accounts from a crystalline state but with a different polymorphic structure, or from a loss of crystallinity. Indeed, the strong capillary forces exerted on the core and resulting from the condensation of the silicate shell during the drying may result in a partially amorphous structure.

2.3.2. Quantum yield

The quantum yield of these NP suspensions was also measured using a calibrated integrative sphere collecting all the emission (2π steradians covered with spectralon). While **NP-II** exhibited a very low quantum yield (<1 %), **NP-I** and **NP-IV** exhibited a quantum yield close to 3% and 1 % respectively as summarised in Table 2.4. This is significantly lower than for the pure dyes in microcrystalline state (Table 2.1). This could be due to a partial deterioration of the crystal quality of the organic nanocrystals because of the capillary pressures exerted at the end of drying of the silicate shells on the dye cores. Nevertheless, the relatively low quantum yields could be compensated through the very high molecular concentrations of dye nanocrystals in the core of NPs.

Table 2. 4. Optical properties of organic dyes confined in NPs

Core-shell NPs	λ_{exc} (nm)	λ_{em} (nm)	Quantum Yield
NP-I	480	614	3 %
NP-II	460	622	< 1%
NP-III	470	600	ND
NP-IV	480	590	1 %

High fluorescence quantum yields are desirable for NPs to be used as tracers. But there are several factors that can influence fluorescence quantum yields, starting with the structure of the dye. For crystal-state emitters, the fluorescence and quantum yield depend on the stacking and arrangement of molecules forming the crystal, which in turn can be engineered. It is important to note that the formation of J-aggregates lead to highly fluorescent crystals, while the formation of H-aggregates leads to quenching.[17] It is therefore very important to deeply investigate the relationship between the molecular structure of the dye and the fluorescence quantum yield.

2.3.3. Two-photon fluorescence

The organic dyes used for the synthesis of the core-shell NPs show interesting non-linear optical phenomena such as two-photon absorption, which make them ideal candidates for non-linear optical microscopy techniques. As described in the previous section, these NPs show fluorescence emission in the red, close to the biological transparency window, making them interesting candidates for bio-imaging applications. It is also important, however, to study their properties under two-photon excitation.

The efficiency of two-photon absorption is expressed in terms of two-photon absorption cross-section (σ), with units of GM (Goeppert-Mayer, 1 GM = 10^{-50} cm^4 s). High values of two-photon absorption cross section are desirable to render these fluorescent core-shell NPs efficient for two-photon microscopy to minimize photodamage and enable three-dimensional imaging of live species.[18]

There are several parameters that have an influence on the two-photon absorption cross section. This includes the polarizability of the dye molecule, its π-electron conjugation length and the strength of donor/acceptor groups of the fluorophore substituents.[19–21] Depending on the spatial arrangement of the electron donor (D) and electron acceptor (A) groups, dyes are often classified as dipolar, quadrupolar and octupolar.[18] Furthermore, the geometry and symmetry of the dye can also impact the 2PA cross section. Typically, dyes used for two-photon studies are designed to maximize the degree of intramolecular charge transfer upon excitation and the transition dipole moment.[18,22,23]

In addition to 2PA cross-section, the brightness of a two-photon fluorophore, also called the two-photon action cross-section is another important parameter that influences the efficiency of the dye. It is expressed as the product of the fluorescence quantum yield (ϕ_F) and the two photon absorption cross section value (σ). High values of 2P action cross-sections allow the use of lower power lasers to reduce the chances of photobleaching.[19] Typically, the most commonly used dyes have $\sigma \times \Phi_F$ values in the range of 1–300 GM.[18]

The organic dyes used in the core-shell NPs are based on the D-π-A dipolar structure. The permanent dipole moment associated with such structures results in strong dipole-dipole interactions which in turn can induce specific organization and orientation of the molecules in the solid state.[17] These D-π-A structures are also characterized by large σ×ΦF values.[19] As listed in Table 1, these dyes also show a large Stokes shift and emission in the red. These dyes allow the use of commercial Ti:Sapphire lasers, whose wavelengths can be tuned between 760-1000 nm, which also corresponds to the biological transparency window.

Direct measurement of two-photon absorption cross section is difficult to perform, due to the small fraction of photons that are absorbed during the two-photon process.[24] Therefore, two-

photon fluorescence excitation is more commonly utilized to measure the two-photon absorption cross-section.[24] Although this method offers better sensitivity, there are several factors that need to be taken into account, while calculating the cross-section values. The most commonly encountered in two photon excitation (TPE) cross section measurements is the dependence of the rate of absorption on spatial and temporal coherence of the excitation light[24], which in turn results in several correction factors that need to be applied to the measured data.

Another major problem in measuring TPE cross sections is that there are very few reference molecules for two-photon absorption, which in turn implies that there are very few measured spectra of reference samples in the literature, with significant differences in measured values between two sets of data. Often, data are available until 920 nm beyond which solvent absorption problems arise.

2.3.3.1. Sample preparation

The samples that were used for the two-photon excitation experiments were treated NP suspensions (See section 2.3). Three samples were measured, **NP-I**, **NP-IV** and functionalized NP-IV (**FNP-IV**), with corrected optical densities close to 0.6, 1.2 and 0.15 respectively. **FNP-IV** refers to **NP-IV** after functionalization with long-chain linear PEG (Mn: 5000), using CuAAC. This was followed by dialysis against 0.0133 M Phosphate buffer to remove unreacted components and copper salts.

The absorbance spectra of the three samples are shown in Figure 2.25. It is evident that the diffusion contribution is significant in **NP-IV** and **FNP-IV**. This diffusion contribution was accounted for and corrected to yield the absorbance curves and optical density values. It can be seen from the fluorescence spectra (Figure 2.26) that the emission is blue shifted in the case of **FNP-IV**, in comparison with **NP-IV**. While **NP-I** and **NP-IV** show an emission wavelength of 588 nm, **FNP-IV** has an emission maximum at 567 nm, which could be attributed to the PEGylation, which results in different polarity of the environment.

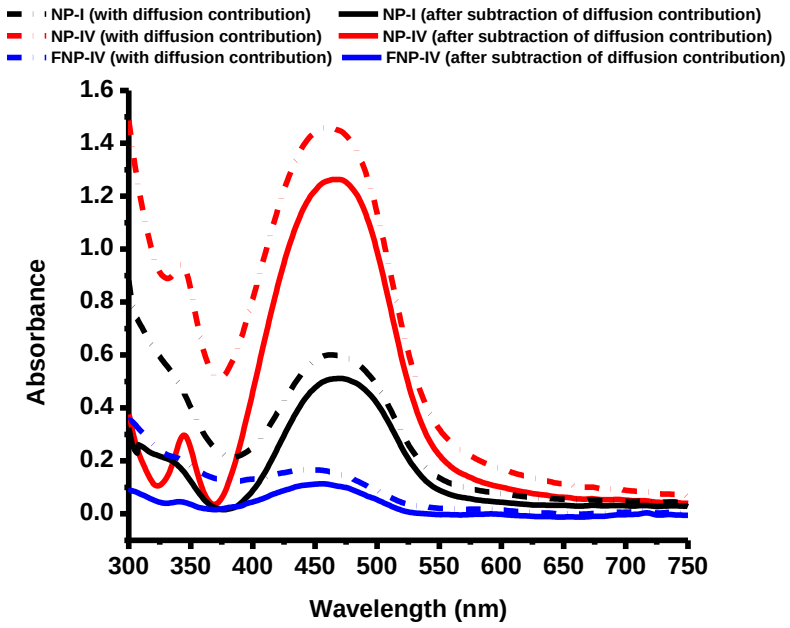

Figure 2. 25. Absorbance spectra of **NP-I**, **NP-IV** and **FNP-IV**, before (dotted) and after removal of diffusion contribution (solid).

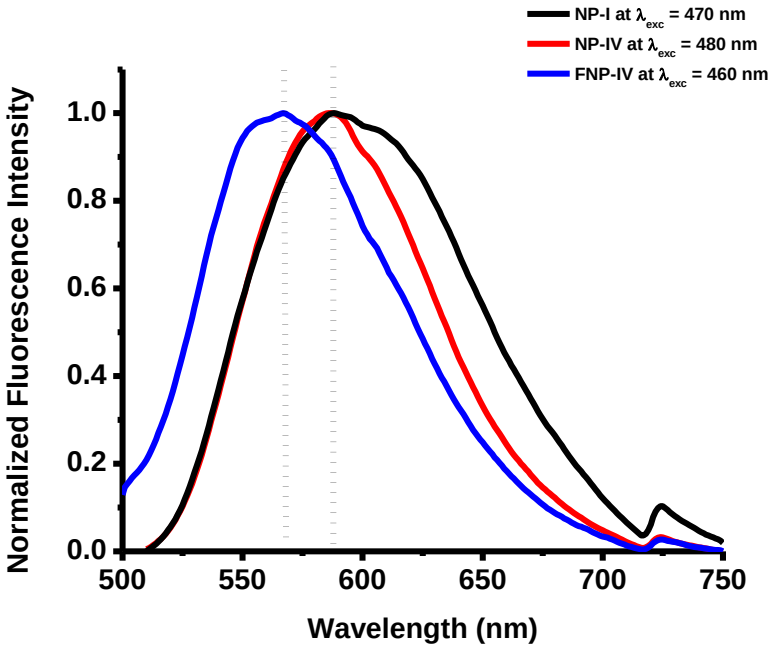

Figure 2. 26. Normalized fluorescence emission spectra of **NP-I**, **NP-IV** and **FNP-IV**

2.3.3.2. Two-photon excitation spectra

The two-photon excitation spectra recorded for the three samples is shown in Figure 2.27 and the emission wavelengths at which the spectra were recorded is summarized in Table 2.5.

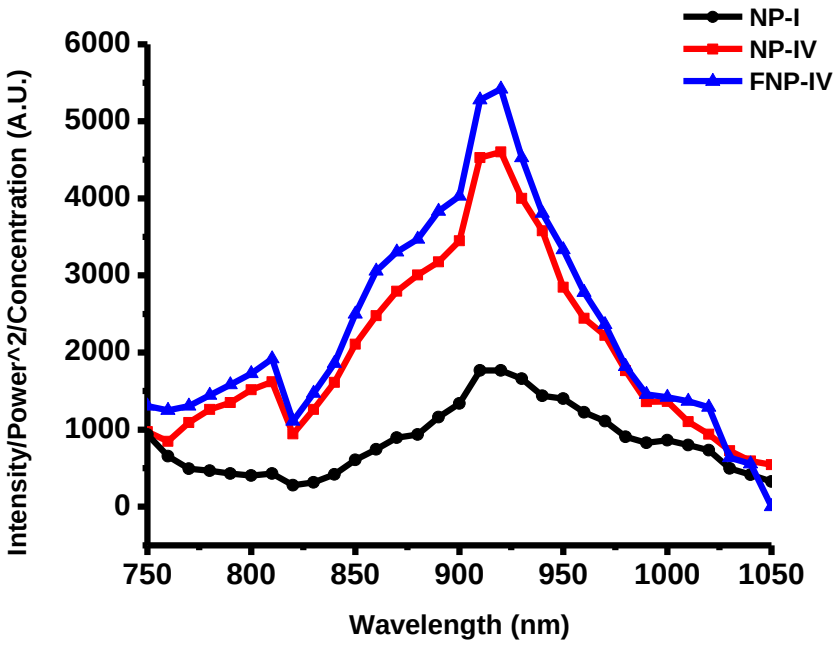

Figure 2. 27. Two-photon excitation spectra of **NP-I**, **NP-IV** and **FNP-IV** (raw data)

Table 2. 5. Emission wavelength for **NP-I**, **NP-IV** and **FNP-IV**

Sample	λ_{em} (Filter 1)	λ_{em} (Filter 2)
NP-I	575 nm	595 nm
NP-IV	572 nm	580 nm
FNP-IV	562 nm	573 nm

It can be seen that a drop was recorded at 820 nm for all three samples (including the reference). While the recorded laser power was constant at 150 mW showing a decrease only after 970 nm, this drop in signal could be attributed to an accidental misalignment in the experimental setup or possibly due to a problem in pulse duration. While **NP-I** and **NP-IV** showed differences in the blue part of the spectrum, the red part seemed to imply that they have the same maxima. Furthermore, **FNP-IV** showed similar characteristics to **NP-IV**, although with a significant drop in intensity, which is due to its low optical density. It is interesting to note that the functionalization did not have a major impact on the two-photon excitation spectra, as was observed with the blue shift in fluorescence emission spectra.

Figure 2.28 shows the superposition of the absorbance and emission spectra of **NP-I** with the one-photon and two-photon excitation spectra. While there is no major shift between the one-photon and two-photon excitation, the one-photon excitation appears rather broad compared

to the two-photon spectrum. This could be due to the absorption of water in the red part of the spectrum that could not be corrected with the references used (styryl being in a different solvent and fluorescein spectra showing slightly different shapes depending on the published reference used). This could also show that the spectral bands implied in one or two photon absorption are not the same. The wide one-photon spectrum is probably constituted of different superimposed states which are not all active in the two photon transition.

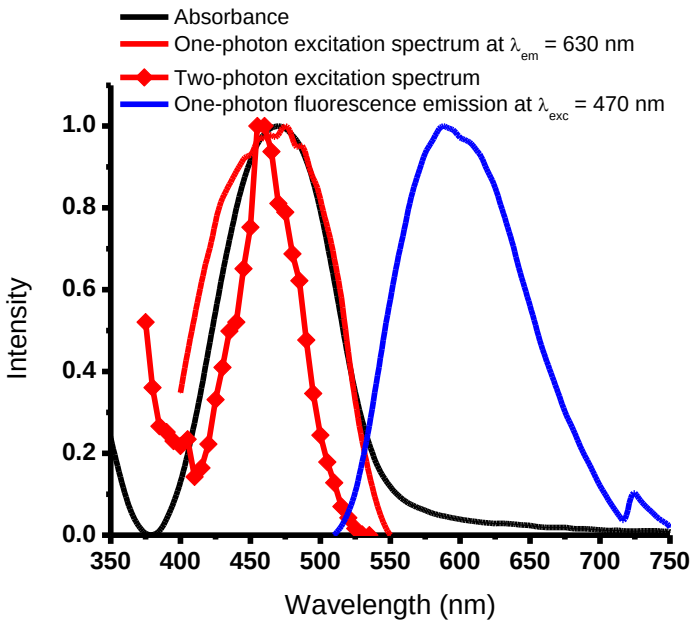

Figure 2. 28. Absorbance (black), one-photon (red) and two-photon excitation spectra (red symbol, raw data) and emission spectra (blue) of **NP-I**

Figure 2.29 shows the superposition of the absorbance and emission spectra of **NP-IV** with the one-photon and two-photon excitation spectra. A similar trend is observed although with a slight blue shift of the two-photon spectrum.

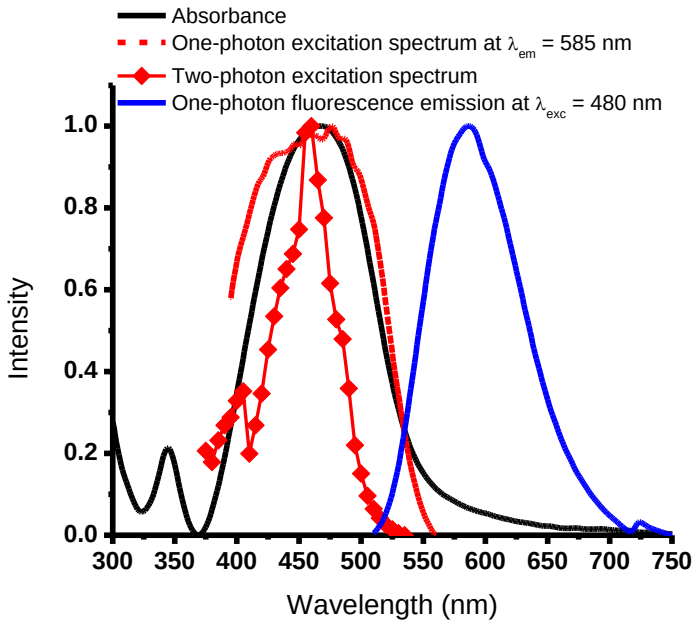

Figure 2. 29. Absorbance (black), one-photon (red) and two-photon excitation spectra (red symbol, raw data) and emission spectra (blue) of **NP-IV**

However, it is important to note that the above two-photon excitation spectra correspond to raw data that have not been fully corrected. Indeed, the corrections to be applied include the following:

The focal spot diameter of the laser changes as a function of the wavelength. The laser power seen by the molecules is inversely proportional to the area of the spot, leading to an inverse quadratic dependence on wavelength. Furthermore, quadratic dependence of the signal on power of the laser leads to a factor of $1/\lambda^4$, which has to be accounted for.

The absorption of water, which typically starts at 900 nm is another significant factor that needs to be accounted for. This phenomenon has a significant effect on the spectra as the spot size of the laser is changed by thermal expansion. For 1 mm of water, the signal drops to approximately 80% of the maximum signal. Although a stirrer can be employed to reduce this thermal effect, with a quadratic dependence on intensity and a measurement spot size of 1 mm, this thermal effect is significant with the possibility of reducing approximately 40% of the signal.

These corrections enabled the extraction of the maximal two photon absorption cross section values as can be seen in Figure 2.30. **NP-IV** exhibited a two-photon absorption cross section value of approximately 280 GM, almost ten times more than that recorded for **NP-I** which exhibited a value of approximately 30 GM. Additionally, the GM values recorded for functionalized **NP-IV** was comparable to that before functionalization, indicating that the functionalization had no adverse effects on the optical properties of the NPs. It is evident from Figure 2.30, that **NP-IV** is more two-photon efficient as compared to **NP-I**, although **NP-I** had a quantum yield three times

more than that of **NP-IV**. Comparison of the two-photon efficiency before (as shown in Figure 2.27) and after applying the correction factors (Figure 2.30) showed similar results in terms of the characteristics of the curves so obtained, with the only difference being that a slight broadening of the curves was observed after correcting the spectra.

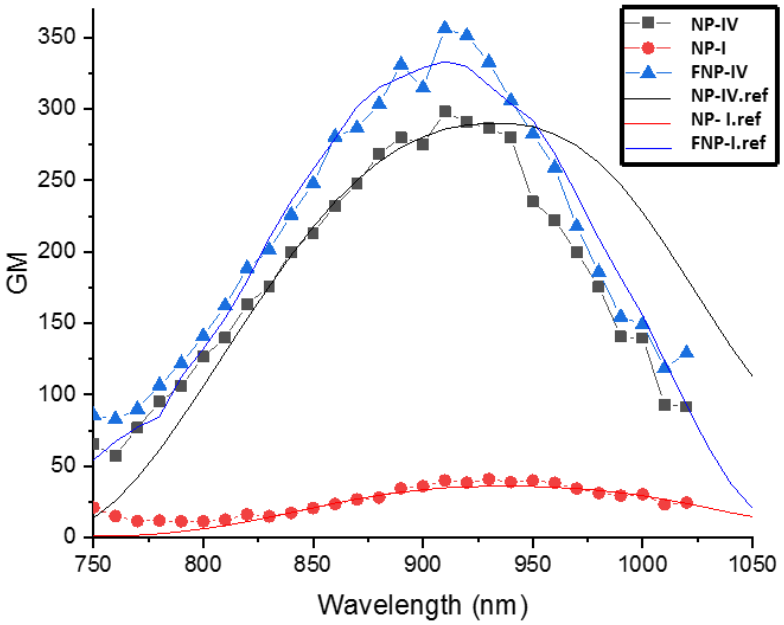

Figure 2. 30. Two-photon absorption cross section spectra of **NP-I**, **NP-IV** and **FNP-IV** after correction

Importantly, despite the low quantum yield values, the NPs suspensions studied showed adequate brightness required for imaging. Although the two-photon action cross section ($\sigma \times \Phi_F$) values recorded were approximately 1.2 GM in the case of **NP-I** and 2.8 GM in the case of **NP-IV**, which is in the lower range of brightness recorded for dyes typically used in two-photon imaging, it is compensated by the very high molecular concentrations of dye nanocrystals in the core of these NPs. This high loading of dye (~40 %wt) is more than an order of magnitude larger than that reported for other fluorescent silica based NPs, which are typically limited to less than 1 %wt dye loading. Overall, this should result in a very high brightness and enable the use of these core-shell NPs for two-photon microscopy *in vivo* in mice provided good colloidal stability is reached.

2.4. Bibliography

(1) Ibanez, A.; Maximov, S.; Guiu, A.; Chaillout, C.; Baldeck, P. L. Controlled Nanocrystallization of Organic Molecules in Sol-Gel Glasses. *Adv. Mater.* **1998**, *10* (18), 1540–1543.

(2) Monnier, V.; Sanz, N.; Botzung-Appert, E.; Bacia, M.; Ibanez, A. Confined Nucleation and

Growth of Organic Nanocrystals in Sol–gel Matrices. *J. Mater. Chem.* **2006**, *16* (15), 1401–1409.

(3) Dubuisson, E.; Szunerits, S.; Bacia, M.; Pansu, R.; Ibanez, A. Fluorescent Molecular Nanocrystals Anchored in Sol-Gel Thin Films: A Label-Free Signalization Function for Biosensing Applications. *New J. Chem.* **2011**, *35* (11), 2416–2421.

(4) Philippot, C.; Dubois, F.; Bacia, M.; Djurado, E.; Ibanez, A. Fluorescent Organic Nanocrystal Confined in Sol-Gel Matrix for Bio-Imaging. *J. Sol-Gel Sci. Technol.* **2011**, *57* (3), 253–257.

(5) Philippot, C.; Dubois, F.; Maurin, M.; Boury, B.; Prat, A.; Ibanez, A. New Core–shell Hybrid Nanoparticles for Biophotonics: Fluorescent Organic Nanocrystals Confined in Organosilicate Spheres. *J. Mater. Chem.* **2012**, *22* (22), 11370.

(6) Debecker, D. P.; Le Bras, S.; Boissiere, C.; Chaumonnot, A.; Sanchez, C. Aerosol Processing: A Wind of Innovation in the Field of Advanced Heterogeneous Catalysts. *Chem. Soc. Rev.* **2018**, *47*, 4112–4155.

(7) Iskandar, F.; Lenggoro, I. W.; Xia, B.; Okuyama, K. Functional Nanostructured Silica Powders Derived from Colloidal Suspensions by Sol Spraying. *J. Nanoparticle Res.* **2001**, *3* (4), 263–270.

(8) Ishimori, T.; Senna, M. Control of Microstructure and Disintegration Properties of Silica Granules from PVA Slurries by Spray Drying. *J. Mater. Sci.* **1995**, *30* (2), 488–495.

(9) Maskara, A.; Smith, D. Agglomeration during the Drying of Fine Silica Powders, Part II: The Role of Particle Solubility. *J. Am. Ceram. Soc.* **1997**, 1715–1722.

(10) Baccile, N.; Grosso, D.; Sanchez, C. Aerosol Generated Mesoporous Silica Particles. *J. Mater. Chem.* **2003**, *13* (12), 3011.

(11) Julián-López, B.; Boissière, C.; Chanéac, C.; Grosso, D.; Vasseur, S.; Miraux, S.; Duguet, E.; Sanchez, C. Mesoporous Maghemite–organosilica Microspheres: A Promising Route towards Multifunctional Platforms for Smart Diagnosis and Therapy. *J. Mater. Chem.* **2007**, *17* (16), 1563–1569.

(12) Alonso, B.; Douy, a; Véron, E. Morphological and Textural Control of Spray-Dried Mesoporous Silica-Based Spheres. *J. Mater. Chem.* **2004**, No. 14, 2006–2016.

(13) Alonso, B.; Clinard, C.; Durand, D.; Véron, E.; Massiot, D. New Routes to Mesoporous Silica-Based Spheres with Functionalised Surfaces. *Chem. Commun.* **2005**, No. 13, 1746–1748.

(14) Philippot, C.; Bourdolle, A.; Maury, O.; Dubois, F.; Boury, B.; Brustlein, S.; Brasselet, S.; Andraud, C.; Ibanez, A. Doped Silica Nanoparticles Containing Two-Photon Luminescent Eu(Iii) Complexes for the Development of Water Stable Bio-Labels. *J. Mater. Chem.* **2011**, *21* (46), 18613.

(15) Bourdolle, A.; D'Aléo, A.; Philippot, C.; Baldeck, P. L.; Guyot, Y.; Dubois, F.; Ibanez, A.; Andraud, C.; Brasselet, S.; Maury, O. NIR-to-NIR Two-Photon Scanning Laser Microscopy Imaging of Single Nanoparticles Doped by Yb ^{III} Complexes. *ChemPhysChem* **2016**, *17* (1),

128–135.

(16) Philippot, C.; Zimmermann, J.; Dubois, F.; Bacia, M.; Boury, B.; Baldeck, P. L.; Brasselet, S.; Ibanez, A. Polymorphism of CMONS Nanocrystals Grown in Silicate Particles through a Spray-Drying Process. *Cryst. Growth Des.* **2013**, *13* (12), 5241–5248.

(17) Redon, S.; Eucat, G.; Ipuy, M.; Jeanneau, E.; Gautier-Luneau, I.; Ibanez, A.; Andraud, C.; Bretonnière, Y. Tuning the Solid-State Emission of Small Push-Pull Dipolar Dyes to the Far-Red through Variation of the Electron-Acceptor Group. *Dye. Pigment.* **2018**, *156*, 116–132.

(18) Kim, D.; Ryu, H. G.; Ahn, K. H. Recent Development of Two-Photon Fluorescent Probes for Bioimaging. *Org. Biomol. Chem.* **2014**, *12* (26), 4550–4566.

(19) Yao, S.; Belfield, K. D. Two-Photon Fluorescent Probes for Bioimaging. *European J. Org. Chem.* **2012**, No. 17, 3199–3217.

(20) Belfield, K. D.; Morales, A. R.; Kang, B.-S.; Hales, J. M.; Hagan, D. J.; Van Stryland, E. W.; Chapela, V. M.; Percino, J. Synthesis, Characterization, and Optical Properties of New Two-Photon-Absorbing Fluorene Derivatives. *Chem. Mater.* **2004**, *16* (23), 4634–4641.

(21) Belfield, K. D.; Morales, A. R.; Hales, J. M.; Hagan, D. J.; Van Stryland, E. W.; Chapela, V. M.; Percino, J. Linear and Two-Photon Photophysical Properties of a Series of Symmetrical Diphenylaminofluorenes. *Chem. Mater.* **2004**, *16* (11), 2267–2273.

(22) Terenziani, F.; Katan, C.; Badaeva, E.; Tretiak, S.; Blanchara-Desce, M. *Enhanced Two-Photon Absorption of Organic Chromophores: Theoretical and Experimental Assessments*; 2008; Vol. 20.

(23) Pawlicki, M.; Collins, H. A.; Denning, R. G.; Anderson, H. L. Two-Photon Absorption and the Design of Two-Photon Dyes. *Angew. Chemie - Int. Ed.* **2009**, *48* (18), 3244–3266.

(24) Xu, C.; Webb, W. W. Measurement of Two-Photon Excitation Cross Sections of Molecular Fluorophores with Data from 690 to 1050 Nm. *J. Opt. Soc. Am. B* **1996**, *13* (3), 481.

Chapter III- Colloidal NP suspensions for bioimaging

The ultimate goal of this project is the use of the core-shell NPs to realize deep tissue imaging of blood vasculature in mice using two-photon microscopy. To realize this, in addition to optimization of the synthesis parameters, it is crucial to also optimize parameters such as NP size and colloidal stability, in order to provide long circulation time in the bloodstream. Additionally, the NPs need to be furtive in order to avoid recognition and clearance by the reticulo-endothelial system (RES). This 'stealth' feature is often realized by grafting the NPs with moieties such as polyethylene glycol (PEG) (Figure 3.1).

This chapter deals with the preparation of stable colloidal NP suspensions after synthesis of the core-shell NPs. The colloidal stability of the NPs is investigated in different biological media, for potential applications in bioimaging. The determination of NP size and the study of the colloidal stability have been carried out primarily using Dynamic Light Scattering (DLS) (which is explained in detail in Appendix II) in collaboration with Aude Barbara (Institute Neel, Specialist in Correlation spectroscopy). Furthermore, functionalization strategies to improve the colloidal stability of the core-shell NPs and the challenges posed in optimization of the NP parameters for bioimaging are discussed in detail. The preliminary *in vivo* tests in mice using these bright nanotracers, in collaboration with Olivier Pascual (INSERM, Claude Bernard University) are also presented.

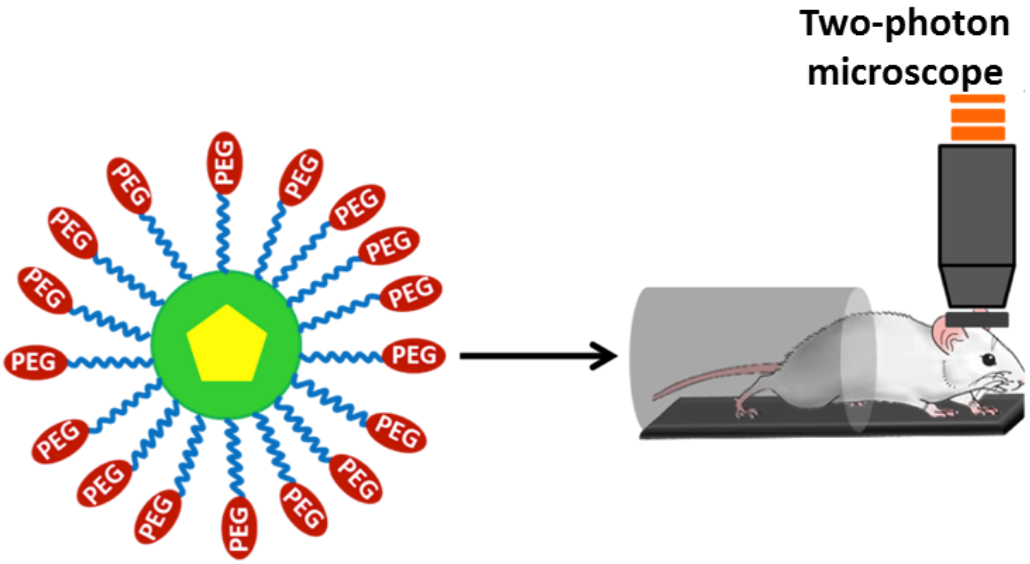

Figure 3. 1. Scheme illustrating the application of organic@silicate core-shell NPs functionalized with PEG in bio-imaging

3.1. Obtaining colloidal suspensions

The core-shell NPs obtained after synthesis using the spray-drying are chemically agglomerated. To prepare them for biological applications, it is important to first segregate them into independent NPs and remove aggregates that are bigger than the desired size range (< 250 nm). This is achieved by performing a controlled partial dissolution around the silicate shell. Following this dissolution, a short centrifugation is performed to get rid of the biggest aggregates followed by a filtration step using 5, 1.2 and 0.8 µm filters for size selection.

3.1.1. Controlled partial dissolution

When the NP suspensions are subjected to basic conditions (pH 12.0), the rate of Si-O-Si re-dissolution is high. The activation barrier for dissolution is lower in alkaline conditions due to the presence of OH^- nucleophiles as compared to acidic conditions.[1,2] Under these alkaline conditions, hydrolysis of Si–O–Si-bonds which is catalysed by nucleophilic attack by OH^- ions results in the dissolution of the silicate matrix (Eq 3.1.1) around the organic nanocrystal. The pH and duration of the basic etching were first chosen after dissolution studies on silicate thin films performed in the group and optimized for each type of NP.[3,4]

$$\mathbf{Si\text{-}O\text{-}Si + HO^-} \longrightarrow \mathbf{Si\text{-}OH + Si\text{-}O^-} \qquad \textit{(Eq. 3.1.1)}$$

The segregation of the agglomerated NPs into independent NPs is shown in Figure 3.2, with FESEM images of the NP suspensions at different time points during the controlled dissolution process.

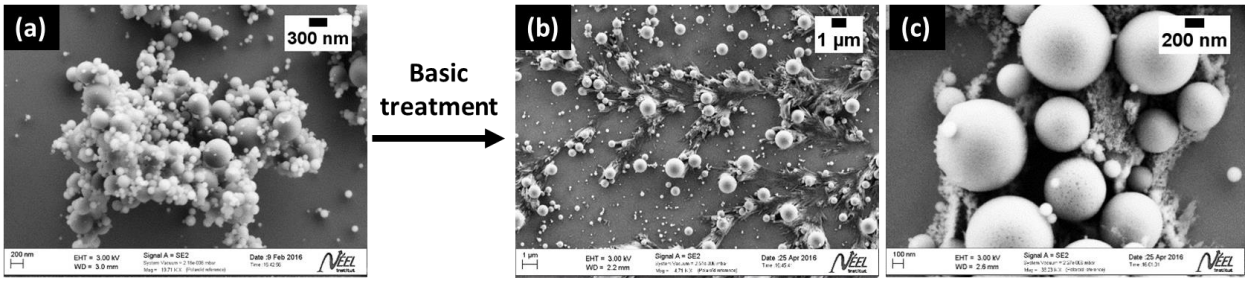

Figure 3. 2. FESEM image of (a) core-shell NPs (**NP-IV**) after synthesis, (b) NPs after basic treatment for 12 hours and (c) 24 hours

The evolution of the surface charge as a function of the pH, measured using zeta potential is shown in Figure 3.3a. and 3.3b. It can be seen that the surface charge is negative under basic conditions. This is because the suspension contains more anionic species when the pH is above the PZC (Point of Zero Charge), which results in the silicate species repelling each other. At acidic pH close to PZC we confirm that the zeta potential is close to 0. It is however important to note that the DLS average size also changes at this pH due to a partial aggregation favoured by a very

weak surface charge of NPs (no repulsive electrostatic charges, see the following section, Figure 3.4), which in turn influences the zeta potential.

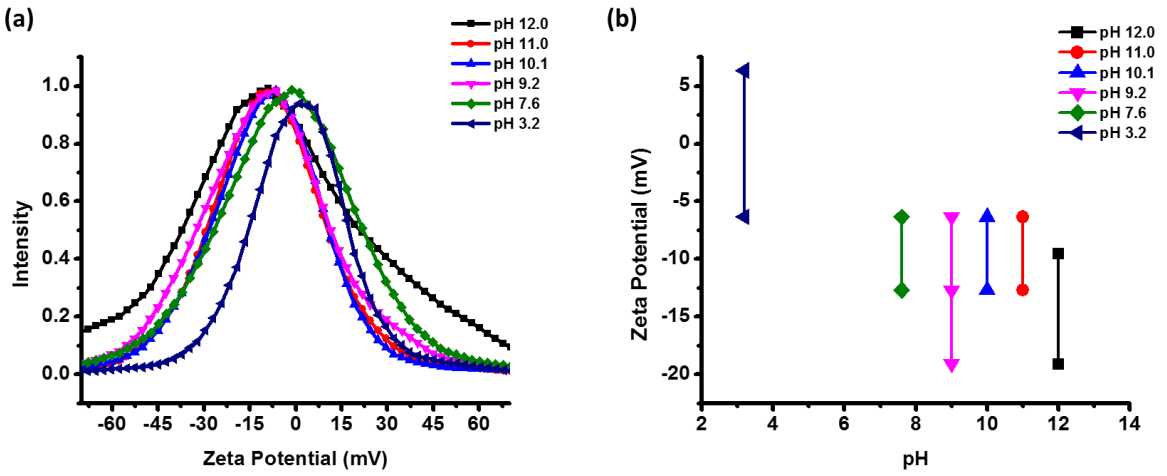

Figure 3. 3. (a) Measured zeta potential of the NP suspensions (**NP-IV**) at different pH, (b) Zeta potential as a function of pH

The size distribution of the treated NPs was also measured at different pH and is shown in Figure 3.4 It can be seen that the mean size moves from *ca* 200 nm to 250 nm (intensity distribution) as the pH drops to 3.2. This increase in size is due to the pH being close to PZC, which in turn leads to destabilisation and aggregation of the NPs, as introduced just above.

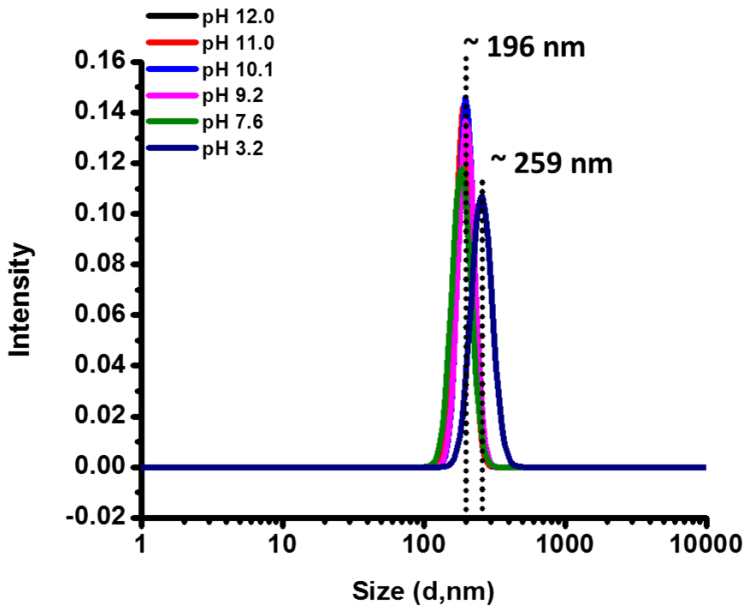

Figure 3. 4. Size distribution of the NP (**NP-IV**) suspensions (in intensity) at different pH

3.1.2. Optimization of the basic treatment parameters

While the control of NP size is a crucial parameter for biological applications, it is also important to obtain concentrated suspensions for bioimaging using two-photon microscopy. This requires precise control of the basic treatment. The following section presents the evaluation of the different strategies employed.

3.1.2.1. Strategy A

In this first strategy, the NP suspensions were subjected to basic conditions for 24 hours for controlled partial dissolution around the silicate shell, followed by neutralisation to pH 7.4, to be in physiologically relevant conditions. This was then followed by filtration of the NPs using 5, 1.2 and 0.8 µm filters to remove aggregates and NPs bigger than 500 nm. However, a significant loss of the NPs was observed in the filters, resulting in a low final optical density. Although a size distribution centred at less than 300 nm was observed using DLS, the final optical density is too low to realize bioimaging. Although concentration strategies could be further applied to improve the optical density, the major loss of NPs in the filters is a major drawback, due to the retention of small NPs in the filter pores. A possible explanation for this loss of NPs in the pores of the filter is that filtration after neutralization results in the loss of charge stabilisation that is observed at highly basic conditions, which could potentially result in the aggregation of NPs. These aggregates in turn block the pores of the filters, thereby retaining the smaller NPs in the suspensions, which ultimately results in reduced concentration of the final NP suspensions obtained.

3.1.2.2. Strategy B

In this strategy, the NP suspensions were filtered using 5, 1.2 and 0.8 µm filters, after controlled dissolution for 24 hours but before pH neutralization. The idea was to minimize losses in the filters by performing the filtration under basic conditions. The presence of anionic silicate species under these conditions result in better stabilisation of the NPs by means of charge repulsion and was therefore expected to reduce the loss of NPs in the pores of the filters. This was investigated by analysing the filters used for treatment, from which the size range of the NPs trapped in the filters was determined, as shown in Figure 3.5. While the fraction of NPs trapped in the filters is the highest for the bigger NPs (> 500 nm), a significant fraction of smaller NPs (< 200 nm) were found to be trapped in the 0.8 µm filters. This could be attributed to the presence of some big aggregates that block the pores of the filters retaining the smaller NPs.

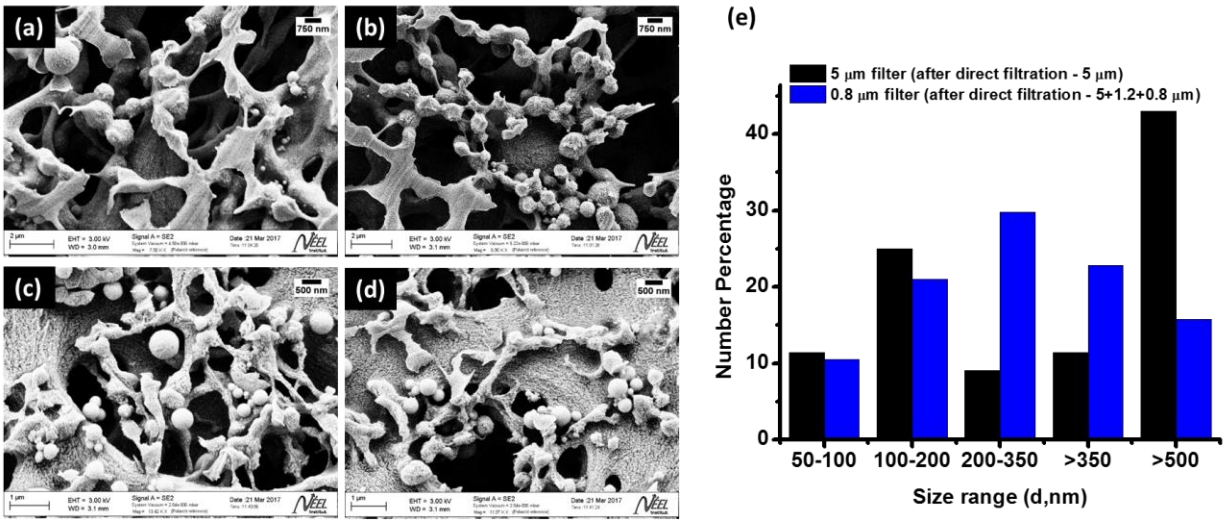

Figure 3. 5. FESEM images of 5 µm filters (a-b), 0.8 µm filter (c-d) and (e) histogram corresponding to the size range of the NPs (**NP-IV**) trapped in the filter pores, after treatment using strategy B.

3.1.2.3. Strategy C

This strategy is similar to Strategy B with the only difference being that an additional centrifugation step was adopted in order to avoid the important losses of NPs in the filters. A short centrifugation for 5 minutes at 5000 rpm was performed after the controlled dissolution of NPs for 24 hours in order to get rid of the biggest aggregates and NPs, which could be collected as a pellet at the end of the centrifugation process. The supernatant was then filtered using 5, 1.2 and 0.8 µm filters followed by neutralization to pH 7.4. The idea was to evaluate the efficacy of the centrifugation step in removing the biggest aggregates, while also testing the reduced loss of NPs in the filters due to charge stabilisation under basic conditions.

The filters used were further analysed in order to estimate the size range of the NPs trapped in the filters, which is shown in Figure 3.6. It can be seen that the highest fraction of NPs trapped in filters are NPs bigger than 500 nm, especially in the 0.8 µm filter. Although there is still a loss of small NPs (< 200 nm) in all three filters, it is significantly lower than the fraction of larger NPs and also when compared to strategy B.

This overall reduced loss of NPs in the filter pores as compared to strategies A and B could possibly be attributed to the filtration and size selection steps being carried out while the NPs are still under basic conditions, which results in better stabilisation by charge repulsion due to the presence of anionic silicate species under these conditions. This in turn validates the use of the centrifugation step to remove the aggregates and reduce the loss of smaller NPs in the filters.

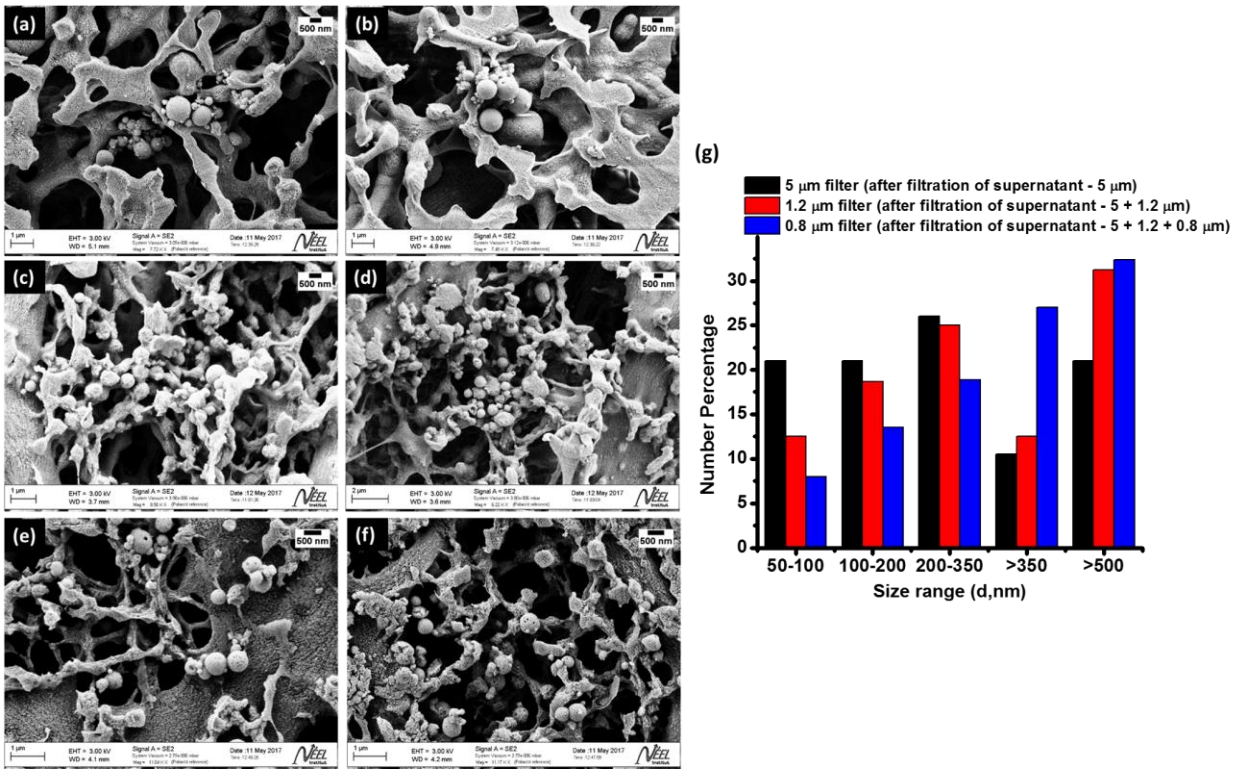

Figure 3. 6. FESEM images of 5 µm filters (a-b), 1.2 µm filter (c-d) and 0.8 µm filter (e-f) and (g) histogram corresponding to the size range of the NPs (**NP-IV**) trapped in the filter pores, after treatment using strategy C.

Furthermore, the size distribution of the NPs obtained after treatment was evaluated for both strategies B and C and is shown in Figure 3.7. It is evident that the mean size is smaller in the case of Strategy C, centred at around 120 nm, while the size is centred around 220 nm in the case of Strategy B, with the initial size distribution centred around 400 nm.

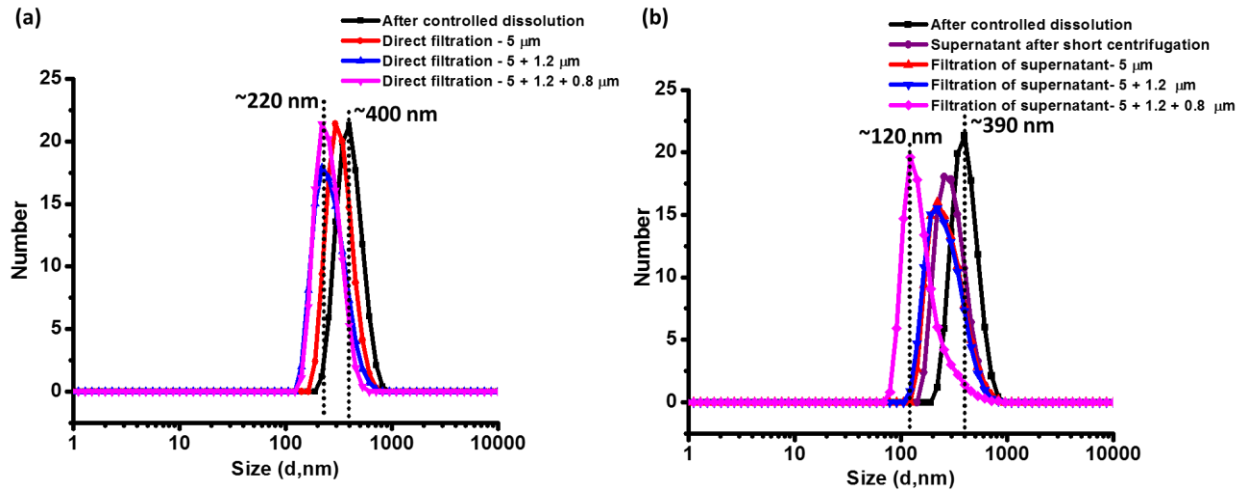

Figure 3. 7. Size distribution of the NPs (**NP-IV**) at each step of treatment for (a) Strategy B and (b) Strategy C

The effect on the concentration of the NPs was also evaluated for both strategies by monitoring the absorbance of the NPs after each step, shown in Figure 3.8. A higher optical density (*ca* 0.35) is obtained in the case of Strategy B, which could be attributed to a higher fraction of bigger NPs in the suspension as compared to Strategy C which shows a low optical density of ~ 0.15. It is important to note than the optical densities recorded in both strategies are too low to realize optical imaging, which typically requires highly concentrated samples with optical densities above 1. Overall, strategy C was evaluated to be better than Strategy B due to the lower sizes obtained.

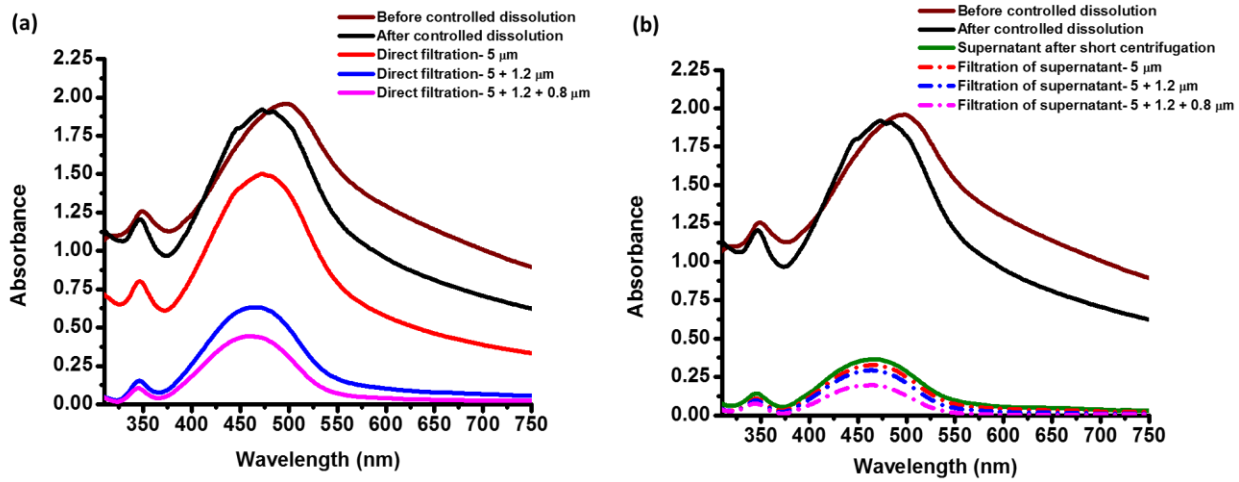

Figure 3. 8. Absorbance of the NPs (**NP-IV**) at each step of treatment for (a) Strategy B and (b) Strategy C

3.1.2.4. Strategy D

A final strategy was evaluated wherein the NP suspension under basic conditions was kept undisturbed in a tube for 24 hours. The size distributions of the NP suspension in the top part of the tube and the residue collected at the bottom are shown in Figure 3.9.

It is clear that the major fraction of NPs collected in the residue corresponds to the biggest aggregates (> 500 nm), with a minimal fraction of smaller NPs. The top part of the NP suspension contains a broad distribution as is evident from the highest contribution of the NP fraction being in the range > 500 nm, which can be reduced using filters.

Although this strategy is comparable to Strategy C, in terms of the reduced loss of smaller NPs after treatment, there is little control over the size selection. This was confirmed by recording the size distribution of the NPs that sediment at the bottom, which was significantly different when recorded at different time points, with a higher fraction of smaller NPs collected after 36 and 48 hours of basic treatment.

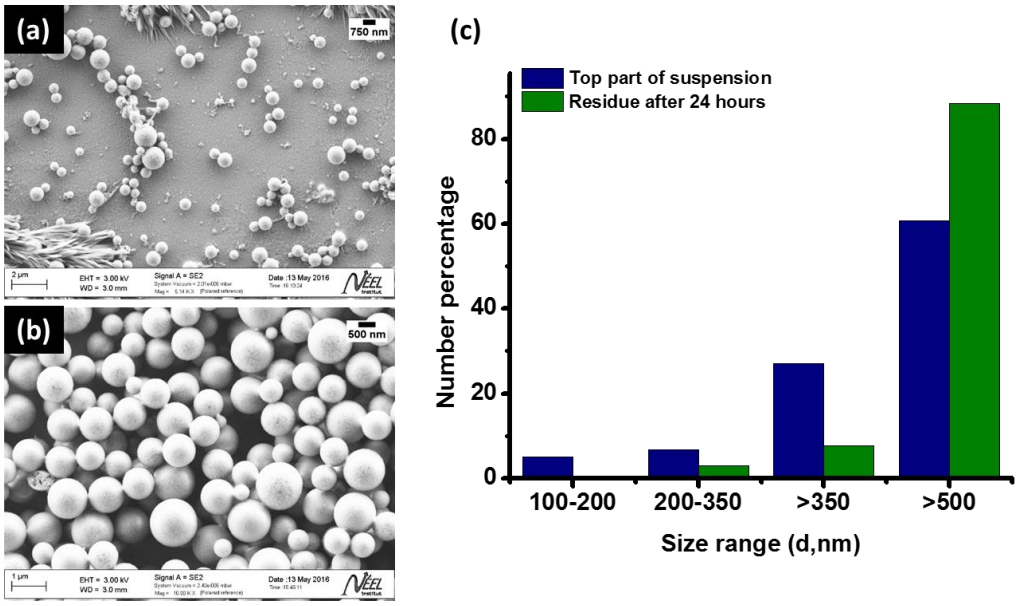

Figure 3. 9. FESEM images of the NPs (**NP-IV**) from the (a) top part of the tube, (b) bottom residue and (c) Histogram corresponding to the size range of the NPs using Strategy D

After evaluating these four strategies, Strategy C was chosen as the treatment protocol for the core-shell NPs.

3.1.2.5. Duration of basic treatment

The layer-by-layer etching of silicate shell is slow with an etching rate of approximately 1 nm/hour at pH 12. Therefore, it is important to optimize the duration of this basic dissolution process. This in turn depends on the initial size distributions obtained after spray-drying. The varied size result from the use of different 's' ([solvent]/[Si]) for synthesis, where higher values of 's' result in smaller sizes due to the production of more dilute droplets containing less silicate and dye species during atomization, with the opposite effect at lower 's'. Therefore, a duration of 24 hours was chosen for s= 500, while 48 hours was chosen for s = 380, for the controlled dissolution process.

3.1.2.6. pH neutralization and influence of buffers

After basic treatment of the NP suspensions, it is important to neutralize the suspensions to pH 7.4 to stop the dissolution process and enable further treatment (section 3.2). This neutralization is done by dropwise addition of 1 M HCl. However, it is important to use buffers to stabilise and maintain the pH at this neutral value.

Several buffers were evaluated and tested, such as Phosphate Buffer Saline (1x PBS), tris-HCl buffer and phosphate buffer (0.133 M). While all three buffers provided immediate stability, aggregation of the NPs was the fastest in the case of PBS, possibly due to the presence of high

amounts of salt in PBS, which results in the screening of charges thereby facilitating NP aggregation.

On the other hand, 1M tris-HCl provided good stability for over a week after which aggregation was observed. The pKa value of Tris is 8.06 at 25°C which implies a relatively low buffer capacity in the actual physiological pH range.[5] Tris is also temperature-sensitive and concentration dependent. Moreover, Tris is toxic for many mammalian cells as it penetrates cells due to its relatively good fat solubility.[5]

The use of phosphate buffer resulted in good stability in water for several weeks. This could be attributed to the pKa value of 7.20, with better buffering capacity in the pH range between 5.8 and 8.0. Moreover, the concentration of the buffer is close to that of PBS in terms of the phosphate content, but without the presence of the saline component.

3.1.3. Colloidal stability in physiological conditions

While the NPs are stable in water, biological media contain a significant percentage of salt, which has an impact on the colloidal stability of the NPs. The salt content results in screening of charges, promoting aggregation of the NPs as is shown in Figure 3.10. It is evident that the NPs aggregate in 0.9 %wt NaCl solution, resulting in a shift of mean size from an initial size of 150 nm in water to 400 nm in salt solution. Furthermore, temperature can have an influence on the colloidal stability. Often at the physiological temperature of 37 °C (indicated by the dotted lines in Figure 3.10), aggregation is promoted due to increased Brownian motion of the NPs. This shows the need for functionalization of the NPs in order to prevent aggregation due to the destabilisation of the NPs in physiological conditions.

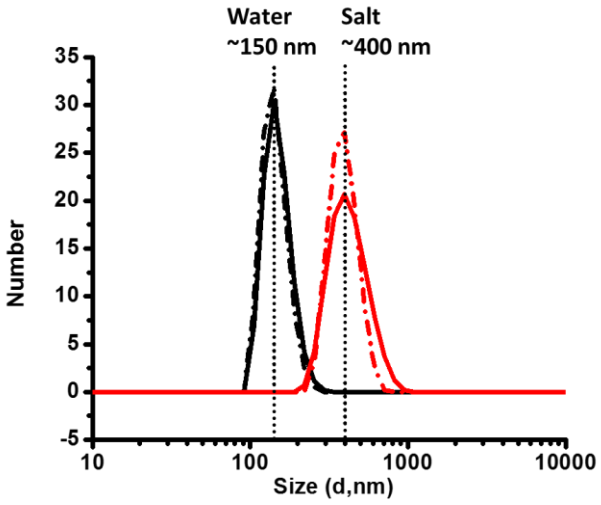

Figure 3. 10. Size distribution of NPs (**NP-IV**) in water (black) and 0.9 %wt salt solution (red) measured at 25 °C (solid line) and 37 °C (dotted line), pH 7.4

3.2. Functionalization of core-shell NPs

The silicate crust of the core-shell NPs enables further functionalisation. The introduction of the functional group can either be done prior to or after the synthesis of the core-shell NPs as shown in Figure 3.11. Post synthesis introduction of functional groups also called 'grafting' involves the reaction of the surface of the silicate shell with the functional group bearing organosilane to form covalent Si-O-Si linkages between the two. However, this reaction is usually carried out in organic solvents such as toluene or ethanol at reflux, conditions that cannot be used in the present study due to the presence of the soluble organic core.

On the other hand, direct synthesis or 'co-condensation' involves the reaction of the silicate precursors with the functional group bearing organosilane prior to spray-drying. The co-condensation strategy offers a significant advantage over the grafting strategy as it results in a random distribution of the functional groups linked to the silicate molecules. In the case of 'clickable' functional groups introduced by co-condensation, a 'click-grafting' reaction can be performed in water on the obtained NPs to provide the desired functionalities.

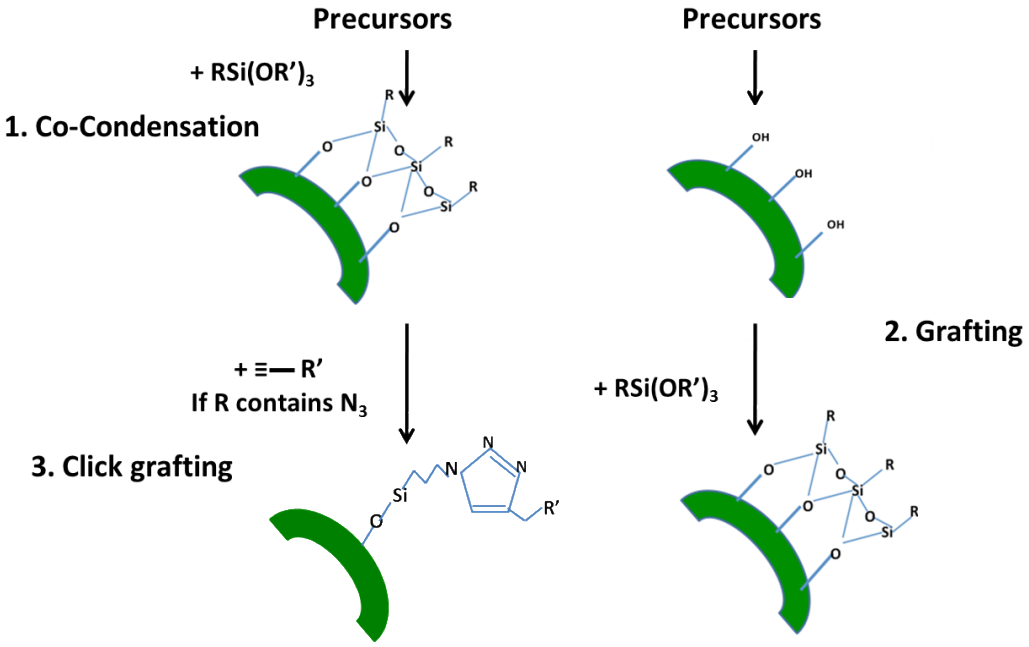

Figure 3. 11. Strategies for introduction of functional groups on the NPs

Core-shell NPs can be functionalised with different moieties such as ligands specific to overexpressed receptors at the target site, drug molecules and antibodies. In the case of core-shell NPs for vascular imaging, functionalisation of the outer surface with PEG (Polyethylene glycol) results in enhanced colloidal stability due to steric stabilisation thereby leading to lesser

agglomeration. Also, PEG renders the core-shell NPs furtive and hence increases their circulation time in the blood as it decreases the interactions of NPs with proteins such as opsonins, thereby decreasing recognition and removal of these NPs by the reticulo-endothelial system. For vascular imaging of tumors, a circulation time of at least a few hours is desired for accurate imaging and diagnosis, which could be achieved following functionalization of the NPs with PEG. The extent of stabilisation depends on several parameters such as the length and structure (linear or branched) of PEG (Figure 3.12).

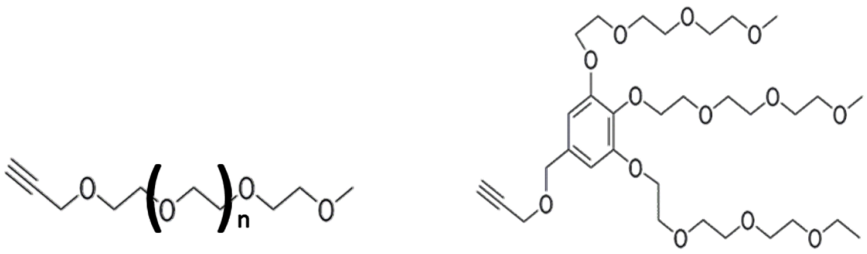

Linear PEG-short (M_n: 500), medium (M_n : 2000) and long (M_n :5000) chain

Ramified PEG

Figure 3. 12. Different forms of PEG

3.2.1. CuAAC functionalization

CuAAC functionalization was used to 'click'/graft alkyne-modified PEG (linear/branched) onto the core-shell NPs containing the azide functionality. CuAAC was chosen as the functionalization strategy due to ease of manipulation and the ability to work in aqueous environments that is essential to preserve the integrity of the organic core of the NPs. Typically, the number of moles of azide in the NPs is estimated and used to determine the ratios of the other reactants required for the reaction. Typically, for a 60 mL NP suspension, 5-10 equivalents of alkynylated PEG is taken along with one equivalent of $CuSO_4.5H_2O$, which serves as a pre-catalyst, four equivalents of sodium ascorbate which serves as a reducing agent to reduce Cu(II) to Cu(I) and one equivalent of a ligand, THPTA, which not only complexes with Cu(I) but also acts a promotor. The CuAAC reaction is carried out overnight at room temperature under continuous stirring. The alkynyl ethers (alkyne-modified PEG) react with the azide group on the NPs to form a 1,2,3-triazole linkage (Figure 3.13).

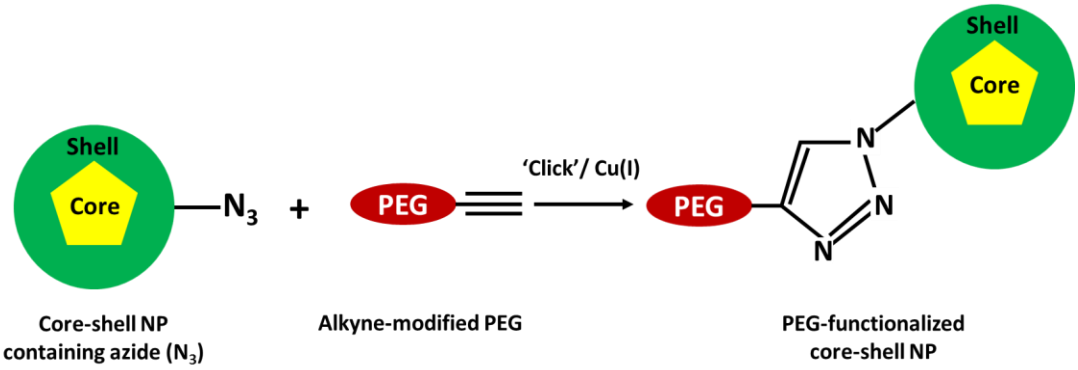

Figure 3. 13. Scheme illustrating CuAAC 'click' functionalization of the core-shell NPs

Infrared spectroscopy

Another advantage of using CuAAC for the functionalization of the core-shell NPs is that the click reaction can be easily monitored using infrared spectroscopy by the decrease of the azide band intensity. The functionalised NPs were centrifuged to collect the biggest particles, dried and analysed using IR spectroscopy.

The normalized IR spectra of **NP-IV** before and after functionalization with linear short-chain PEG (SCPEG) is shown in Figure 3.14. The band at 1100 cm^{-1} corresponds to the siloxane groups (Si-O-Si). The bands between 1350 cm^{-1} and 1480 cm^{-1} correspond to the C-C bonds of the TMSE. The bands between 1670 cm^{-1} and 1820 cm^{-1} correspond to the carbonyl group (C=O) of the dye **IV**. The band at 2100 cm^{-1} corresponds to the azide (N=N=N, stretch) functionality. This azide band intensity is stronger in **NP-IV** prior to functionalisation as is evident from the black curve in Figure 3.14. There is also an appearance of bands corresponding to the C-H stretch (symmetrical and antisymmetrical) of the CH_2 groups, from TMSE and short-chain PEG between 2800-2900 cm^{-1}. The bands between 3000 cm^{-1} and 3700 cm^{-1} correspond to the OH groups (stretch, free/H-bonded). The conversion efficiency obtained by integrating the azide and siloxane bands before and after functionalization was 37% ± 10%.

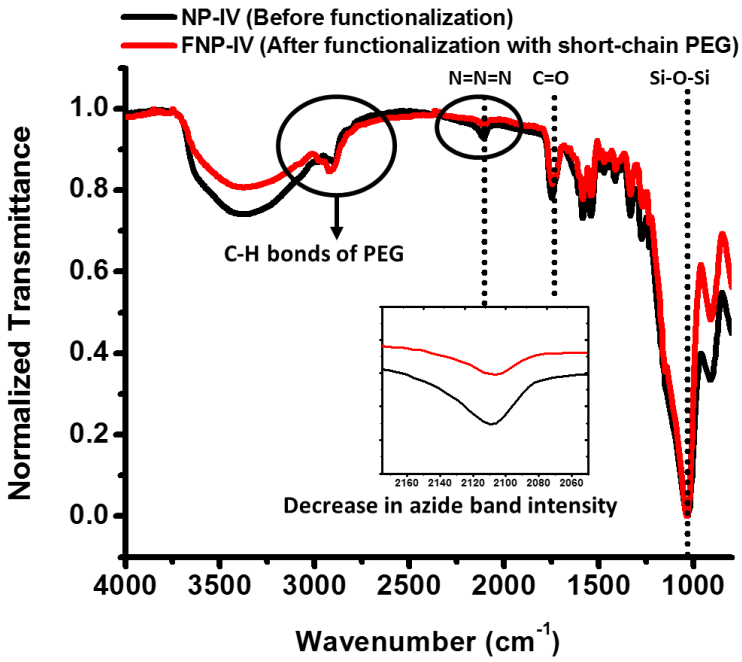

Figure 3. 14. IR spectrum of **NP-IV** before and after functionalization with short-chain linear PEG

The normalized IR spectra of **NP-I** before and after functionalisation with long chain linear PEG (LCPEG) is shown in Figure 3.15. This spectrum also shows similar characteristics to Figure 3.14. The band at 1052 cm^{-1} corresponds to the siloxane groups (Si-O-Si) while the band at 1573 cm^{-1} corresponds to the C=C bonds in dye I in both curves. The azide band intensity is stronger in **NP-I** prior to functionalisation as is evident from the black curve, while it is hardly distinguishable in the functionalized **NP-I** due to the click reaction between the alkynyl ether (long chain linear PEG) and the azide group, as is evident from the red curve. There is also an appearance of bands corresponding to the C-H bonds of the long chain linear PEG between 2800-2900 cm^{-1}. Due to the poor quality of the spectrum, it was difficult to calculate the conversion efficiency.

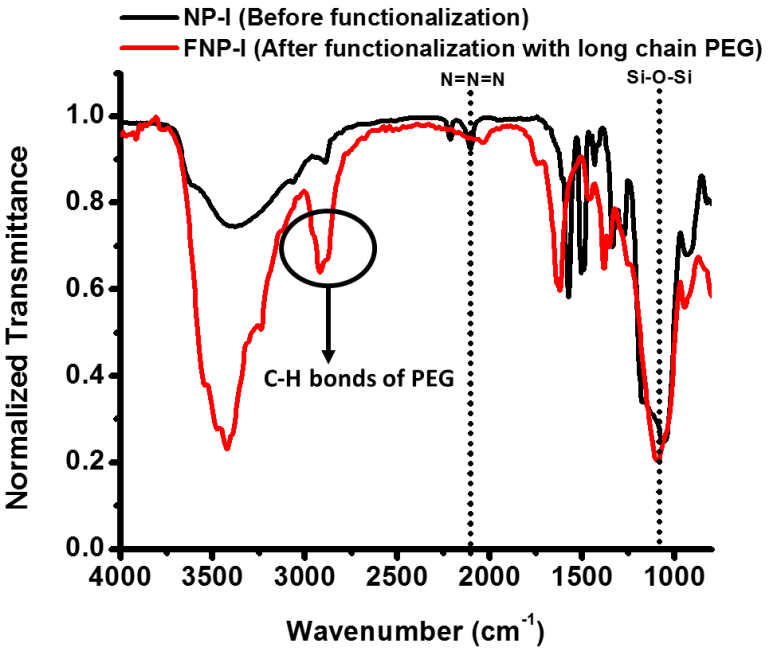

Figure 3. 15. IR spectrum of **NP-I** before and after functionalization with long-chain linear PEG (M_n =5000)

The non-total conversion of the azide groups in both cases is due to the presence of azide groups both on the outer part of the silicate shell as well as within the dense silicate matrix due to the co-condensation strategy used for the introduction of the azide groups on the core-shell NPs. While the azide groups present on the outside are highly reactive due to ease of accessibility by the PEG molecules, the ones within the matrix cannot be accessed easily due to insufficient porosity of the NPs thereby leading to low reactivity.

3.2.2. Impact of click functionalization on core-shell NP properties

The NPs were functionalized with different forms of PEG- ramified, short, medium and long chain linear PEG. Colloidal stability in simulated physiological conditions was only obtained with long chain linear PEG (LCPEG; M_n = 5000). Furthermore, partial aggregation was observed either during or after the click functionalization process in the case of short and medium chain linear PEG and ramified PEG. This was due to a drop in pH of the NP suspensions from 7.4 to pH 3-4. This acidic pH is close to the isoelectric point of silicate NPs, resulting in NP aggregation. Therefore, the reactants used for functionalization and the click reaction conditions were thought to contribute to the destabilisation of the NPs. This was further investigated by studying the effect of different combinations of the reactants on the pH, stability and optical properties of the NPs. Six different conditions were studied, (i) NPs (in water) before functionalization, (ii) NPs + sodium ascorbate (reducing agent) + THPTA (ligand used as promotor) + $CuSO_4$ (pre-

catalyst) + PEG, (iii) NPs + sodium ascorbate + THPTA + $CuSO_4$ ('Click' without PEG), (iv) NPs + sodium ascorbate + $CuSO_4$, (v) NPs + sodium ascorbate and (vi) NPs + $CuSO_4$. All the reactions were performed at room temperature under continuous stirring for 24 hours with Ar bubbling at the beginning of the reaction to remove any traces of oxygen, to maintain uniformity.

For cases (iv)- (vi), no significant drops in pH were observed, except in the case of **NP-I** where case (iv) resulted in a relatively higher drop in pH (pH 7.6 to 6.8) as compared to **NP-IV** (pH 7.7 to 7.4) under the same conditions. The suspensions looked clear in all three cases, with no visible aggregation, although a discoloration was observed for case (v). Although, no significant drop in pH was recorded for case (ii), an aggregation was observed, implying that the combination and concentration of the reactants required for functionalization induced destabilisation of the NPs. This could be a potential explanation for the aggregation of NPs when functionalized with short and medium chain linear PEG and ramified PEG, in combination with their insufficient steric stabilisation strength. On the other hand, the same combination and concentration of reactants with long chain linear PEG resulted in a slight increase in pH and yielded clear suspensions with no aggregation, thereby confirming the steric stabilisation efficacy of LCPEG.

Furthermore, the absorbance of each suspension was recorded as shown in Figure 3.16a (for **NP-I**) and 3.16b (for **NP-IV**). The click medium without PEG (case (iii)) resulted in a strong precipitation of the NPs, as was also confirmed by the absorbance spectra for both **NP-I** and **NP-IV**. This clearly shows the need for a significantly long chain PEG in order to overcome these precipitation-inducing conditions. Interestingly, a blue shift was observed in the case of **NP-IV** after functionalization with LCPEG, possibly due to the covalent grafting of the PEG on the NP which has an effect on the local polarity of the silicate shell. Furthermore, it also serves as a good complexing agent for salts through the easily available oxygen atoms.

Table 3. 1. Evaluation of different conditions to study the effect of CuAAC on NP stability

Case	pH of NP-I	pH of NP-IV
(i) Before functionalization	7.6	7.7
(ii) NPs + sodium ascorbate + THPTA + $CuSO_4.5H_2O$ + PEG ('Click' with PEG)	7.8	8.1
(iii) NPs + sodium ascorbate + THPTA + $CuSO_4.5H_2O$ ('Click' without PEG)	7.2	7.5
(iv) NPs + sodium ascorbate + $CuSO_4.5H_2O$	6.9	7.4
(v) NPs + sodium ascorbate	7.5	7.7
(vi) NPs + $CuSO_4.5H_2O$	7.4	7.6

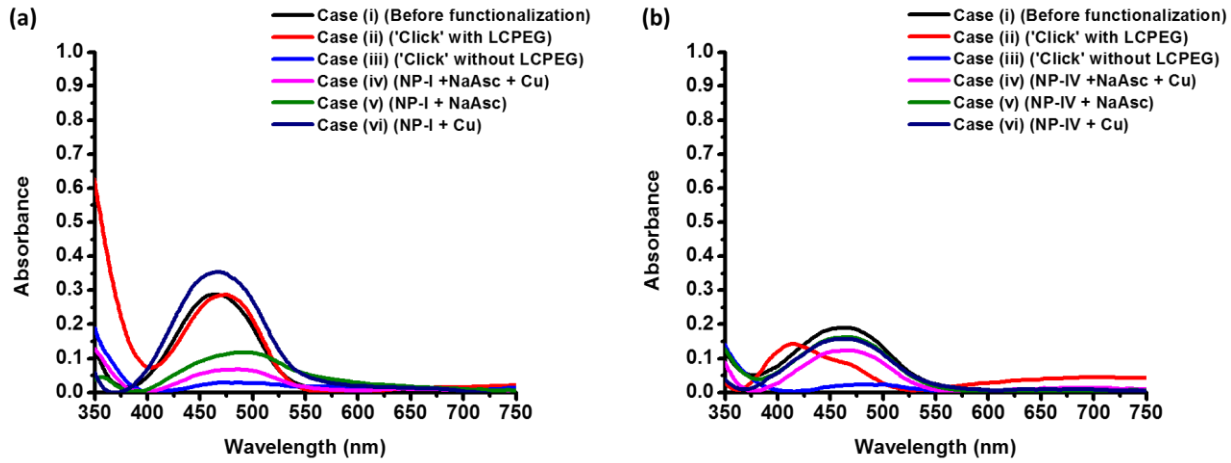

Figure 3. 16. Absorbance of (a) **NP-I** suspensions and (b) **NP-IV** suspensions under different conditions

Moreover, the fluorescence spectra of each suspension corresponding to the different cases were also recorded as shown in Figure 3.17a (for **NP-I**) and 3.17b (for **NP-IV**). It is noteworthy that the NP suspensions before and after functionalisation exhibited good results, with comparable brightness after functionalisation, suggesting that no quenching occurred in the presence of copper salts. This was also physically confirmed by illumination of the functionalized NP suspensions under a UV lamp (λ_{exc} =365 nm), which showed fluorescence. A blue shift similar to that observed in the absorbance spectra, was observed in the case of **NP-IV** functionalized with LCPEG (**FNP-IV**) resulting in a shift of fluorescence emission from 580 nm to 550 nm, while no such shift was observed in the case of LCPEG functionalized **NP-I** (**FNP-I**).

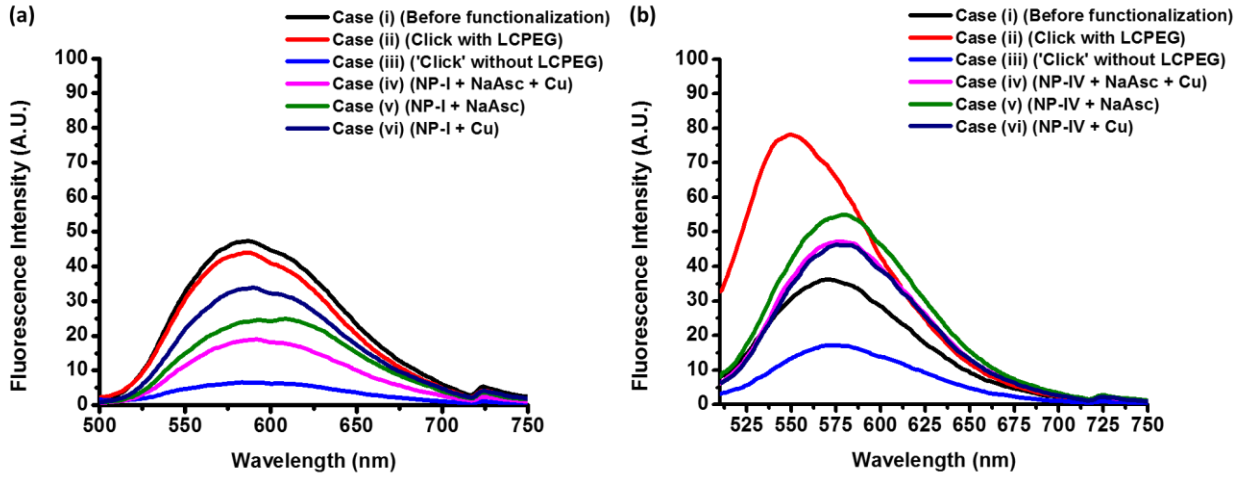

Figure 3. 17. Fluorescence of (a) **NP-I** suspensions and (b) **NP-IV** suspensions under different conditions

3.2.3. Purifying and concentrating NP suspensions

After NP functionalization, it is important to remove unreacted components and also get rid of cytotoxic elements such as copper salts, that are used as catalyst for click functionalization. This purification which is crucial for further *in vivo* applications to avoid aggregation or agglomeration can be achieved by dialysis.[6] However, this purification step results in dilution of the NP suspensions and hence necessitates a subsequent concentration step.

3.2.3.1. Dialysis

Dialysis is a classic separation technique that relies on selective diffusion of molecules across a semi-permeable membrane from a volume of higher concentration to lower concentration, based on different rates of diffusion of the molecules. Dialysis is carried out by placing the sample and a buffer solution (also called dialysate) on opposite sides of a dialysis membrane of a certain pore-size. Molecules in the sample that are smaller than the pore size pass through the membrane, while objects bigger than the pore size are retained in the sample. The driving force is the osmotic pressure that tends to equilibrate the concentrations of each species on both sides. Dialysis of the functionalized NP suspensions is done against diluted phosphate buffer (0.0133 M) using 3.5 kDa MWCO (molecular weight cut-off) regenerated cellulose membrane dialysis tubes. MWCO is defined as the lowest molecular weight solute at which greater than 90% of the solute is retained by the membrane. For example, a dialysis membrane with a 10 kDa MWCO will generally retain entities having a molecular mass of at least 10 kDa. Dialysis of a small volume of functionalized NPs (10 mL) against a large volume of 0.0133 M PB (2.5 L) for two days, allowed the removal of the unreacted and unwanted components in the NP suspensions.

3.2.3.2. Ultrafiltration

As explained earlier, NP suspensions used for bioimaging are quite concentrated, while the core-shell NPs obtained after basic treatment, functionalization and dialysis show a rather low optical density that is insufficient to realize imaging. Therefore, after dialysis of the functionalized NPs, concentration strategies were used to improve the optical density of the NP suspensions. Harsh strategies such as direct water evaporation were avoided in order to preserve the colloidal stability. Therefore, centrifugation filtration was employed using 100 kDa MWCO PES (Polyethersulfone) membranes. Polyethersulfone (PES) membrane is a hydrophilic membrane that aids in fast filtration with superior flow rates and high throughputs. This ultrafiltration was performed at a low speed of 3000 rpm for 3 minutes in batches of 2 mL. Successive filtrations yielded significant increase in optical densities of the NP suspensions as shown in Figure 3.18.

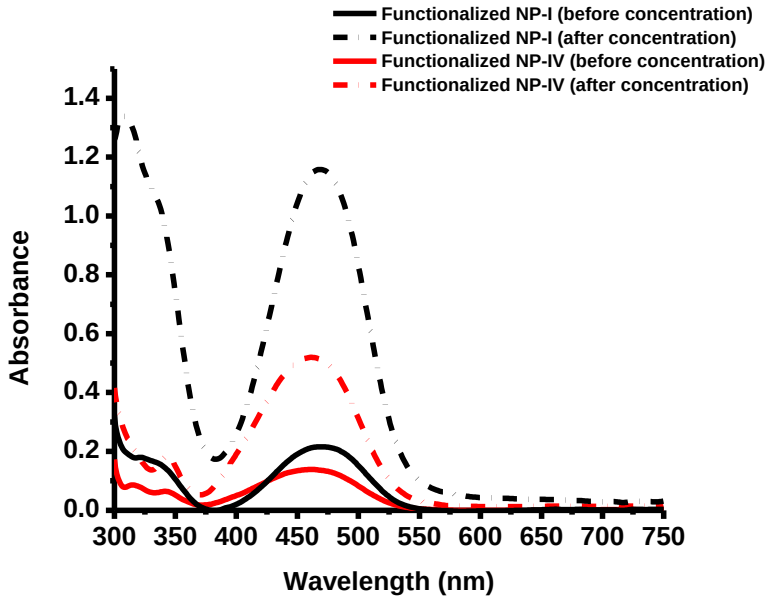

Figure 3. 18. Absorbance of functionalized **NP-I** (black) and **NP-IV** (red) before (solid) and after (dotted) concentration.

3.2.4. Colloidal stability of NPs in physiological conditions

The size distribution of **FNP-I** and **FNP-IV** (functionalized with long-chain linear PEG), in water and 0.9 %wt salt solution (obtained by adding 10 %vol of a 9 %wt salt solution to the starting suspension) each tested at 25 °C and 37 °C is shown in Figure 3.19. It is evident that the functionalized NPs are thermally stable in physiological conditions with a mean size lower than 200 nm in all cases for both **FNP-I** and **FNP-IV**.

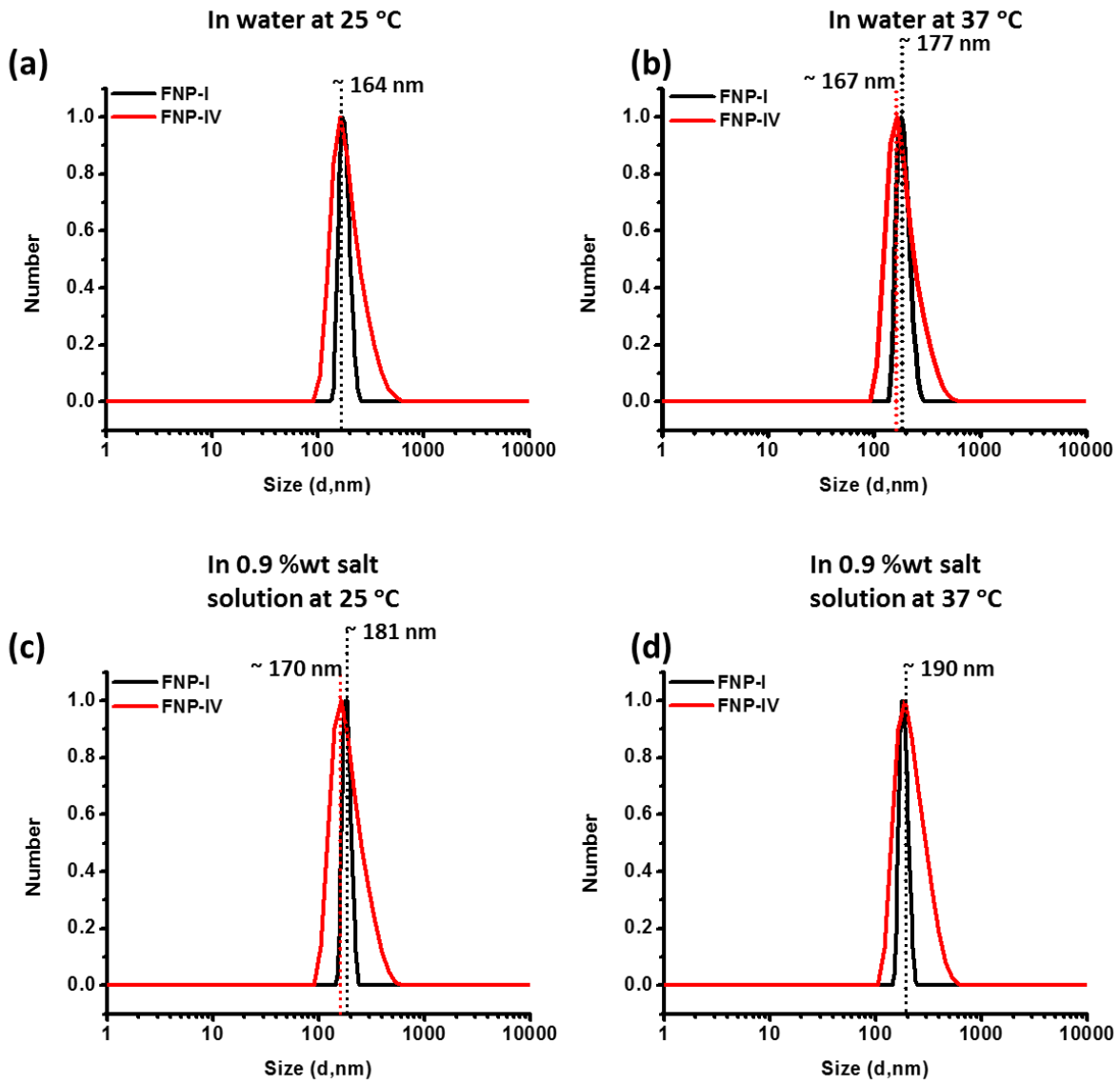

Figure 3. 19. Size distribution of LCPEG-functionalized **NP-I** (Black) and **NP-IV** (red) in (a) water at 25 °C, (b) in water at 37 °C, (iii) in 0.9 %wt salt solution at 25 °C and (iv) in 0.9 %wt salt solution at 37 °C.

The colloidal stability of these functionalized NPs was further confirmed by monitoring the absorbance of the functionalized NPs after concentration, in 0.9 %wt salt solution over a period of 15 hours to study the possible aggregation of the NPs in these physiological conditions, as shown in Figure 3.20. It can be clearly seen than there is no drop in absorbance in both cases, confirming colloidal stability in physiological conditions. There was a small decrease in absorbance (less than 5%) for **NP-IV** as can be observed from Figure 3.20. These fluctuations in signal could be attributed to instrument parameters like stabilization of the photomultiplier tube (detector) and also the UV lamp intensity. Overall, the drop in absorbance is very low (less than 5%), which is highly promising, as it indicates that the colloidal NP suspensions are stable in physiologically relevant conditions, even after concentration.

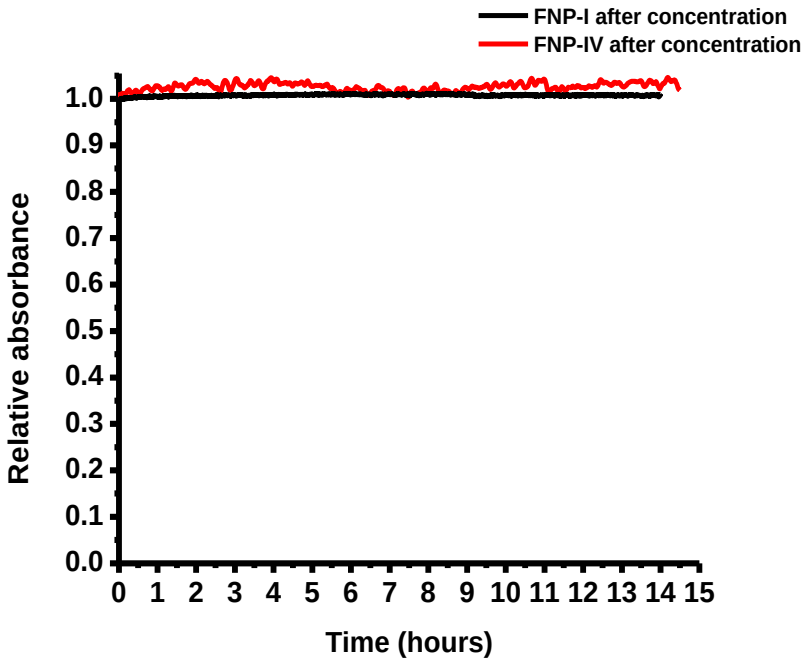

Figure 3. 20. Relative absorbance of **FNP-I** (black; OD =1.1) and **FNP-IV** (red; OD = 0.7) after concentration, in 0.9 %wt salt solution for 15 hours recorded at λ= 470 nm and λ = 480 nm respectively.

3.2.4.1. Simulated Body Fluid (SBF)

Simulated Body Fluid (SBF) is an acellular medium with ion concentrations approximately equal to those of human blood plasma as shown in Table 3.2.[7,8] In this study, SBF has been used to mimic the physiological conditions to investigate how the different ion concentrations impact the colloidal stability of the functionalized NPs.

Table 3. 2. Comparison between blood plasma and simulated body fluid (SBF)

	Na^+	K^+	Mg^{2+}	Ca^{2+}	Cl^-	HCO_3^-	HPO_4^{2-}	SO_4^{2-}
Blood plasma	142.0	3.6-5.5	1.0	2.1-2.6	95.0-107.0	27.0	0.65-1.45	1.0
1x SBF	142.0	6.5	1.5	2.5	148.0	4.2	1.0	0

The LCPEG-functionalized NPs after concentration were tested in SBF (1x) and their size distribution was measured using DLS 15 minutes after incubation. In the case of **FNP-I**, a size distribution close to 180 nm (in number) and 190 nm (in intensity) in SBF at both 25 °C and 37 °C as can be seen from Figure 3.21a and 3.21b respectively.

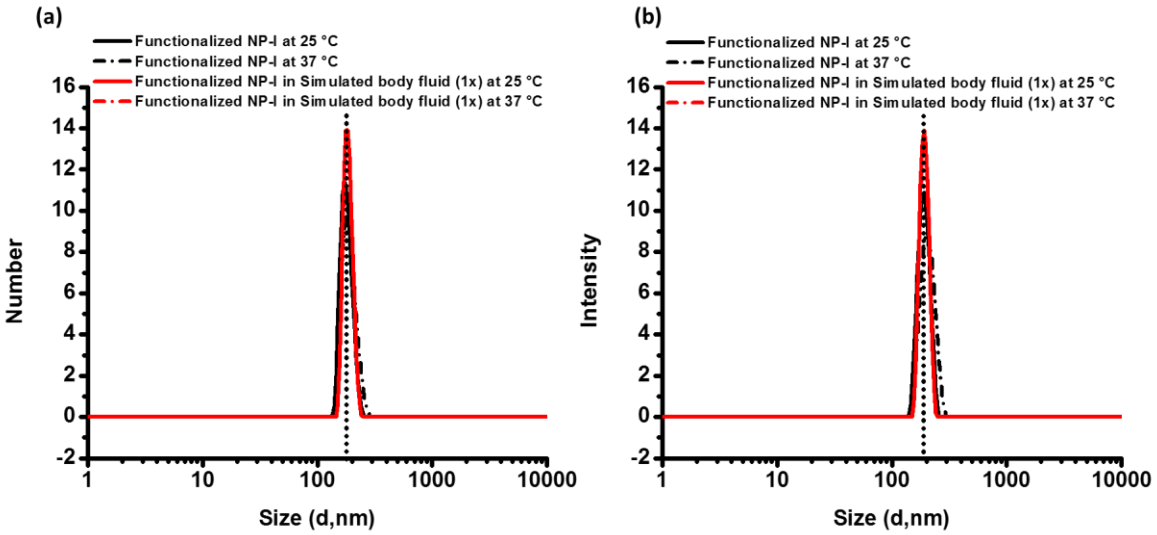

Figure 3. 21. (a) Number and (b) Intensity distribution of **FNP-I** in water (black) and SBF (red) at 25 °C (solid) and 37 °C (dotted).

On the other hand, a slightly higher mean size of 190 nm (in number) and 220 nm (in intensity) was measured for **FNP-IV** under the same conditions as can be seen from Figure 3.22a and 3.22b respectively. This could be attributed to the difference in synthesis parameters and dissolution conditions used for **NP-IV** and **NP-I**. It is interesting to note that the synthesis parameters used for **NP-IV** corresponded to s = 500 as opposed to s = 380 for **NP-I**, which should have theoretically yielded smaller NPs in the case of **NP-IV**. But the basic treatment was performed for 48 hours for **NP-I** as opposed to 24 hours for **NP-IV**, which in turn could be responsible for this difference in final size distribution after functionalization.

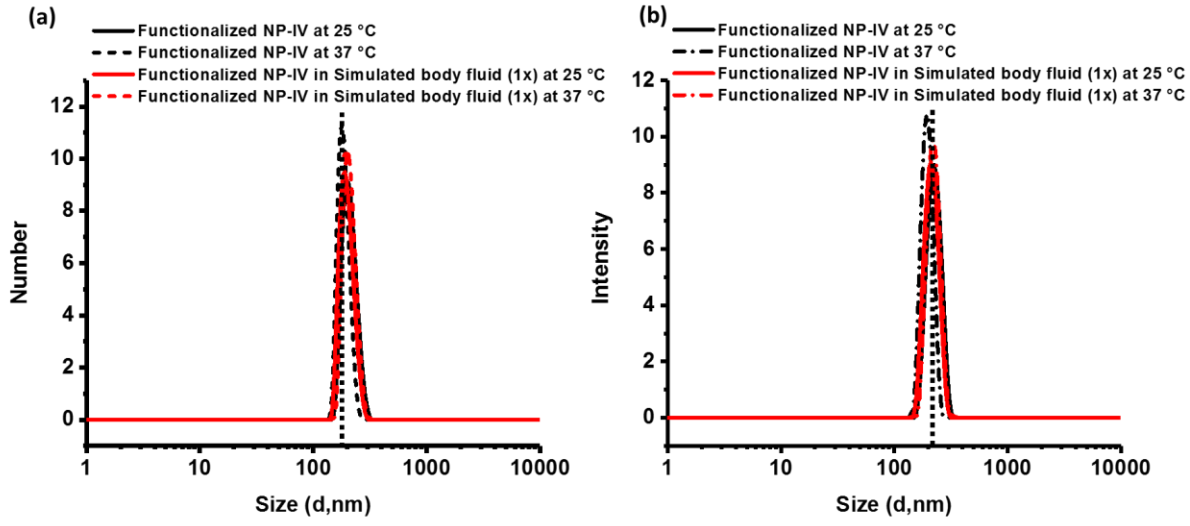

Figure 3. 22. (a) Number and (b) Intensity distribution of **FNP-IV** in water (black) and SBF (red) at 25 °C (solid) and 37 °C (dotted).

3.2.4.2. Plasma Proteins

As described earlier, blood is composed of various components, of which plasma proteins constitute a major fraction. While serum albumin constitutes 55% of the total amount of blood plasma proteins, globulins constitute 38 % with the remaining 7% constituted by fibrinogen. Each of these proteins have a different function, with serum albumin mainly responsible for maintaining the plasma osmotic pressure, globulins for transporting ions, hormones and lipids necessary for immune action and fibrinogen which plays the main role in blood clotting. Therefore, it is important to study the effect of these concentrations of plasma proteins on the colloidal stability of the NPs. A step-by-step evaluation was preferred to clearly understand the effect of each protein, summarised in Table 3.3, on the stability of the functionalized NPs.

The first protein that was investigated was bovine serum albumin. It is noteworthy that Bovine (BSA) and human (HSA) serum albumins are similar in structure (Figure 3.23) with approximately 76% sequence homology and a repeating pattern of disulfides which are strictly conserved.[9,10] Their molecular weights are also close, 66267 g mol−1 for BSA and 66439 for HSA. The only major difference between the two proteins is that BSA has two tryptophan residues (W134 and W212) while HSA has only one (W214).[11]

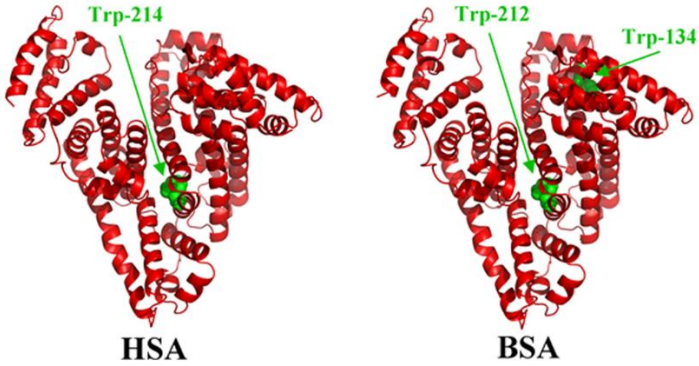

Figure 3. 23. Three-dimensional structures of HSA and BSA

Table 3. 3. Properties of the different proteins

Protein	Number of amino acid residues	Molecular weight	Isoelectric point in water at 25 °C	Stokes Radius (r_s)
BSA	583	66.5 kDa	4.7	3.5 nm [12]
γ-Globulin	1250[13]	155-160 kDa [14]	7.6	5.3 nm[15]

The colloidal stability of the functionalized NPs in the presence of Bovine Serum Albumin (BSA) was tested at 37 °C using DLS. The concentration of albumin in the body is 35 - 50 mg/mL.

Therefore, the effect of BSA at different concentrations was tested on LCPEG functionalized **NP-I** (**FNP-I**) and **NP-IV** (**FNP-IV**).

In the case of **FNP-I**, at low concentrations of BSA, 6-30 mg/mL, no aggregation was observed. It is important to note that the contribution from the NPs is no longer visible in the number distribution (Figure 3.24a) when the concentration of BSA exceeds 15 mg/mL. The observed peaks at 8 nm recorded at higher concentrations of BSA correspond to the size of the protein. On the other hand, in the intensity distribution (Figure 3.24b), the NP contribution is clearly seen in all cases due to the higher contribution of higher sizes to the signal. It is important to note that the primary size distribution obtained using DLS is a plot of the relative intensity of light scattered by particles of different sizes, which is further used to generate the number distribution. Therefore, it can be seen from the intensity distribution that there is a slight aggregation of **FNP-I** at the highest concentration of BSA (60 mg/mL) resulting in a size increase from 220 nm to ~ 260 nm. It is important to note that this concentration is higher than the upper limit of the normal albumin concentration in the body, showing the stability of the functionalized NPs in nominal conditions.

The inconsistencies between the number and intensity distributions often arise from poor fitting of the autocorrelation data and hence need to be treated with caution. The autocorrelation data generated by the DLS is indeed the measured data which is fitted by different algorithms to generate a size distribution. Plotting the autocorrelation data in log-log scale allows to observe the evolution of the autocorrelation function and also indicates the emergence of the different contributions to the signal and their relative intensities.

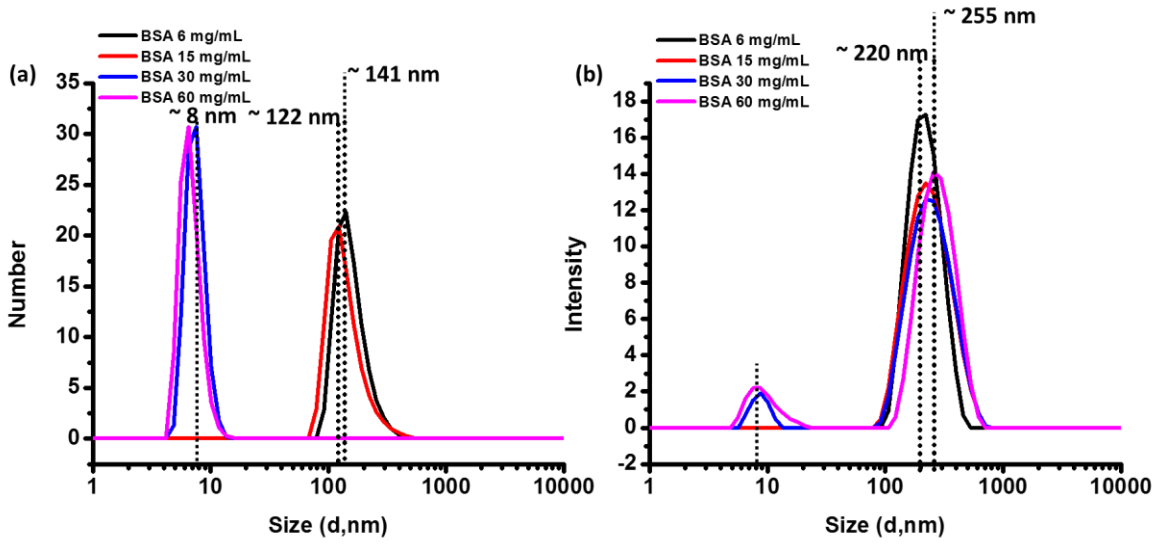

Figure 3. 24. (a) Number and (b) Intensity distribution of **FNP-I** in SBF at 37 °C with different concentrations of BSA.

The inconsistencies between the number and intensity distributions were investigated by plotting the autocorrelation data as shown in Figure 3.25. It can be seen that there is a slight aggregation observed for all cases, although this is more pronounced for the highest concentration of BSA. However, this increase in τ corresponds to a relatively small contribution to the intensity signal, thereby indicating colloidal stability of the NPs in the presence of BSA.

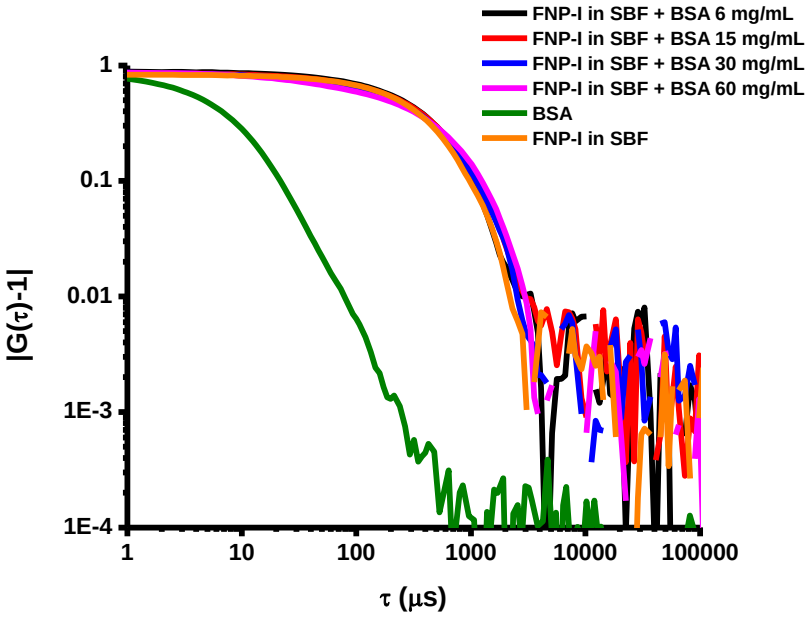

Figure 3. 25. Autocorrelation data corresponding to **FNP-I** in SBF with varying concentrations of BSA at 37 °C.

FNP-IV on the other hand, yielded size distribution fits that were incoherent, showing no conformity to real data. This typically is an effect of poor fitting of the autocorrelation data using the Cumulants Analysis. These incongruities in fitting autocorrelation data normally arise from the assumption of a Gaussian distribution around a specific size ($z_{average}$) in the Cumulants Analysis method. This is turn results in a final size corresponding to an average of the different populations detected, often resulting in illogical data. Additionally, the angle at which scattered light is collected contributes to the data analysis, resulting in a variation of fit.

Therefore, the colloidal stability of **FNP-IV** in the presence of BSA was directly investigated using the autocorrelation data presented in Figure 3.26. Using the autocorrelation data, the contribution of BSA and the initial NPs in SBF can be clearly seen, corresponding to a τ of ~ 5 and 200 μs respectively. It can be seen that there is no major change in size towards larger distributions upon addition of BSA to the NPs. The contribution at high τ values observed at concentrations of 30 and 60 mg/mL of BSA corresponds to less than 1 % of an increase in the intensity signal. It is important to keep in mind that the intensity contribution is proportional to d^6 and is therefore strongly impacted by the presence of aggregates. Therefore, it is acceptable to conclude that the functionalized NPs are stable in the presence of BSA, with only a slight

aggregation at the highest concentration of BSA (60 mg/mL), which exceeds the upper limit of the nominal concentration in blood.

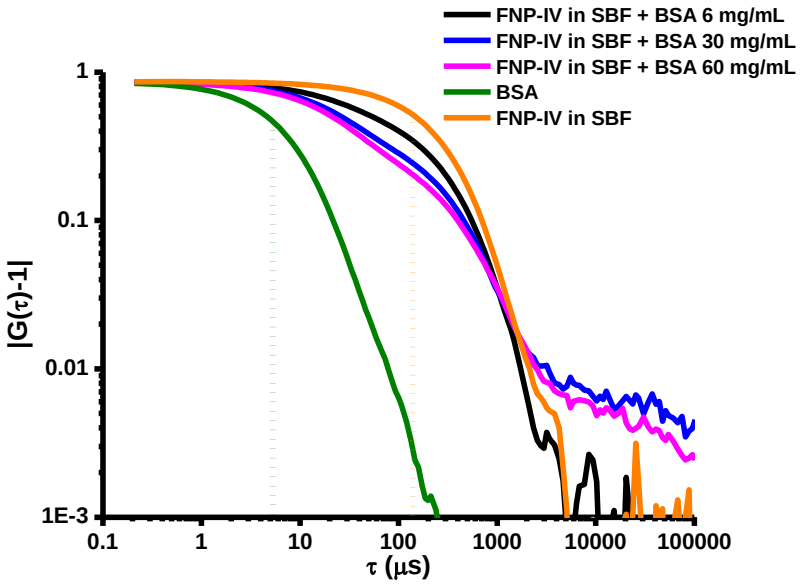

Figure 3. 26. Autocorrelation data corresponding to **FNP-IV** in SBF at 37 °C with different concentrations of BSA.

Next, the effect of the second most abundant protein in the blood plasma, γ-globulin, was investigated. Globulins are a family of globular proteins that are heavier than serum albumin protein, as can be seen from its properties in Table 3.3. The typical concentration of globulins in blood is 24-46 mg/mL. There are different types of globulins such as α1, α2, β and γ–globulins. An interesting point to note is that a subclass of the γ–globulins are the immunoglobulins, also known as antibodies, which constitute the immune system. This makes the use of γ-globulins to test the colloidal stability of the functionalized NPs particularly relevant.

In the case of **FNP-I**, at low concentrations of γ-globulin (10 mg/mL), no aggregation was observed. It is important to note that the contribution from the NPs is not visible in the number distribution (Figure 3.27a) even at the lowest concentration of γ-globulin. The observed peak at 10 –12 nm clearly corresponds to the size of the γ-globulin. On the other hand, in the intensity distribution (Figure 3.27b), the NP contribution is clearly seen in all cases due to the higher contribution of the larger size to the signal. It can be seen from the intensity distribution that the NPs are quite stable at the different concentrations of γ-globulins (10-45 mg/mL), with a size distribution peaking at less than 200 nm. The peaks corresponding to the γ-globulins are also visible in the intensity distribution at 14 nm.

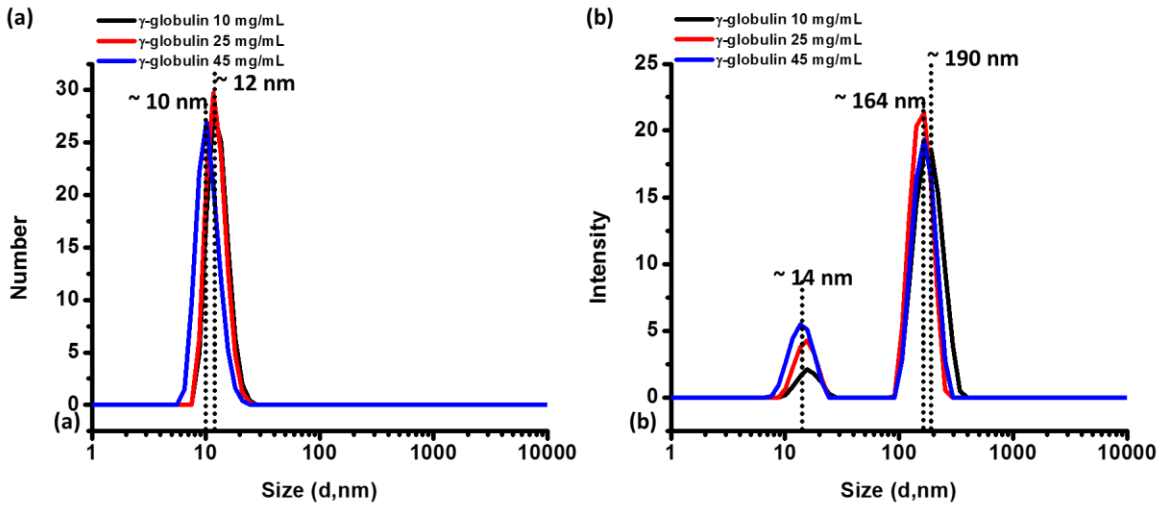

Figure 3. 27. (a) Number and (b) Intensity distribution of **FNP-I** in SBF at 37 °C with different concentrations of γ-globulin.

This can be confirmed using the autocorrelation curves shown in Figure 3.28. It can be seen that there is a slight aggregation observed for the highest concentration of γ-globulin (45 mg/mL). However, this increase in τ does not make a significant contribution to the intensity signal, thereby indicating colloidal stability of the **FNP-I** in the presence of γ-globulin.

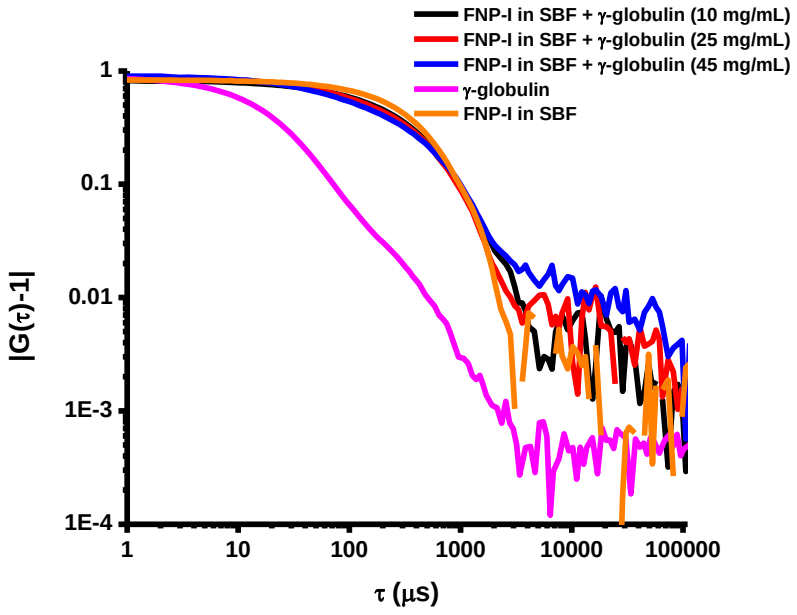

Figure 3. 28. Autocorrelation data corresponding to **FNP-I** in SBF at 37 °C with different concentrations of γ-globulin.

In the case of **FNP-IV**, the number and intensity distributions showed poor fitting of the autocorrelation data resulting in inconsistent data. But investigation of the autocorrelation data corresponding to increasing concentrations of γ-globulin revealed colloidal stability of the NPs

(Figure 3.29). Using the correlation curves, the contributions corresponding to the γ-globulin and the starting NPs could be clearly differentiated corresponding to a τ of ~ 10 and 200 μs respectively. Furthermore, addition of increasing concentrations of γ-globulin resulted in a less than 1% increase in intensity signal. Although a slight contribution of aggregates is observed for the highest concentration of γ-globulin (45 mg/mL), the overall contribution to the increase in intensity is very small, indicating stability of the NPs.

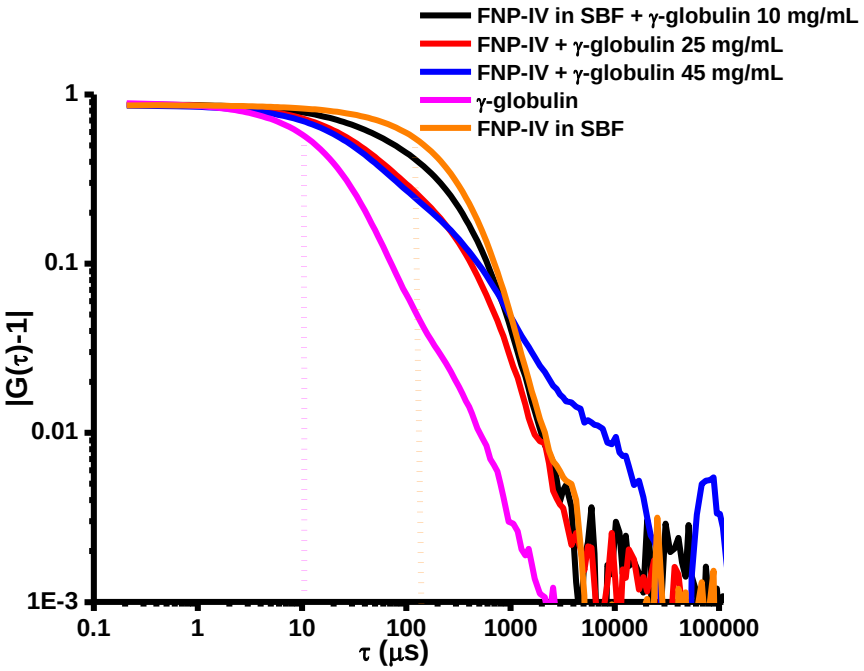

Figure 3. 29. Autocorrelation data corresponding to **FNP-IV** in SBF at 37 ºC with different concentrations of γ-globulin.

After investigating the effect of the major proteins in the blood plasma, the effect of glucose on the NP stability was studied. Glucose is another major component of blood and while the blood glucose level is individual-dependent, it typically ranges between 0.7-1.0 mg/mL. The colloidal stability of the functionalized NPs was tested at the highest concentration of blood glucose, 1.0

mg/mL. While **FNP-1** yielded a size close to 190 nm at both 25 °C and 37 °C (Figure 3.30a), **FNP-IV** resulted in a size close to ~ 205 nm at 37 °C (Figure 3.30b).

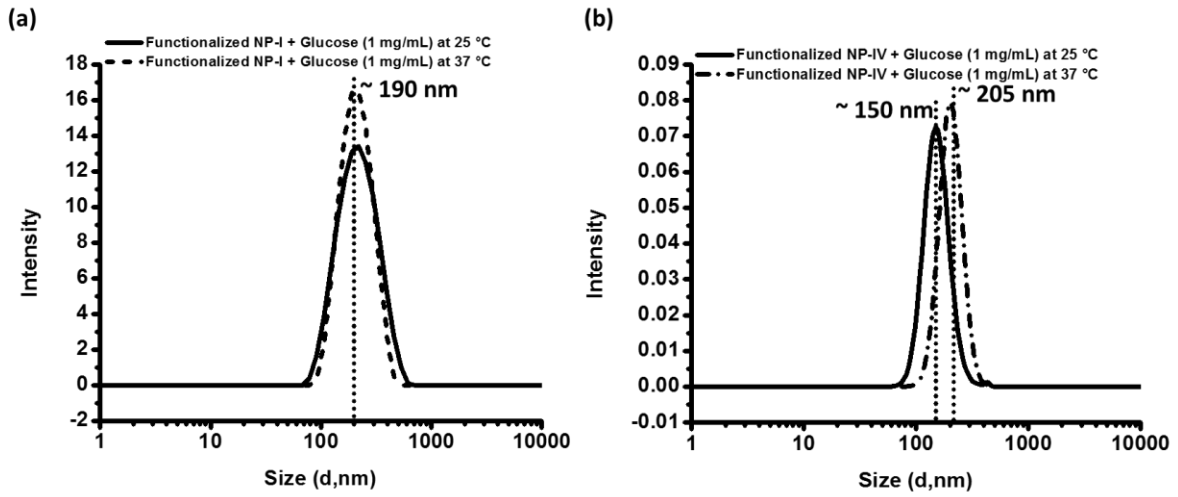

Figure 3. 30. Intensity distribution of (a) **FNP-I** + Glucose (1 mg/mL) and (b) **FNP-IV** + Glucose (1 mg/mL) at 25 (solid line) and 37 °C (dotted line)

Finally, the colloidal stability of the functionalized NPs was investigated in an environment composed of a combination of individually tested elements at their highest concentrations. **FNP-I** showed good colloidal stability as is evident from the autocorrelation data presented in Figure 3.31. Although the autocorrelation data revealed a small shift in τ, it can be seen that there is a small aggregation of **FNP-I** only at the highest concentration of γ-globulin (45 mg/mL) as was shown earlier in Figure 3.28. Moreover, the autocorrelation curve corresponding to the combination of the different proteins looks very similar to the case corresponding to **FNP-I** in γ-globulin. This indicates a slight aggregation or the presence of a contaminant in the suspension that is responsible for this small shift. Overall, this is promising, as **FNP-I** do not aggregate under these drastic conditions corroborated by the fact that there is no major shift in size to larger distributions and is comparable to their starting size after functionalization (~180-200 nm).

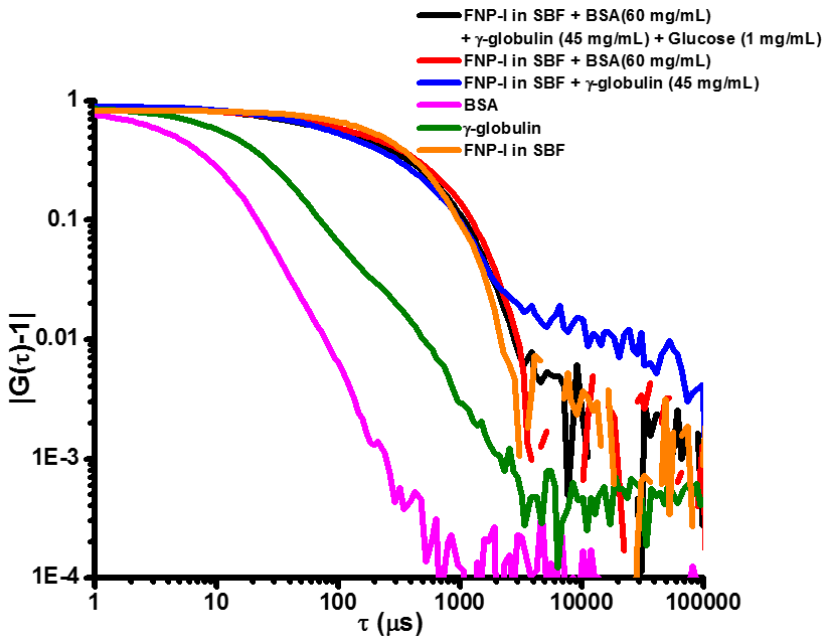

Figure 3. 31. Autocorrelation data corresponding to **FNP-I** in SBF + BSA (60 mg/mL) + γ-globulin (45 mg/mL) + Glucose (1 mg/mL) at 37 °C

On the other hand, for **FNP-IV**, the correlation curves indicated a small increase in size for the case corresponding to BSA (30 mg/mL), globulin (25 mg/mL) and glucose (1 mg/mL) (Figure 3.32), as shown by the presence of two values of τ corresponding to 10 and 600 μs.

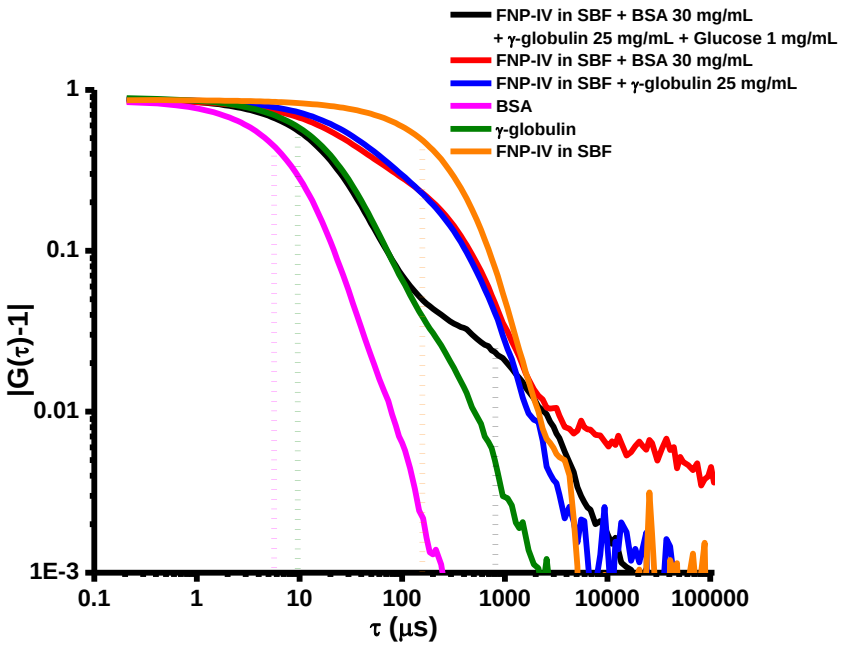

Figure 3. 32. Autocorrelation data corresponding to **FNP-IV** in SBF at 37 °C + BSA (30 mg/mL) + γ-globulin (25 mg/mL) + Glucose (1 mg/mL) at 37 °C

Although this indicates a slight aggregation and can be fitted by taking into account the different τ values so obtained, the overall increase in intensity signal is still acceptable.

However, the correlation curves indicated a significant aggregation of **FNP-IV** for the case corresponding to BSA (60 mg/mL), globulin (45 mg/mL) and glucose (1 mg/mL). This yielded a contribution at $\tau = \sim 10^6$ µs. Such a high value of τ is indicative of either very big aggregates or the presence of dust or other contaminants. Interestingly, Pade Laplace fitting of the data yielded two populations, one at 17 nm, which correspond to the proteins and the other at around 800 nm corresponding to the aggregates respectively.

Therefore, the colloidal stability of both **FNP-I** and **FNP-IV** was confirmed in physiological conditions and in the presence of proteins. Minimal aggregation was observed in the presence of the highest concentrations of BSA and globulin individually, resulting in around 1% increase in intensity signal at higher τ values as observed in the autocorrelation data. When both proteins are mixed above the usual blood concentrations, the aggregation is however significant. These results suggest that the performance of these functionalized NPs can be tested *in vivo*, without risk of aggregation as for the *in vivo* tests the NPs will be strongly diluted in blood.

Overall, the colloidal stability of **FNP-I**, was relatively better than **FNP-IV**, in physiologically relevant conditions and was therefore chosen for the preliminary *in vivo* tests.

3.3. In vivo tests

The colloidal stability of the functionalized NPs (particularly **FNP-I**) in different biological media under physiologically relevant conditions, resulted in their investigation *in vivo* in mice. For this study, CX3CR1-GFP mice, expressing GFP only in microglia in the brain were used. Thinned-skull cortical window preparation over the somatosensory cortex was performed, for transcranial imaging where the skull was reduced to a thickness of 20-30 µm. Imaging was performed using a two-photon microscope with a Ti:Sapphire laser with an excitation wavelength of 940 nm. Images were acquired every 0.9 seconds over an area of 200x200 µm and a resolution of 521x521 pixels.

In a first study, 200 µL of **FNP-I** (38 µg/mL NPs corresponding to 15 µg/mL dye), with OD = 1.1, *ca* 180 nm ϕ) was introduced into the mouse through retro-orbital injection. Imaging was performed approximately 5 minutes after injection. Although bright particles were observed in the bloodstream, the fluorescence intensity recorded was quite low. These bright particles disappeared quickly within a time span of 10-15 minutes but the fluorescence was still faintly visible in the blood flow. A 10% drop in fluorescence signal was observed for a 400 second imaging window. Thirty minutes post-injection, fluorescence was still visible in the blood vessels, but was much weaker, indicating rapid clearance of the NPs from the bloodstream.

In a second test, on another CX3CR1-GFP mouse, the level of an eventual noise in the blood vessels was recorded prior to injection of the NPs. This level of noise was undetectable. 200 µL of **FNP-I** was injected into the mouse. However, imaging was performed within 30 seconds post injection.

In this case, the fluorescence recorded was much higher as shown in Figure 3.33., which shows the NPs in the blood vessels (ϕ *ca* 20 and 40 µm), where they appear as bright red spots in the red channel. The fluorescence intensity of the surrounding glial cells in the green channel does not evolve much with time and can be used as a reference to ascertain the fluorescence intensity of the circulating NPs at different time points. The spots in the red channel correspond to **FNP-I** with some spots brighter than the others, which could either result from the presence of the NPs in the focal plane of the microscope or due to the presence of a small percentage of aggregates of NPs as can be seen at t_{90s}, t_{120s}, t_{300s} and t_{600s}. These bright spots are also bigger in size as compared to the smaller faint spots, possibly due to the presence of bigger sized NPs. Moreover, these bright NPs were observed to flow through the blood stream, without sticking to the walls of the vessels, which is an indication of their colloidal stability.

The detection and clearance of the bigger NPs and aggregates from the bloodstream was corroborated by an important and rapid drop in fluorescence intensity, recorded within 15-20 minutes of imaging, as can be seen from Figure 3.33(after t = 900 s) and is also evident from the drop in fluorescence signal detected, shown in Figure 3.34.

However, even with this drop in fluorescence signal, these bright spots were visible even after one-hour post injection indicating the circulation of the NPs in the bloodstream. This can be further confirmed in Figure 3.33 at t = 3600 s, where some faint spots are still visible (circled in white), resulting in lower fluorescence signal.

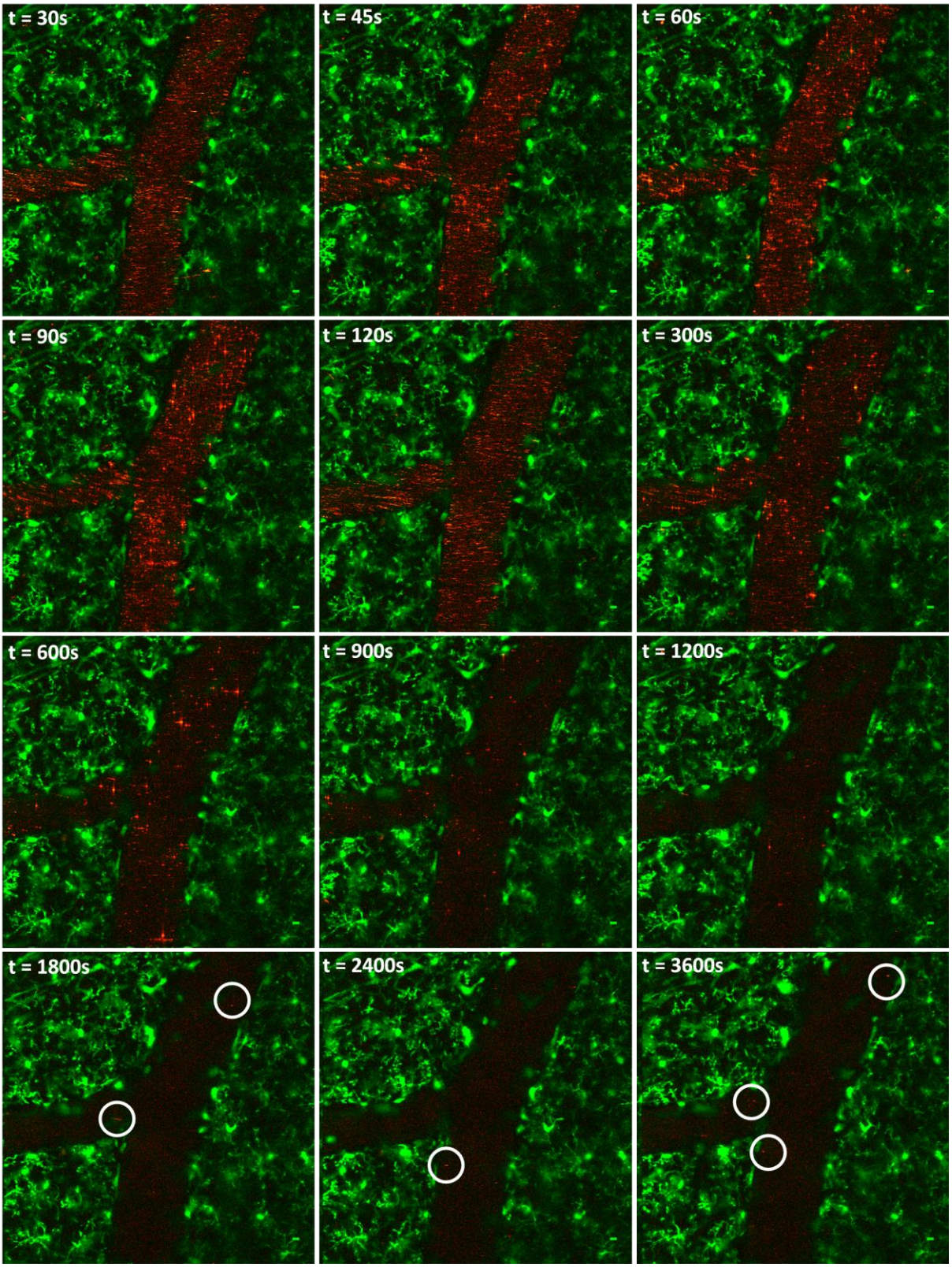

Figure 3. 33. Circulation of **FNP-I** (red spots) in the bloodstream recorded in blood vessels at different points after injection (image size corresponds to 200 x 200 μm^2)

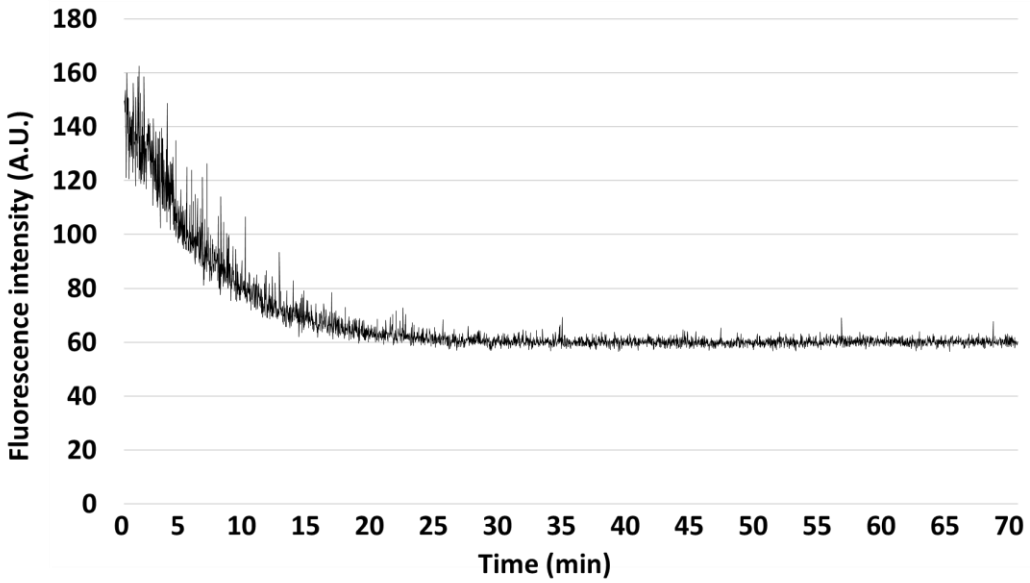

Figure 3. 34. Drop in Fluorescence Intensity over time

The drop in fluorescence intensity could be an indication that most NPs were rapidly cleared from the blood stream, most likely by the liver. Although the functionalized NPs are colloidally stable in biological media, NPs bigger than a few tens of nm are easily detected and cleared by the macrophages, while smaller NPs can circulate for longer periods of times[16]. This further explains the scarce bright spots and faint fluorescence that is seen in the blood vessels even after one-hour post injection, which could be due to the smaller sized NPs that are still circulating in the blood stream. It is evident from Figure 3.34 that the fluorescence drops to a much lower signal within 20 minutes but some NPs still circulate the blood stream although fewer in number due to the elimination of the biggest NPs.

Although three-dimensional imaging of vascularization could not be performed due to the significant drop in fluorescence intensity, these preliminary results are very promising. Additionally, there was no aggregation and accumulation of the NPs on the walls of the blood vessels, a phenomenon that was observed in earlier trials (with CMONS NPs), thanks to their colloidal stability.

The primary challenge to ensure longer circulation time and reduced clearance by the RES is to tune the size of the NPs to below 100 nm to impart furtivity. Considering the method used for the synthesis of NPs, spray-drying, which inherently results in polydisperse NPs, the challenge is to not only tune the synthesis parameters to reduce the size but to also use improved filtration techniques to reach the targeted size ranges. The second challenge that this would entail is to overcome the low optical densities obtained upon filtration of the NPs. This could be achieved by applying ultrafiltration strategies to concentrate the NPs to reach maximum optical density values without provoking aggregation. Other techniques such as tangential field flow

fractionation could also be investigated to segregate the polydisperse NPs into the desirable size ranges, before concentration.

3.4 Bibliography

(1) Xiao, Y.; Lasaga, A. C. Ab Initio Quantum Mechanical Studies of the Kinetics and Mechanisms of Quartz Dissolution: OH− Catalysis. *Geochim. Cosmochim. Acta* **1996**, *60* (13), 2283–2295.

(2) Braun, K.; Pochert, A.; Beck, M.; Fiedler, R.; Gruber, J.; Lindén, M. Dissolution Kinetics of Mesoporous Silica Nanoparticles in Different Simulated Body Fluids. *J. Sol-Gel Sci. Technol.* **2016**, *79* (2), 319–327.

(3) Dubuisson, E.; Szunerits, S.; Bacia, M.; Pansu, R.; Ibanez, A. Fluorescent Molecular Nanocrystals Anchored in Sol-Gel Thin Films: A Label-Free Signalization Function for Biosensing Applications. *New J. Chem.* **2011**, *35* (11), 2416–2421.

(4) Dubuisson, E. Nanocristaux Organiques Fluorescents Insérés En Couche Mince Sol-Gel : Vers Le Développement d'un Nouveau Type de Biopuces, 2009.

(5) https://www.applichem.com/fileadmin/Broschueren/BioBuffer.pdf.

(6) Landmann, H.; Menzel, K. https://www.sartorius.com/mediafile/Appl_Guide_Nanoparticles_SL-4001-e.pdf.

(7) Oyane, A.; Kim, H. M.; Furuya, T.; Kokubo, T.; Miyazaki, T.; Nakamura, T. Preparation and Assessment of Revised Simulated Body Fluids. *J. Biomed. Mater. Res. - Part A* **2003**, *65* (2), 188–195.

(8) Kokubo, T. Bioactive Glass Ceramics: Properties and Applications. *Biomaterials* **1991**, *12* (2), 155–163.

(9) Gelamo, E. L.; Tabak, M. Spectroscopic Studies on the Interaction of Bovine (BSA) and Human (HSA) Serum Albumins with Ionic Surfactants. **2000**, *56*, 2255–2271.

(10) Gelamo, E. L.; Silva, C. H. T. P.; Imasato, H.; Tabak, M. Interaction of Bovine (BSA) and Human (HSA) Serum Albumins with Ionic Surfactants: Spectroscopy and Modelling. *Biochim. Biophys. Acta - Protein Struct. Mol. Enzymol.* **2002**, *1594* (1), 84–99.

(11) Belatik, A.; Hotchandani, S.; Carpentier, R.; Tajmir-Riahi, H. A. Locating the Binding Sites of Pb(II) Ion with Human and Bovine Serum Albumins. *PLoS One* **2012**, *7* (5).

(12) Axelsson, I. Characterization of Proteins and Other Macromolecules by Agarose Gel Chromatography. *J. Chromatogr. A* **1978**, *152* (1), 21–32.

(13) Crumpton, M. J.; Wilkinson, J. M. Amino Acid Compositions of Human and Rabbit Gamma-Globulins and of the Fragments Produced By Reduction. *Biochem. J.* **1963**, *88* (1959), 228–234.

(14) Sigma-Aldrich. https://www.sigmaaldrich.com/content/dam/sigma-

aldrich/docs/Sigma/Product_Information_Sheet/2/g4386pis.pdf.

(15) Armstrong, J. K.; Wenby, R. B.; Meiselman, H. J.; Fisher, T. C. The Hydrodynamic Radii of Macromolecules and Their Effect on Red Blood Cell Aggregation. *Biophys. J.* **2004**, *87* (6), 4259–4270.

(16) Chou, L. Y. T.; Chan, W. C. W. Fluorescence-Tagged Gold Nanoparticles for Rapidly Characterizing the Size-Dependent Biodistribution in Tumor Models. *Adv. Healthc. Mater.* **2012**, *1* (6), 714–721.

Conclusion and Perspectives

The primary objective of this thesis was to develop organic@inorganic core-shell nanoparticles for use as tracers to perform *in vivo* vascular imaging. This not only involved synthesis and physico-chemical characterization of the NPs, but also optimisation of the synthesis conditions in order to produce a family of core-shell NPs. It has been demonstrated in this work that it is possible to synthesize various organic@silicate core-shell NPs with organic cores strictly selected from a molecular engineering of dyes exhibiting efficient fluorescence in the crystal state. Thus, the selected dyes are crystal-state emitters, with a fluorescence emission around red wavelengths and featuring a high solubility associated to relatively high melting point. The encapsulation of the dye was only made possible after the sol-gel conditions were modified to increase the polycondensation of the silicate species present in the sol in order to enhance dye nanocrystal confinement. An organosilane, AzPTES, was also introduced to the sols, to impart an azide functionality to the NPs for further functionalisation using CuAAC. The introduction of this organosilane did not induce significant changes to the morphologies of the NPs and spherical defect-free NPs were obtained.

Optimisation of this one-step synthesis approach was made possible by the ability to control both the dye nanocrystallization and the silicate polycondensation by tuning the physical parameters of the spray-drying reactor (temperature of oven and electrostatic filter, gas flow and atomization parameters). Several types of NPs were synthesized by changing the choice of organic dye forming the nanocrystalline core of the NPs and also by changing the composition of the inorganic-silicate crust.

The presence of crystalline cores was visualized by SEM after the complete dissolution of the sol-gel layer, while the crystallinity was unambiguously proven, particularly for **NP-IV**, by electron diffraction. The obtained NPs feature a very high organic loading (ca 29-42%wt). These very high dye concentration is an important advantage of these core-shell NPs to impart strong brightness by enhancing absorption and emission cross sections through the high number of fluorescent molecules. Compared to the dyes in microcrystalline powders, the fluorescence spectra were globally preserved, while for **NP-I** the emission was shifted from 640 to 620 nm. This could be the outcome of a partial amorphization occurring during the drying of the silicate crust. Overall, bright fluorescent NPs were produced with emission spectra maxima between 580 and 620 nm, lying close the border of the biological window that is required for application in bio-imaging. The quantum yields of these NP suspensions were also measured and were around 3% for **NP-I** and 1% for **NP-IV**, significantly lower than for the pure dyes in microcrystalline state but enough to impart a strong brightness. This was attributed to a partial deterioration of the crystal quality of

the organic nanocrystals because of the capillary pressures exerted at the end of drying of the silicate shells on the dye cores. Nevertheless, even if the quantum yields are rather low, they could be compensated through the very high molecular concentrations of dye nanocrystal.

Colloidal NP solutions were obtained after a basic partial dissolution of the shells of the NPs followed by acidic neutralization to physiological pH. These NPs were then functionalised with different forms of alkyne-modified Polyethylene Glycol (PEG), (i) linear chain PEG and (ii) ramified PEG, using CuAAC, which is a commonly used click reaction. This CuAAC functionalisation of the NPs was done to improve the stability of the NPs by preventing aggregation between the NPs, and to render the NPs furtive so as to avoid their recognition by the reticulo-endothelial system of the body in order to increase their circulation time in the blood stream. CuAAC was chosen as the functionalisation strategy not only due to ease of manipulation, but also due to the ability to work in aqueous environments that is essential to maintain the integrity of the organic core of the NPs that is otherwise easily dissolved in organic solvents. Colloidal stability was best observed with the use of long-chain linear PEG (M_n = 5000) thanks to its effective steric stabilisation efficacy.

The functionalized NPs were purified by dialysis and concentrated using ultrafiltration techniques to reach optical densities close to 1 so as to have high fluorescence intensity for deep-tissue imaging. The colloidal stability of the functionalised NPs was investigated using dynamic light scattering and fluorescence spectroscopy. Dynamic light scattering experiments were performed on colloidal suspensions of **FNP-I** and **FNP-IV** (functionalised with long chain linear PEG) in two media, water and 0.9 % wt NaCl solution, each tested at two different temperatures, 25 °C and 37 °C resulting in size distributions peaking at less than 200 nm in all four cases. This confimed the colloidal stability of the suspensions of functionalized core-shell NPs under physiological conditions, even at 37°C, which was not observed in earlier trials. This is a highly promising result for the use of these core-shell NPs as tracers *in vivo*. Absorbance of the functionalized and concentrated NP suspensions in 0.9 % wt salt solutions recorded over 15 hours resulted in less than 10% in drop in signal, suggesting colloidal stability. The NPs also showed comparable brightness after functionalisation, suggesting that no quenching occurred in the presence of Cu salts.

Furthermore, the colloidal stability of both **FNP-I** and **FNP-IV** was tested in simulated body fluid and in the presence of proteins such as BSA and globulins, by studying the autocorrelation data generated by the DLS. Both **FNP-I** and **FNP-IV** showed good colloidal stability in these conditions. Minimal aggregation was observed in the presence of the highest concentrations of BSA and globulin, resulting in less than 1% increase in intensity signal as observed in the autocorrelation data. Overall, the colloidal stability of **FNP-I**, was relatively better than **FNP-IV**, in physiologically relevant conditions and was therefore chosen for the preliminary *in vivo* tests.

Preliminary *in vivo* tests were performed by injecting **FNP-I** into a mouse. Imaging was performed within 30 seconds after injection and resulted in the observation of bright spots, that disappeared quickly from the blood stream (within 15-20 minutes post injection). However, fluorescence was still faintly visible in the blood flow even after a day. The rapid disappearance of the NPs was attributed to the clearance of the NPs by the macrophages, most likely into the liver. This in turn was attributed to the size of the NPs (~ 150-200 nm), which are recognizable by the RES. Therefore, this is a challenge that needs to be overcome in order to realize deep tissue imaging, in which case sufficiently high fluorescence intensity and furtivity are required for prolonged time periods (typically for 24 hours to enable passive or active targeted imaging). Nevertheless, the colloidal stability of the functionalized NPs in blood resulted in their circulation without aggregation in the walls of the blood vessels, as opposed to the observation of aggregation in earlier trials.

Future Outlooks

These preliminary results obtained are highly promising and encourage further studies to develop these NPs for *in vivo* vascular imaging. Comprehensive studies of the NP-interaction with human serum would further open doors to understanding better the formation of the protein corona and its effects on the fate and clearance of the NPs, although with the added complexity of the polydispersity of these NPs.

However, for the use of these core-shell NPs as tracers, the primary challenge is to tune the size of the NPs to be below 80 nm in order to ensure longer circulation time and reduced clearance by the RES. Considering the method used for the synthesis of NPs, spray-drying, which inherently results in polydisperse NPs, the challenge is to not only tune the synthesis parameters to reduce the size but to also use improved filtration techniques to reach the targeted sizes.

The second challenge that this would entail is to overcome the low optical densities obtained upon filtration of the NPs. This could be achieved by applying ultrafiltration techniques to concentrate the NPs to reach maximum optical density values without provoking aggregation. Other techniques such as tangential field flow fractionation could also be investigated to segregate the polydisperse NPs into the desirable size ranges, before concentration.

A third challenge is to further ensure the crystallinity of the core and obtain high quantum yields in order to have maximum fluorescence emission intensity for deep-tissue imaging. Although this work demonstrated the ability to load a high percentage of organic dyes into the NPs, the capillary forces exerted on the nanocrystalline core during the spray-drying process, could partially deteriorate the dye crystal quality.

This could be overcome using a two-step process to synthesise these core-shell NPs, by first growing the crystalline core in water and then coating it with a silicate layer to impart

biocompatibility. The ability to grow these organic nanocrystals has already been demonstrated by spraying an organic solution into a non-solvent (such as water) under strong sonication. This results in the creation of droplets with confined nucleation during mixing and growth of the NCs during solvent mixing. The quantum yields of these nanocrystals resulted in significantly higher values than the core-shell NPs, (18% for NCs of Dye-I and 22% for CMONS NCs) which were comparable with the quantum yields of the pure dyes in solid state (micrometer sized crystals), and are therefore extremely promising. These high quantum yields arise as a result of strong crystallinity thereby leading to excellent optical properties well suited for deep-tissue imaging. Moreover, the colloidal stability of these NCs also yielded a stable size range of 200 nm for over a month.

The current challenge is to further reduce the size of these organic NCs and optimize the synthesis parameters to ensure excellent crystallization of the dyes and obtain monodisperse NCs. The next step is to add a silicate coating in order to not only protect the organic core but to also impart biocompatibility and functionality. This silicate layer could then be functionalized either with PEG or with PEG and other ligands to add specificity to these core-shell NPs.

These core-shell NPs could be made more specific by functionalization with a ligand specific to certain receptors that are over-expressed on tumour cells to enable active targeting. Furthermore, it could be possible to include moieties such as iron-oxide or Au/Ag NPs, within the silicate matrix, to add more functionality, which could further enable the use of these NPs for biological application such as cell sorting using Fluorescence Activated Cell Sorting (FACS).

Experimental section

5.1. Chemicals and reagents

The silicate precursors, tetramethoxysilane (TMOS) and 1,2-bis (trimethoxysilyl)ethane (TMSE) were purchased from ABCR, distilled and stored in a moisture-free environment. The organosilane (3-Azidopropyl) triethoxysilane (AzPTES) was synthesized at Institute Neel according to the protocol described in the literature.[1] Dyes **I**-**IV** were synthesized at ENS Lyon by Dr. Yann Bretonnière following the syntheses reported in the Ph.D. thesis of G. Eucat.[2] Briefly, CMONS was synthesized by the Knoevenagel condensation reaction of 4-methoxybenzaldehyde and 4-nitrophenylacetonitrile then recrystallized in toluene and acetic acid, as described in the literature.[3] Hydrochloric acid (1.0 M), Sodium hydroxide pellets, dibasic sodium phosphate, monobasic potassium phosphate and Tetrahydrofuran (THF, inhibitor free, >99.9%) were purchased from Fischer Scientific and used directly without any other purification. Sodium ascorbate and Copper sulphate pentahydrate were purchased from Sigma Aldrich. Alkynylated PEG[4] and THPTA[5,6] were synthesized as described in the literature. Minisart® NML syringe filters with surfactant-free cellulose acetate (SFCA) membrane with pore sizes 5, 1.2, 0.8 and 0.45 µm were purchased from Sartorius. Pur-A-Lyzer™ Mega (10 mL tubes; 3.5 kDa) dialysis kits were purchased from Sigma-Aldrich. Vivaspin® 2 concentrators with 100 kDa MWCO pore size polyethersulfone (PES) membrane were purchased from Sigma for concentration of the NPs. Proteins, Bovine Serum Albumin (35% in 0.85% sodium chloride, aseptically filled) and γ-globulin (from bovine blood; ≥99% agarose gel electrophoresis) were purchased from Sigma.

5.2. Synthesis of sols

The sols were prepared using a 2:1 ratio of TMOS and TMSE, varying proportions of AzPTES and acidic water (1 M HCl) in THF according to parameters, s = [solvent]/[Si] and h = [H2O]/[-OR] (where [Si] is the molar concentration in silicon atoms and [-OR] is the molar concentration of alkoxide functions) summarized in Table 5.1. Three different protocols were followed. In protocol A, described in previous works, the silicate precursors were weighed in a 100 mL bottle to which 60 mL of THF was added, followed by 1 M HCl. The sol was aged at 60 °C for two weeks. In protocols B and C, the acidic water was directly added to the silicate precursors in a small amount of THF (3 mL- Protocol B; 5 mL – Protocol C) under vigorous stirring, followed by ageing for a few days (2 days - Protocol B; 3/5 days - Protocol C) at 60 °C with the addition of remaining amount of solvent after ageing. The prepared sols were stored at 4 °C. An amount of the dye (calculated from the d parameter, d = [dye]/[Si]) was dissolved in the sol just before nebulization. The

maximum amount of dye, d_{max}, that can be encapsulated in the NPs is determined by screening SEM images as a function of increasing values of d for each dye. When non-spherical objects start to be observed outside of the NPs, d_{max} is reached: limit of dye nanocrystal confinement by the silicate shell.

Table 5. 1. Different protocols for the preparation of sols

Protocol	s	h	Ageing	Preparation
A	500	1	14 days	- Silicate precursors + THF (60 mL) + HCl/H_2O - Ageing for two weeks at 60 °C
B	500	1	2 days	- Silicate precursors + THF (3 mL) + HCl/H_2O - Ageing for 2 days at 60 °C - Addition of 57 mL THF after ageing
C	380	1	3 days/5 days	- Silicate precursors + THF (5 mL) + HCl/H_2O - Ageing for 3/5 days at 60 °C - Addition of 55 mL THF after ageing

As an example, for a sol made using protocol B with s = 500, h = 1 and d = 0.10 for dye IV, TMSE (98.5 mg, 93 µL, 0.36 mmol) and TMOS (110 mg, 107 µL, 0.72 mmol) were weighed in a 100 mL bottle. THF (3.0 mL) then aqueous HCl (1.0 M, 92 µL) were added under vigorous stirring. This transparent mixture was aged for two days at 60 ˚C in the sealed bottle after which THF (57 mL) was added. In the case of dye **IV**, the dye (69 mg, 0.15 mmol) was dissolved in the sol just before sol nebulization.

5.3. Synthesis of Tris(3-hydroxypropyltriazolylmethyl)amine

Tris(3-hydroxypropyltriazolylmethyl)amine (THPTA) was synthesized using a protocol described in the literature.[5,6]

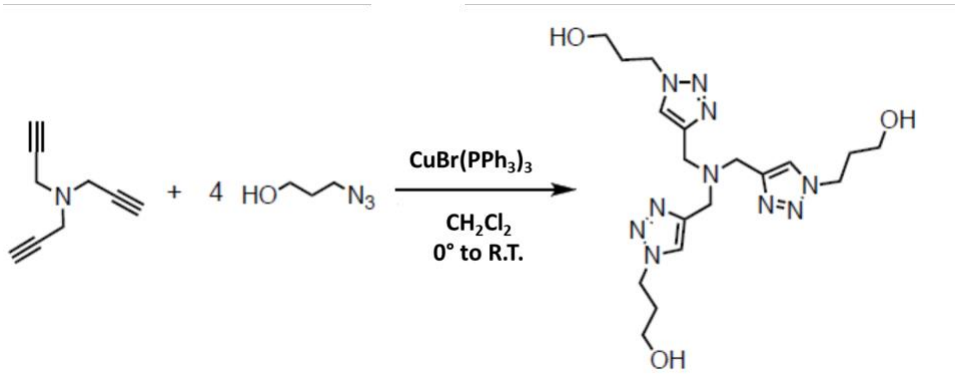

3-Bromo-1-propanol (20.0 g, 144 mmol) and sodium azide (18.7 g, 288 mmol) were dissolved in water (150 mL) and the resulting solution was stirred at 90°C overnight. The mixture was

extracted with dichloromethane (3 x 150 mL). The combined organic layers were dried over $MgSO_4$ and concentrated by rotary evaporation under reduced pressure using a bath kept at room temperature, to obtain 3-azido-1-propanol as a pale-yellow oil.

To a stirred solution of tripropargylamine (0.80 g, 6.1 mmol) and 3-azido-1-propanol (2.46 g, 24.3 mmol) in DCM (15 mL) at 0 °C under N_2 was added $CuBr(PPh_3)_3$ (0.056 g) and the resulting solution was stirred overnight under an inert atmosphere. An ice bath was used as the reaction mixture has been shown to be violently exothermic within the first two hours of the reaction.

The reaction was stopped after 24 hours and the DCM was evaporated. The product so-obtained was a brown liquid, to which 25 mL acetonitrile was added. This mixture was placed in a fridge overnight to induce precipitation. The product so obtained was filtered and vacuum dried, to give an off-white solid (1.52 g, 3.49 mmol) with a yield of 56%. ^{1}H NMR data were in accordance with the literature.[6]

5.4. Synthesis of alkyne-modified PEG

Two forms of linear (short-chain and long chain) PEG and one form of ramified PEG were synthesized.

5.4.1. Synthesis of short-chain PEG

The synthesis reported by D.V. Francis et al[4] was followed to obtain the alkynyl ethers. Triethyleneglycol monomethyl ether (2.46 g, 15 mmol) was weighed in a 50 mL round bottom (RB) flask. THF (15 mL) was added to the RB flask. The flask was then immersed in an ice bath and powdered NaOH (2.4 g, 60 mmol) was added to the RB flask. After stirring for ten minutes, propargyl bromide (2.5 mL, 22.5 mmol) was added dropwise to the reaction mixture using a syringe. The reaction mixture was allowed to stir for 24 hours, gradually warming to room temperature. The reaction mixture was then poured into ethyl acetate (EtOAc, 20 mL) and water (50 mL) and the layers were separated using a separation funnel. Further extraction of the aqueous fraction was done using EtOAc (2*20 mL). The combined organic extracts were further washed with 10% aq. HCl, followed by saturated $NaHCO_3$ (Sodium hydrogen carbonate) solution and brine and finally dried over anhydrous $MgSO_4$ (Magnesium Sulphate). The solvent extraction was done using a rotary evaporator at 40 °C. Thin layer chromatography was done using cyclohexane and EtOAc (7:3 ratio) as the eluant, to confirm the presence of the expected compound. The product was further purified using column chromatography (silica gel, EtOAc/cyclohexane, 3:7). The final product was analysed using ^{1}H NMR.

Triethyleneglycolmonomethyl ether (2.46 g) gave *3-(2-(2-(2-methoxyethoxy)ethoxy)ethoxy)prop-1-yne* as a colorless oil (1.5 g). ^{1}H NMR (300 MHz, $CDCl_3$): 2.41(t, J 2.4 Hz, 1H), 3.36 (s, 3H), 3.54 (m, 2H), 3.62 (m, 2H), 3.65 (m, 4H), 3.66 (m, 2H), 3.67 (m, 2H), 4.18 (d, J 2.4Hz, 2H).

5.4.2. Synthesis of long-chain PEG (M_n = 5000)

For the synthesis of long chain alkyne-modified PEG, a similar procedure was followed with a few modifications. The starting material, polyethyleneglycol monomethyl ether (M_n: 5000, 5 g, 15 mmol) was taken in an RB flask. THF (40 mL) and water (10 mL) were poured into it to dissolve the starting compound, after which the flask was immersed into an ice bath. Next, powdered NaOH (5.4 g, 120 mmol) was added to the mixture followed by stirring for fifteen minutes. Propargyl bromide (5.7 mL, 50 mmol) was added dropwise to the RB flask and the reaction was allowed to proceed for 24 hours, gradually warming to room temperature. Product extraction was done using dichloromethane. The aqueous and organic fractions were further extracted (using dichloromethane) and washed as described in the synthesis protocol of the short chain PEG.

Polyethyleneglycolmonomethyl ether (5 g) gave *Propargyl Polyethyleneglycolmethyl ether* as a white solid. ^{1}H NMR data were in accordance with the literature.

5.4.3. Synthesis of ramified PEG

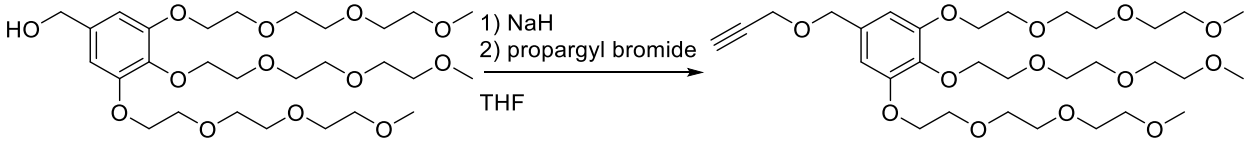

The starting alcohol was synthesized as described By W.Li. [7]

Sodium hydride (60%$_w$ in oil 762 mg, 19 mmol) was washed thrice with pentane, then added to a solution of the ramified alcohol (5.66 g, 9.5 mmol) in THF at 0 °C. After 30 min, the temperature was raised to 20 °C, and the mixture was stirred for 30 min. The mixture was cooled again to 0 °C then propargyl bromide solution (80%$_w$ in toluene, 1.7 g, 11.4 mmol) was added. After overnight stirring, water was added cautiously followed by dilute HCl. The mixture was extracted thrice with dichloromethane, and the organic phase was washed with water and brine, then dried over magnesium sulfate. After concentration, the product was purified by column chromatography (DCM/MeOH 9/1), yielding the product (4.76 g, 7.53 mmol) in 79% yield.

^{1}H NMR (400 MHz, $CDCl_3$): 2.46(t, J 2.5 Hz, 1H), 3.34 (s, 9H), 3.49-3.53 (m, 6H); 3.59-3.65 (m, 12H); 3.66-3.72 (m, 6H); 3.74-3.77 (m, 2H); 3.80-3.83 (m, 4H); 4.08-4.16 (m, 8H); 4.45 (s, 2H); 6.56 (s, 2H).

5.5. Spray-drying

The organic@silicate core-shell NPs were synthesized in a home-made spray-dryer reactor. The mixture of sol and organic dye which is first introduced into a 1 L flask, is sucked into a pneumatic atomizer (TSI model 3076- Constant Output Atomizer) by a nitrogen gas flow (56 L/h), diluted with air (8 - 16 L/h) and driven into a tubular oven (35 mm diameter × 1.4 m) set to a specific temperature. The oven is connected to an electrostatic filter kept at 140 °C and charged to a potential of 10 kV where the NPs are collected on electrodes. The core-shell NPs containing the different dyes I-IV will henceforth be referred to as NP-I, NP-II, NP-III and NP-IV, respectively.

5.5.1. Treatment of NPs

In order to segregate the chemically agglomerated NPs recovered from the electrostatic filter, a controlled dissolution of the silicate shell of the NPs was performed. This was achieved by sonicating all the collected NPs in water (60 mL) for 20 minutes in an ultrasonic bath (150 W) before adding a 1 M NaOH solution until pH 12 and stirring the suspension for 24 h in a closed bottle. The NP suspension was then subjected to centrifugation for 5 minutes at 5000 rpm and the supernatant was filtered using 5 µm, 1.2 µm and 0.8 µm filters, to ensure the removal of the biggest aggregates. This step was followed by neutralization of the NP suspension to pH 7.4 by the dropwise addition of 1 M HCl. These treated NP suspensions were used for the fluorescence spectroscopy measurements. The pH of the neutralized core-shell NPs for click functionalization was further stabilized using 0.133 M Phosphate Buffer by adding a volume corresponding to 10% of the volume of NP suspension.

This buffer (100 mL) was prepared by mixing 80.4 mL of 0.133 M Na_2HPO_4 (18.89 g Na_2HPO_4 Anhydrous in 1 L H_2O) and 19.6 mL of 133 mM KH_2PO_4 (9.08 g KH_2PO_4 in 0.5 L H_2O) to reach pH 7.4.

5.5.1.1. Complete dissolution of silicate shell

In order to visualize the organic core by FESEM, a small volume (5 mL) of the above basic NP suspension (pH 12) was stirred for a week before neutralization. The suspension was then dialyzed twice against pure water (2.5 L) before electron microscopy imaging.

5.6. Click functionalization

Functionalisation of the treated core-shell NPs was carried out using CuAAC. The number of moles of AzPTES in the sol used for the synthesis of the core-shell NPs was first estimated so as to determine the amount of PEG required for the conjugation. The equivalent PEG amounts for the different ratios of AzPTES for a sol corresponding to s = 500 and h = 1, are summarized in

Table 2. The protocol described by N.Moitra et al.[8] was followed. The synthesized PEG was first weighed in a bottle into which the treated NP suspension was added with constant stirring. One equivalent each of Tris-(hydroxypropyltriazolylmethyl)amine (THPTA) and of the pre-catalyst, copper sulphate ($CuSO_4.5H_2O$) were then added to this solution. Argon was bubbled into the colloidal suspension for a few minutes to remove any traces of oxygen before the addition of the reducing agent (sodium ascorbate) to start the click reaction. Four equivalents of sodium ascorbate were then added to this solution, more Ar was bubbled into the suspension and the bottle was closed and kept under constant stirring at room temperature for 24 hours.

Table 1. Different parameters for click functionalization

Sol	**No. of moles of azide (mmol)**	**PEG**			**Sodium ascorbate (mg; mmol)**	**THPTA (mg; mmol)**	**$CuSO_4.5H_2O$ (mg; mmol)**
2TMOS + TMSE +AzPTES (1%)	0.014	**Type**	**LCPEG**	**Ramified**	11.5; 0.58	6.3; 0.014	3.6 mg; 0.014
		Equivalents	5	10			
		Amount (mg)	357	94.1			
		No. of moles (mmol)	0.07	0.14			
2TMOS + TMSE +AzPTES (3%)	0.043	**Type**	**LCPEG**	**Ramified**	34.6; 0.17	19.0; 0.043	11.0; 0.043
		Equivalents	5	10			
		Amount (mg)	1083	282.9			
		No. of moles (mmol)	0.215	0.43			
2TMOS + TMSE +AzPTES (5%)	0.072	**Type**	**LCPEG**	**Ramified**	57.6; 0.29	31.0; 0.072	18.0; 0.072
		Equivalents	5	10			
		Amount(mg)	1814	473.7			
		No. of moles (mmol)	0.36	0.72			

5.6.1. Dialysis

Purification of the functionalized NPs was performed by dialyzing the NP suspension (10 mL in Pur-A-Lyzer tubes with 3.5 kDa pore size) against 2.5 L of 0.0133 M PB for two days.

5.6.2. Concentration of NPs

The purified NP suspensions were concentrated using Vivaspin 2 (2 mL) concentrators. Centrifugation was performed at 3000 rpm for 3 minutes on volumes of 2 mL. Successive centrifugations were performed to reach an optical density close to 1.0 in all cases.

5.7. Preparation of Simulated Body Fluid (4x)

Concentrated SBF was prepared according to literature.[9] First, approximately 200 mL of ultra-pure water was poured into a 250 mL polypropylene beaker, and this was stirred using a magnetic bar at 36.5°C. After each preceding reagent had completely dissolved, the reagents were dissolved in the water in the sequence listed as follows: 550 mM NaCl (8.036 g), 17 mM $NaHCO_3$ (0.352 g), 12 mM KCl (0.225 g), 4 mM $K_2HPO_4.3H_2O$ (0.230 g), 6 mM $MgCl_2.6H_2O$ (0.311 g), 10 mL 2.0 M HCl, 11 mM $CaCl_2$ (0.293 g), 2 mM Na_2SO_4 (0.072 g), 200 mM Tri(hydroxymethyl) aminomethane (6.063 g). Finally, the fluid was adjusted to a final pH of 7.40 at 36.5°C by titrating aqueous 2.0 M of HCl into the SBF and the volume was made up to 250 mL.

5.8. *In vivo* tests

CX3CR1-GFP mice, expressing GFP only in microglia in the brain were used. Thinned-skull cortical window preparation over the somatosensory cortex was performed, for transcranial imaging where the skull was reduced to a thickness of 20-30 µm. Briefly, mice were deeply anesthetized with isoflurane (3-4%, Isovet, Piramal Healthcare, UK Ltd.) and mounted in a stereotaxic apparatus (D. Kopf Instruments). Carprofen (5 mg/kg s.c.) was injected at the beginning of the surgery to diminish post-surgical pain and inflammation. After the skull was exposed, a thin custom-made metal implant was glued allowing to delimit the area over the somatosensory cortex. The skull was then carefully thinned using a high-speed dental drill. To avoid heat-induced damage, drilling was repeatedly interrupted and cold sterile saline was applied. When a 20 to 30 µm skull thickness was reached, a thin layer of cyanoacrylate glue was applied and a cover glass was placed on top of the thinned skull.

Imaging was performed using a two-photon microscope (Olympus) with a Ti:Sapphire laser (Mai-Tai, Spectra-Physics) tuned to 940 nm. A 20x water-immersion objective (0.95 N.A. Olympus) was used to acquire images and the laser power was maintained below 30 mW. Fluorescence was detected using a 560 nm dichroic mirror coupled to a 525/50 nm emission filter and a photomultiplier tube in whole-field detection mode. Images were acquired every 0.9 seconds over an area of 200x200 μm^2 and a resolution of 521x521 pixels.

5.9. Characterization

5.9.1. ^{29}Si NMR

^{29}Si NMR experiments were carried out by Dr Béatrice Gennaro at the Département de Chimie Moléculaire, Grenoble, with a Bruker AVANCE III 500 MHz spectrometer equipped with a cryo-probe Prodigy. Data were processed with Topspin software (Bruker). The program uses zggpse using spin echo with gradients. The two gradients files name is SMSQ10.100 that use 1% gradient ratio each for 1 ms gradient pulse. The relaxation delay is 1 s. The experiments were recorded with 65536 points. Two thousand and forty-eight scans were acquired over a spectral width of 29762 Hz.

5.9.2. Field Emission Scanning Electron Microscopy (FESEM)

FESEM images were recorded using a Zeiss Ultra+ scanning electron microscope. The NPs in powder form collected just after synthesis were deposited on doped silicon wafers for observation. A voltage of 3 kV was used at a working distance of 3 mm.

5.9.3. Transmission Electron Microscopy (TEM)

TEM was performed on a Philips CM300 microscope operating at 300 kV at 100 K using a liquid nitrogen-cooled sample holder. The TEM grid was prepared by depositing a dilute drop of the NPs after synthesis in water on a carbon-coated copper grid. Images and diffraction patterns were collected on a TemCam F416 TVIPS, which is a rapid, large field of view, high-resolution and high dynamic range CMOS camera (4kx4k, 16 bits). Diffraction patterns were recorded with an exposure time of 0.4 s to avoid sample damage while NP images were obtained with 2-5 s exposure time.

5.9.4. Thermogravimetric analysis coupled with Differential thermal analysis (TGA-DTA)

Thermogravimetric analyzes (TGA) were carried out with a SETARAM TAG 16 equipment, using 3 mg samples within a 100 µL alumina crucibles and a heating rate of 8 °C.min^{-1}.

5.9.5. Absorbance and Fluorescence

The absorbance spectra of the treated NP suspensions were recorded using a SAFAS Xenius XC Cuvette spectrofluorometer with a Xenon source UV lamp. Fluorescence emission spectra on NP suspensions were measured using a Horiba-Jobin Yvon Fluorolog-3 spectrofluorimeter equipped with a Hamamatsu R928 photomultiplier tube. Spectra were reference corrected for both the excitation source light intensity variation (lamp and grating) and the emission spectral response (detector and grating). Measurements were performed using a calibrated integrative sphere collecting all the emission (2π steradians covered with spectralon®), model F-3018 from Horiba Jobin Yvon. Absolute quantum yields were determined as explained in Appendix-IV.

Correction factors

The absorbance spectra recorded were corrected for diffusion contribution. This was done by accounting for Mie scattering using a λ^4 dependency. The spectra were fitted using the following function, Diffusion = (a *10^8)/ λ^4, where a is a constant of proportionality. After subtracting this diffusion contribution from the absorbance curves, the spectra were further corrected to remove any baseline errors by subtracting another constant for a better fit.

5.9.6. X-ray Diffraction (XRD)

XRD data of the pure microcrystalline dyes and the core-shell NPs was collected in a Bruker D8 Advance diffractometer equipped with a monochromatic Cu Kα1 (λ = 1.5406 Å) source operated in a Bragg-Brentanno geometry. The data were collected from 2θ, 5 – 40 ˚ with a 0.200 ˚ step size. A Lynxeye detector was used for data collection.

XRD data of the core-shell NPs was also recorded with Capillary XRD using a 4-circles Nonius Kappa-CCD, equipped with an Apex-II detector (75 µm pixels). The data collected were corrected from dark and summed azimuthally with Nonius Powderize routine. The source used was an Incoatec IµS (50 kV, 600 µA) Ag Kα1 (λ = 0.56087 Å) source (30 w) with Montel focusing optics. The capillary used made of borosilicate, had a diameter of 0.7 mm, with 0.01 mm wall thickness. The XRD data were recorded at two distances between the capillary and the detector (DX60 and DX80). Eight images corresponding to 30 minutes of collection and a spin of 1 s/deg were collected for each distance for NP-IV, eight images corresponding to 1 hour of collection were recorded for dye-free silica NPs and an empty capillary, while eight images corresponding to 2 hours of collection were recorded for NP-I.

5.9.7. Two-photon fluorescence

A Ti:Sapphire Laser called Chameleon (repetition rate 80 MHz, pulse duration around 100 fs), from Coherent was used. A variable density filter was utilized to choose the intensity focused on the sample. A lens with 100 mm focal length was chosen. The beam was focused inside the solution close to the entrance of the quartz cuvette (10 mm square) to avoid absorption before the focus and close to the 90° face of the cuvette to avoid absorption of the fluorescence before detection at 90° of the focal point. A S2000 spectrometer from Ocean Optics with a 1 mm diameter optical fiber was used for detection and the maximum signal was measured. Two filters were used, (i) Filter 1 between 750-890 nm (which cuts at 650 nm) and Filter 2 between 900-1060 nm (which cuts at 850 nm). Two references were used, fluorescein ($1.0\ 10^{-4}$ M in water at pH 11) and styryl ($1.0\ 10^{-4}$ M in chloroform).

5.9.8. Dynamic Light Scattering

Most of the DLS experiments on the treated NP suspensions were determined using a Malvern Zetasizer Nano ZS. Ten measurements were performed on each sample at 25 °C and 37 °C. 1- 1.5 mL of sample was measured in a cuvette. General purpose analysis was used for the conversion of the autocorrelation function into size distribution. Other experiments were performed using the Vasco Kin particle size analyzer by Cordouan Technologies. Time-resolved analysis of real-time correlation data was done using NanoKin® software to generate three different fits, namely Pade Laplace, Cumulants and SBL (sparse Bayesian learning) methods of analysis.

5.9.9. Zeta Potential

The zeta potential of the treated NP suspensions was determined using a Wallis$^{\zeta TM}$ zeta potential analyzer by Cordouan Technologies. Six measurements of medium resolution were performed on each sample. Smoluchowski equation was applied for the treatment of data using ZetaQ software.

5.10. Bibliography

(1) Malvi, B.; Sarkar, B. R.; Pati, D.; Mathew, R.; Ajithkumar, T. G.; Sen Gupta, S. “Clickable” SBA-15 Mesoporous Materials: Synthesis, Characterization and Their Reaction with Alkynes. *J. Mater. Chem.* **2009**, *19* (10), 1409.

(2) Eucat, G.; University of Grenoble; France. Ph.D. Dissertation: Molecular Engineering of New Organic Fluorophores and Encapsulation in a Sol-Gel Shell for Medical Imaging, 2014.

(3) BLAIR, H. S.; BOYD, N. L. The Effect of the Substrate on the Isomerization of Model Disperse Dyes Based on Stilbene. *J. Soc. Dye. Color.* **1976**, *92* (1), 14–16.

(4) Francis, D. V.; Miles, D. H.; Mohammed, A. I.; Read, R. W.; Wang, X. Towards Functional Fluorous Surfactants. Synthesis of Hydrophilic Fluorous 1,2,3-Triazolylmethyl Ethers and Di(1,2,3-Triazolylmethyl) Ethers. *J. Fluor. Chem.* **2011**, *132* (11), 898–906.

(5) Kislukhin, A. A.; Hong, V. P.; Breitenkamp, K. E.; Finn, M. G. Relative Performance of Alkynes in Copper-Catalyzed Azide-Alkyne Cycloaddition. *Bioconjug. Chem.* **2013**, *24* (4), 684–689.

(6) Hong, V.; Presolski, S. I.; Ma, C.; Finn, M. G. Analysis and Optimization of Copper-Catalyzed Azide-Alkyne Cycloaddition for Bioconjugation. *Angew. Chemie - Int. Ed.* **2009**, *48* (52), 9879–9883.

(7) Li, W.; ETH Zurich; Switzerland. Ph.D. Dissertation: Novel Dendritic Macromolecules with Water-Soluble, Thermoresponsive and Amphiphilic Properties, 2010.

(8) Moitra, N.; Trens, P.; Raehm, L.; Durand, J. O.; Cattoën, X.; Chi Man, M. W. Facile Route to Functionalized Mesoporous Silica Nanoparticles by Click Chemistry. *J. Mater. Chem.* **2011**, *21* (35), 13476–13482.

(9) Braun, K.; Pochert, A.; Beck, M.; Fiedler, R.; Gruber, J.; Linden, M. Dissolution kinetics of mesoporous silica nanoparticles in different simulated body fluids. *J Sol-Gel Sci Technol* 2016 79, 319–327

Appendix I - Electron Diffraction

Electron diffraction using Transmission Electron Microscopy (TEM) is a powerful tool to characterize material structure and crystallinity. There are several differences between electron and X-ray diffraction. The first difference is that electrons are less penetrating than X-rays, which requires the specimen and the detector to all be enclosed in vacuum. Electron scattering is more intense than X-ray scattering (10^3 to 10^4 times stronger) which in turn implies that a very thin layer is capable of giving a strong diffraction pattern in a short time.[1] The intensity of electron diffraction decreases with increasing 2θ, which means that the entire diffraction pattern is limited to an angular range of about ±4° 2θ.[1] Other advantages include extremely short wavelength (≈2 pm), and the ability to examine tiny volumes of matter (≈10 nm^3).[1]

When an incoming planar electron wave interacts with atoms, secondary waves are generated which interfere with each other, either constructively (reinforcement at certain scattering angles generating diffracted beams) or destructively.[2] This scattering event can be described as a reflection of the beams at planes of atoms (lattice planes). Bragg's law gives the relation between interplanar distance d and diffraction angle θ which is the distance between the reflection and the origin of the reciprocal lattice:

$$n\lambda = 2d\sin\theta$$

Each set of parallel lattice planes, which correspond to planes decorated with atoms in the structure, generates a pair of spots in the electron diffraction pattern with the direct beam in their center (see scheme below).[3] Since the wavelength λ of the electrons is known, interplanar distances can be calculated from the diffraction patterns, using which information about crystal symmetry can be obtained.

These spots have a distance of $1/d_{hkl}$ from the origin and are perpendicular to the reflecting set of lattice planes. The two basic lattice planes (blue lines) of the two-dimensional rectangular lattice shown below are transformed into two sets of spots (blue) (Figure A1.1). The diagonals of the basic lattice (green lines) have a smaller interplanar distance and therefore cause spots that are farther away from the origin than those of the basic lattice.[3]

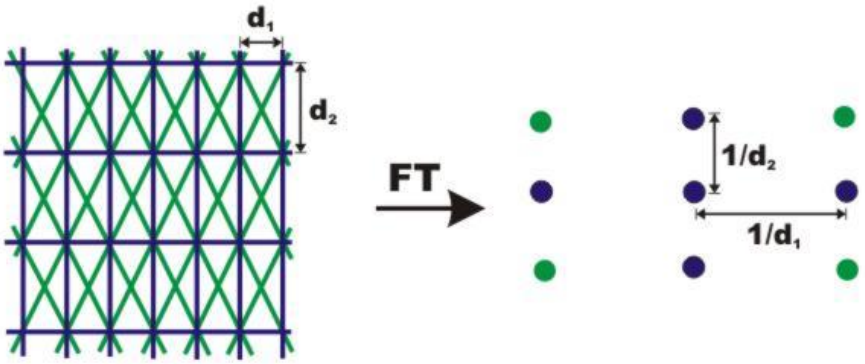

Figure A1.1. Fourier transform of real space into reciprocal space generating diffraction spots[3]

Diffraction spots are formed on the back focal plane by scattering of diffracted waves by the sample. Recombination of the diffracted waves forms an image on the image plane. Diffracted electrons can be focused into a regular arrangement of diffraction spots that can be projected and recorded as an electron diffraction pattern using electromagnetic lenses. This pattern is formed in a reciprocal space, while the image plane is in the real space. Mathematically, the real space can be converted into reciprocal space using Fourier transform.

The complete set of all possible reflections of a crystal constitutes its reciprocal lattice. The Ewald sphere, which has radius 1/λ, drawn through the origin of the reciprocal lattice, describes the diffraction event in reciprocal space (Figure A1.2). The Bragg condition is satisfied for each reciprocal lattice point that is located on the Ewald sphere of reflection.[3] The radius of the Ewald sphere is large as the wavelength of electrons is small.

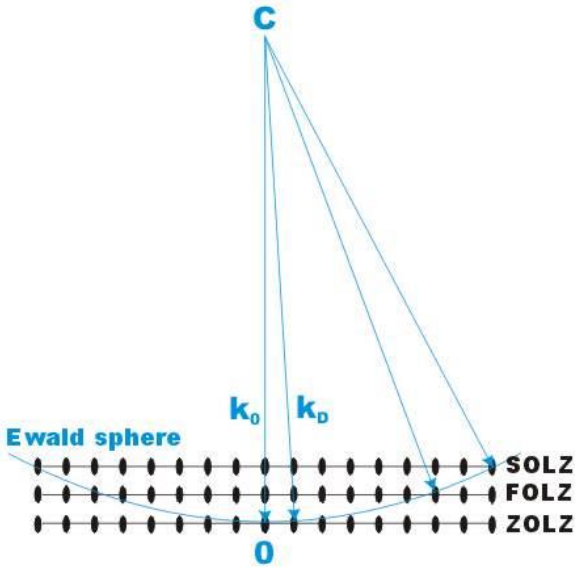

Figure A1.2. Ewald Sphere with point 0 is the origin of reciprocal lattice, k_0 is the wave vector of the incident wave, k_D is the wave vector of a diffracted wave, ZOLZ is Zero Order Laue Zone and FOLZ(SOLZ) is First (Second) Order Laue Zone[3]

Furthermore, the lattice points in the reciprocal lattice of thin samples are elongated so that the Ewald sphere intersects several of the rods.[3] Because of that, diffraction occurs even if the Bragg condition is not exactly satisfied, and many reflections appear simultaneously. [3]

If the interplanar distance in direction of observation is large (that means a small distance between ZOLZ and FOLZ in reciprocal space), higher order Laue zones (HOLZ) can be observed as well (Figure A1.2).

A diffraction pattern is formed in the back focal plane with electrons scattered by the sample, which are combined by the objective lens to generate an image in the image plane (Figure A1.3). Both the diffraction pattern and the image are generated simultaneously, but it depends on the focusing of the intermediate lens, which one appears in the plane of the second intermediate image and is magnified on the viewing screen by the projective lens. Switching from real space (image) to reciprocal space (diffraction pattern) is easily achieved by changing the strength of the intermediate lens.[3]

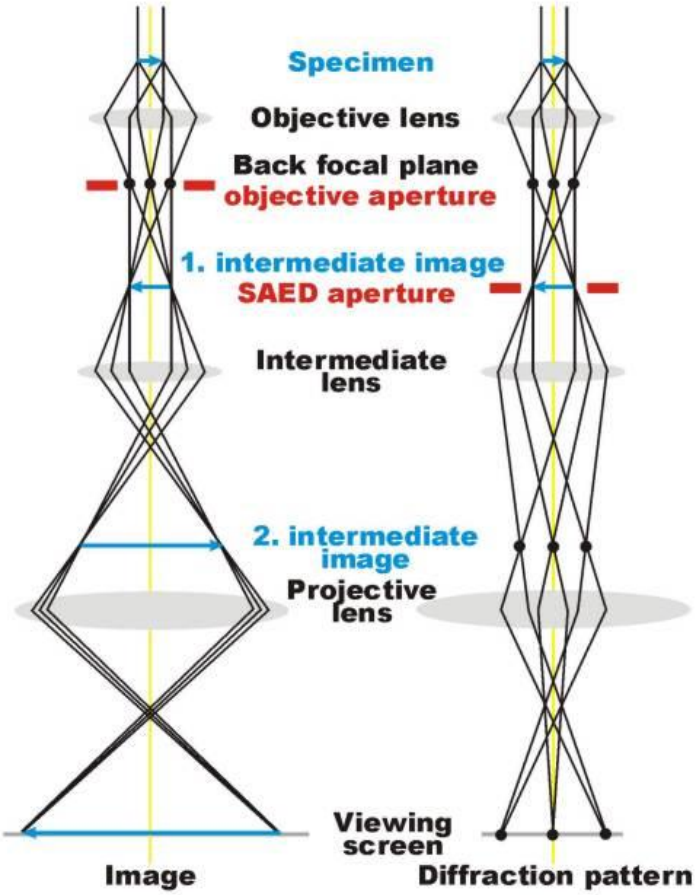

Figure A1.3. Schematic of how an image and diffraction pattern is collected in a TEM[3]

Typically, the final image is constituted by inserting an objective aperture in the back focal plane to observe the image with enhanced contrast. When one diffracted beam is selected, it is called the dark field method (and a dark field image) (Figure A1.4). For selected area electron diffraction (SAED), an aperture in the plane of the first intermediate image defines the region of which the diffraction is obtained.[1]

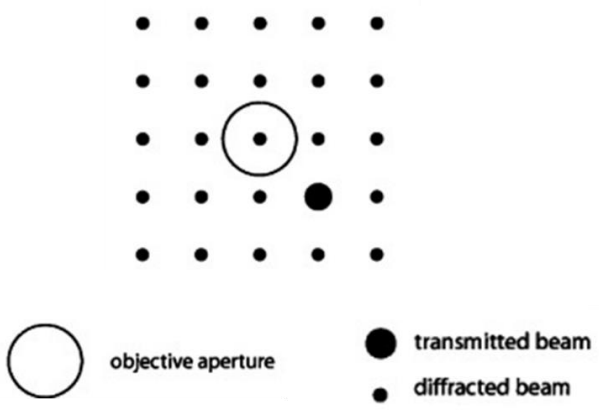

Figure A1.4. Dark-field observation method[1]

Changes in amplitude of either the transmitted or diffracted beam due to absorption and dynamic scattering by the specimen gives rise to the contrast. The diffraction pattern obtained is an indication of the number of grains contributing to the pattern or crystallinity of the sample (Figure A1.5).[2]

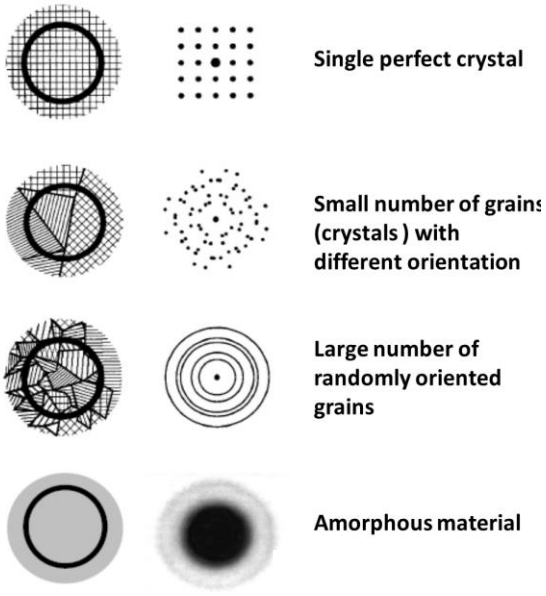

Figure A1.5. Different diffraction patterns[2]

Appendix I - Electron Diffraction

While a single crystal gives rise to a spot pattern, diffraction from several crystals causes an overlapping of spot patterns, in which these spots lie along Debye rings. An amorphous sample on the other hand results in no diffraction pattern.

(1) Bendersky, L. A.; Gayle, F. W. Electron Diffraction Using Transmission Electron Microscopy. *J. Res. Natl. Inst. Stand. Technol.* **2001**, *106* (6), 997.

(2) http://coen.boisestate.edu/faculty-staff/files/2012/01/Electron_Diffraction.pdf.

(3) http://www.microscopy.ethz.ch/ED-Ewald.htm.

Appendix II - Dynamic Light Scattering

Dynamic Light Scattering (DLS) also called Photon Correlation Spectroscopy (PCS) or Quasi-Elastic Light Scattering (QELS) is an optical technique for measuring the size distribution of particles in the sub µm to nm range. It measures the Brownian motion of particles and converts it into size. Brownian motion is the random thermal motion that particles in a suspension undergo due to collision by the solvent molecules that surround them. This Brownian motion can be modeled using the Stokes-Einstein equation as:

$$D_h = \frac{k_B T}{3\pi\eta D} \qquad \textit{(Eq. II.1)}$$

where D_h is the hydrodynamic diameter, D is the translational diffusion coefficient, k_B is Boltzmann's constant, T is thermodynamic temperature and η is dynamic viscosity. While T and η are known and k_B is a constant, D is the parameter that is obtained by the DLS and converted into size using the above equation.

Larger particles diffuse slower than smaller particles. The translational diffusion coefficient will depend not only on the size of the particle core, but also on any surface structure, and the concentration and type of ions in the medium. D_t is obtained by measuring the speed at which particles are diffusing due to Brownian motion. This in turn is measured by monitoring the fluctuations in scattered light intensity.

A cuvette containing the particles is illuminated by a laser. This light is scattered by the particles in the sample. The intensity fluctuation rate depends on the size of the particles, with smaller particles resulting in rapid fluctuations as compared to larger ones (Figure A2.1).

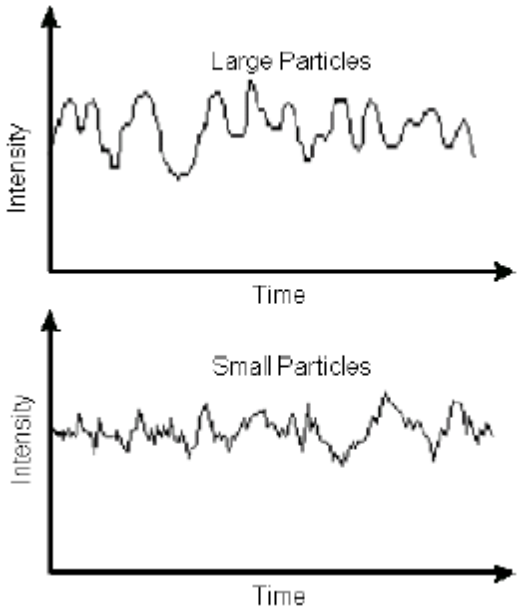

Figure A2.1. Typical intensity fluctuations for larger and smaller particles[1]

These fluctuations are measured using a correlator, which basically measures the degree of similarity between two signals or one signal with itself at different time intervals. If the intensity of a signal is compared with itself at a particular point in time and a time much later, then for a randomly fluctuating signal it is obvious that the intensities are not going to be related in any way, i.e. there will be no correlation between the two signals.

However, there is a strong correlation between the intensity of signal at time =t and the intensity a very small time later (t+ δt). If the signal at t is compared to the signal at t+2δt, there will still be a reasonable correlation between the two signals, although lesser than between t and t+δt. The correlation reduces with time (Figure A2.2).

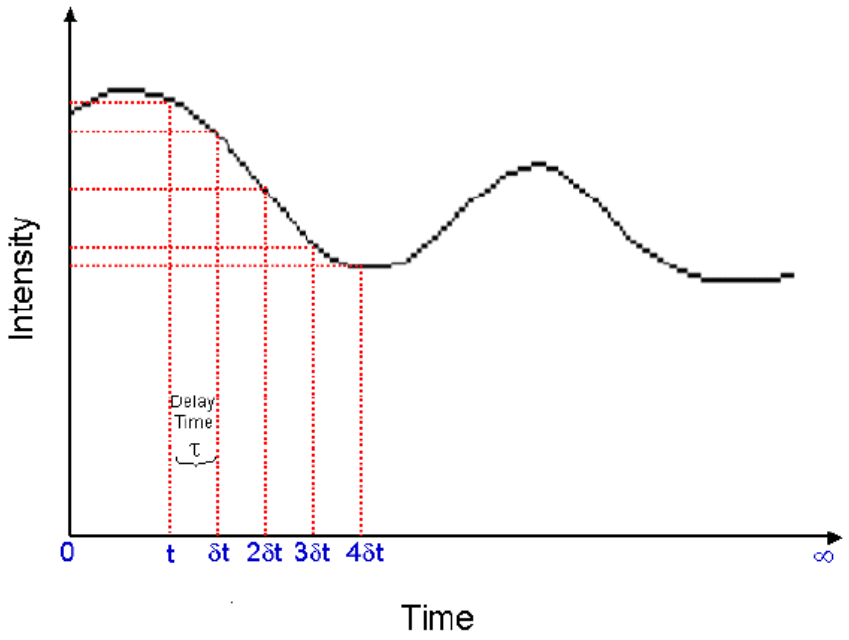

Figure A2.2. Schematic showing the fluctuation in the intensity of scattered light as a function of time[1]

The period of time t is typically a few nanoseconds or microseconds and is called the sample time of the correlator, while t = ∞ corresponds to an order of a millisecond or tens of milliseconds. If the signal intensity at t is compared with itself, there is perfect correlation, indicated by unity (1.00), while no correlation is indicated by zero (0.00). Correlation decreases as the signal at time = t is compared with the signals at t+2δ t, t+3δ t, t+4δ t etc, until at some time, effectively when t = ∞, there will be no correlation (Figure A2.3).

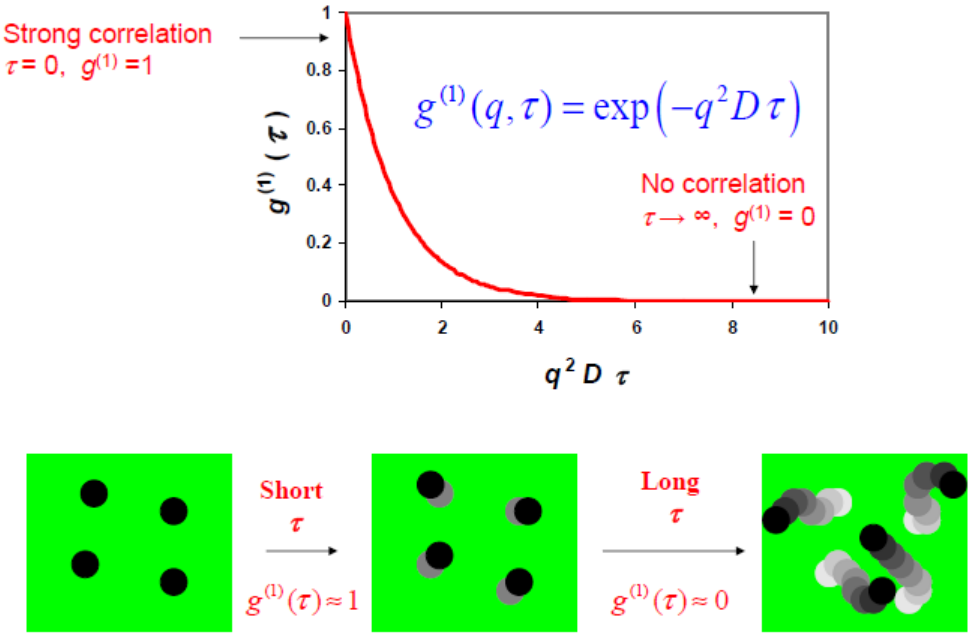

Figure A2.3. Different correlator conditions[2]

Correlation persists for a longer time for larger particles while the contrary is true for smaller particles and the correlator typically generates an autocorrelation function that can be mathematically expressed in terms of the fluctuations of the scattered light intensity (Figure A2.4), as:

$$g2(q,\tau) = \frac{\langle I_s(q,t) I_s(q,t+\tau)\rangle}{\langle |I_s(q,t)(q,t)|^2\rangle} \qquad \textit{(Eq. II.2)}$$

where τ is the time lag and q is the scattering vector module. Using the Siegert relation g2(q,τ) can be related to the electric field correlation function g1(q,τ) as:

$$g2(q,\tau) = 1+\beta|g1(q,\tau)|^2 \qquad \textit{(Eq. II.3)}$$

$$g1(q,\tau) = \frac{\langle E_s(q,t)\langle E_s(q,t+\tau)\rangle}{\langle |E_s(q,t)|^2\rangle} \qquad \textit{(Eq. II.4)}$$

where β is the so-called intercept. Eq.II.4 may be used to determine the translational diffusion coefficient D. For a monodisperse sample, it is fitted to an exponential function

$$g1(q,\tau)=\exp(-\Gamma\tau) \qquad \textit{(Eq. II.5)}$$

yielding the decay rate, Γ. This can be further correlated to the diffusion coefficient using:

$$\Gamma=q^2D \qquad \textit{(Eq. II.6)}$$

$$q = \frac{4\pi\lambda_0}{2} \sin\frac{\theta}{2} \qquad \textit{(Eq. II.7)}$$

where n is the refractive index of the dispersant, λ_0 is the wavelength of the laser and θ is the scattering angle. The D so obtained can be further used to estimate the size using Eq. II.1.

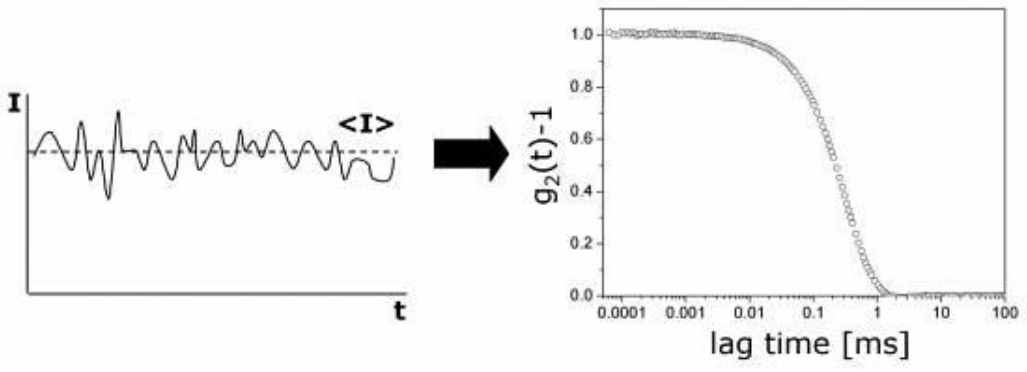

Figure A2.4. Intensity fluctuations converted into a correlation function[3]

The translational diffusion coefficient is converted into size using different algorithms. The two main approaches used are: (i) to fit a single exponential to the correlation function to obtain the mean size (z-average diameter) and estimate of the width of polydispersity index (used by the Cumulants Analysis) or (ii) to fit multiple exponentials to the correlation function to obtain distribution of particle sizes (such as Non-negative least squares (NNLS) or CONTIN).

The two main theories of light scattering used are Rayleigh scattering and Mie theory. If the particles are small compared to the wavelength of the laser used (typically less than d = λ/10 or around 60 nm for a He-Ne 633 nm laser), then the scattering from a particle illuminated by a vertically polarised laser will be essentially isotropic. Rayleigh approximation states that $I \alpha d^6$ and also that $I \alpha 1/\lambda^4$, Where I = intensity of light scattered, d = particle diameter and λ = laser wavelength. The d^6 term tells us that a 100 nm particle will scatter 10^6 times as much light as a 10 nm particle. So, the contribution from the larger particles will supersede the scattered light from the smaller ones. This also implies that it is difficult to measure a mixture of 1000 nm and 10 nm particles because the contribution to the total light scattered by the small particles will become negligible. The λ^4 factor means that as the wavelength of the laser used decreases, a higher scattering intensity is obtained.

The Mie theory applies when the size of the particles becomes roughly equivalent to the wavelength of the laser, resulting in a complex function of maxima and minima with respect to angle. Mie theory is the only theory that explains correctly the maxima and minima in the plot of intensity with angle and will give the correct answer over all wavelengths, sizes and angles. Mie theory is used in most DLS software for conversion of the intensity distribution into volume.

The primary size distribution obtained is a plot of the relative intensity of light scattered by particles of different sizes and is therefore known as an intensity size distribution. This is further used to generate a volume and number distribution. If the intensity distribution results in a single peak, conversion into a volume distribution using the Mie theory will only result in a slightly different shaped peak. However, if the plot shows more than one peak, then Mie theory can convert the intensity distribution to a volume distribution to give a more realistic view of the importance of the second peak, using the samples refractive index. In general, it will be seen that:

d(intensity) > d(volume) > d(number)

This can be easily understood by assuming two populations of spherical particles of diameters 10 nm and 100 nm present in equal numbers. A number distribution will result in a plot consisting of 2 peaks (positioned at 10 and 100 nm) of a 1 to 1 ratio (Figure A2.5). A volume distribution will result in a 1:1000 ratio of the two peaks (because the volume of a sphere is equal to $4/3\pi\,(d/2)^3$). AN intensity distribution would result in a 1:1000000 ratio between the 2 peaks (because the intensity of scattering is proportional to d^6 (from Rayleigh's approximation).

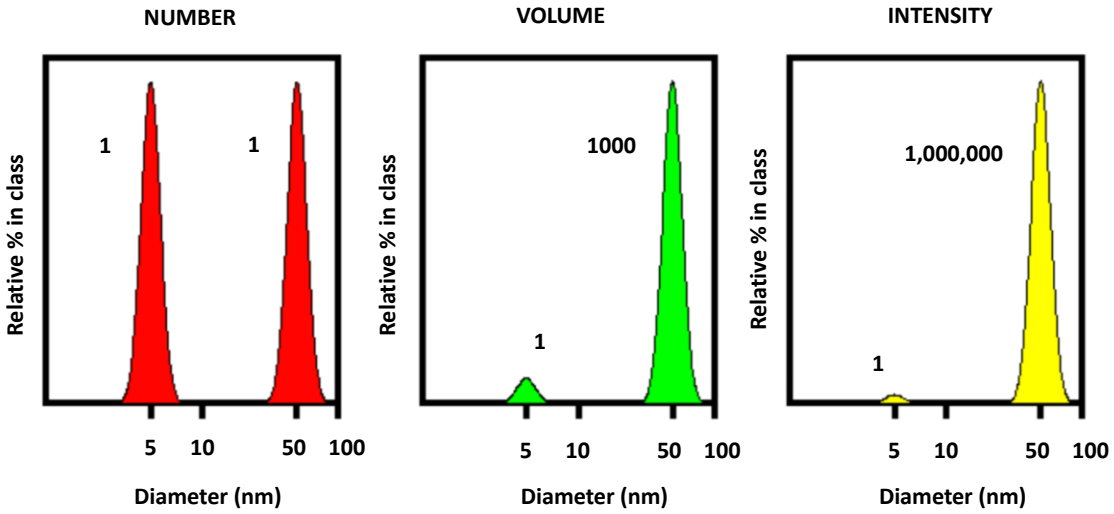

Figure A2.5. Number, volume and intensity distributions of a bimodal mixture of 10 and 100 nm particles[1]

A typical DLS consists of six main components (Figure A2.6). First the sample is illuminated using a laser light source (1). While the laser beam will pass through the sample for dilute concentrations, some part may be scattered, which is measured by a detector. The scattering can either be collected at 173 ° (3) (back scattering) or at 90 °(2) (forward scattering). It Is important that the intensity of scattered light be within a specific range for the detector to successfully measure it. Too much light results in the detector becoming saturated. To overcome this, an attenuator (4) is used to reduce the intensity of the laser source and hence reduce the intensity

of scattering. For samples that do not scatter much light, such as very small particles or samples of low concentration, the attenuator allows more laser light through to the sample, while for samples that scatter more light, such as large particles or samples at higher concentration, the intensity of scattered light is reduced.

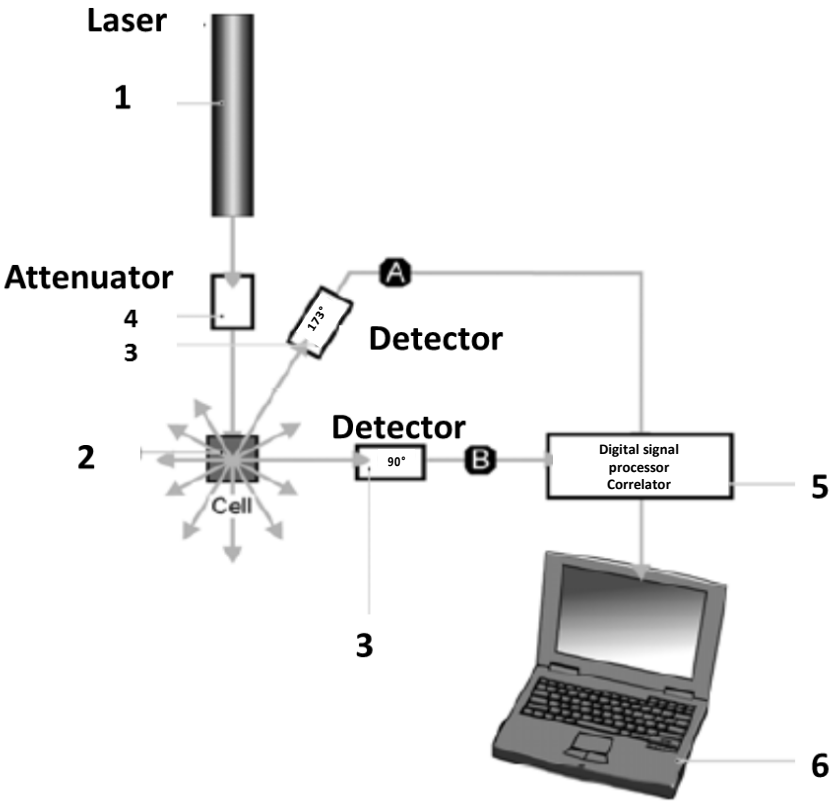

Figure A2.6. Optical configurations of a commercial DLS setup[1]

(1) Malvern. Dynamic Light Scattering : An introduction in 30 minutes https://warwick.ac.uk/fac/cross_fac/sciencecity/programmes/internal/themes/am2/booking/particlesize/intro_to_dls.pdf.

(2) https://warwick.ac.uk/fac/cross_fac/sciencecity/programmes/internal/themes/am2/booking/particlesize/intro_to_dls.pdf.

(3) https://www.lsinstruments.ch/technology/dynamic_light_scattering_dls/.

Appendix III - Calculation of sol parameters

Solvent: THF (60 mL) s = 500

Silicate matrix: 2TMOS + 1TMSE h = 1

Fluorophore: Dye IV d = 0,1

Acidic catalysis at 60°C

Calculation of the volume of TMSE:

$n_{TMOS} = 2*n_{TMSE}$

$$\frac{V_{TMOS}\cdot \rho_{TMOS}}{M_{TMOS}} = 2.\frac{V_{TMSE}\cdot \rho_{TMSE}}{M_{TMSE}} \leftrightarrow V_{TMSE} = \frac{M_{TMSE}.V_{TMOS}\cdot \rho_{TMOS}}{2.\ M_{TMOS}\cdot \rho_{TMSE}}$$

Calculation of the volume of solvent, THF : s = $\frac{[THF]}{[Si]}$

$[THF] = s.\ [Si] \quad \leftrightarrow \quad \frac{n_{THF}}{V_{TOT}} = s.\frac{n_{Si}}{V_{TOT}}$

$n_{Si} = 2n_{TMOS} + n_{TMSE}$ and $n_{TMOS} = 2.n_{TMSE}$ therefore, $n_{Si} = 4.n_{TMSE}$

$$n_{THF} = s.4.n_{TMSE} \quad \leftrightarrow \quad \frac{V_{THF}\cdot \rho_{THF}}{M_{THF}} = s.4.\frac{V_{TMSE}\cdot \rho_{TMSE}}{M_{TMSE}}$$

$$\frac{V_{THF}\cdot \rho_{THF}}{M_{THF}} = s.4.\frac{V_{TMSE}\cdot \rho_{TMSE}.M_{THF}}{M_{TMSE}\cdot \rho_{THF}}$$

Calculation of the volume of acidic water, h = $\frac{[H_2O]}{[-OR]}$

-OR corresponds to the alkoxide functions, there are six for TMSE and 4 for TMOS.

$$[H_2O] = h.\ [\text{-OR}] \quad \leftrightarrow \quad \frac{n_{H_2O}}{V_{TOT}} = h.\frac{n_{-OR}}{V_{TOT}}$$

$n_{-OR} = 4*n_{TMOS} + 6*n_{TMSE}$ and $n_{TMOS} = 2.n_{TMSE}$, therefore $n_{-OR} = 14*n_{TMSE}$

$n_{H_2O} = h.14.\, n_{TMSE} \quad \leftrightarrow \quad \frac{V_{H_2O} \cdot \rho_{H_2O}}{M_{H_2O}} = h\,.\,14.\frac{V_{TMSE} \cdot \rho_{TMSE}}{M_{TMSE}}$

$V_{H_2O} = h\,.\,14.\frac{V_{TMSE} \cdot \rho_{TMSE}}{M_{TMSE}}.\frac{M_{H_2O}}{\rho_{H_2O}}$

Calculation of the amount of dye, d= $\frac{[dye]}{[Si]}$

[dye] = d. [Si] $\quad \leftrightarrow \quad \frac{m_{dye}}{M_{dye}.\, V_{TOT}} = d.\ \frac{n_{Si}}{V_{TOT}}$

$n_{Si} = 2n_{TMOS} + n_{TMSE}$ and $n_{TMOS} = 2.n_{TMSE}$ therefore, $n_{Si} = 4.n_{TMSE}$

$m_{dye} = 4.\, d.\frac{V_{TMSE}.\, \rho_{TMSE}.\, M_{dye}}{M_{TMSE}}$

As an example, for a sol made using protocol B with s = 500, h = 1 and d = 0.10 for dye IV, TMSE (98.5 mg, 93 µL, 0.36 mmol) and TMOS (110 mg, 107 µL, 0.72 mmol) were weighed in a 100 mL bottle. THF (3.0 mL) then aqueous HCl (1.0 M, 92 µL) were added under vigorous stirring. This transparent mixture was aged for two days at 60 ˚C in the sealed bottle after which THF (57 mL) was added. In the case of dye IV, the dye (69 mg, 0.15 mmol) was dissolved in the sol just before sol nebulization.

Sol	s	h	TMOS (µL)	TMSE (µL)	AzPTES (µL)	HCl (µL)	THF (mL)
2TMOS + TMSE	380	1	142.1	122.7	-	122	60
2TMOS + TMSE + AzPTES (1%)	380	1	125.6	121.5	19.8	122	60
2TMOS + TMSE + AzPTES (3%)	380	1	92.5	119.0	59.6	122	60
2TMOS + TMSE + AzPTES (5%)	380	1	59.6	116.5	99.1	122	60
2TMOS + TMSE	500	1	107.6	93.3	-	92	60
2TMOS + TMSE + AzPTES (1%)	500	1	94.4	92.1	15.0	92	60
2TMOS + TMSE + AzPTES (3%)	500	1	69.6	90.2	45.0	92	60
2TMOS + TMSE + AzPTES (5%)	500	1	44.6	88.4	75.0	92	60
2TMOS + TMSE	750	1	72.0	62.2	-	61.9	60
2TMOS + TMSE + AzPTES (1%)	750	1	63.6	61.5	10.0	61.9	60
2TMOS + TMSE + AzPTES (3%)	750	1	46.9	60.3	30.2	61.9	60
2TMOS + TMSE + AzPTES (5%)	750	1	30.2	59.1	50.3	61.9	60

Appendix IV – Quantum Yield

Fluorescence Quantum yield (QY) is the ratio between the number of fluorescence photons emitted and the number of photons absorbed. It is the fraction of photons absorbed resulting in emission of fluorescence and is represented as:

$$\emptyset_F = \frac{number\ of\ photons\ emitted}{number\ of\ photons\ absorbed}$$

Where $\emptyset_F$ is the quantum yield.

There are two methods to calculate the quantum yield of a fluorophore, the Comparative Method and the absolute method. The comparative method relies on the use of fluorescence standards with known fluorescence quantum yields and is mainly applicable to solution phase measurements.[1] The principle behind the comparative method is that solutions of the standard and test samples with identical absorbance at the same excitation wavelength can be assumed to be absorbing the same number of photons. Hence, the quantum yield of the test sample can be determined by taking the ratio of the integrated fluorescence intensities of the two solutions recorded under identical conditions.

On the other hand, the absolute method directly determines the number of photons emitted and absorbed. This in turn is facilitated by using an integrated sphere. The inner surface of the integrating sphere is highly reflective such that all light entering the sphere has only two possible fates: (a) absorption by the sample or (b) collection by the fluorimeter detection optics.[1] So, the integrated area under the corrected fluorescence spectrum of the sample represents the total number of photons emitted (per unit time) by the sample. The number of photons absorbed by the sample (per unit time) is also readily determined as the difference between the number of photons at the excitation wavelength reaching the detector with the sample in or out of the integrating sphere - i.e. the difference between the integrated areas under the “emission” curves representing the excitation peak.[1]

The quantum yield of the NP suspensions was determined using an absolute method originally developed by de Mello et al.[2] Four measurements were recorded for each sample to give four integrated intensities to determine the quantum yield with the following equation.

Appendix IV – Quantum Yield

$$\emptyset_F = \frac{E_c - E_a}{Filter\ Density * (L_a - L_c)}$$

Where

E_c is the integrated fluorescence as a result of direct excitation of the sample in the beam

E_a is the integrated fluorescence without sample (background of the sphere)

L_a is the integrated excitation profile with the empty sphere

L_c is the integrated excitation profile with the sample inside the sphere in the beam

L_a and L_c were obtained by measuring the emission signal at the excitation wavelength (λ_{exc}), measured between λ_{exc}-10 nm and λ_{exc}+10 nm with an increment reduced to 0.1 nm to ensure proper integration. Additionally, a neutral density filter of 0.5 % was used to reduce the intensity without changing the excitation profile and ensure that the maximal intensity stayed below $2x10^6$ CPS, the limit of the detector when recording the L_a and L_c signals. E_c and E_a were obtained by measuring the emission signal (between λ_{exc}+10 nm and 850 nm) at the excitation wavelength (λ_{exc}).

(1) http://www.nanocotechnologies.com/sites/default/files/attachments/pdf/Nanoco%2BTech%2BWhite%2BPaper%2BPLQY.pdf.

(2) De Mello, J. C.; Wittmann, H. F.; Friend, R. H. An Improved Experimental Determination of External Photoluminescence Quantum Efficiency. *Adv. Mater.* **1997**, *9* (3), 230–232.

Résumé

Nanoparticules fluorescentes cœur-coquille organique@silicates pour l'imagerie vasculaire in vivo

Chapitre I

Le développement des techniques d'imagerie biologique a permis non seulement d'étudier des processus biologiques fondamentaux, mais aussi une amélioration du diagnostic de maladies. L'imagerie biologique regroupe différentes techniques qui nécessitent des agents de contraste pour donner des informations sur les cibles biologiques à différents niveaux de résolution. Les techniques d'imagerie optique comme les imageries par bioluminescence ou par fluorescence offrent divers avantages par rapport à d'autres techniques utilisées actuellement (IRM, TEMP ou TEP) car elles sont bénignes, peu onéreuses, offrent une sensibilité élevée, une haute résolution spatiale ainsi qu'un fort rapport signal sur bruit dans le domaine spectral de l'infrarouge. La spectroscopie biphotonique, qui utilise l'absorption simultanée de deux photons d'énergie moitié (longueur d'onde double) par rapport à la transition monophotonique correspondante pour exciter le fluorophore permet une pénétration plus profonde dans les tissus en décalant la longueur d'onde d'excitation du bleu vers la fenêtre de transparence biologique dans le proche infra-rouge (typiquement 650-1050 nm).

En plus des progrès technologiques en instrumentation, le développement de traceurs à base de nanoparticules joue un rôle clef dans les avancées en imagerie biologique. Différents types de nanoparticules (NPs) fluorescentes ont été développés au cours des dernières années, comme les points quantiques (*quantum dots*, QD), les NPs métalliques, les NPs aux propriétés d'*upconversion* et les NPs polymériques ou à base de silice dopées avec des fluorophores.[1] Ces NPs doivent être biocompatibles, stables sous forme de colloïdes dans les milieux biologiques, éliminables facilement, présenter une émission forte dans la fenêtre de transparence biologique ainsi qu'une bonne photostabilité.[2–4]

Parmi les nanotraceurs fluorescents, les NPs à base de silice ont été l'objet de nombreuses recherches grâce à l'existence d'un très grand nombre de protocoles de synthèse permettant le contrôle de la taille, à leur faible toxicité et à la facilité de fonctionnalisation qui permet d'augmenter fortement la stabilité colloïdale.[5,6] Cependant, ce type de NPs donne des brillances relativement faibles car les molécules de fluorophore doivent être fortement dispersées dans la matrice afin d'éviter les désexcitations dues à l'agrégation moléculaire. Ceci limite typiquement les quantités de fluorophore à environ 1%wt.[6–8]

Afin de franchir l'obstacle de la faible concentration en fluorophore qui limite la brillance de ces systèmes, une nouvelle classe de NPs est en cours d'investigation à l'institut Néel. Il s'agit de NPs à architecture cœur-coquille organique@inorganique. Ces NPs sont constituées d'un cœur organique cristallin à propriété de fluorescence à l'état solide, enrobé d'une coquille de silice qui rend l'objet biocompatible.

Ces NPs ne sont actuellement synthétisables que par un procédé de séchage d'aérosol (*spray-drying*), en une seule étape, développé par le groupe d'A. Ibanez,[9] qui peut être rendu facilement reproductible et peu onéreux. Cette préparation est rendue possible grâce aux contrôles des réactions sol-gel et des procédés de nanocristallisation qui ont lieu simultanément.

L'encapsulation de nanocristaux organiques en matrice sol-gel[9–12] a été d'abord contrôlée dans des gels monolithiques, les nanocristaux croissant en milieu confiné au sein des pores du réseau sol-gel en formation.[10,11] Cette technique a ensuite été étendue à des couches minces de silice préparées par centrifugation (*spon-coating*). Des recherches poussées sur les nanocristaux formés dans les couches minces ont montré que le confinement spatial de la nanocristallisation est à l'origine du positionnement des nanocristaux à l'intérieur de la couche mince (Figure 6.1a). Les molécules organiques et les oligomères de silice sont initialement en solution (A1), puis lors de la centrifugation conduisant à l'évaporation brusque du solvant, une croûte de silice se forme à la surface (A2). Le réseau inorganique est bien plus fortement réticulé dans cette croûte que dans le volume en dessous, ce qui engendre une nucléation dans le volume de la couche mince (A3).

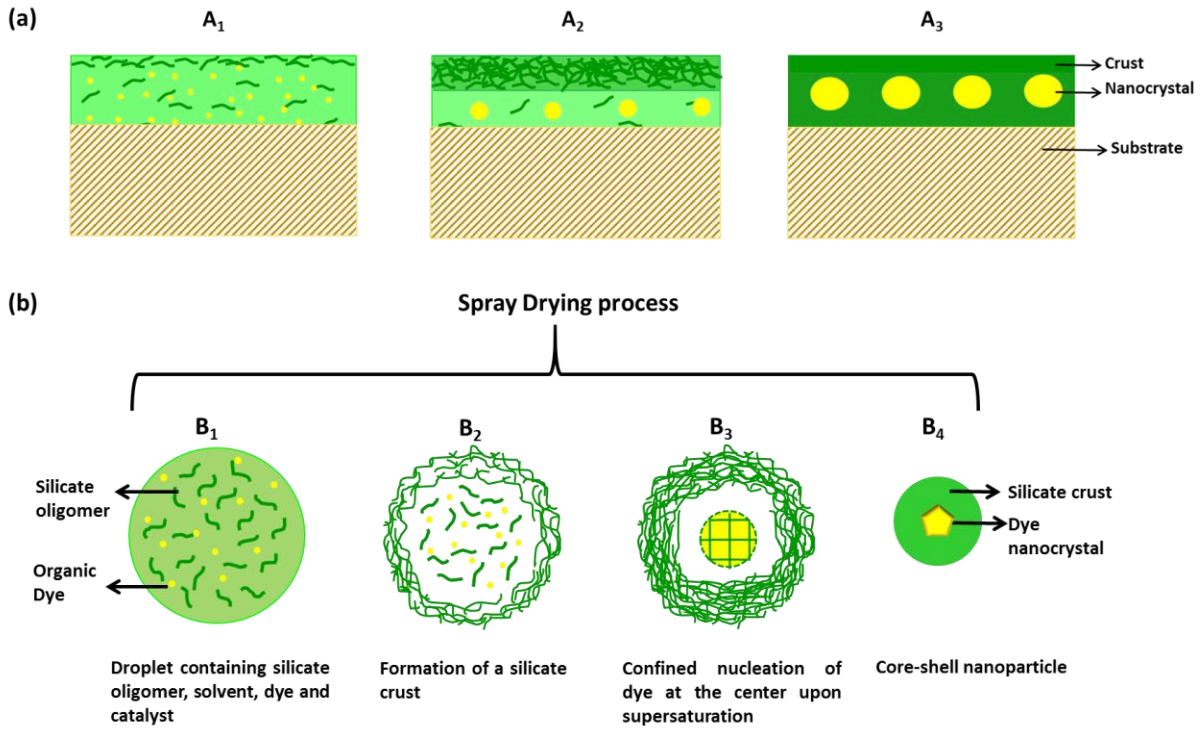

Figure 6.1. Schéma de principe de l'auto-organisation (a) Nanocristaux enterrés dans un film de couche mince par spin coating et (b) nanoparticules de types core-shell obtenus par séchage d'aérosol.

Ce concept a ensuite été étendu à la formation de NPs cœur-coquille par séchage d'aérosols.[9] Ce procédé est simple et facilement reproductible, et a été appliqué non seulement à des nano- ou microparticules de silice dense,[13,14] mais aussi à de la silice mésostructurée.[15–18] Il est basé sur la production de gouttelettes microniques par atomisation de sols de silice.

Dans le procédé étudié au laboratoire, les gouttelettes présentes dans l'aérosol ainsi formé contiennent une dispersion aléatoire d'oligomères de silice, de molécules de fluorophore et d'eau acide dans un solvant volatile (Figure 6.1b). L'évaporation du solvant dans le four provoque d'abord la formation d'une croûte de silice (B2) ; ensuite, la nucléation confinée du fluorophore a lieu au centre de la goutte (B3) par le même mécanisme de nucléation confinée que dans le cas des couches minces. Le nanocristal organique croît ainsi au centre de la nanoparticule en formation, qui est complètement sèche à la fin du passage dans le four (B4). La combinaison des procédés sol-gel et de nanocristallisation permet ainsi de former des NPs originales nanocristal organique@silice.

Le réacteur de séchage d'aérosol permettant la synthèse de ces NPs a été optimisé durant la thèse de C Philippot.[19] Ensuite, l'optimisation des paramètres de synthèse pour produire des NPs du colorant CMONS a été réalisée par J Zimmerman.[20] Enfin, une famille de fluorophores à l'état cristallin émettant dans le rouge a été conçue par G Eucat, avec des premiers essais d'encapsulation.[21] Pour l'heure, les NPs cœur-coquille organique@silicate ont été rapportées

dans le cas du CMONS et du rubrène,[9,22] alors que des nanoparticules similaires contenant des complexes de lanthanide luminescents ont aussi été produites.[23,24] Le cas du CMONS est particulièrement intéressant car deux polymorphes différents de ce composé ont pu être caractérisés selon la composition de l'organosilice utilisée dans la coquille,[25] ce qui met en évidence les difficultés possibles de ce type de synthèse.

Le travail présenté dans ce manuscrit est axé sur le développement d'une famille de NPs composites nanocristal fluorescent@coquille silicatée émettant dans le rouge en étudiant l'impact des conditions des réactions sol-gel et du procédé de séchage d'aérosol pour former des nanotraceurs pour l'imagerie biologique. Ces NPs devront être dispersées en solution colloïdale stable en milieu biologique afin de réaliser des expériences d'imagerie par fluorescence à deux photons de la vascularisation du cerveau de souris.

Une bonne compréhension des facteurs influençant la stabilité colloïdale des NPs en milieu biologique est extrêmement importante car la stabilité colloïdale des suspensions de NPs est largement affectée lors de l'introduction en milieu complexe. Ceci est dû aux différentes forces auxquelles sont soumises les NPs et qui conduisent à leur agrégation. Une stratégie permettant d'augmenter la stabilité colloïdale dans le sang consiste à PEGyler les NPs, c'est-à-dire à fonctionnaliser leur surface avec du poly(éthylène glycol), qui est une famille de polymères hydrophiles peu toxiques, approuvé par la FDA et qui est largement utilisée pour stabiliser les NPs vis-à-vis de l'agglomération, et de diminuer les processus d'opsonisation et de phagocytose permettant d'augmenter la furtivité de ces objets dans le sang.[26,27]

Différentes stratégies sont utilisées dans la littérature pour PEGyler les NPs de silice, comme le greffage post-synthétique de silanes à la surface ou bien la co-condensation sol-gel avec ces mêmes silanes durant la synthèse. Cependant, afin de préserver le cœur organique il est nécessaire de travailler dans l'eau à température ambiante. Aussi, nous avons choisi d'utiliser la réaction *click* de type CuAAC entre des fragments azoture inclus par co-condensation pendant la synthèse et des chaînes PEG dérivatisés par une fonction alcyne (Figure 6.2).

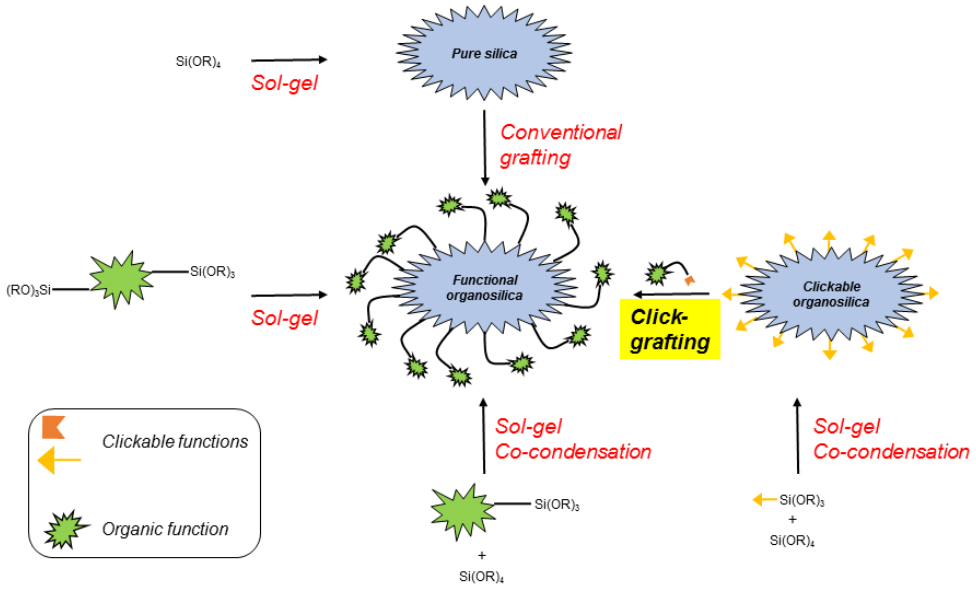

Figure 6.2.Différentes stratégies de fonctionnalisation de NPs silicatée incluant le post-greffage par chimie click de type CuAAC.[28]

En résumé, les objectifs de cette thèse sont les suivants :

- Optimiser les protocoles de synthèse des NPs cœur-coquille en utilisant le procédé de séchage d'aérosol.
- Caractériser les NPs ainsi obtenues pour connaître leur morphologie, leur cristallinité et leurs propriétés optiques.
- Optimiser la dispersion des NPs en suspension colloïdale
- Etudier la stabilité colloïdale dans différents milieux biologiques par diffusion dynamique de la lumière (DLS)
- Fonctionnaliser les NPs pour les rendre furtives dans les milieux biologiques et accéder à des temps de circulation longs dans le sang.
- Valider leur utilisation possible comme nanotraceurs en fluorescence sous excitation biphotonique en imageant la vascularisation cérébrale de souris.

Chapitre II

Ce chapitre s'intéresse au développement et à l'optimisation d'une famille de nanotraceurs fluorescents constitués de NPs cœur-coquille organique@silice contenant un cœur organique enrobé dans une coquille d'organosilice, avec un taux très important de fluorophore organique (30-40 %) pour l'imagerie biphotonique. Les colorants organiques utilisés pour le cœur organique ne sont pas commerciaux et ont été spécifiquement conçus au Laboratoire de Chimie de l'ENS Lyon (C Andraud, Y Bretonnière). Ce sont des émetteurs à l'état cristallin optimisés pour des

applications en imagerie biologique. Les précurseurs d'organosilice, le tétraméthoxysilane et le bis(trimethoxysilyl)éthane ont été choisi pour former la coquille hybride. De plus, le (3-azidopropyl)triéthoxysilane (AzPTES) a été ajouté au précurseurs silicatées afin de conférer des fonctions azoture aux NPs pour les fonctionnaliser ultérieurement par chimie click en milieu aqueux.

L'encapsulation des différents colorants n'a été rendue possible qu'après modification des conditions de réaction sol-gel, afin d'augmenter la polycondensation au sein du sol de départ et ainsi favoriser le confinement de la nucléation. Par ailleurs, l'introduction de l'AzPTES n'a pas conduit à des modifications particulières de la morphologie des NPs. L'optimisation de cette synthèse en une étape a été possible grâce au contrôle simultané des procédés de nanocristallisation et des conditions des réactions sol-gel en modulant les paramètres physiques du réacteur de séchage d'aérosol (température du four et du filtre électrostatique, débits de gaz et paramètres de nébulisation). Différents types de NPs ont été synthétisés selon le fluorophore organique utilisé pour former le cœur. Les NPs contenant les fluorophores **I**-**IV** (Figure 6.3) seront appelées **NP-I**-**NP-IV**.

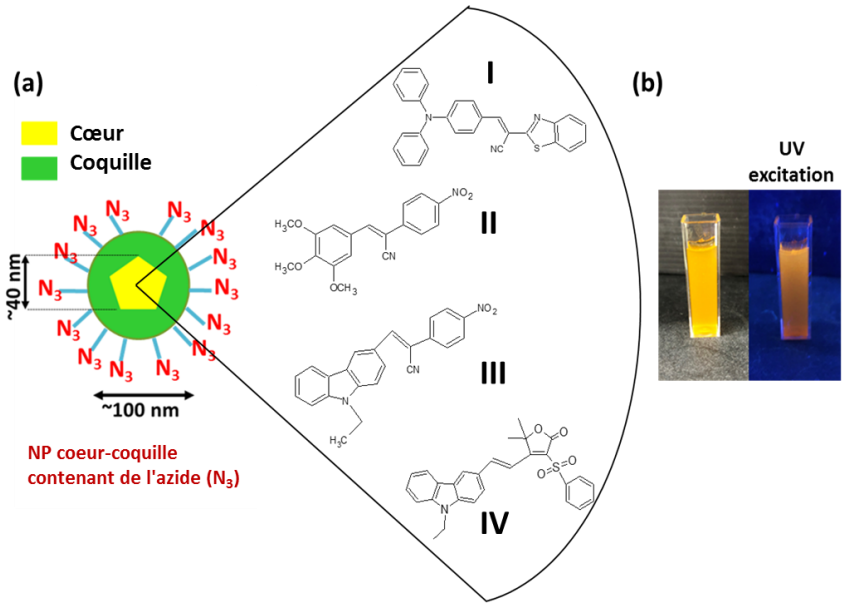

Figure 6.3. (a) Schéma générales des NPs et description des quatre fluorophores différents utilisées comme Cœur fluorescent cristallin. (b) Suspension colloïdale de NPs sous illumination UV.

La présence des cœurs organiques cristallins a été mise en évidence par microscopie électronique à balayage (MEB) après dissolution basique totale de la coquille silicatée (Figure 6.4). Par ailleurs, la cristallinité du cœur a pu être prouvée sans ambiguïté pour **NP-IV** par diffraction électronique dans un microscope électronique à transmission. Les NPs obtenues présentent un taux de charge en composé organique très élevé (29-42%), ce qui contribuera de façon importante à conférer une brillance forte aux NPs synthétisées.

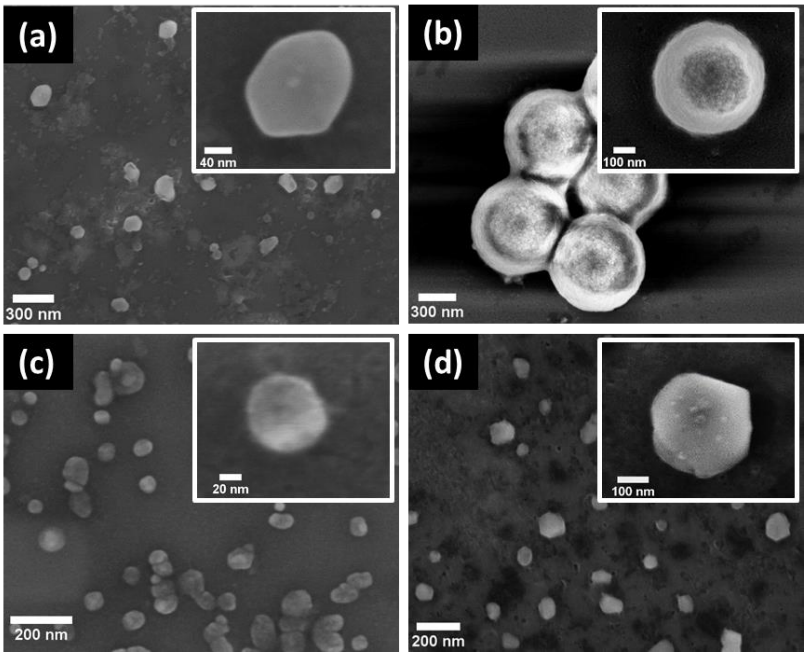

Figure 6.4. L'image FESEM des cœurs nanocristallin pour (a) **NP-I**, (b) **NP-II**, (c) **NP-III** et (d) **NP-IV**, après dissolution complète de la coquille silicatée

Les spectres de fluorescence des NPs sont similaires à ceux des poudres microcristallines sauf pour **NP-I** dont les maxima des spectres d'émission sont décalés vers le bleu de 640 à 620 nm. Cet effet est probablement dû à une amorphisation partielle sous l'effet des contraintes fortes exercées par la coquille de silice en formation durant la synthèse. En résumé, des NPs très brillantes ont été produites avec des maxima de spectres d'émission allant de 580 à 620 nm selon les colorants (Figure 6.5). Ceci est proche de la fenêtre de transparence biologique. Les rendements quantiques d'émission de ces suspensions de NPs sont de 3% pour **NP-I** et 1% pour **NP-IV**, significativement plus bas que dans les poudres microcristallines (18% et 46%, respectivement), mais suffisants pour que les NPs obtenues soient fortement brillantes, grâce notamment à la charge très élevée en fluorophores. Cette baisse de rendement quantique semble être due en particulier à la détérioration de la qualité cristalline des nanocristaux organiques sous l'effet des contraintes exercées par les coquilles de silice lors de leur séchage.

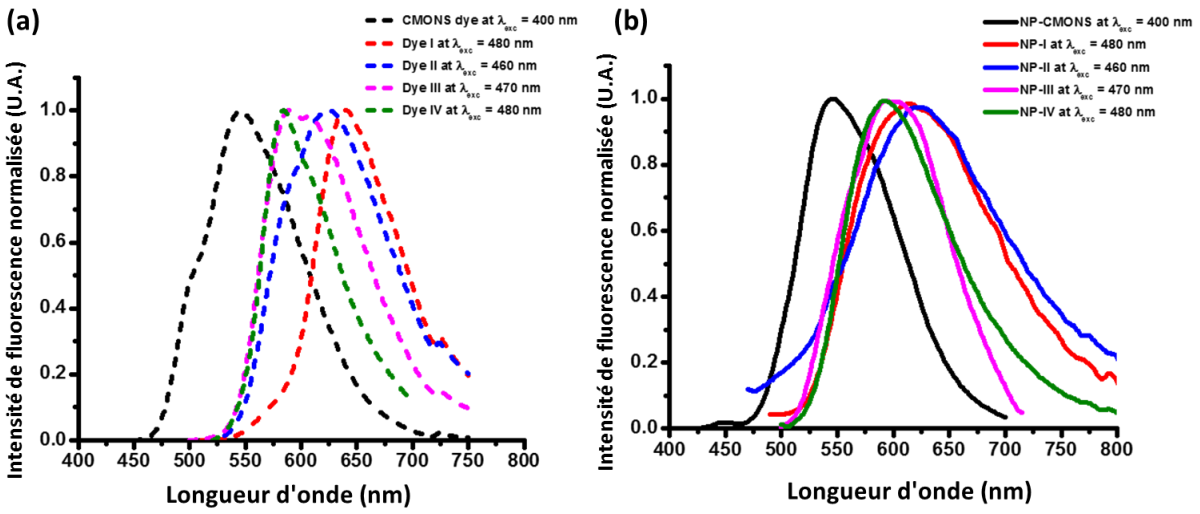

Figure 6.5. Spectre de fluorescence normalisée des différents colorants (a) sous forme de microcristaux et (b) confinée dans les nanoparticules silicatées

Chapitre III

Ce chapitre décrit la préparation de suspensions colloïdales stables après la synthèse des NPs, qui sont produites sous forme agglomérée en poudre sèche. Après dissolution partielle des coquilles silicatées en milieu basique puis neutralisation, des suspensions colloïdales de NPs ont pu être obtenues. Les NPs ont ensuite été fonctionnalisées par des chaînes PEG de différentes longueur et géométrie (linéaire ou ramifiée) par réaction de CuAAC (Figure 6.6). Les meilleures stabilités colloïdales ont été observées avec un PEG à longue chaîne (Mw = 5 kDa), probablement grâce à une stabilisation stérique efficace.

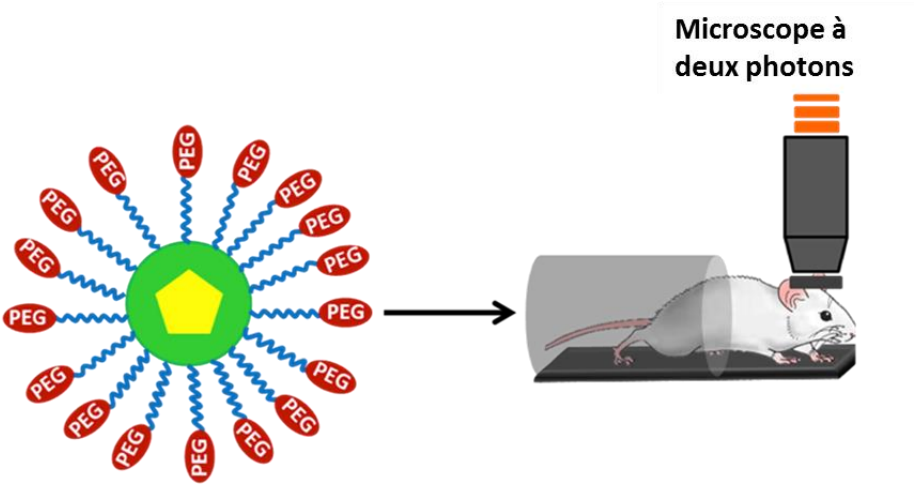

Figure 6.6. Nanoparticules fonctionnelles obtenues pour application en bio-imagerie

Les colloïdes de NPs fonctionnalisées ont été purifiées par dialyse, et concentrées par une technique d'ultrafiltration afin d'arriver à une densité optique de l'ordre de 1, nécessaire pour avoir assez de brillance pour des expériences d'imagerie biologique dans le sang. La stabilité colloïdale a été étudiée par DLS et par le suivi de l'intensité de fluorescence dans le temps. Les expériences de DLS ont été réalisées sur des suspensions colloïdales de **FNP-I** et **FNP-IV** (NPs après fonctionnalisation par du PEG 5k) dans l'eau pure et dans l'eau salée (NaCl 0.9%w), à 25 et 37 °C (Figure 6.7). Dans tous les cas, les distributions en taille montrent des maxima en dessous de 200 nm, ce qui constitue un progrès important par rapport aux études précédentes. L'absorbance des suspensions concentrées en milieu salin est stable sur 15 h, avec une baisse limitée à 10%. Les NPs montrent une brillance stable après fonctionnalisation, ce qui suggère qu'aucune désactivation n'a lieu sous l'effet des sels de cuivre. De plus, la stabilité colloïdale de **FNP-I** et **FNP-IV** a été testée en fluide biologique simulé et en présence de protéines comme le BSA et les globulines, en étudiant l'évolution des fonctions d'autocorrélation de DLS. Les deux types de suspensions sont bien stables dans ces conditions. Une agglomération minime a été observée en présence de concentrations élevées de BSA et globuline. Les colloïdes de **FNP-I**, qui présentent une meilleure stabilité que **FNP-IV**, ont été ainsi sélectionnés pour les tests d'imagerie *in vivo*.

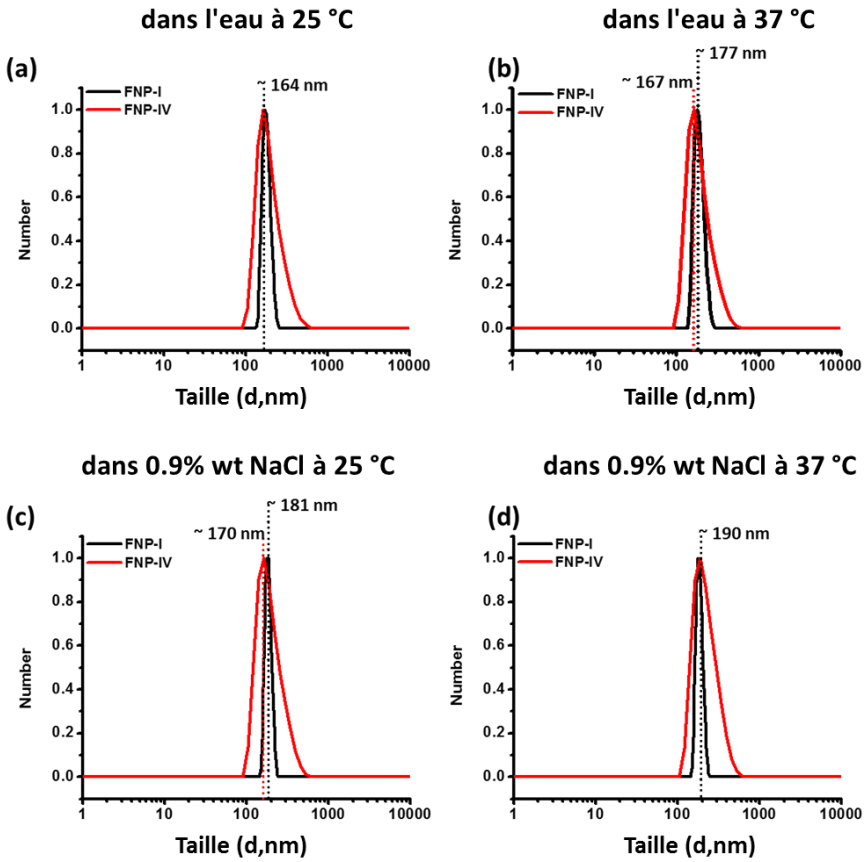

Figure 6.7. Mesure en DLS de la Distribution en taille de suspensions colloidales de FNP-1 (noir) et FNP-IV (rouge) dans (a) l'eau à 25°, (b) l'eau à 37 °C, (iii) dans une solution contenant 0.9 %w de sel NaCl à 25 °C et (iv) dans une solution contenant 0.9 %w de sel NaCl à 37 °C

Les tests d'imagerie ont été réalisés en injectant **FNP-I** par voie intraveineuse dans une souris. La prise d'image a été commencée environ 30 s après injection, et a permis d'observer des points très brillants dans le flux sanguin de la vascularisation cérébrale (Figure 6.8). La quantité de points lumineux dans ce flux sanguin disparait cependant rapidement dans le temps (en 15-20 minutes).

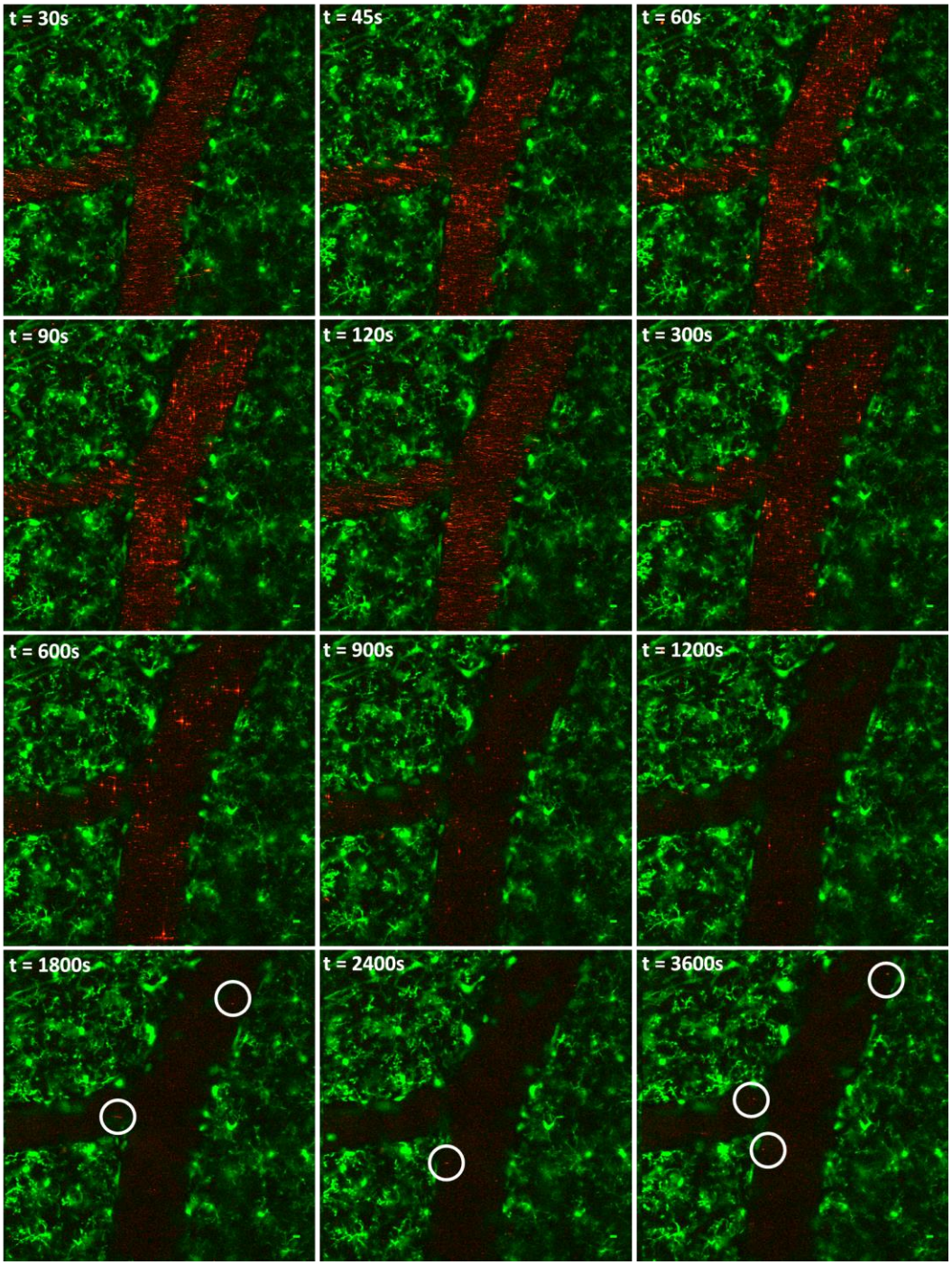

Figure 6.8. Circulation de FNP-I (points rouges) dans le flux sanguin à l'intérieur d'un vaisseau, enregistrée à différents temps après l'injection (la taille de l'image correspond à 200 x 200 μm^2)

La fluorescence reste cependant discernable un jour après injection. La disparition rapide des NPs du sang est attribuable à leur élimination par les macrophages, probablement vers le foie. Ceci peut être attribué à la taille des NPs (150-200 nm), qui sont alors reconnues par le système réticulo-endothélial. Il reste donc à sélectionner les NPs les plus petites et à les concentrer de

manière à obtenir suffisamment de brillance afin d'avoir une furtivité permettant de réaliser l'imagerie sur une période prolongée permettant un scan 3D. Il faut cependant retenir que la stabilisation colloïdale réalisée a permis d'observer la circulation de ces NPs dans le sang sans agrégation sur les parois des vaisseaux sanguins ce qui constitue un progrès important par rapport aux expériences précédentes.

Conclusion et perspectives

Les résultats préliminaires obtenus sont très prometteurs et nous encouragent à continuer ces études pour optimiser ces NPs pour l'imagerie *in vivo* de la vasculature. Des études approfondies des interactions entre le sérum humain et les NPs devraient permettre de mieux comprendre la formation et la composition de la couronne de protéines et de ses effets sur l'élimination des NPs. Cependant, une difficulté supplémentaire réside ici dans la polydispersité des NPs.

Afin de pouvoir utiliser ces NPs comme traceurs, le premier défi consiste à moduler la taille des NPs à moins de 80 nm pour allonger la durée de circulation en minimisant les chances de reconnaissance par le système réticulo-endothélial. Le deuxième défi est d'obtenir des solutions suffisamment concentrées après les différentes étapes de filtration. Un troisième défi est de conserver un cœur suffisamment bien cristallisé pour ne pas perdre les propriétés de fluorescence dans le cas des NPs les plus petites.

Afin de limiter la baisse du rendement quantique de fluorescence, une alternative en deux étapes peut être envisagée, en commençant par préparer des nanocristaux organiques en solution aqueuse puis en enrobant ces NPs par chimie sol-gel. La préparation de nanocristaux est en cours de développement à l'institut Néel, par atomisation d'une solution organique de fluorophore dans l'eau. Ceci résulte en la formation de gouttelettes dont la taille décroît par mélange, induisant la nucléation puis la croissance de cristaux du composé organique en milieu confiné. Les rendements quantiques des colloïdes obtenus sont bien plus élevés que dans le cas du procédé de séchage d'aérosol et parfois comparables aux poudres microcristallines, ce qui est très prometteur. Il reste encore à diminuer les tailles des NPs, puis à les enrober en solution aqueuse d'une couche de silice. La stabilisation colloïdale pourrait alors être optimisée en se basant sur les résultats obtenus au cours de cette thèse.

Bibliographie

(1) Liu, G.; Sheng, J.; Zhao, Y. In Vivo Near-Infrared Fluorescence Imaging. In *Nanotechnology Characterization Tools for Biosensing and Medical Diagnosis. Springer, Berlin, Heidelberg*; 2018; pp 67–125.

(2) Wolfbeis, O. S. An Overview of Nanoparticles Commonly Used in Fluorescent Bioimaging. *Chem. Soc. Rev.* **2015**, *44* (14), 4743–4768.

(3) Pierce, M.; Javier, D.; Richards-Kortum, R. Optical Contrast Agents and Imaging Systems for Detection and Diagnosis of Cancer. *Int J Cancer* **2008**, *123* (9), 1979–1990.

(4) Liu, T. M.; Conde, J.; Lipiński, T.; Bednarkiewicz, A.; Huang, C. C. Revisiting the Classification of NIR-Absorbing/Emitting Nanomaterials for in Vivo Bioapplications. *NPG Asia Mater.* **2016**, *8* (8), 1–25.

(5) Montalti, M.; Prodi, L.; Rampazzo, E.; Zaccheroni, N. Dye-Doped Silica Nanoparticles as Luminescent Organized Systems for Nanomedicine. *Chem. Soc. Rev.* **2014**, *43* (12), 4243–4268.

(6) Rampazzo, E.; Genovese, D.; Palomba, F.; Prodi, L.; Zaccheroni, N. NIR Fluorescent Dye Doped Silica Nanoparticles for in Vivo Imaging, Sensing and Theranostic. *Methods Appl. Fluoresc.* **2018**, *6*, 022002.

(7) Zhang, W.-H.; Hu, X.-X.; Zhang, X.-B. Dye-Doped Fluorescent Silica Nanoparticles for Live Cell and In Vivo Bioimaging. *Nanomaterials* **2016**, *6* (12), 81.

(8) Reisch, A.; Klymchenko, A. S. Fluorescent Polymer Nanoparticles Based on Dyes: Seeking Brighter Tools for Bioimaging. *Small* **2016**, *12* (15), 1968–1992.

(9) Philippot, C.; Dubois, F.; Bacia, M.; Djurado, E.; Ibanez, A. Fluorescent Organic Nanocrystal Confined in Sol-Gel Matrix for Bio-Imaging. *J. Sol-Gel Sci. Technol.* **2011**, *57* (3), 253–257.

(10) Monnier, V.; Sanz, N.; Botzung-Appert, E.; Bacia, M.; Ibanez, A. Confined Nucleation and Growth of Organic Nanocrystals in Sol–gel Matrices. *J. Mater. Chem.* **2006**, *16* (15), 1401–1409.

(11) Ibanez, A.; Maximov, S.; Guiu, A.; Chaillout, C.; Baldeck, P. L. Controlled Nanocrystallization of Organic Molecules in Sol-Gel Glasses. *Adv. Mater.* **1998**, *10* (18), 1540–1543.

(12) Dubuisson, E.; Szunerits, S.; Bacia, M.; Pansu, R.; Ibanez, A. Fluorescent Molecular Nanocrystals Anchored in Sol-Gel Thin Films: A Label-Free Signalization Function for Biosensing Applications. *New J. Chem.* **2011**, *35* (11), 2416–2421.

(13) Ishimori, T.; Senna, M. Control of Microstructure and Disintegration Properties of Silica Granules from PVA Slurries by Spray Drying. *J. Mater. Sci.* **1995**, *30* (2), 488–495.

(14) Maskara, A.; Smith, D. Agglomeration during the Drying of Fine Silica Powders, Part II: The Role of Particle Solubility. *J. Am. Ceram. Soc.* **1997**, 1715–1722.

(15) Baccile, N.; Grosso, D.; Sanchez, C. Aerosol Generated Mesoporous Silica Particles. *J. Mater. Chem.* **2003**, *13* (12), 3011.

(16) Julián-López, B.; Boissière, C.; Chanéac, C.; Grosso, D.; Vasseur, S.; Miraux, S.; Duguet, E.; Sanchez, C. Mesoporous Maghemite–organosilica Microspheres: A Promising Route towards Multifunctional Platforms for Smart Diagnosis and Therapy. *J. Mater. Chem.* **2007**, *17* (16), 1563–1569.

(17) Alonso, B.; Douy, a; Véron, E. Morphological and Textural Control of Spray-Dried

Mesoporous Silica-Based Spheres. *J. Mater. Chem.* **2004**, No. 14, 2006–2016.

(18) Alonso, B.; Clinard, C.; Durand, D.; Véron, E.; Massiot, D. New Routes to Mesoporous Silica-Based Spheres with Functionalised Surfaces. *Chem. Commun.* **2005**, No. 13, 1746–1748.

(19) Philippot, C.; University of Grenoble; France. PhD Dissertation: Elaboration et Caractérisation de Nanocristaux Organiques Fluorescents Insérés En Coquille Sol-Gel : Vers Le Développement d'un Nouveau Type d'agent Imageant Biologique, 2010.

(20) Zimmerman, J.; University of Grenoble; France. PhD Dissertation: Fluorescent Organic Nanocrystals Embedded in Organosilicate Shells : Towards Very Bright Tracers for Medical Imaging, 2014.

(21) Eucat, G.; University of Grenoble; France. PhD Dissertation: Molecular Engineering of New Organic Fluorophores and Encapsulation in a Sol-Gel Shell for Medical Imaging, 2014.

(22) Philippot, C.; Dubois, F.; Maurin, M.; Boury, B.; Prat, A.; Ibanez, A. New Core–shell Hybrid Nanoparticles for Biophotonics: Fluorescent Organic Nanocrystals Confined in Organosilicate Spheres. *J. Mater. Chem.* **2012**, *22* (22), 11370.

(23) Philippot, C.; Bourdolle, A.; Maury, O.; Dubois, F.; Boury, B.; Brustlein, S.; Brasselet, S.; Andraud, C.; Ibanez, A. Doped Silica Nanoparticles Containing Two-Photon Luminescent Eu(Iii) Complexes for the Development of Water Stable Bio-Labels. *J. Mater. Chem.* **2011**, *21* (46), 18613.

(24) Bourdolle, A.; D'Aléo, A.; Philippot, C.; Baldeck, P. L.; Guyot, Y.; Dubois, F.; Ibanez, A.; Andraud, C.; Brasselet, S.; Maury, O. NIR-to-NIR Two-Photon Scanning Laser Microscopy Imaging of Single Nanoparticles Doped by Yb ^{III} Complexes. *ChemPhysChem* **2016**, *17* (1), 128–135.

(25) Philippot, C.; Zimmermann, J.; Dubois, F.; Bacia, M.; Boury, B.; Baldeck, P. L.; Brasselet, S.; Ibanez, A. Polymorphism of CMONS Nanocrystals Grown in Silicate Particles through a Spray-Drying Process. *Cryst. Growth Des.* **2013**, *13* (12), 5241–5248.

(26) Suk, J. S.; Xu, Q.; Kim, N.; Hanes, J.; Ensign, L. M. PEGylation as a Strategy for Improving Nanoparticle-Based Drug and Gene Delivery. *Adv. Drug Deliv. Rev.* **2016**, *99*, 28–51.

(27) Veronese, F. M.; Pasut, G. PEGylation, Successful Approach to Drug Delivery. *Drug Discov. Today* **2005**, *10* (21), 1451–1458.

(28) Shenoi-Perdoor, S.; Noureddine, A.; Dubois, F.; Wong Chi Man, M.; Cattoën, X. Click Functionalization of Sol--Gel Materials. In *Handbook of Sol-Gel Science and Technology*; 2018; pp 3001–3040.

Summary

The aim of this work is the synthesis, optimization and functionalization of fluorescent organic@inorganic core-shell nanoparticles (NPs) to be used for two-photon deep tissue imaging of tumor vascularization. They comprise an organic dye nanocrystalline core surrounded by a silicate crust, and are synthesized using an original spray-drying method. This one-step synthesis requires the control of both the sol-gel chemistry and the nanocrystallization process. Alkoxide precursors, tetramethoxysilane and 1.2-bis(trimethoxysilyl)ethane are chosen to form the silicate shell while an azide-containing organosilane is added to enable further functionalization with alkyne-modified moieties using a click reaction. The organic dyes for the nanocrystalline core are designed to exhibit high fluorescence intensity in the crystal state under two-photon excitation in the near infrared and the appropriate physico-chemical properties to enable their nanocrystallization. Defect-free NPs with high brightness under two-photon excitation were obtained for four of these dyes. The synthesized NPs were then derivatized with different forms of alkyne-modified polyethylene glycol (PEG) to improve their colloidal stability by steric stabilization. The effects of the functionalization were studied using different characterization tools such as fluorescence spectroscopy and dynamic light scattering (DLS) under physiological conditions. The interactions of these core-shell NPs with different plasma proteins were thus investigated, with minimal aggregation in the presence of high concentrations of proteins. Preliminary two-photon fluorescence imaging tests in mice show high brightness.

Keywords: Silica nanoparticles, Fluorescence, Biophotonics, Sol-gel.

Résumé

Le but de cette thèse est la synthèse, l'optimisation et la fonctionnalisation de nanoparticules (NPs) coeur-coquille organique@inorganique pour l'imagerie profonde à deux photons de la vascularisation des tumeurs. Ces NPs contiennent un cœur nanocristallin organique enrobé d'une coquille de silice et sont synthétisées en utilisant une méthode de séchage d'aérosol originale. Ce procédé en une étape est rendu possible grâce au contrôle à la fois de la chimie sol-gel et du procédé de nanocristallisation. Les précurseurs silicatés sont des alcoxydes de silicium : le tétraméthoxysilane et le bis(triméthoxysilyl)éthane choisis pour former la coquille d'organosilice. De plus, un organosilane à fonction azoture est ajouté pour permettre une fonctionnalisation ultérieure avec des fragments organiques contenant des fragments alcyne par une réaction click. Les colorants organiques sont conçus pour fluorescer de façon très brillante à l'état cristallin sous excitation biphotonique dans le proche infra-rouge. Des NPs sans défaut ont été obtenues, avec une forte brillance sous excitation biphotonique. Les NPs synthétisées ont été dérivatisées avec des fonctions polyéthylène glycol pour augmenter leur stabilité colloïdale par effet stérique. L'influence de la fonctionnalisation a été étudiée en utilisant différentes techniques de caractérisation comme la spectroscopie de fluorescence et la diffusion dynamique de la lumière (DLS) en conditions physiologiques. L'interaction de ces NPs cœur-coquille avec différentes protéines sanguines a aussi été étudiée par DLS, et une très faible agrégation en présence de doses élevées de protéines a été montrée. Les premiers tests d'imagerie par fluorescence à deux photons sur souris ont montré une très forte brillance de ces NPs.

Mots-clés: Nanoparticules silicatées, Fluorescence, Biophotonique, Sol-gel.

Summary

The aim of this work is the synthesis, optimization and functionalization of fluorescent organic@inorganic core-shell nanoparticles (NPs) to be used for two-photon deep tissue imaging of tumor vascularization. They comprise an organic dye nanocrystalline core surrounded by a silicate crust, and are synthesized using an original spray-drying method. This one-step synthesis requires the control of both the sol-gel chemistry and the nanocrystallization process. Alkoxide precursors, tetramethoxysilane and 1.2-bis(trimethoxysilyl)ethane are chosen to form the silicate shell while an azide-containing organosilane is added to enable further functionalization with alkyne-modified moieties using a click reaction. The organic dyes for the nanocrystalline core are designed to exhibit high fluorescence intensity in the crystal state under two-photon excitation in the near infrared and the appropriate physico-chemical properties to enable their nanocrystallization. Defect-free NPs with high brightness under two-photon excitation were obtained for four of these dyes. The synthesized NPs were then derivatized with different forms of alkyne-modified polyethylene glycol (PEG) to improve their colloidal stability by steric stabilization. The effects of the functionalization were studied using different characterization tools such as fluorescence spectroscopy and dynamic light scattering (DLS) under physiological conditions. The interactions of these core-shell NPs with different plasma proteins were thus investigated, with minimal aggregation in the presence of high concentrations of proteins. Preliminary two-photon fluorescence imaging tests in mice show high brightness.

Keywords: Silica nanoparticles, Fluorescence, Biophotonics, Sol-gel.

Résumé

Le but de cette thèse est la synthèse, l'optimisation et la fonctionnalisation de nanoparticules (NPs) coeur-coquille organique@inorganique pour l'imagerie profonde à deux photons de la vascularisation des tumeurs. Ces NPs contiennent un cœur nanocristallin organique enrobé d'une coquille de silice et sont synthétisées en utilisant une méthode de séchage d'aérosol originale. Ce procédé en une étape est rendu possible grâce au contrôle à la fois de la chimie sol-gel et du procédé de nanocristallisation. Les précurseurs silicatés sont des alcoxydes de silicium : le tétraméthoxysilane et le bis(triméthoxysilyl)éthane choisis pour former la coquille d'organosilice. De plus, un organosilane à fonction azoture est ajouté pour permettre une fonctionnalisation ultérieure avec des fragments organiques contenant des fragments alcyne par une réaction click. Les colorants organiques sont conçus pour fluorescer de façon très brillante à l'état cristallin sous excitation biphotonique dans le proche infra-rouge. Des NPs sans défaut ont été obtenues, avec une forte brillance sous excitation biphotonique. Les NPs synthétisées ont été dérivatisées avec des fonctions polyéthylène glycol pour augmenter leur stabilité colloïdale par effet stérique. L'influence de la fonctionnalisation a été étudiée en utilisant différentes techniques de caractérisation comme la spectroscopie de fluorescence et la diffusion dynamique de la lumière (DLS) en conditions physiologiques. L'interaction de ces NPs cœur-coquille avec différentes protéines sanguines a aussi été étudiée par DLS, et une très faible agrégation en présence de doses élevées de protéines a été montrée. Les premiers tests d'imagerie par fluorescence à deux photons sur souris ont montré une très forte brillance de ces NPs.

Mots-clés: Nanoparticules silicatées, Fluorescence, Biophotonique, Sol-gel.